Ultrafast Dynamics of Magnetic Multilayer Films: Magneto-Optical Spectroscopy and Resonant Scattering in the Extreme Ultraviolet and Soft X-ray Spectral Regions

by

Dmitriy Zusin

B.S., Belarusian State University, 2009

M.S., University of Colorado Boulder, 2014

A thesis submitted to the

Faculty of the Graduate School of the

University of Colorado in partial fulfillment

of the requirements for the degree of

Doctor of Philosophy

Department of Physics

2018

This thesis entitled:
Ultrafast Dynamics of Magnetic Multilayer Films: Magneto-Optical Spectroscopy and Resonant Scattering in the Extreme Ultraviolet and Soft X-ray Spectral Regions
written by Dmitriy Zusin
has been approved for the Department of Physics

_____

Prof. Margaret M. Murnane

_____

Prof. Henry C. Kapteyn

Date _____

The final copy of this thesis has been examined by the signatories, and we find that both the content and the form meet acceptable presentation standards of scholarly work in the above mentioned discipline.

Zusin, Dmitriy (Ph.D., Physics)

Ultrafast Dynamics of Magnetic Multilayer Films: Magneto-Optical Spectroscopy and Resonant Scattering in the Extreme Ultraviolet and Soft X-ray Spectral Regions

Thesis directed by Prof. Margaret M. Murnane and Prof. Henry C. Kapteyn

Magnetism has been known for millennia. Yet, even today, our understanding of the interplay of various interactions and processes in a material that give rise to its magnetic properties and, in particular, are responsible for their dynamics is quite limited. Such understanding, however, is critical not only from the standpoint of fundamental research. From an applied perspective, there is a strong motivation to explore the possibility of utilizing the spin degree of freedom in the quest of improving the efficiency, increasing the speed, and reducing the size of logic devices, which requires a detailed understanding of magnetic interactions and their dynamics. Part of the reason for a lack of such understanding is related to experimental challenges in capturing materials' magnetism at its natural time and length scales. Recent advances in ultrafast extreme ultraviolet (EUV) and soft X-ray sources have enabled element-specific studies of magnetic materials with nanometer spatial and femtosecond temporal resolution by use of magneto-optics.

In this thesis, I present temporally and spatially resolved studies of ferromagnetic thin films. In Chapter 4, I develop a new magneto-optical technique that allows a direct measurement of the full resonant complex magneto-optical coefficient of a material with tabletop high harmonic (HHG) sources of EUV light. I apply it, along with a conventional magneto-optical technique, to a thin Co film in a pump-probe experiment to study the dynamic response of the film to a femtosecond laser pulse. By comparing the experimental results with theoretical predictions, a connection to the microscopic mechanisms of ultrafast demagnetization is made, and it is found that the transient magnetization dynamics in Co are mostly dominated by magnon excitations with possible smaller contributions from other mechanisms. In Chapter 5, I develop an approach for resonant magnetic scattering (RMS) on a tabletop with an HHG source that does not require

wavelength-selective optics and instead relies on the resonant nature of the scattering process. I use this approach to study magnetic textures with spatial resolution and, by applying a field to a ferromagnetic multilayer film, observe a transition from a disordered network of stripe domains to an ordered lattice of magnetic vortices. In Chapter 6, I present the results of a dynamic soft X-ray RMS experiment on a disordered domain network performed at the Linear Coherent Light Source (LCLS) at SLAC. By directly applying the experimental data to a carefully simulated domain pattern, I capture laser-induced transient changes in the domains in real space and observe strong non-uniformities in the demagnetization across the sample, which, with the help of simulations, are attributed to a combined effect of ultrafast spin-polarized currents and a gradient in the pump absorption throughout the thickness of the sample. In Chapter 7, I show preliminary simulations and provide an outlook towards time-resolved lensless magnetic spectro-microscopy with HHG sources.

Dedication

To my family.

Acknowledgements

I would like to thank my advisors Margaret Murnane and Henry Kapteyn for giving me the opportunity to join their group at JILA and for their generous support both within and outside of academic research. I am grateful to you for this truly remarkable experience. My special thank you goes to Tom Silva. I have aspired to absorb even a small fraction of your infinite wealth of knowledge and expertise in magnetism. I would also like to thank our long-time collaborators Justin Shaw, Hans Nembach, Eric Fullerton, Raj Medapalli, Dominik Legut, Karel Carva and Peter Oppeneer for putting up with sample requests, teaching techniques, lending equipment and providing theory support. The beam time at LCLS was a great opportunity, and I want to thank the entire SXR team and, in particular, Alex Reid, Loïc Le Guyader, Ezzio Iacocca, and Hermann Dürr for their help during and after the experimental run. Thank you to the entire Kapteyn-Murnane group for letting me learn from their broad scope of expertise, especially to the magnetics team, which at various points in time included Ronny Knut, Patrik Grychtol, Emrah Turgut, Adam Blonsky, Christian Gentry, Phoebe Tengdin, and Drew Morill. It has been a privilege to work with you. Michael Tanksalvala, thank you for offering your help so selflessly in a last minute push experiment. A special thank you to Dan Adams for patiently explaining to me the concepts of lasers, optics, and imaging and for always lifting my spirits. You are one of the smartest people I have ever met and an undefeated ping pong partner. But most importantly, I want to thank my parents, my sister, my grandparents, and my entire family, and, of course, Maithreyi Gopalakrishnan and Javier Orjuela-Koop, who are like family. Without you, none of this would have happened, and, frankly, none of this would matter either.

Contents

Tables

Table

Figures

Figure

Chapter 1

Motivation and Scope

Throughout its history, the research of magnetism has always been at the frontier of scientific knowledge. The discovery of electromagnetic induction by Michael Faraday in 1831 laid the foundation for the unification of electricity and magnetism and the subsequent development of the classical electromagnetic theory by James Maxwell.

In the late 1920's, the concept of spin, an intrinsic angular momentum of elementary particles, was introduced in quantum mechanics by George Uhlenbeck, Samuel Goudsmit, and Ralph Kronig, and the theoretical formalism was later developed by Wolfgang Pauli and Paul Dirac for the non-relativistic and relativistic cases, respectively. The property of spin gives rise to the intrinsic magnetic moments of elementary particles, and, therefore, the magnetic moments of atoms, which they make up, and, in turn, the magnetic moments of solids, which those atoms constitute. Around the same time, in 1928, Werner Heisenberg proposed his model of the spin-dependent exchange interaction, which became the first successful quantum mechanical picture of ferromagnetism and explained the nature of the phenomenological molecular field inside a ferromagnet postulated by Pierre-Ernest Weiss in 1907.

In the 1930's, developments in the band theory of ferromagnetism were made by Edmund Stoner, John Slater, and Neville Mott. However, despite this progress and the success of the density functional theory in the second half of the 20th century, our understanding of magnetism is still lacking. Even for the simple itinerant ferromagnets (Fe, Co, and Ni) there is no satisfactory theory that simultaneously explains their fractional magnetic moments and finite-temperature properties.

The dynamical evolution of a ferromagnet arising in response to a strong excitation, e.g. by a laser pulse, is a similarly poorly understood phenomenon.

Yet such understanding is of paramount importance for reasons that are both fundamental and applied in nature. From a fundamental standpoint, the understanding of magnetic materials, perhaps, holds an answer to high temperature superconductivity and, in more general terms, to a better understanding of strongly correlated quantum systems.

From an applied standpoint, the motivation for a better understanding comes from the technology sector, as it historically has. Specifically, the chip manufacturing industry is at a point where it has become increasingly difficult to fulfill the projections of Moore's law. Modern lithographic techniques are exploring the emerging extreme ultraviolet technology in order to manufacture chips with smaller features, but this same challenge of miniaturizing features on a chip will have to be faced again once the benefits of this technology have been exhausted. In addition, such miniaturization is often associated with increased energy dissipation.

A possible solution to these problems would be to exploit the spin degree of freedom in order to encode and transfer information, which is the subject of the field of spintronics [1, 2, 3]. It has been shown that spintronic devices, such as the non-volatile magnetic random access memory (MRAM), can be very energy-efficient [4, 5], which is highly relevant in the context of wide-spread battery-powered personal devices, and can be readily integrated with existing semiconductor microchips. Spintronic devices are also remarkably well suited for neuro-inspired computer architectures [6]. Such architectures, as opposed to the classical von Neumann architecture with centralized processing, are very desirable for data mining and deep learning algorithms that are needed to analyze the vast amount of data that is being generated worldwide at an ever increasing rate. A significant portion of this data can be of great value. New markets relying on big data analytics are already to emerging, and tailor-engineered magnetic materials can be an underpinning technology for all of this.

Additionally, a problem associated with high rates of data production is its storage. Despite significant progress in the flash-based data storage technology, the cost and lifetime of solid-state

drives prohibit their use for archival purposes. Hard-disk drives thus remain relevant—although their use has started to shift from personal devices to cloud storage facilities—and research is still being done to increase their capacity and efficiency while lowering the cost. For a new generation of spintronic and magnetic devices, a possibility of switching their state with laser pulses—the fastest man-made events in the Universe—is being explored in order to achieve the fastest possible switching speeds.

As elements on microchips become smaller and faster, and are expected to reach nanometer spatial and femtosecond temporal scales in the future, the applications listed above will ultimately require a coherent control of the spin degree of freedom in order to overcome the speed limit imposed by the induction laws of classical electromagnetism. This goal requires a fundamental understanding of the magnetic interactions in a material at various time and length scales.

A lack of such understanding is caused by the fact that, until recently, there hadn't been experimental tools that allowed us to observe magnetism at its relevant time and length scales. The relevant timescale in magnetism can be estimated from the time-energy uncertainty relation $\Delta E \Delta t \sim \hbar$. With the characteristic exchange interaction energy of ~ 0.5 eV, $\Delta t \sim \hbar/\Delta E \sim 1$ fs. The relevant length scales for magnetism range from interatomic distances (~ 1 Å) for the exchange interaction to correlation lengths extending to several tens of nm for magnetostatic interactions [7, 8]. This motivates the need for a tool that can probe magnetism on femtosecond time and, ideally, sub-nanometer length scales.

Figure 1.1 demonstrates the characteristic time and length scales for various systems and processes in the nano-world, and the temporal and spatial resolution of the tools currently available to carry out measurements of such systems. Unsurprisingly, there is no universal tool capable of providing both a very high temporal and spatial resolution . As shown in the figure, synchrotrons have the highest spatial resolution [9], while laser-driven high harmonic sources are unrivaled in terms of their temporal resolution [10, 11, 12, 13, 14]. Free-electron lasers (FELs) occupy the middle ground between synchrotrons and high harmonic sources with regards to their spatial and temporal resolution [15] and, in addition, provide a very high brightness. There has also been recent progress

in time-resolved electron [16] and Lorentz [17] microscopy. For the purposes of studying magnetism,

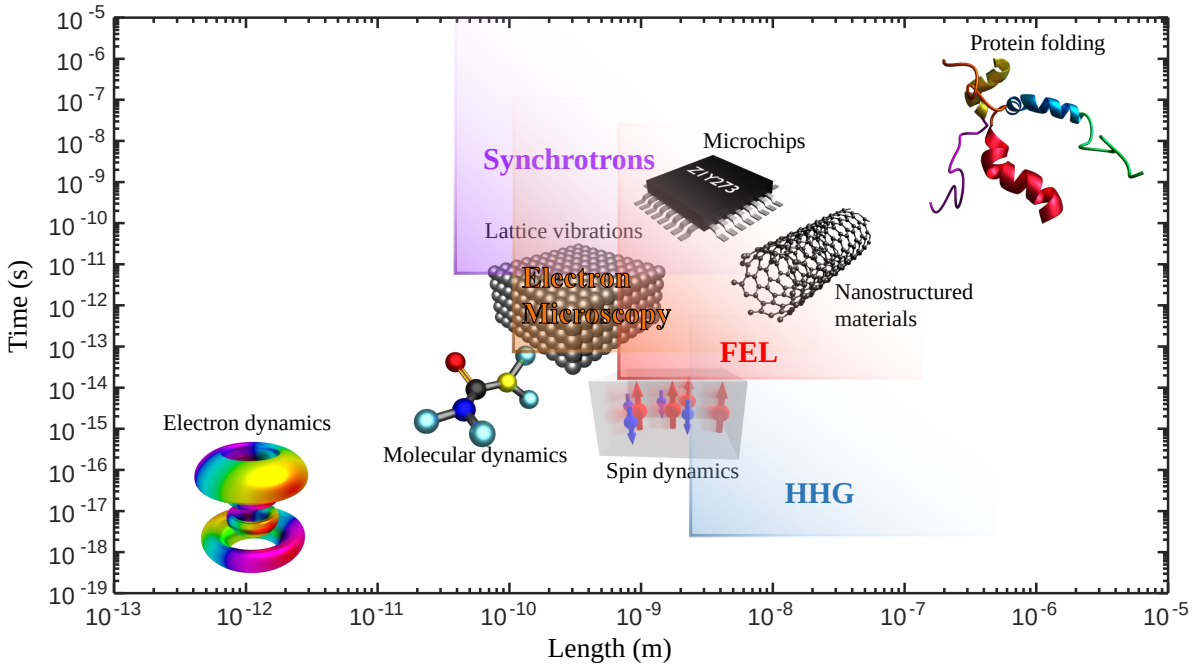

Figure 1.1: Relevant time and length scales of nano-systems and spatial and temporal resolution of selected tools available to study them.

the tool also needs to be sensitive to the spin degree of freedom. Apart from purely scientific merits, usability considerations, such as ease of access to the tool, must be taken into account. The latter makes tabletop high-harmonic sources very attractive for time-resolved EUV magneto-optical spectroscopy. Additionally, such sources generate short wavelength light, which makes them well suited for imaging magnetic textures with ∼10 nm features, which is relevant in a wide variety of magnetic systems and devices. Current developments in the mid-infrared (mid-IR) laser technology will enable soft X-ray (SXR) high harmonics, which will further improve the resolution to ∼1 nm. High harmonic sources thus have a potential of becoming a mainstream instrument for dynamic magnetic microscopy with high temporal and spatial resolution. This development would make the resources of state-of-the-art large-scale facilities available for more demanding experiments that, for example, require a high-brightness X-ray probe and would ultimately accelerate the progress in the study of materials and their magnetism.

This thesis is primarily focused on studying the phenomenon of ultrafast magnetization dynamics in multilayer films with tabletop high harmonic sources by use of both spectroscopic and spatially-resolved resonant scattering approaches. A portion of the thesis is dedicated to a development of high harmonic sources with full polarization control and to a time-resolved resonant magnetic scattering experiment at the LCLS FEL. In the introductory Chapter 2, I discuss the nature of magnetism in metals and its interaction with polarized light that leads to various magneto-optical phenomena, which thus allow us to measure magnetic systems with an optical probe. In Chapter 3, I discuss the process of high harmonic generation in detail and present a method of generating high harmonics with a two-color laser driver, which makes it possible to fully control their polarization. I also briefly discuss generation of coherent soft X-ray pulses in an FEL. In Chapter 4, the development of new EUV magneto-optical techniques is described. These techniques enable a complete characterization of a material's magneto-optical permittivity and, through *ab initio* density functional theory calculations, can capture the microscopic mechanisms at play during ultrafast demagnetization. In Chpater 5, I develop a spatially resolved EUV magneto-optical approach by use of resonant magnetic scattering (RMS) and study the formation of field-induced magnetic textures. In Chapter 6, I report the experimental results of a dynamic RMS experiment performed at LCLS. The analysis of the results, along with the relevant simulations, reveals the role of spin transport and non-uniform pump absorption in the laser-induced dynamics of magnetic domains. Finally, in Chapter 7, I provide an outlook for future work in the field and explore avenues for real-space time-resolved EUV magnetic microscopy.

Chapter 2

Introduction

In this chapter, I review several fundamental aspects pertaining to the field of materials' magnetism and its dynamics. I discuss the fundamentals of magnetism in materials and the effect it has on their optical properties, which, in turn, give rise to various magneto-optical phenomena and thus allow us to observe magnetism with an optical probe.

2.1 Magnetism of metals

Our present-day understanding of magnetism is rooted in two distinctly different models: the Heisenberg model and the Stoner model. The former describes the macroscopic magnetization as arising from an alignment of microscopic magnetic moments in the Heisenberg exchange field inside a material and successfully explains finite-temperature phenomena such as the temperature dependence of the magnetization and magnetic susceptibility. However, this model fails to explain the magnitude of the microscopic moments. The latter Stoner model considers delocalized electrons which form energy bands in the periodic potential of the crystal lattice. In this model, the difference in the number of electrons in the bands with opposite spins gives rise to an uncompensated magnetic moment. The Stoner model, on the other hand, cannot predict the finite-temperature properties of magnetic materials. Historically, attempts to develop a unified description of magnetism have taken either the Stoner or the Heisenberg model as a starting point, but, to date, a first principles unified theory is still lacking.

In the following, I review the Stoner and Heisenberg models with an emphasis on the $3d$ tran-

sition metals (Fe, Co, and Ni). I also provide a brief overview of the other two aspects of magnetism that this thesis is concerned with: Magnetic domains and textures, and ultrafast magnetization dynamics.

2.1.1 Origin of the band structure and the Stoner model

The Stoner model of ferromagnetism in metals was developed in the 1930's by Mott, Slater, and Stoner in an attempt to explain the broken magnetic moment values of ferromagnetic metals [18, 19, 20, 21, 22]. The magnetic moments of atoms are well known to be multiples of the Bohr magneton μ_B: $m = (2s + l)\mu_B/\hbar$, where s and l are the spin and orbital moments, respectively. Consider, for example, atoms of the $3d$ magnetic metals Fe, Co, and Ni. For Fe, the ground state electronic configuration is $[\mathrm{Ar}]3d^6 4s^2$, which leaves 4 unfilled electron states in the d-shell. According to Hund's rules, the minimum energy configuration must maximize the total spin quantum number in that shell, which leads to 4 unpaired electrons and thus to a magnetic moment of Fe of $4\mu_B$. Similarly, for Co and Ni, the corresponding moments are $3\mu_B$ and $2\mu_B$. In principle, the orbital moment also needs to be included, but in any case, a prediction based on the single atom picture gives integer magnetic moments. This compares poorly with the measured magnetic moment values in solids of $2.216\mu_B$ for Fe, $1.715\mu_B$ for Co, and $0.616\mu_B$ for Ni. The Stoner model was able to successfully predict the correct values of the magnetic moments of metals by taking into account the fact that in solids atomic levels become broadened and form energy bands. The formation of the bands can be understood qualitatively as a result of a perturbation of the atomic Coulomb potential due to bonding interactions. Valence states are less localized and are subject to stronger perturbations than the more localized core-level states, which is why valence energy levels are broadened stronger than the core levels. The periodicity of the lattice potential determines the exact details of the band structure.

Today, density functional theory (DFT) [23, 24, 25, 26] can be used to carry out precise band structure calculations. The details of DFT are beyond the scope of this thesis, but I shall briefly outline its main principles.

DFT is concerned with finding the ground state of a many-electron system, which could be a bulk solid, an interface, or a nano-particle, for example. In other words, the goal is to find the minimum energy eigen-solution of the non-relativistic time-independent Schrödinger equation for a system of N electrons

$$\hat{H}\left|\psi\left(\vec{r}_1,\ldots,\vec{r}_N\right)\right\rangle = E\left|\psi\left(\vec{r}_1,\ldots,\vec{r}_N\right)\right\rangle \tag{2.1}$$

where $\hat{H}$ is the Hamiltonian of the system, E is its eigenvalue, and $\left|\psi\left(\vec{r}_1,\ldots,\vec{r}_N\right)\right\rangle$ is the eigen-function, $\vec{r}_i$ are the spatial coordinates of the particles. The Hamiltonian has several terms, each describing a specific type of interaction

$$\hat{H} = \hat{T} + \hat{V} + \hat{U} = \sum_i^N \left(-\frac{\hbar^2}{2m_i}\nabla_i^2\right) + \sum_i^N V\left(\vec{r}_i\right) + \frac{1}{2}\sum_{i\neq j}^N U\left(\vec{r}_i,\vec{r}_j\right) \tag{2.2}$$

where $\hat{T}$ is the kinetic energy term, $\hat{V}$ is the potential energy of the electron-lattice Coulomb interaction, and $\hat{U}$ describes the electron-electron interaction. Because of this interaction, electrons cannot be considered as independent, and the eigenvalue problem (2.1) becomes virtually intractable without applying special techniques.

One particular advantage of DFT is that it simplifies the problem by reformulating it in terms of a single-particle in an effective potential. As a result, the number of degrees of freedom is reduced to four (three spatial coordinates and spin) from $4N$. This is done by introducing an electron density $\rho\left(\vec{r}\right)$. In the framework of the Hohenberg-Kohn-Sham DFT method [27, 28], the ground-state wavefunction $\left|\psi_0\left(\vec{r}_1,\ldots,\vec{r}_N\right)\right\rangle$ is uniquely determined by the ground-state electron density. In other words, the wavefunction is a functional of the electron density:

$$\left|\psi_0\right\rangle = \left|\psi\left[\rho_0\right]\right\rangle. \tag{2.3}$$

By extension, any observable, particularly the ground-state energy, is also a functional of ρ

$$E = E\left[\rho\right] = \left\langle\psi\left[\rho\right]\right|\hat{T} + \hat{V} + \hat{U}\left|\psi\left[\rho\right]\right\rangle. \tag{2.4}$$

The second Hohenberg-Kohn theorem [27] states that $E\left[\rho\right]$ is minimized for the ground-state electron density ρ_0, and it thus follows that the first order variation of the energy with respect to ρ is

stationary. Under a particle number constraint $N = \int d^3\vec{r}\rho(\vec{r})$ this statement can be expressed as

$$\frac{\delta\left(E\left[\rho\right] - \mu N\right)}{\delta\rho} = 0, \tag{2.5}$$

where μ is the chemical potential. Problem (2.5) is solved by introducing an auxiliary system of non-interacting particles moving in an external effective potential $\hat{V}_s$. Equation (2.5) then yields the Kohn-Sham equations:

$$\begin{gathered}\left[-\frac{\hbar^2}{2m}\nabla^2 + \hat{V}_s\right]\left|\phi_i\left(\vec{r}\right)\right\rangle = \epsilon_i\left|\phi_i\left(\vec{r}\right)\right\rangle, \\ \rho\left(\vec{r}\right) = \sum_i^N \left\langle\phi_i\left(\vec{r}\right)\right\rangle^2.\end{gathered} \tag{2.6}$$

The effective potential $\hat{V}_s$ consists of three terms: the periodic lattice potential $\hat{V}_l\left(\vec{r}\right)$, the electron-electron Coulomb repulsion $\hat{V}_H$, known as the Hartree term, and the exchange correlation term $\hat{V}_{XC}\left[\rho\right]$

$$\hat{V}_s = \hat{V}_l + \hat{V}_H + \hat{V}_{XC} = \hat{V}_l + \frac{e^2}{4\pi\epsilon_0}\int d^3\vec{r}\,'\frac{\rho\left(\vec{r}\,'\right)}{\left|\vec{r} - \vec{r}\,'\right|} + \hat{V}_{XC}\left[\rho\right]. \tag{2.7}$$

Since $\hat{V}_s$ depends on ρ, equations (2.6) must be solved in a self-consistent manner. Typically, the procedure starts with a guess for $\rho\left(\vec{r}\right)$, then $\hat{V}_s$ is calculated and eqs. (2.6) are solved. The solution is then used to update $\rho\left(\vec{r}\right)$. The steps are repeated iteratively until a convergence condition is reached.

In magnetic materials, the total electron density is a sum of the spin-up and spin-down densities $\rho\left(\vec{r}\right) = \rho_\uparrow\left(\vec{r}\right) + \rho_\downarrow\left(\vec{r}\right)$. The exchange correlation potential in eq. (2.7) then becomes spin-dependent, i.e., $\hat{V}_{XC} = \hat{V}_{XC}\left[\rho\left(\vec{r}\right), \sigma\left(\vec{r}\right)\right]$, where $\sigma\left(\vec{r}\right) = \rho_\uparrow\left(\vec{r}\right) - \rho_\downarrow\left(\vec{r}\right)$. The first equation in (2.6) is split into two—one for each spin direction, and the iterative solution procedure described above yields a spin-dependent band structure which defines a dispersion relation for each band index n in a 3-dimensional k-space $\epsilon_n^{\uparrow\downarrow} = \epsilon_n^{\uparrow\downarrow}\left(\vec{k}\right)$. From this dispersion relation, the total (spin-resolved) density of states (DOS) can be obtained by counting available states per unit volume in an energy interval $[\epsilon; \epsilon + d\epsilon]$. Mathematically, this is expressed as an integral over surfaces of constant energy ϵ (such as the Fermi surface shown in Fig. 2.1) in k-space [29]

$$g_{\uparrow\downarrow}\left(\epsilon\right) = \frac{1}{\left(2\pi\right)^3}\sum_n \int \frac{dS_{\vec{k}}}{\left|\nabla_{\vec{k}}\epsilon_n^{\uparrow\downarrow}\right|}, \tag{2.8}$$

where $dS_{\vec{k}}$ is a surface element (see Fig. 2.1). The spin-resolved density of states for fcc cobalt is

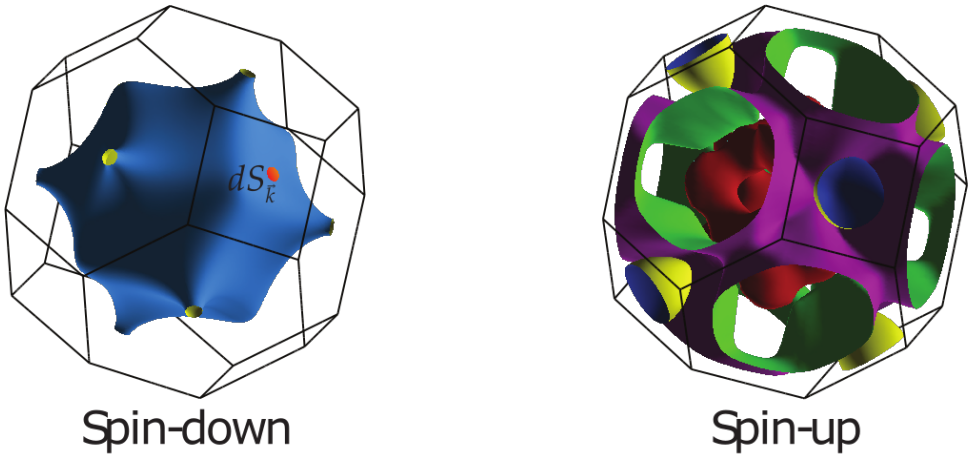

Figure 2.1: Fermi surfaces of fcc cobalt for spin-up and spin down states in the Brillouin zone. The surfaces were computed using the Elk code [30]. An area element used in eq. (2.8) is shown on the spin-down surface. Note that there are several spin-up Fermi surfaces originating from different bands.

shown in Fig. 2.2. The spin-up energy band is shifted by an amount Δ_{ex} relative to the spin-down band. This shift is called the exchange splitting, and it originates from the exchange-correlation potential $\hat{V}_{XC}$ in eq. (2.7). On a more fundamental level, it is caused by the Pauli exclusion principle. Because electrons are fermions, the same state cannot be occupied by more than one electron, and when a spin is flipped from, say, the spin-up to the spin-down band, it will occupy a higher energy state. The Pauli exclusion principle thus gives rise to an energy cost associated with a single spin flip in the presence of all the other spins. For that reason, the exchange splitting is called the spin-flip energy. Spin-flip excitations are known as Stoner excitations and are on the order of $\sim$1 eV, which is determined by the magnitude of the exchange splitting. The relative strength of interactions within the Stoner and Heisenberg models is discussed in subsection 2.1.3. Notice that the number of occupied states for the spin-up band (blue shaded area) is smaller than that for the spin-down band (orange shaded area). This is because in equilibrium, the chemical potentials of particles in both bands must be equal, and so the highest filled energy level is the

same in the spin-up and the spin-down bands. This leads to a greater total number of electrons in the spin-down band, which is called the majority band. The spin-up band is called the minority band. The choice of up and down is arbitrary, but it is important that the spins in the two bands are aligned in opposite directions relative to one another.

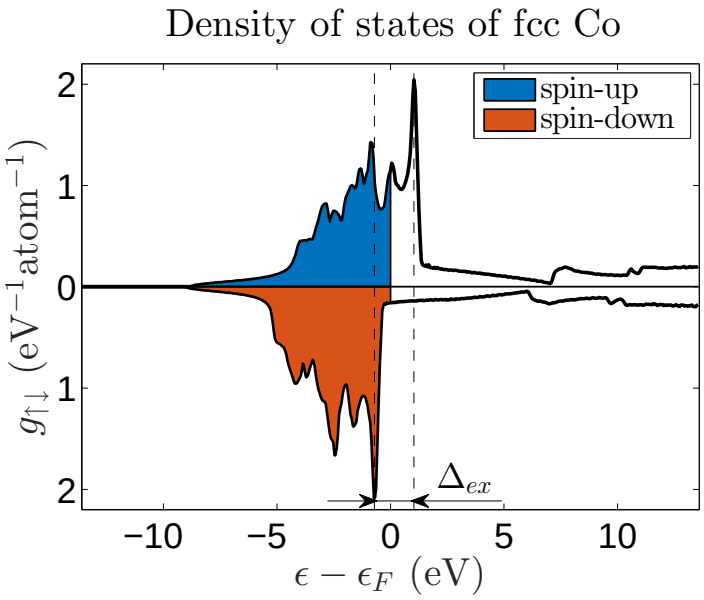

Figure 2.2: Spin-up (minority states) and spin-down (majority states) DOS for fcc Co. Filled states up to the Fermi level are shaded with color. The majority and minority bands are shifted in energy with respect to one another by an amount Δ_{ex} called the exchange splitting.

The difference in the number of majority and minority electrons gives rise to an uncompensated magnetic moment

$$m_{tot} = \frac{\hbar}{2}\gamma_e \int \left(g_\downarrow(\epsilon) - g_\uparrow(\epsilon)\right) f(\epsilon, T)\, d\epsilon, \tag{2.9}$$

where γ_e is the electron gyromagnetic ratio, and $f(\epsilon, T) = \left(e^{(\epsilon-\mu)/k_B T} + 1\right)^{-1}$ is the Fermi-Dirac distribution, where μ is the chemical potential that also depends on the temperature T. Because the gyromagnetic ratio for the electron is negative, the magnetic moment points in the direction of the minority spins. Equation (2.9) yields fractional magnetic moments for ferromagnetic metals that agree well with experiment.

Because of its ability to explain fractional magnetic moments, the Stoner model became a

significant breakthrough in the 1930's. To reiterate, in the Stoner model, valence electron states form energy bands, one spin-up and one spin-down. The two bands are shifted in energy with respect to one another, which, in equilibrium, results in a difference in the number of electrons filling each band. This difference leads to an uncompensated magnetic moment that is, generally speaking, non-integer, according to eq. (2.9). However, despite the success of this model, it still has major limitations. In particular, the Stoner model cannot predict the temperature dependence of the magnetic properties, such as, for instance, the Curie temperature of metals.

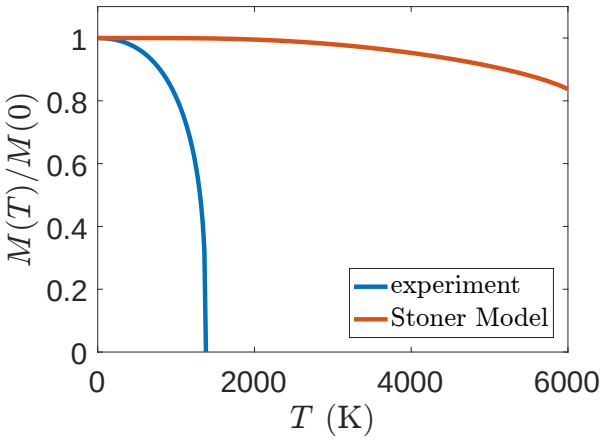

Figure 2.3: Comparison of the experimental temperature-dependent magnetization [31] and the Stoner model prediction for Co.

The Curie temperature is a temperature at which the macroscopic magnetization of a ferromagnet vanishes. In eq. (2.9), the temperature dependence of the magnetic moment is entirely due to the temperature dependence of the Fermi-Dirac distribution $f(\epsilon, T)$. This leads to an overestimation of the Curie temperature by a very significant amount. A comparison of the experimental temperature-dependent saturation magnetization of Co and a Stoner model prediction calculated with eq. (2.9) is shown in Fig. 2.3. In the figure, the calculated decay of the magnetization with temperature is underestimated because the density of states from Fig. 2.2 used in eq. (2.9) remains rigid, i.e., it is temperature-independent. If the exchange splitting was reduced at elevated temperatures, the magnetization would reduce faster. But even if an exchange splitting reduction were to

be accounted for, the large magnitude of Δ_{ex} on the order of $\sim$1 eV, as mentioned above, requires temperatures of $\sim 10^4$ K in order for the exchange splitting, and thus the magnetic moment, to vanish. This renders the Stoner model unsuited for explaining the temperature-dependent magnetic properties of materials. This problem is solved in the Heisenberg model.

2.1.2 Localized electrons and the Heisenberg model

Unlike the Stoner model, the Heisenberg model does not start from first principles. Rather, it considers a chain of localized magnetic moments that interact with one another by means of a quantum mechanical exchange. The strength of this exchange is an input parameter for the model. The Heisenberg model is closely related to the Weiss mean-field model of ferromagnetism, and for the sake of simplicity, I will first derive the temperature dependence of the magnetization in the Weiss mean-field approximation and then explain the nature of the mean field in the context of the Heisenberg exchange.

In 1907, Peter Weiss postulated the existence of a molecular field inside a ferromagnet that aligned all the microscopic magnetic moments in the direction of the field and that was proportional to the magnetization with a field constant β [32]

$$H_W = \beta M. \tag{2.10}$$

The mean B-field in the material is $B_W = \mu_0 (1 + 1/\beta) H_W$, where μ_0 is the magnetic permeability of vacuum.

Note that this is based on the SI system definition of the H-field $\vec{H} = \vec{B}/\mu_0 - \vec{M}$. By this definition, magnetization $\vec{M}$ has the units of A/m, the same as the field strength $\vec{H}$. An alternative definition is sometimes encountered where $\vec{H} = 1/\mu_0 \left(\vec{B} - \vec{M}\right)$, and $\vec{B}$ and $\vec{M}$ both have the units of Tesla. The first definition $\vec{H} = \vec{B}/\mu_0 - \vec{M}$ is used throughout this thesis.

Consider N identical magnetic dipoles $\vec{\mu}$ in a field $\vec{B}_W$. The potential energy of the i^{th} dipole in the field $\vec{B}_W$ is $E_i = -\vec{\mu}_i \cdot \vec{B}_W = -\mu B_W \cos\theta_i$, where θ is the angle between $\vec{\mu}$ and $\vec{B}_W$. A

single-dipole partition function is then [33]

$$Z = \sum_i \exp\left[\frac{\mu B_W \cos\theta_i}{k_B T}\right]. \tag{2.11}$$

Assuming $\vec{B}_W$ is along the z-axis, the average magnetic moment μ_z along this axis can be written as [33]

$$\mu_z = \frac{\sum_i \mu\cos\theta_i \exp\left[\frac{\mu B_W \cos\theta_i}{k_B T}\right]}{\sum_i \exp\left[\frac{\mu B_W \cos\theta_i}{k_B T}.\right]}. \tag{2.12}$$

And the total magnetization of a system of N dipoles is $M = N\mu_z$. If the system is quantized and the dipole moments are due to unpaired spin-1/2 electrons, then the angle θ_i takes only two values: 0 and π, and the magnitude of the magnetic moment is one Bohr magneton $\mu = \mu_B$. In this case, eq. (2.12) can be simplified, and the magnetization becomes

$$M = \mu_B N \frac{\exp\left[\frac{\mu_B B_W}{k_B T}\right] - \exp\left[-\frac{\mu_B B_W}{k_B T}\right]}{\exp\left[\frac{\mu_B B_W}{k_B T}\right] + \exp\left[-\frac{\mu_B B_W}{k_B T}\right]} = \mu_B N \tanh\left(\frac{\mu_B B_W}{k_B T}\right). \tag{2.13}$$

This equation, together with eq. (2.10) and the magnetization at 0 K $M(0) = \mu_B N$, gives an equation for the temperature-dependent magnetization

$$\frac{M(T)}{M(0)} = \tanh\left(\frac{\mu_B \mu_0 (\beta+1) M(T)}{k_B T}\right). \tag{2.14}$$

The argument of the tanh is small near the Curie temperature T_C, and, keeping only the first order term in its Taylor series expansion, one can obtain an expression for T_C

$$T_C = \frac{\mu_B}{k_B}\mu_0(\beta+1)M(0). \tag{2.15}$$

With an experimental value of the Curie temperature for a given material, eq. (2.14) can be solved numerically to find $M(T)/M(0)$. A result for Cobalt is shown in Fig. 2.4. An agreement with the experimental data is much better than that in Fig. 2.3.

Because the Weiss mean-field theory gives a fairly accurate prediction of the temperature-dependent magnetization, it is possible to use expressions (2.15) and (2.10) to estimate the magnitude of the molecular field B_W inside a material. From typical values of $\sim 10^3$ K for the Curie

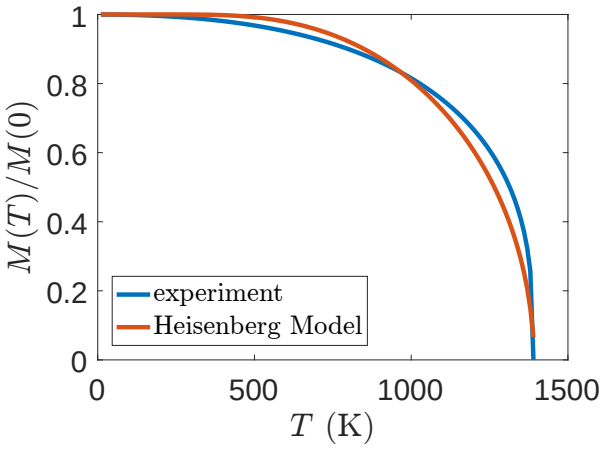

Figure 2.4: Comparison of the experimental temperature-dependent magnetization [31] and the Heisenberg model prediction for Co.

temperature of the ferromagnetic $3d$ metals, such as Fe, Co, and Ni, an estimated molecular field $B_W \sim 10^3$ T. If this was an actual magnetic field, it would require the presence of charge currents of such a high density that it would be above the damage threshold of the material itself.

The fact that ferromagnets exist means that the molecular field is not generated by charge currents. It arises from a purely quantum phenomenon of exchange interaction due correlation terms in the Hamiltonian describing a particular system, such as, for example, $\hat{U}$ in eq. (2.2).

The minimal system necessary to understand the exchange interaction is a system with two electrons, e.g., the He atom. Because electrons are fermions, the total wavefunction of a multi-electron system must be antisymmetric under an exchange of any pair of electrons, according to the spin-statistics theorem [34]. The Pauli exclusion principle is a consequence of this theorem. For a two-electron system, the total wavefunction is a product of the spatial part $|\psi(\vec{r}_1, \vec{r}_2)\rangle$ and the spin part $|\chi(\vec{s}_1, \vec{s}_2)\rangle$

$$|\psi_{asym}(\vec{a}, \vec{b})\rangle = |\psi_{sym,asym}(\vec{r}_1, \vec{r}_2)\rangle \, |\chi_{asym,sym}(\vec{s}_1, \vec{s}_2)\rangle \, . \tag{2.16}$$

In order for $|\psi(\vec{a}, \vec{b})\rangle$ to be antisymmetric, either $|\psi(\vec{r}_1, \vec{r}_2)\rangle$ must be symmetric and $|\chi(\vec{s}_1, \vec{s}_2)\rangle$ antisymmetric or vice versa. These two possibilities correspond to the singlet and triplet states of the two-electron system, respectively. In the singlet state, the spin part is antisymmetric, and the total spin quantum number is $S = 0$; hence, the projection on the z-axis $M_S = 0$. In the triplet state, the spin part is symmetric, and the total spin quantum number $S = 1$, and the spin projection quantum number $M_S = -1; 0; 1$. When applied to the He atom, the electron-electron interaction term in the Hamiltonian of the form $\hat{H}_{ee} = e^2/4\pi\epsilon_0 \, |\vec{r}_1 - \vec{r}_2|$, treated as a first order perturbation, gives rise to an energy difference ΔE between the singlet and triplet excited states. This difference is called the exchange energy. Thus, the exchange interaction is a result of the Coulomb repulsion between the electrons and a requirement of the Pauli exclusion principle that the total wavefunction of the system must be antisymmetric. For a detailed derivation of ΔE see Refs. [8] and [35].

In the Heisenberg Hamiltonian, which describes a system of interacting spins, the interaction

between the spins is parametrized with an exchange coupling J_{ij}

$$\hat{H}_{Heis} = -\sum_{i \neq j}^{N} J_{ij} \hat{\vec{s}}_i \cdot \hat{\vec{s}}_j = -2 \sum_{i<j}^{N} J_{ij} \hat{\vec{s}}_i \cdot \hat{\vec{s}}_j, \tag{2.17}$$

where the exchange integral (or exchange coupling) J_{ij} is similar to that for the He atom:

$$J_{ij} = \iint \psi_i(\vec{r}_1)\psi_j(\vec{r}_2) \frac{e^2}{4\pi\epsilon_0 |\vec{r}_1 - \vec{r}_2|} \psi_i^*(\vec{r}_2)\psi_j^*(\vec{r}_1) d^3\vec{r}_1 d^3\vec{r}_2. \tag{2.18}$$

Unlike in the He atom case, this exchange integral cannot be readily evaluated in a solid where the interactions are much more complex. An additional aspect that makes the evaluation of J_{ij} even more difficult for a realistic ferromagnetic system is the fact that the magnetic moments are not spin-1/2 electrons but are composite atomic spins. For those reasons, J_{ij} is normally taken as a model parameter.

With the Heisenberg Hamiltonian (2.17), it is possible to express the energy of the interaction of the i^{th} spin with all other spins as

$$E_i = -2\vec{s}_i \cdot \sum_j J_{ij} \vec{s}_j. \tag{2.19}$$

In the Weiss model, $E_i = -\vec{\mu}_i \cdot \vec{B}_W$, where the magnetic moment $\vec{\mu}_i = g\mu_B \vec{s}_i$, and g is the gyromagnetic factor. With this, the Weiss mean field can be identified in eq. (2.19).

$$\vec{B}_W = -\frac{2}{g\mu_B} \sum_j J_{ij} \vec{s}_j \tag{2.20}$$

From this expression, it becomes immediately clear that the origin of the Weiss molecular field is entirely due to the quantum mechanical exchange interaction. For this reason, it is also called the Heisenberg exchange field. The DFT result discussed in the previous subsection is mapped onto the Heisenberg model by separating the spin $\vec{s}_i$ into a constant component $\langle \vec{s}_i \rangle$ and a fluctuating component $\Delta\vec{s}_i = \vec{s}_i - \langle \vec{s}_i \rangle$ and making a substitution $\vec{s}_i \to \langle \vec{s}_i \rangle$ in eq. (2.20). For a lack of a satisfactory first principles theory, this approach is able to capture the fractional magnetic moment predicted by the band theory at $T = 0$ K as well as the finite temperature predictions of the Heisenberg model. More details on this topic can be found in Refs. [23] and [8].

2.1.2.1 Spin waves

The Heisenberg model together with the mean-field theory gives a good prediction of the finite temperature magnetic properties. However, the Hamiltonian in (2.17) needs to be examined further in order to understand what microscopic excitations lead to the predicted temperature dependence of the magnetization.

Consider a one-dimensional chain of spin-1/2 moments, such as in Fig. 2.5. It is described by

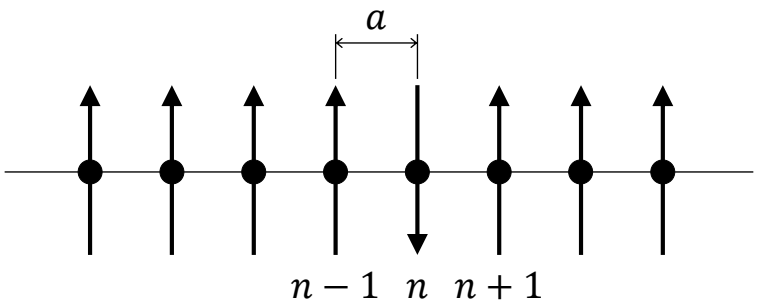

Figure 2.5: One-dimensional infinite periodic spin chain. The lattice period is a. The position of spin n is na

the Hamiltonian (2.17). I will consider a simplified case where only the nearest neighbors interact. In this case, the exchange integral $J_{ij} = J$ when $j = i \pm 1$ and $J_{ij} = 0$ otherwise. This simplifies the expression for the Heisenberg Hamiltonian. It can be simplified even further by using a realtion between the Pauli vectors and the permutation operator $\hat{\vec{s}}_i \cdot \hat{\vec{s}}_j = 2\hat{P}_{ij} - 1$, which yields [36]

$$\hat{H}_{Heis} = -2J \sum_n \left(\hat{P}_{n,n+1} - 1 \right). \tag{2.21}$$

I label the state of the spin chain with the n^{th} flipped moment as $|n\rangle$. In this notation, the action of the permutation operator on the states is as follows:

$$\begin{aligned} \hat{P}_{n,n+1}|m\rangle &= |m\rangle \text{ if } m \neq n, n+1, \\ \hat{P}_{n,n+1}|n\rangle &= |n+1\rangle, \\ \hat{P}_{n,n+1}|n+1\rangle &= |n\rangle. \end{aligned} \tag{2.22}$$

With these relations, the matrix elements $H_{n,m} = \langle n|\hat{H}_{Heis}|m\rangle$ of the Hamiltonian (2.21) can be evaluated [36]

$$\begin{aligned} H_{n,n} &= 4J, \\ H_{n,n+1} = H_{n,n-1} &= -2J, \\ H_{n,m} &= 0 \text{ if } |n-m| > 1. \end{aligned} \tag{2.23}$$

Now, consider a state of the chain which is a superposition of states with a spin flipped at each possible site

$$|\psi\rangle = \sum_n |n\rangle\langle n|\psi\rangle = \sum_n C_n|n\rangle. \tag{2.24}$$

where C_n is the probability amplitude that the spin on the n^{th} site is flipped. If the spin-flip excitation propagates down the chain, the probability that on any given site the spin is flipped evolves with time, and this evolution must obey the time-dependent Schrödinger equation

$$i\hbar\frac{d|\psi\rangle}{dt} = \hat{H}_{Heis}|\psi\rangle, \tag{2.25}$$

which, with eqs. (2.23) and (2.24), turns into an infinite system of equations

$$i\hbar\frac{dC_n}{dt} = \sum_m H_{mn}C_m = -2J\left(C_{n-1} + C_{n+1} - 2C_n\right). \tag{2.26}$$

If an excitation were to propagate unaltered, all the probability amplitudes C_n would have to change at the same rate. In other words, this means that $|\psi\rangle$ is a definite energy state. Thus an ansatz solution for C_n is

$$C_n = \alpha_n e^{\frac{-iEt}{\hbar}}. \tag{2.27}$$

Substituting this expression into eq. (2.26), a linear system of equations for the coefficients α_n, which determine the properties of an excitation, can be obtained

$$E\alpha_n = -2J\left(\alpha_{n-1} + \alpha_{n+1} - 2\alpha_n\right). \tag{2.28}$$

Since the spin chain under consideration is periodic with a lattice constant a, it is reasonable to expect that the coefficients α_n are connected with one another also in a periodic manner. With a

periodic ansatz $\alpha_n = e^{inka}$, a dispersion relation for an excitation propagating along the chain with a wavenumber $k = 2\pi/\lambda$ can be derived [36]

$$E = -2J\left(e^{-ika} + e^{ika} - 2\right) = 4J\left(1 - \cos ka\right). \tag{2.29}$$

For long wavelengths (small k's), the cosine in the expression above can be Taylor expanded, and, keeping terms up to second order, the dispersion relation is simplified to

$$E = 2Jk^2a^2. \tag{2.30}$$

Through the kinetic energy of a particle $E_{kin} = \hbar^2k^2/2m$, such an excitation corresponds to a particle with an effective mass [36]

$$m_{eff} = \frac{\hbar^2}{4Ja^2}. \tag{2.31}$$

These particles are called magnons. A magnon can be interpreted as a propagating excitation corresponding to a single spin flip distributed across an entire lattice. In the Heisenberg model, these excitations are responsible for the finite-temperature properties of ferromagnets.

Even though the derivation above was performed for a one-dimensional spin chain, it contains all of the essential physics, and the result can be generalized to three dimensions. Since an electron spin is 1/2, a single spin flip reduces the total spin angular momentum of the chain by 1, which means that magnons are integer-spin particles and, therefore, obey the Bose-Einstein statistics. A magnetization reduction due to magnon excitations can then be calculated simply by counting magnons. This can be done analytically at low temperatures (long magnon wavelengths) by integrating the Bose-Einstein distribution, with the energy given by (2.30), over k. Since the number of magnons is not conserved, the chemical potential is zero, and the Bose-Einstien distribution turns into the Planck distribution

$$n_k = \frac{1}{e^{E(k)/k_BT} - 1}. \tag{2.32}$$

Integrating this expression, with $E(k)$ given by eq. (2.30), over k in three dimensions gives the famous Bloch law for the temperature dependence of the magnetization [37]

$$M(T) = M(0)\left(1 - (T/\Theta)^{3/2}\right). \tag{2.33}$$

This dependence holds at low temperatures, and there are deviations from it near surfaces where some magnon states are prohibited.

Because magnons are bozons, a single state can be occupied by an unlimited number of magnons. Therefore, when the temperature is raised above 0 K, very long wavelength excitations would destroy the magnetic order. In order to prevent this from happening, a small energy gap must exist that prohibits such magnons. Magnetic anisotropy, which I discuss below, provides such a gap.

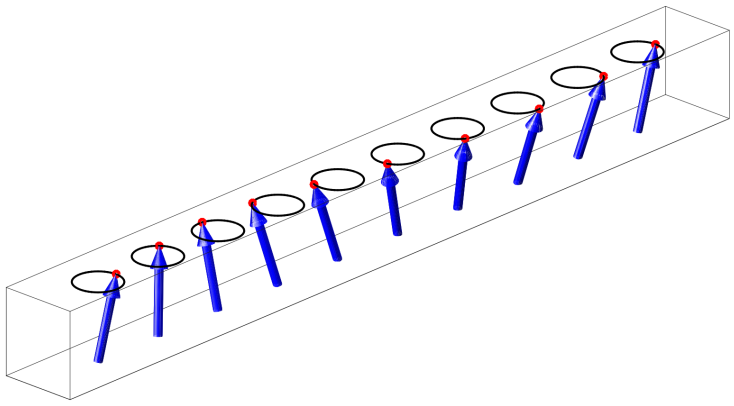

Figure 2.6: Spin waves are classical analogs of magnons. The magnetic moments precess around the direction of the mean field in a coherent manner: the phases of the precession for each spin are correlated.

Sometimes, it is helpful to consider the classical analog of a magnon—a spin wave. I shall provide a breif description of a spin wave, which is shown in Fig. 2.6. Just like a magnon, a spin wave excitation is distributed along an entire lattice. Each magnetic moment precesses around the direction of the mean magnetization. As a result, the magnitude of the moments' projections on this axis is reduced, which leads to an overall magnetization reduction. The precessional motion of different spins is coherent, i.e., their phases are locked relative to one another. Such collective dynamics amount to a propagating precession phase. This classical approximation can be useful when DFT results are mapped onto the Heisenberg model. Particularly, there are DFT methods

that yield correct finite-temperature results by applying a "frozen magnon" scheme, i.e., a spin spiral in which magnetic moments are tilted in the same way as they are in a classical spin wave [38]

2.1.3 Magnetic interactions in metals: itinerant and localized electrons

The reason that the Stoner and Heisenberg models result in such drastically different predictions and have limited applicability is that they start from two contrasting initial assumptions. The Heisenberg model assumes that the electrons are localized in real space, while the Stoner model assumes that they are localized in reciprocal space [39]. In reality, the applicability of each of these models is determined by the localization of the wavefunction of the electrons responsible for the magnetic properties of a material, which is highly system dependent. In general, it depends on the shape of the effective atomic potential, which includes a centrifugal term due to the orbital angular momentum as a correction to the screened Coulomb potential [8]

$$V_{eff}(r) = -\frac{Z^* e^2}{4\pi\epsilon_0 r} + \frac{l(l+1)\hbar^2}{2m_e r^2}, \tag{2.34}$$

where l is the orbital angular momentum quantum number. and Z^* is an effective charge of the nucleus that takes into account the screening by the inner shell electrons. An example effective potential and a $3d$ radial wavefunction are shown in Fig. 2.7. With a typical lattice constant of several Bohr radii a_0, the wavefunctions from the neighboring lattice sites will overlap.

In rare-earth metals, such as Gd, the $4f$ valence shell is only partially filled and thus produces an uncompensated magnetic moment. The wavefunction of the $4f$ electrons is highly localized [40], and, therefore, the magnetic moments have a local, atomic character. Rare earth metals are well described by the Heisenberg model.

The situation with the $3d$ transition metals Fe, Co, and Ni, is more complicated. The spatial extent of the $3d$ orbitals is in the intermediate range (although they are localized in some insulators [8]). The orbitals are localized enough to generate a significant local moment and, at the same time, broad enough to provide a sizable overlap with the neighbors. The $3d$ electrons are often referred

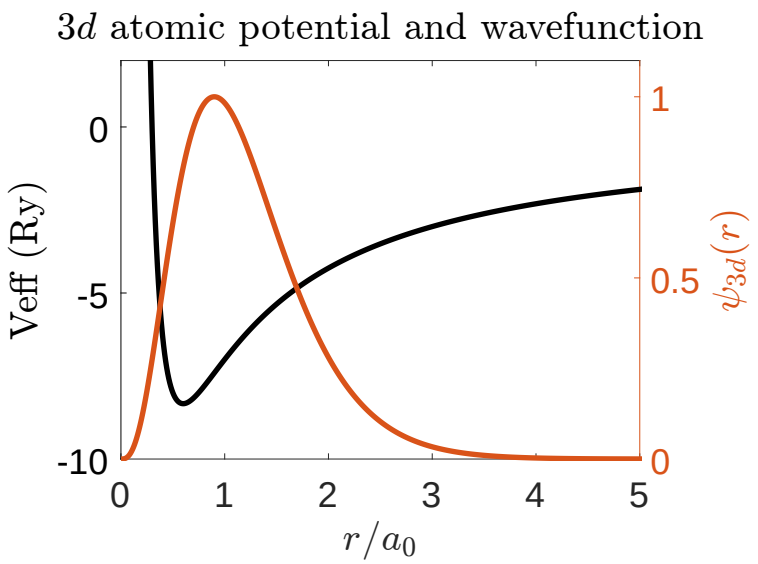

Figure 2.7: An effective potential and an outer shell wavefunction of a $3d$ element ($Z^* = 10$). The wavefunction extends to a few Bohr radii, which, in a solid, provides an overlap with the neighboring wavefunctions.

to as "itinerant" meaning that they are neither fully localized nor fully independent but rather jump from atom to atom. The Stoner and Heisenberg models by themselves cannot fully explain the full range of magnetic properties of the $3d$ ferromagnets, which necessitates a new theory of magnetism that is currently lacking.

There have been attempts to develop a unified theory of magnetism that have chosen either the Stoner or the Heisenberg model as a starting point. At present, a promising approach, called the self-consistent renormalization theory, starts with the Stoner model and considers the feedback of spin fluctuations on the band structure in a self-consistent manner. The details of this theory are beyond the scope of this thesis and can be found in Ref. [39].

For a lack of a better theory, at the moment, it is customary to map the DFT zero-temperature ground state onto the Heisenberg model, as mentioned above. In doing so, it is important to understand the meaning of exchange in both models. In the Heisenberg model, the exchange energy is the energy required to reverse a local moment composed of unpaired moments inside an atom in the molecular mean field of all other moments. This energy is typically $\sim$200 meV. In the Stoner model, the exchange energy corresponds to a single electron spin reversal in the sea of all other delocalized electrons. Its value is close to the energy difference of the singlet and triplet states of a two-electron atom and is on the order of $\sim$1 eV. The difference in the meaning of exchange in the two models is illustrated in Fig. 2.8.

The large value of the exchange splitting in the Stoner model is the reason why it predicts such high Curie temperatures, as discussed above. Because the exchange energy in the Heisenberg model is much lower, the T_C values predicted by it are much closer to the experimental ones. Ultimately, this brings up the question of whether the magnetic moment is completely quenched above T_C or whether the macroscopic magnetization vanishes because of the disorder, while the microscopic moments persist. The agreement of the Curie temperature predicted by the Heisenberg model with the experimental values suggests that the latter is the case. This is important in the context of ultrafast demagnetization, which I discuss below, because it limits the number of available relaxation channels for an excited spin system.

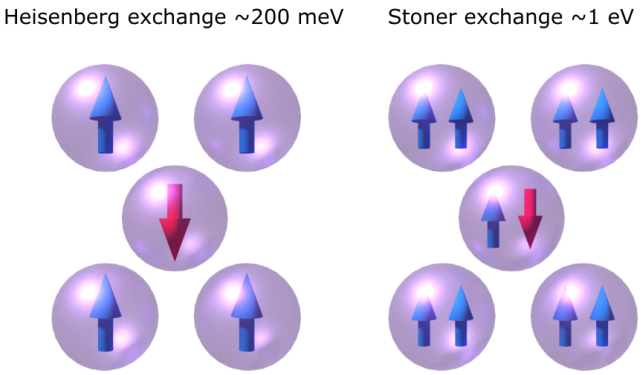

Figure 2.8: Exchange in the Stoner and Heisenberg models. In the Heisenberg model (left), the exchange energy corresponds to a reversal of a local magnetic moment in the mean exchange field of other moments. In the Stoner model, it corresponds to a spin flip of a single electron in the sea of all other electrons.

2.1.4 Spin-Orbit Interaction

The spin-orbit interaction couples spins to the lattice and leads to the magnetocrystalline anisotropy K_u [41] by breaking the symmetry of the isotropic exchange interaction and thus sets a macroscopic magnetization direction. It was discovered spectroscopically through the fine structure of atomic spectra of alkali metals. Qualitatively, it can be understood as the coupling of the spin of a bound electron to its orbital motion. In the frame of reference of the electron, the nucleus effectively orbits it creating a magnetic field $\vec{B}$. The field strength depends on the orbital angular momentum $\vec{L}$ of the electron and its distance to the nucleus, which is determined by the n quantum number. The interaction of the electron spin $\vec{S}$ with this field causes a shift in its energy by $E_{so} = -\vec{B} \cdot \vec{S}$. Since $\vec{B}$ is proportional to $\vec{L}$, the spin-orbit Hamiltonian $\hat{H}_{so}$ can be written as [8]

$$\hat{H}_{so} = \xi_{nl} \vec{S} \cdot \vec{L}, \tag{2.35}$$

where ξ_{nl} is referred to as the spin-orbit coupling constant which depends on the quantum numbers n and l and has the units of energy. It determines the strength of the spin-orbit interaction, which is rather weak in the $3d$ ferromagnets—on the order of $\sim 10 - 100$ meV and leads to a relatively small orbital magnetic moment [8]. Despite its low magnitude, the spin-orbit coupling plays an important role in setting a macroscopic magnetization direction. Because the crystal lattice has a preferred direction, due to the anisotropy of the bonding between atoms, it breaks the isotropic symmetry of $\vec{L}$ [42], which, in turn, sets the orientation of $\vec{S}$ since, in the minimum energy configuration, $\vec{S}$ must be parallel to $\vec{L}$. The energy difference between the parallel and perpendicular alignment of $\vec{S}$ and $\vec{L}$ is equal to the energy required to rotate the spins from their preferred easy-axis direction to one orthogonal to it. This energy is referred to as the magnetocrystalline anisotropy energy.

Despite a direct connection with the spin-orbit interaction, the magnetocrystalline anisotropy is still very difficult to estimate accurately because of the complex band structure calculations involved, which precludes a clear physical insight into its origins [43]. Nonetheless, it is understood that the magnetocrystalline anisotropy can be enhanced at interfaces due to missing chemical bonds [44, 45] and used to engineer magnetic films with a magnetization direction perpendicular to their

surface. The latter is critical for the creation of nanoscale magnetic domains and other magnetic textures, which is why in order to obtain them, stacks of ultrathin magnetic layers, with a high number of layer repeats to increase the number of interfaces, are typically grown.

2.1.5 Magnetic domains and textures

If a magnetic film were uniformly magnetized in the easy direction determined by its magnetocrystalline anisotropy, it would produce a stray magnetic field. In order to minimize this field, the magnetization breaks into domains of opposite directions. Additionally, the shape anisotropy K_s also contributes to the total internal energy of the film and thus affects the domain formation [46]. In nanometer-thin samples with the easy axis parallel to the surface of the film, the stray field is very small because it exits the film through the side surface whose area is negligible compared to the front and back surfaces of the film, and, therefore, the film typically stays uniformly magnetized. In samples with perpendicular magnetic anisotropy, the stray magnetic field is large, and, in the absence of an external field, magnetic domains are formed. The domain size and shape depend strongly on the magnetic interactions inside the sample, which can be controlled through the multilayer structure of the film. Typically, the thinner the film the smaller the domains.

The transition region between two oppositely magnetized domains in which the magnetization rotates from one direction to the other is called the domain wall. There are two distinct types of domain wall, the Néel wall, where the magnetic moments rotate around the axis parallel to the plane of the wall, and the Bloch wall, where the moments rotate around the axis perpendicular to the plane of the wall. The two wall types are shown in Fig. 2.9. The type, size and energy of domain walls are determined by the energy of the exchange interaction and magnetic anisotropy, which compete with one another. For example, if the anisotropy is large, an alignment of the moments parallel to the easy axis is favored. In order to minimize the total internal energy of the film, the volume with any other orientation of the magnetic moments would have to be minimized. For that reason, the width of the domain walls would have to be reduced. To the contrary, if the exchange energy is high, changing the orientation of a magnetic moment relative to other moments

becomes energetically unfavorable. Hence, in order to minimize the energy cost, the wall width increases [8].

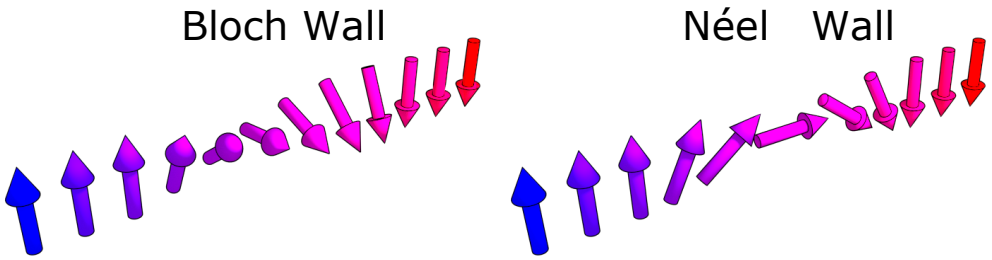

Figure 2.9: Bloch (left) and Néel (right) domain walls. The magnetization in the Bloch wall rotates around the axis perpendicular to the plane of the wall, while in the Néel wall, it rotates around the axis parallel to the wall plane.

Similarly to the formation of magnetic domains, various competing interactions lead to other magnetic textures. A particularly interesting example is magnetic vortices referred to as skyrmions [47, 48, 49], which arise due to the $\vec{\mu}\times\vec{\mu}$-type Dzyaloshinsky-Moriya interaction [50, 51] or competing domain wall energy and long-range dipolar interactions [52, 53, 54]. Skyrmions are said to be topologically stable in a continuous field approximation, which breaks down on the scale of a discrete atomic lattice. This topological stability makes them particularly attractive as information carriers in energy-efficient logic devices [55, 56]. A skyrmion can be thought of as a magnetic domain collapsed into a point and surrounded by a domain wall. Depending on the wall type, skyrmions can either be chiral or non-chiral. The former originate from Bloch-type walls and the latter from the Néel-type, as shown in Fig. 2.10.

Apart from topologically protected skyrmions, there is a variety of other textures such as magnetic bubbles, spin spirals, etc. Because magnetic textures span a broad range of correlation lengths from sub-nm to tens of nm and even μm, studying their static and dynamic behavior could provide critical insight into the microscopic origins of magnetism. I report such studies in Chapters 5 and 6.

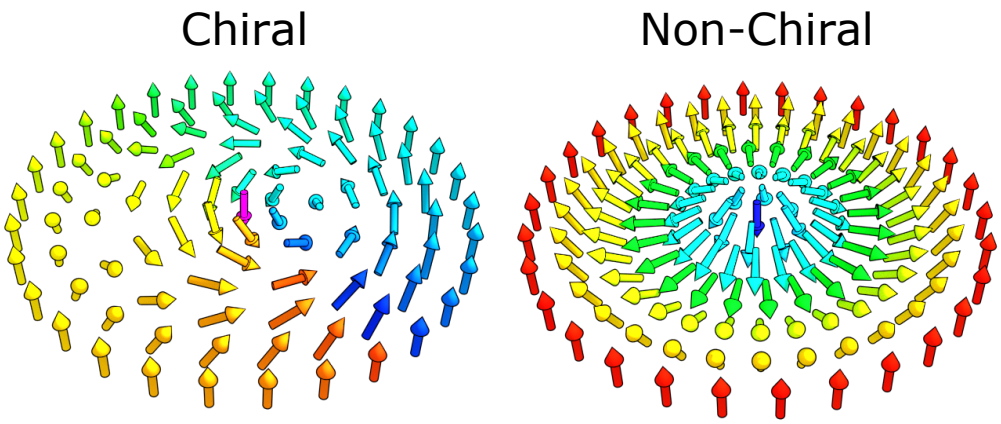

Figure 2.10: Bloch (chiral) and Néel (non-chiral) skyrmions.

2.1.6 Optically-induced ultrafast magnetization dynamics

The phenomenon of ultrafast magnetization dynamics driven by a femtosecond laser pulse was discovered in Ni in 1996 [57]. In this pioneering work, a magneto-optical polarization rotation of the probe pulse reflected from a Ni film was observed at various delay times after an excitation of the film by a 60 fs laser pulse. A sharp drop in the magneto-optical signal followed by a slower recovery was observed. An example curve measured in Co is shown in Fig. 4.4 in Chapter 4. This work opened up a new field in the magnetism research with the goal of understanding the microscopic mechanisms behind ultrafast magnetization dynamics. Such an understanding is needed not only from the perspective of fundamental research but also from an applied standpoint as it could lead to a new generation of spintronic devices that can be operated on the natural timescales of magnetism through a coherent control of their properties with light. Additionally, it could also have implications for high-temperature superconductivity as it is closely related to magnetism.

Since the original discovery, various types of laser induced magnetization dynamics have been found. They include type I and type II demagnetization dynamics and the phenomenon of all-optical switching. Type I demagnetization is observed in the $3d$ ferromagnets where a recovery phase happens immediately after an initial rapid loss of magnetization [58]. Type II demagnetization, where the rate of magnetization loss slows down significantly with time, is observed in rare-earth metals, their alloys, and other systems[59, 60, 61]. A magnetization reversal referred to as the all-optical switching (AOS) by a single as well as multiple laser pulses has also been demonstrated [62, 63, 64]. AOS suggests that light could directly couple to the spin system.

The difficulty in solving the puzzle of ultrafast demagnetization has to do with the complexity of the interactions involved. The coupled electron, phonon, and spin systems are strongly out of equilibrium, particularly on femtosecond timescales (see Fig. 2.11). There is also evidence suggesting that the phonon system could be out of equilibrium even on picosecond timescales [65]. This presents a great challenge for both theory and experiment. The theoretical challenge is in describing the transient dynamics of a many-body strongly coupled quantum system from first prin-

ciples. The experimental challenge is to unambiguously capture the dynamics of each of the three interacting systems, i.e., the electrons, lattice, and spins. Typically, a single technique is used for the purpose of measuring the response of a particular system to a laser excitation. For example, the lattice response can be accessed using EUV nanometrology [66], which measures the reflectivity and diffraction efficiency of patterned films, or resonant X-ray diffraction. Electron dynamics can be measured using photoemission or X-ray absorption spectroscopy or EUV and X-ray reflectometry, and the response of the spin system can be captured with the help of magneto-optical spectroscopies in the visible, EUV and X-ray spectral ranges as well as spin polarized photoemission. However, each experimental method measures a certain observable, which might not necessarily represent a pure electron, phonon, or spin system. For example, visible magneto-optical measurements have been shown to be affected by non-magnetic contributions to the signal [67, 68]. For that reason, studying the sample using multiple techniques can be advantageous because it can help disentangle the magnetic and non-magnetic contributions, as, for example, was done in Ref. [69], which reported a laser-induced ultrafast phase transition in Ni.

Although ultrafast demagnetization is a difficult subject, and, to date, no universal picture of this phenomenon exists, the general underlying microscopic mechanisms, illustrated in Fig. 2.11, can be understood, at least qualitatively, based on the conservation of energy and angular momentum, which is key for magnetism. On timescales of a few femtoseconds to tens of femtoseconds, the

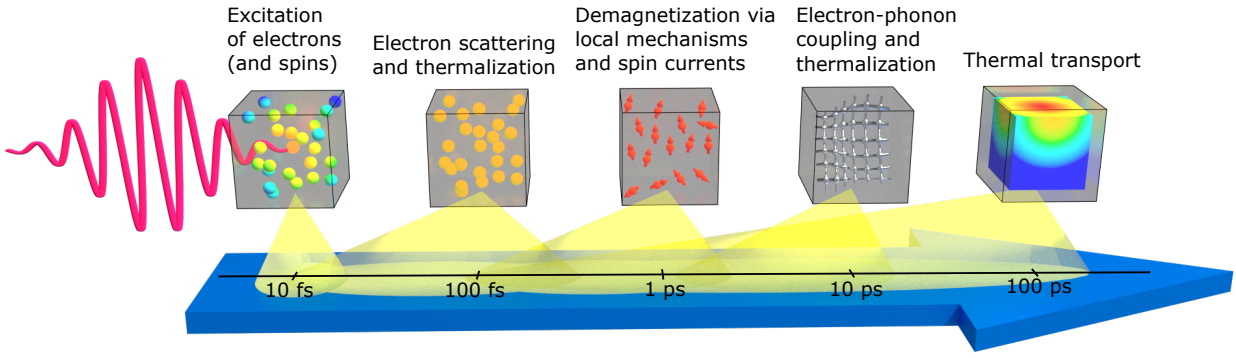

Figure 2.11: Timescales of electron, lattice, and spin dynamics after a laser excitation.

electron system absorbs the energy from the laser pulse. If the laser pulse is circularly polarized, it carries angular momentum, which upon absorption is transferred to the material and can eventually result in a magnetization reversal via the AOS process discussed above. If the pulse is linearly polarized, its net angular momentum is zero, and the energy absorbed by electrons is transferred to the spin and lattice systems on timescales that range from tens of femtoseconds to tens of picoseconds. Simultaneously, the three systems thermalize by means of various electron, magnon, and phonon scattering processes. Spin excitations lead to a decrease in spin polarization. Because angular momentum must be conserved and the net angular momentum transferred to the material by the pulse is zero, a reduction in spin polarization generates a net angular momentum anti-parallel to the direction of the majority spins. This means that an equal and opposite angular momentum must be absorbed somehow.

One possibility is to transfer this excess angular momentum to the lattice via the spin-orbit coupling, which is greatly enhanced for highly excited electrons and can thus happen on sub-picosecond timescales [8]. This process would generate a phonon and a magnon with opposite angular momenta, and magnons would reduce the net magnetization of the sample. Since the specific heat of the spin system is much smaller than that of the lattice (see Appendix C), the rise in the lattice temperature accompanying the exchange of angular momenta would be relatively small, compared to the rise in the spin temperature.

Another possibility is to drive the excited majority spins out of the pumped volume. The magnetization would then be reduced locally and enhanced elsewhere. In the case of magnetic domains or two oppositely magnetized films, such spin-polarized currents would reduce the magnetization everywhere due to a direct exchange of angular momentum between either the domains or the films.

Alongside all these processes, thermal diffusion also takes place. In metals, thermal transport is mediated by electrons and can thus be rather fast, while lattice heating is limited by the strength of electron-phonon coupling.

Laser-driven ultrafast magnetization dynamics is one of the main subjects of this thesis and

is considered in both uniformly magnetized films as well as in the presence of a network of magnetic domains in Chapters 4 and 6, respectively.

2.2 Origin of magneto-optical effects in the EUV and soft X-ray regions

The magnetic state affects the transition probabilities between different energy levels and can therefore be probed optically. I start by discussing the effect of X-ray magnetic circular dichroism (XMCD) which results in different absorption of left and right circularly polarized light. XMCD was first predicted theoretically in 1975 at the M-edge of Ni[70] and measured experimentally in 1987 at the K-edge of Fe [71]. It can be understood with the help of the two-step model of XMCD [72]. In the first step of the model, electrons are excited from the core $3p$-states to $3d$ states by circularly polarized photons, as seen in Fig. 2.12, which shows XMCD at the M-edge of a model ferromagnet. A careful analysis of the transitions with appropriate dipole selection rules, namely

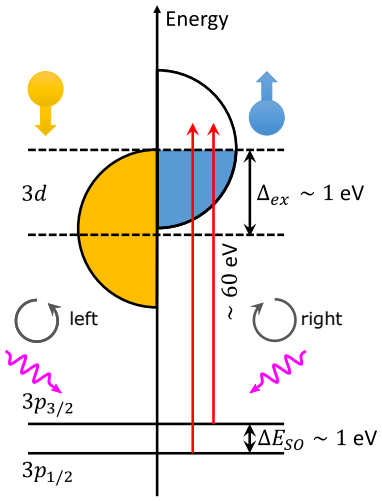

Figure 2.12: $3p \rightarrow 3d$ transitions in a model ferromagnet.

$\Delta l = \pm 1$, $\Delta s = 0$, $\Delta m_l = \pm 1$, and $\Delta m_s = 0$, yields an imbalance in the transition intensities for spin-up and spin-down electrons (see Refs. [8] and [72] for details). In the absence of the exchange splitting of the d-bands Δ_{ex}, however, this imbalance does not manifest itself as XMCD. The latter requires a second step, in which the exchange-split d-bands act as a spin detector. In Fig. 2.12,

unoccupied states above the Fermi level exist only for the minority spin-up states, which means that only spin-up electrons photoexcited from the $3p$ states can be absorbed. Combined with an asymmetry in transition intensities between spin-up and spin-down electrons for circularly polarized incident light, this results in an absorption asymmetry between the two circular polarizations.

The dipole matrix elements of the transitions between initial i and final f states for linear and right and left circular polarizations are [72]

$$\begin{aligned} D_{linear} &= \langle i| \hat{z} |f\rangle , \\ D_{right} &= \langle i| \hat{x} + i\hat{y} |f\rangle , \\ D_{left} &= \langle i| \hat{x} - i\hat{y} |f\rangle . \end{aligned} \tag{2.36}$$

First principles calculations of the transition elements are difficult yet necessary for the computation of the optical properties of materials by use of the linear response theory [73], which allows one to calculate the rank 2 optical conductivity tensor $\hat{\sigma}$ [74, 75] related to the dielectric tensor $\hat{\epsilon}$ as

$$\hat{\epsilon} = \hat{\mathbf{I}} + \frac{4\pi i}{\omega}\hat{\sigma}, \tag{2.37}$$

where $\hat{\mathbf{I}}$ is the identity matrix.

The dielectric tensor, in general, has non-zero off-diagonal components ϵ_{xy}, referred to as the magneto-optical dielectric permittivity, which give rise not just to XMCD, but to other magneto-optical effects as well. Because the transition matrix elements given by eq. (2.36) are complex, ϵ_{xy} is also complex and therefore affects both the amplitude and the phase of the transmitted EUV light. The latter, in the case of linearly polarized light incident normal to the surface of an out-of-plane magnetized film, leads to a magneto-optical rotation of the polarization, known as the Faraday effect. More details on the magneto-optical effects in a transmission geometry can be found in Chapter 5.

In reflection geometries, ϵ_{xy} affects the Fresnel reflection coefficients and leads to magneto-optical changes in the amplitude, phase and polarization of the reflected light, known as the magneto-optical Kerr effect (MOKE). Based on the symmetry of the dielectric tensor, there are three special cases when the magnetization is oriented in three distinct directions with respect to

the material's surface and the plane of incidence, as shown in Fig. 2.13, which are called longitudinal (L), polar (P), and transverse (T) MOKE.

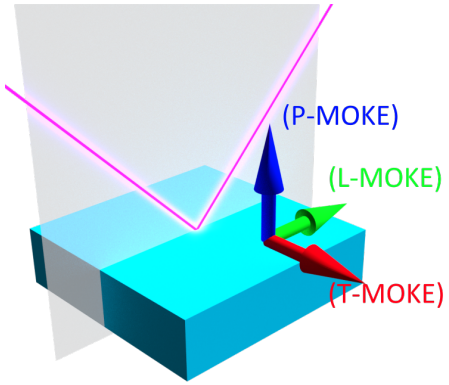

Figure 2.13: P- (blue), L- (green), and T-MOKE (red) geometries. The geometries are defined with respect to the plane of incidence of the probe and the surface of the sample. In P-MOKE, the magnetization m_z is orthogonal to the surface and parallel to the plane of incidence; in L-MOKE, m_y is parallel to both; in T-MOKE, m_x is parallel to the surface and orthogonal to the plane of incidence.

An analysis of the Maxwell boundary conditions at an interface between vacuum and a semi-infinite magnetized layer yields magneto-optical Kerr rotation θ_{MOKE} and ellipticity E_{MOKE} for the incident s- and p-polarizations for L- and P-MOKE, which, combined in a single complex quantity, are written as [73]

$$\begin{aligned}
\theta^{(s)}_{L-MOKE} + iE^{(s)}_{L-MOKE} &\approx \frac{\epsilon_{xy}}{\sqrt{\epsilon_{xx}}(\epsilon_{xx}-1)}\left(\frac{\cos\phi_i \tan\phi_t}{\cos(\phi_i-\phi_t)}\right), \\
\theta^{(p)}_{L-MOKE} + iE^{(p)}_{L-MOKE} &\approx \frac{\epsilon_{xy}}{\sqrt{\epsilon_{xx}}(\epsilon_{xx}-1)}\left(\frac{\cos\phi_i \tan\phi_t}{\cos(\phi_i+\phi_t)}\right), \\
\theta^{(s)}_{P-MOKE} + iE^{(s)}_{P-MOKE} &\approx \frac{\epsilon_{xy}}{\sqrt{\epsilon_{xx}}(\epsilon_{xx}-1)}\left(\frac{\cos\phi_i}{\cos(\phi_i-\phi_t)}\right), \\
\theta^{(p)}_{P-MOKE} + iE^{(p)}_{P-MOKE} &\approx \frac{\epsilon_{xy}}{\sqrt{\epsilon_{xx}}(\epsilon_{xx}-1)}\left(\frac{\cos\phi_i}{\cos(\phi_i+\phi_t)}\right),
\end{aligned} \tag{2.38}$$

where ϕ_i is the angle of incidence and ϕ_t is the angle of refraction, and ϵ_{xx} is the diagonal element of the dielectric tensor. L-MOKE and P-MOKE geometries require a polarization analysis of the magneto-optical reflections, which is difficult in the EUV spectral range due to a lack of efficient polarizers. Unlike L- and P-MOKE, T-MOKE shows no change in the polarization, however, for p-polarization, there is a magneto-optical change in amplitude, which makes this geometry well suited

for EUV magneto-optical spectroscopy. More details on EUV T-MOKE as well as an introduction of a new magneto-optical spectroscopic technique can be found in Chapter 4.

2.3 Conclusions

In this chapter, the Stoner and Heisenberg models of magnetism have been discussed. In the former model, electrons are delocalized whereas in the latter they are treated as local. The Stoner model explains the fractional magnetic moments of metals, and the Heisenberg model correctly predicts their thermodynamic properties. Spin fluctuations in the two models play an important role in the magnetization dynamics of materials following an ultrafast laser excitation. I also discussed the origin of magnetic domains and other textures, which may provide additional microscopic relaxation channels for laser-driven magnetization dynamics.

The splitting of the spin-up and spin-down bands in a ferromagnet leads to a polarization- and magnetization-dependent absorption of light, which underlies magneto-optical effects. The latter effects allow us to access the magnetic state of a material with light, and the magnetic contrast is enhanced at the elemental absorption edges.

Chapter 3

Ultrafast Sources of Coherent EUV and Soft X-ray Radiation

In this chapter, I discuss sources of extreme ultraviolet (EUV) and soft X-ray radiation, which are capable of producing temporally and spatially coherent femtosecond pulses and can thus be used in experiments studying ultrafast dynamics of materials and devices at the nanoscale with a high temporal and spatial resolution. My main focus is on tabletop laser-driven sources based on high harmonic generation (HHG), as they are the primary tool used in the experiments reported in this thesis. I also briefly discuss the working principles of a free-electron laser (FEL), which was used in the experiment reported in Chapter 6.

Historically, the first X-rays were produced in vacuum discharge tubes via bremsstrahlung and X-ray fluorescence. Synchrotron radiation was discovered in 1947 [76], and conversions of synchrotrons from particle accelerators into light sources started in the 1950's. In synchrotrons, radiation is produced by accelerating charged particles (most often electrons) moving at nearly the speed of light, and the spectrum ranges from infrared wavelengths to hard X-rays. Due to its small wavelengths, synchrotron light has been used to study many material and molecular systems, but it lacks the temporal resolution necessary to study such systems at their natural timescales (see Fig. 1.1). Today, laser-driven HHG sources and FELs are capable of providing both a high spatial and temporal resolution and can be used for element-specific ultrafast studies of material and molecular systems. HHG sources are particularly attractive as they are suited for laboratory-scale experiments and provide ease of access and require less maintenance and operation costs than large scale experimental facilities.

3.1 High Harmonic Generation

The first observation of HHG was reported in 1987 [77, 78], and a broad HHG spectrum generated with IR lasers with roughly similar harmonic intensities throughout the spectrum up to an HHG cutoff energy was reported shortly thereafter [79, 80]. The development of the theory of HHG started around the same time.

3.1.1 The three-step model

Historically, the first model of HHG was a semiclassical three-step model [81, 82, 83], shown in Fig. 3.1. Within this model, in a single-atom picture, an electron starts in the ground state and, when the atomic potential is distorted by the electric field of an incident laser pulse, it can tunnel out of the atom. Given the typical ionization energies of noble gases of ∼15-20 eV, the tunnel ionization requires laser intensities $> 10^{14}$ W/cm^2, which can be easily achieved using chirped pulse amplification (CPA) [84, 85] of femtosecond laser pulses. The ionization rate is known as the ADK rate after Ammosov, Delone, and Krainov who performed the original fully quantum calculations [86]. In the second step, the electron is accelerated in the laser field. Finally, for a range of phases of the laser field, the electron trajectory is closed, and the electron recombines with the parent ion emitting the energy it gained from the laser field in the form of a short-wavelength burst of light.

An electron motion in the field can be described classically by Newton's equations of motion. For a linearly polarized laser driver, the problem becomes one-dimensional. Consider an electron (charge $-e$, and mass m_e) in a harmonic field $E_0 \cos \omega t$, where ω is the angular frequency of the field. An equation of motion then reads

$$m_e \ddot{x} + eE_0 \cos \omega t = 0. \tag{3.1}$$

Integrating this equation with the initial condition that, at the time of the ionization t_i, of zero

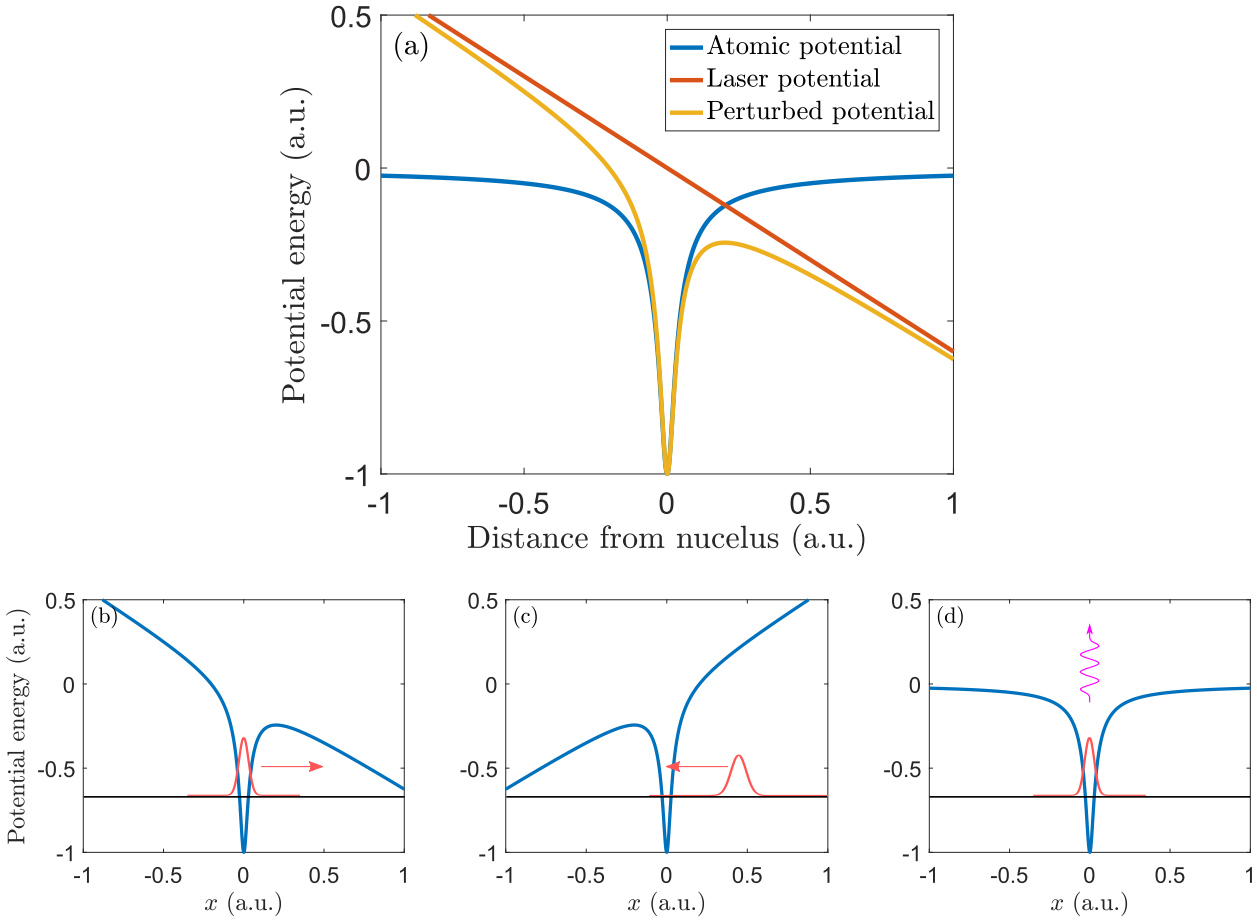

Figure 3.1: Three-step model of HHG. (a) Original and perturbed atomic potential along with the driving laser potential. (b)-(d) Steps of the three-step model. (b) The atomic potential is disorted by the laser field allowing tunnel ionization (the electron wavepacket is shown in red). (c) The ionized electron is accelerated in the field gaining energy, (d) which is released in the form of a high energy photon (purple) upon recombination with the parent ion.

position x and velocity $\dot{x}$ of the electron yields

$$\begin{aligned} \dot{x} &= -\frac{eE_0}{m_e\omega}\left(\sin\omega t - \sin\omega t_i\right), \\ x &= \frac{eE_0}{m_e\omega}\left(\left(t-t_i\right)\sin\omega t_i + \frac{1}{\omega}\left(\cos\omega t - \cos\omega t_i\right)\right). \end{aligned} \tag{3.2}$$

Solutions for different ionization phases ωt_i are plotted in Fig. 3.2. Note that in order for the

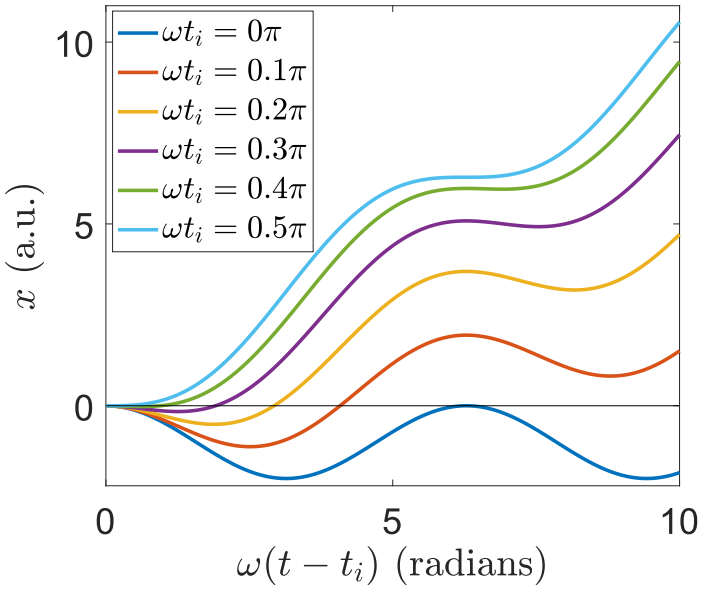

Figure 3.2: Solutions of the three-step model for different ionization phases.

electron to recombine with the parent ion, the solution must cross zero, which is only true when the initial phase $0 \leq \omega t_i \leq \pi/2$, within a single cylce of the laser driver.

The ponderomotive energy U_p is defined as the time-averaged kinetic energy of the ionized electron, and from eq. (3.2), it is found that

$$Up = \frac{e^2E_0^2}{4m_e\omega^2}. \tag{3.3}$$

Eq. (3.2) can be solved numerically to find t_i that gives the maximum possible kinetic energy T_{max} of an electron upon recombination. The solution yields $T_{max} \approx 3.17U_p$. The maximum possible HHG photon energy $h\nu_{max}$ is given by T_{max} and the atomic ionization energy I_p, which is

the potential energy of the ionized electron relative to its ground state

$$h\nu_{max} = I_p + 3.17U_p. \tag{3.4}$$

$h\nu_{max}$ is also called the cutoff energy. It scales linearly with I_p, which, of the noble gases, is the highest for He (24.59 eV), and is also linearly dependent on the laser intensity I_L and the square of the laser wavelength λ^2. Therefore, in order to maximize the HHG photon energy, one must use a gas with a high I_p, a laser driver with a high peak intensity I_L, which can be obtained by compressing the pulse temporally, and a long wavelength λ.

3.1.2 Electron wavefunction dynamics

The three-step model is included in the more general quantum picture of HHG [87, 88]. A rigorous quantum model must take into account the selection rules in a multi-electron atom. An approximation of a single active electron in an effective field created by the nucleus and the rest of the electrons in an atom allows one to simplify the full Schrödinger equation to a single particle problem [87], for which the time-dependent Schrödinger equation (TDSE) reads

$$\left[-\frac{\hbar^2}{2m_e}\nabla^2 + \hat{V}(\vec{r},t)\right]|\psi(\vec{r},t)\rangle = i\hbar\frac{\partial}{\partial t}|\psi(\vec{r},t)\rangle\,. \tag{3.5}$$

The time-dependent potential $\hat{V}(\vec{r},t)$ includes a static atomic potential $\hat{V}_a(\vec{r})$ and a time-dependent laser potential $\hat{V}_L(\vec{r},t)$

$$\hat{V}(\vec{r},t) = \hat{V}_a(\vec{r}) + \hat{V}_L(\vec{r},t) = -\frac{e^2}{4\pi\epsilon_0\sqrt{r^2+\alpha^2}} - e\vec{E}(t)\cdot\vec{r}, \tag{3.6}$$

where the laser field $\vec{E}(t)$ in the case of a linearly polarized laser driver is

$$\vec{E}(t) = \vec{E}_0(t)\cos\omega t, \tag{3.7}$$

where $\vec{E}_0(t)$ is the envelope of the pulse.

An initial condition for $|\psi(\vec{r})\rangle$ is the ground state wavefunction of an unperturbed atom. Therefore, the minimum energy eigenvector of the time-independent Hamiltonian $\hat{H} = -\frac{\hbar^2}{2m_e}\nabla^2 + \hat{V}_a(\vec{r})$ must be found prior to solving the time-dependent problem. This can be done by use of a

finite-difference numerical scheme [89]. TDSE (3.5) can then be solved. The solution can formally be written as

$$|\psi(\vec{r},t)\rangle = \exp\left(-\frac{i}{\hbar}\left[-\frac{\hbar^2}{2m_e}\nabla^2 + \hat{V}(\vec{r},t)\right]t\right)|\psi(\vec{r},t=0)\rangle\,. \tag{3.8}$$

With a known evolution operator $\hat{U(t)} = \exp\left(-\frac{i}{\hbar}\left[-\frac{\hbar^2}{2m_e}\nabla^2 + \hat{V}(\vec{r},t)\right]t\right)$, eq. (3.8) can be used to find the laser-driven dynamics of the electron wavepacket. The difficulty in evaluating $\hat{U}$ is that the kinetic and potential energy operators $\hat{T} = -\frac{\hbar^2}{2m_e}\nabla^2$ and $\hat{V}(\vec{r},t)$ do not commute and, therefore, $e^{\hat{T}+\hat{V}} \neq e^{\hat{T}}e^{\hat{V}}$. However, on small time steps Δt, the Trotter approximation can be applied $\lim_{\Delta t\to 0}\left(e^{(\hat{T}+\hat{V})\Delta t}\right)^{1/\Delta t} = \left(e^{\hat{T}\Delta t}e^{\hat{V}\Delta t}\right)^{1/\Delta t}$ [90], and thus the evolution operator becomes

$$\hat{U}(\Delta t) \approx e^{\hat{T}\Delta t}e^{\hat{V}\Delta t}. \tag{3.9}$$

The spectral theorem [91] states that for a diagonal operator $\hat{O}$ there is a space, on which the representation of $\hat{O}$ is a multiplication operator. For the potential energy operator $\hat{V}$ this is real space. Also, for a diagonal operator, $e^{\hat{O}} = \mathrm{diag}(e^{O_i})$, where O_i are the eigenvalues of $\hat{O}$. Hence, the action of $e^{\hat{V}\Delta t}$ on $|\psi\rangle$ in real space is equivalent to multiplying $|\psi(\vec{r})\rangle$ by $e^{V(\vec{r})\Delta t}$. The kinetic energy operator $\hat{T} = \frac{\hbar^2 k^2}{2m_e}$ is diagonal in momentum space, which is related to real space via Fourier transform, and, therefore, the multiplication by $e^{T(\vec{k})\Delta t}$ is performed in momentum space. With this, the time propagation of $|\psi(\vec{r},t)\rangle$ can be written as

$$|\psi(\vec{r},t+\Delta t)\rangle = \mathcal{F}^{-1}\left\{e^{-\frac{i\hbar k^2}{2m_e}\Delta t}\mathcal{F}\left\{e^{-\frac{i}{\hbar}V(\vec{r},t)\Delta t}|\psi(\vec{r},t)\rangle\right\}\right\}. \tag{3.10}$$

In the numerical implementation of eq. (3.10), the multiplication in real space was split in two steps before and after the multiplication in Fourier space in order to improve the stability of the method, and an apodizing mask was applied at each time step to simulate an open boundary of a finite computation window.

Simulated dynamics of an electron wavefunction in a hydrogen-like atom are shown in Fig. 3.3 along with the ground-state wavefunction. The highly localized ground-state wavefunction is spread around by the laser field and forms time dependent ripples. The spreading amounts to the tunnel ionization discussed above, and the ripples lead to a time-dependent dipole moment which produces dipole radiation.

According to the Larmor formula, the total power radiated by an accelerating charge is [92]

$$P(t) = \frac{\mu_0 q^2 \left|\ddot{x}\right|^2}{6\pi c} = \frac{\mu_0 \left|\ddot{p}\right|^2}{6\pi c}, \tag{3.11}$$

where μ_0 is the permeability of free space and q is the electric charge, and the dipole moment p is defined as $p = qx$ (for a dipole in the x-direction). With a known time dependence of the

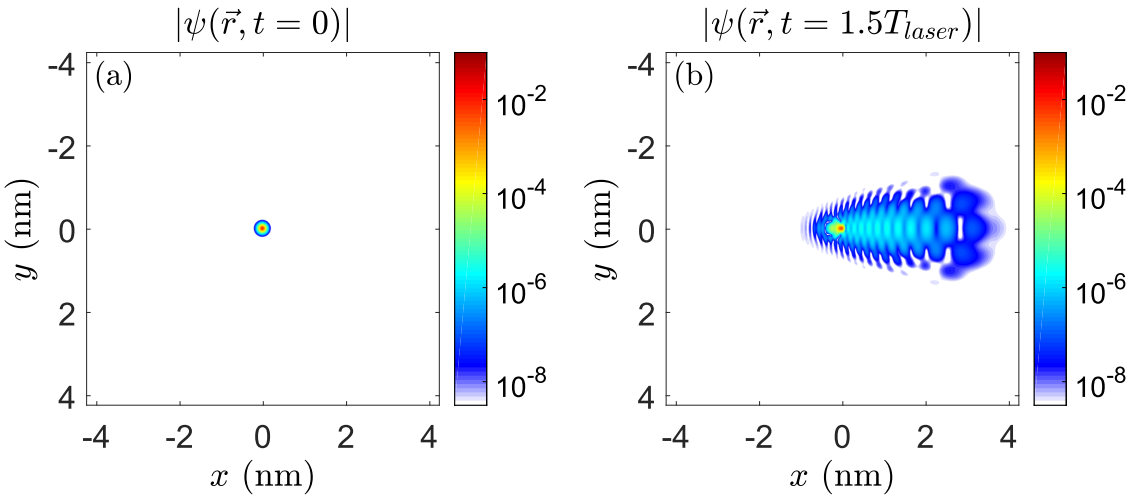

Figure 3.3: (a) Ground-state and (b) laser-driven dynamics of the electron wavefunction in a hydrogen-like atom. The ripples in the wavefunction in (b) give rise to dipole radiation.

wavefunction, the dipole moment can be computed as

$$\vec{p}(t) = e \left\langle \psi\left(\vec{r}, t\right)\right| \vec{r} \left|\psi\left(\vec{r}, t\right)\right\rangle . \tag{3.12}$$

The power spectrum of HHG is proportional to $\mathcal{F}\left\{P(t)\right\}$, where the time-dependent radiated power is given by eq. (3.11). The dipole selection rules allow only odd harmonics in the spectrum, which is confirmed experimentally in Fig. 3.4.

3.1.3 Circularly polarized HHG

Intuitively, it would seem that in order to produce circularly polarized harmonics, the HHG process would have to be driven by a circularly polarized laser, for which the field in the (x, y) plane is given by

$$\vec{E}_{circ}(t) = E_0(t)(\hat{x}\cos\omega t + \hat{y}\sin\omega t), \tag{3.13}$$

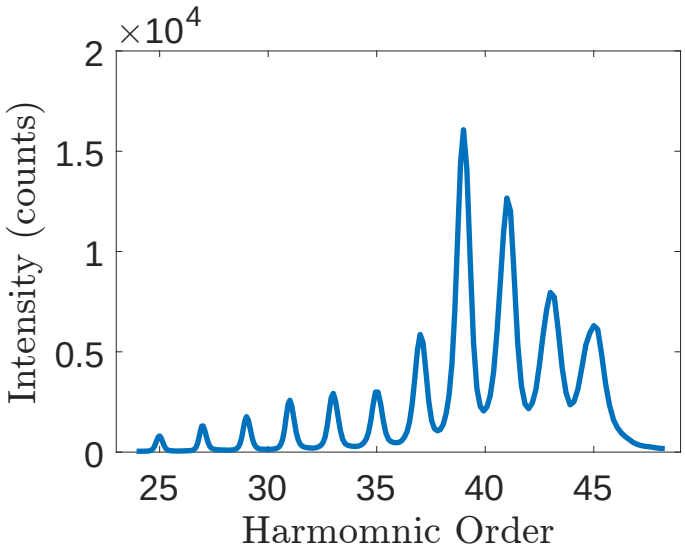

Figure 3.4: Experimental spectrum of linearly polarized HHG in He. The fundamental wavelength is 800 nm. Only odd harmonic orders are present.

where $\hat{x}$ and $\hat{y}$ are unit vectors in the x and y directions, respectively. However, solving eq. (3.5) with $\vec{E}_{circ}$ given by eq. (3.13) yields no dipole oscillations, as seen in Fig. 3.5(a). Instead the wavefunction is driven away from the ion and the recombination never occurs.

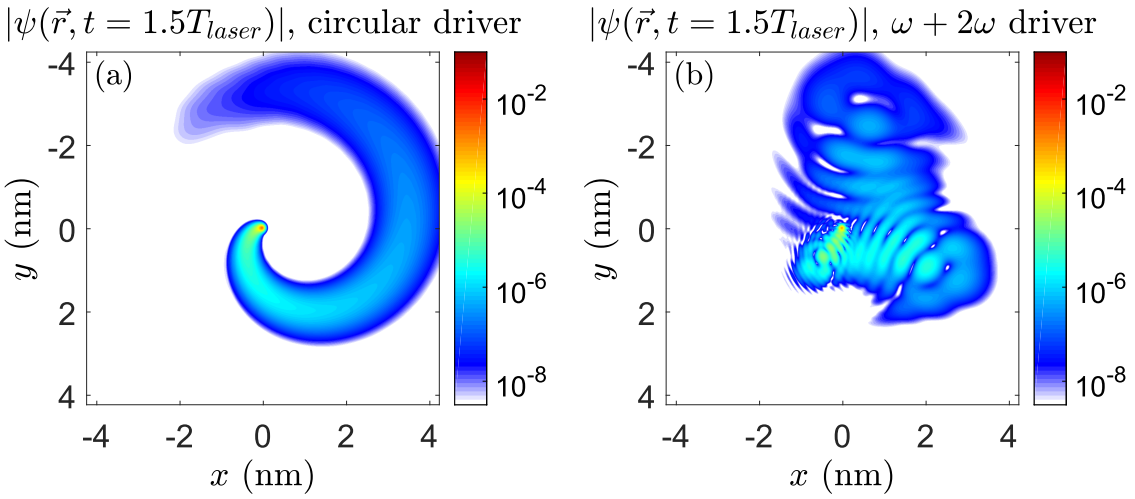

Figure 3.5: Dynamics of an electron wavefunction in (a) a single-color circular and (b) a bichromatic trefoil-shaped field. With a circularly polarized laser driver, the wavefunction is driven away from the ion and never recombines. The dipole oscillations responsible for HHG are missing. With a bichromatic $\omega + 2\omega$ trefoil-shaped driver, the dipole oscillations appear in three directions, which effectively leads to circularly polarized HHG.

It would seem that circular polarization could only be achieved by conversion from linear [93]. However, such an approach is very lossy and can only be implemented in a rather narrow spectral range. A direct production of circularly polarized HHG is possible, but it requires a specially shaped laser field that would not only drive the wavefunction in both x- and y-directions, but would also allow its re-collision with the parent ion. Such an approach was first proposed in 1995 [94, 95]. In it, two co-propagating circularly polarized pulses rotating in opposite directions make up the laser driver. The two pulses have different wavelengths: one is at the fundamental wavelength and the other is at its second harmonic. When added together, the two pulses produce an electric field that is given by the following expression

$$\vec{E}_{\omega+2\omega}(t) = E_0(t)(\hat{x}(\cos\omega t + \cos 2\omega t) + \hat{y}(\sin\omega t - \sin 2\omega t)). \tag{3.14}$$

The field vector $\vec{E}_{\omega+2\omega}(t)$ travels on a trefoil-like trajectory over a single cycle of the fundamental, as shown in Fig. 3.6. When an electron is driven by such a field, it can recombine with the parent

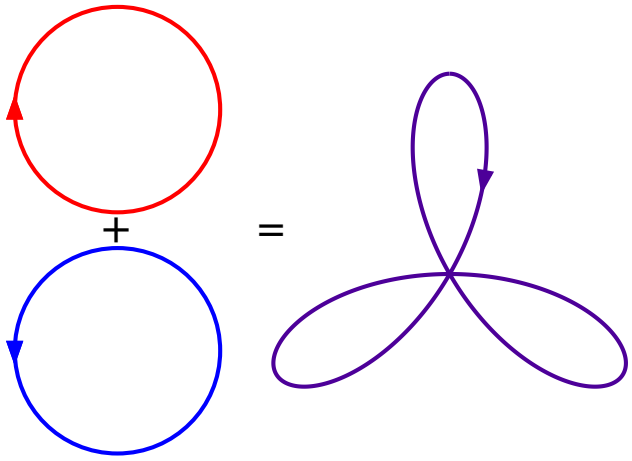

Figure 3.6: The field of a two-color laser driver for circularly polarized HHG. A combination of two circularly polarized co-propagating fields at the fundamental wavelength (red) and its second harmonic (blue) that rotate in opposite directions results in a trefoil-like field pattern.

ion producing dipole oscillations (see Fig. 3.5(b)) and thus making HHG possible. A measurement of the ellipticity of HHG produced using the method described above is reported in Ref. [96] and the helicity was measured in Ref. [97].

Notably, upon closer inspection of Fig. 3.5(b), it can be seen that the ripples in the wavefunction occur predominantly in three distinct directions. This threefold symmetry is imposed by the symmetry of the bichromatic driver and results in three linearly polarized EUV bursts per one laser cycle of the fundamental that are delayed with respect to one another, and the plane of polarization of each burst is rotated by 120° relative to the other bursts. Together the three EUV bursts result in right and left circularly polarized HHG [98]. The existence of the sequential linearly polarized bursts was confirmed experimentally by analyzing quantum pathways of photoemitted electrons from a metallic surface irradiated by circularly polarized harmonics [99].

A setup for circularly polarized HHG is shown in Fig. 3.7. A pulse train from a Ti:Sapphire laser amplifier at a central wavelength of ∼790 nm travels through a BBO crystal to generate pulses at 395 nm. The two beams are split into separate arms by a dichroic mirror, and a delay stage

is introduced in one arm to overlap the red and blue pulses in time; a set of waveplates in each arm controls the polarization of the respective beam; another dichroic mirror recombines the two beams in space, and the combined beam is focused into a hollow-core waveguide filled with He where the HHG process takes place. The light emitted from the waveguide is measured with an EUV spectrometer.

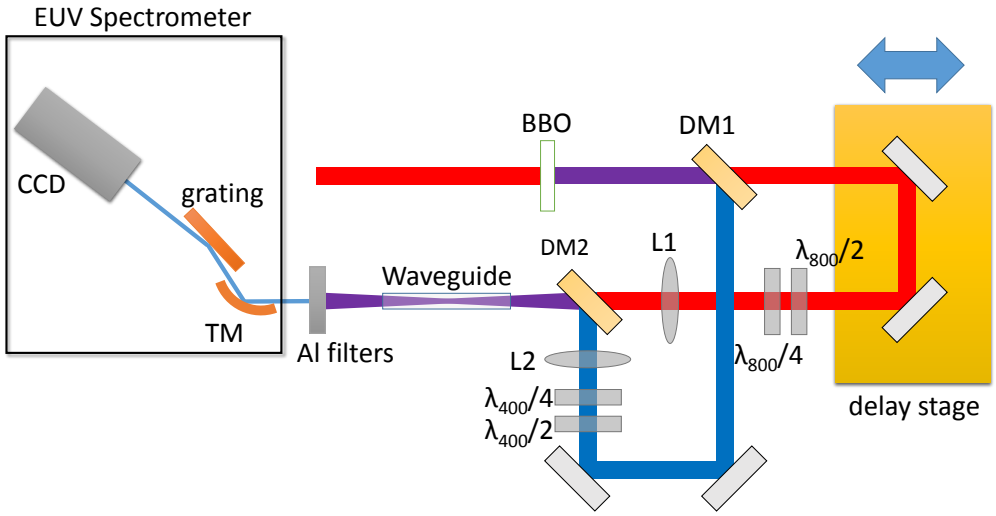

Figure 3.7: Setup for circularly polarized HHG. A delay stage is used for a temporal overlap of the red and blue pulse trains. DM1 and DM2 are dichroic mirrors that split and recombine the two beams, respectively. The lenses L1 and L2 focus each beam into the waveguide, and the toroidal mirror TM re-images the output of the waveguide onto the CCD.

The conservation of energy and angular momentum determines which circularly polarized harmonic orders are allowed in the HHG spectrum. The harmonic order q is defined relative to the fundamental frequency ω. First, for n absorbed photons of frequency ω and m absorbed photons of frequency 2ω, the conservation of energy gives

$$q\omega = n\omega + m2\omega. \tag{3.15}$$

Second, because the harmonics are either right or left circularly polarized, the conservation of the spin angular momentum requires that

$$n - m = \pm 1. \tag{3.16}$$

From eqs. (3.15) and (3.16), it follows that the allowed harmonic orders are

$$q = 3m \pm 1. \tag{3.17}$$

Therefore, circularly polarized harmonics driven by a bichromatic driver defined by eq. (3.14) are expected to appear in pairs, which is confirmed by an experimental spectrum in Fig. 3.8, in which every third harmonic is suppressed.

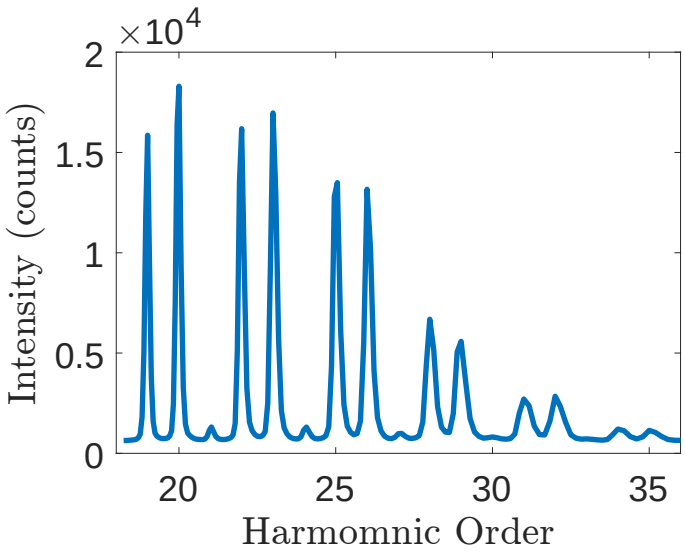

Figure 3.8: Experimental spectrum of circularly polarized HHG in He. Every third harmonic is suppressed, in agreement with the selection rules.

The helicity of each harmonic in the spectrum can be derived from eq. (3.16) and (3.17). For instance, if $n - m = 1$, the helicity of the corresponding harmonic order $q = 3m - 1$ is determined by the helicity of the field at the fundamental frequency ω, while for $n - m = -1$, the harmonic order $q = 3m + 1$ has the same helicity as the second harmonic 2ω.

Circularly polarized HHG has been demonstrated in non-collinear geometries, where harmonics of different helicities could be separated spatially [100], and in the soft X-ray region with a bichromatic driver composed of optical fields at 1.3 μm and 800 nm [101].

Both the semiclassical and quantum models of HHG discussed above deal with radiation by a single atom. In reality, the HHG process takes place in a finite volume of gas that is pumped by

a laser, and the total HHG flux is built up from the light emitted by multiple atomic sources. If radiation from these sources can be added in-phase, a significant improvement in HHG flux can be obtained. Such coherent addition is known as phase matching.

3.1.4 Phase matching

The concept of phase matching originated in nonlinear optics [102] in the context of parametric processes, e.g. four-wave mixing, second harmonic generation, sum and difference frequency generation, etc. In order for such processes to be efficient, the correct phase relationships between the interacting waves have to be maintained. Similarly, in HHG, the phase of EUV light emitted at different points along the propagation direction of the laser driver needs to be the same in order for the HHG signal to add constructively. The requirement that the phase between the laser driver and the EUV light remains the same along the propagation direction means that their phase velocities defined as $v_p = \omega/k$ have to be equal, i.e.,

$$\frac{\omega_f}{k_f} = \frac{\omega_q}{k_q}, \tag{3.18}$$

where ω_f and k_f are the fundamental angular frequency and wavenumber, and ω_q and k_q are the angular frequency and wavenumber of the harmonic of order q. Assuming that $\omega_q = q\omega_f$, eq. (3.18) becomes

$$\Delta k = qk_f - k_q = 0, \tag{3.19}$$

where Δk is called the phase mismatch. In the limit of perfect phase matching, when $\Delta k = 0$, the EUV photon flux grows quadratically with the interaction length, greatly exceeding the non-phase-matched flux, and reaches saturation when the absorption by the medium is taken into account (see Ref. [103] for details).

The difficulty in achieving phase matching for HHG has to do with the dispersion of the refractive index of the neutral gas and plasma. At EUV wavelengths, the refractive index is close to 1, and their phase velocity is nearly equal to the speed of light $c = 3 \cdot 10^8$ m/s, while for the IR laser driver that is not the case. A solution to this problem was proposed in Ref. [104]. Instead of

a gas jet, the HHG process took place in a gas filled hollow-core waveguide (see Fig. 3.9), which allowed the balancing of the dispersion of neutral atoms and plasma by a mode dispersion due to the confinement of light in the waveguide.

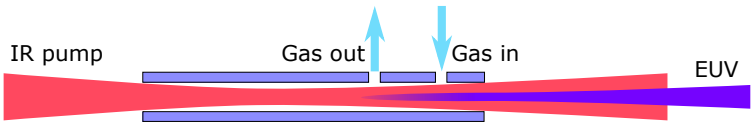

Figure 3.9: Hollow-core waveguide for phase-matched HHG. The laser driver is focused into the waveguide such as to match its lowest order mode (EH_{11})

The expression for the phase mismatch in a hollow-core waveguide for a harmonic order q is given by [105, 106]

$$\Delta k \approx q\left(\frac{u_{11}^2\lambda_f}{4\pi a^2} - P(1-\eta)\frac{2\pi}{\lambda_f}(\Delta\delta + n_2 I_L) + P\eta N_a r_e \lambda_f\right), \tag{3.20}$$

where λ_f is the fundamental wavelength of the driving laser, $u_{11} = 2.405$ is the first zero of the zeroth order Bessel function of the first kind J_0, a is the radius of the waveguide, P is the gas pressure, η is the ionization fraction of the gas, $\Delta\delta = \mathrm{Re}(n(\lambda_f) - n(q\lambda_f))$ is the difference in the real parts of the indices of refraction at the fundamental wavelength and its q^{th} harmonic, n_2 is the nonlinear refractive index, which is small and is often neglected [105], I_L is the driving laser intensity, N_a is the number density of the gas per unit pressure, and r_e is the classical electron radius. The first term in parentheses represents the waveguide dispersion, the second term is due to the dispersion of neutral atoms and the third is due to plasma dispersion. The parameters that can be fairly easily controlled in an experiment are the waveguide radius a, the gas pressure P and the ionization fraction η, which depends on the intensity of the laser and can be computed from the ADK tunnel ionization rate discussed above.

With $\Delta k = 0$, eq. (3.20) can be solved to find the phase-matching pressure

$$P \approx \frac{u_{11}^2\lambda_f^2}{4\pi a^2(2\pi\Delta\delta - \eta N_a r_e \lambda_f^2)}. \tag{3.21}$$

At the critical ionization level $\eta_c \approx 2\pi\Delta\delta/N_a r_e\lambda_f^2$, the denominator vanishes and $P \to \infty$, which means that phase matching above the critical ionization level is impossible. In He, the critical

ionization is ∼0.5%, and the corresponding laser fluence, based on the ADK rate calculations mentioned above and assuming a 150 μm diameter waveguide and a 25 fs pulse with the central wavelength of 800 nm, is ∼1.5 mJ/cm^2 [107, 108]; the maximum possible harmonic order is 91 [108].

The concept of phase matching is applicable for linearly as well as circularly polarized HHG, albeit with helicity-dependent considerations [109], and bright phase-matched circularly polarized harmonics were demonstrated in Ref. [97].

3.2 X-ray free-electron lasers

Another source of ultrafast coherent EUV and X-ray pulses is a free-electron laser (FEL). Although the idea of an FEL originated in the 1970's [110], X-ray FELs are fairly recent [111, 15]. In an FEL, a coherent X-ray pulse is produced when a relativistic electron bunch passes through a periodic series of alternating magnets, known as the undulator [112]. The power radiated by an accelerating electron is given by the relativistic generalization of the Larmor formula (3.11)

$$P = \frac{q^2\gamma^6}{6\pi\epsilon_0 c}\left[(\dot{\vec{\beta}})^2 - (\vec{\beta}\times\dot{\vec{\beta}})^2\right], \tag{3.22}$$

where $\vec{\beta}$ is the ratio of the charge velocity to the speed of light, and $\gamma = 1/\sqrt{1-\beta^2}$ is the relativistic Lorentz factor. At relativistic speeds, $\gamma > 1$ and the γ^6 factor in eq. (3.22) leads to a significant increase in radiated power, which makes FELs so bright.

The key components of an X-ray electron laser are an electron injector that sends a short electron bunch into an accelerator section, in which it is accelerated to GeV energies, and an undulator where the X-ray light is emitted. The discussion of FELs below is limited to the Linear Coherent Light Source (LCLS) FEL at SLAC since the experiment reported in Chapter 6 was performed there.

At LCLS, electrons are emitted from the copper photocathode of an RF electron gun by a UV laser operating at 253 nm (third harmonic of an amplified Ti:Sapphire laser) [113]. The RF gun boosts the energy of photoelectrons to 135 MeV and sends them into two sequential bunch

compressors, which accelerate and shorten the duration of electron bunches. The stochastic nature of the photoesmission process at the cathode results in fluctuations of the X-ray pulse brightness and introduces an uncertainty in the pulse arrival time thus limiting the temporal resolution of the FEL, which can be improved by measuring the relative arrival time of the pulses [114]. After the compressors, an electron bunch is injected into the tunnel of a linear accelerator re-purposed from particle physics experiments. After the accelerator section, high energy electrons enter the undulator where the generation of an X-ray pulse takes place as the electrons are forced to move on a curved trajectory in an alternating magnetic field. As they propagate along the undulator, electrons and X-ray photons couple to one another. Such coupling results in self-amplified spontaneous emission (SASE) from the spontaneous emission arising from the initial electron beam shot noise. Again, due to its stochastic nature, SASE gives rise to fluctuations in the beam brightness and leads to a rather low temporal coherence [115]. To improve the latter, SASE can be used to self-seed the FEL [115]. Because X-rays are amplified through interactions with relativistic electrons, the latter can be viewed as a laser gain medium, and X-ray FELs can thus be considered single-pass laser amplifiers. Gain saturation in a SASE FEL is achieved by use of very long undulators or gain media [111].

In the soft X-ray and EUV regions, external seeding methods, which include seeding with HHG, have been proposed to reduce fluctuations [116, 117, 118] and a fully seeded operation has been implemented at the FERMI FEL in Trieste [119, 120].

FELs can provide coherent ultrashort X-ray pulses of very high brightness. However, due to their complex design and high operational costs, there are only a few FEL user facilities available worldwide. Currently, they can deliver an X-ray beam to only one experimental end station at a time. For these reasons, their accessibility is severely limited. Due to their compactness and relatively low cost, HHG sources are much more accessible and can be used in a broad range of materials science, biology and chemistry experiments that are not as demanding with regards to the photon flux but require a high temporal resolution, broad spectrum, or good coherence properties of the probe.

3.3 Conclusions

In this chapter, I reviewed HHG and FEL sources of EUV and soft X-ray light suited for studying material and molecular systems with high temporal and spatial resolution as well as element specificity. Both the classical three-step model of HHG in a single atom and a full quantum picture based on a solution of the time-dependent Schrodinger equation for an electron in a combined atomic and laser potential were presented. Quantum simulations show that circularly polarized HHG cannot be achieved with a cicularly polarized single-color laser driver and a complex field pattern is required to generate circular polarization directly. Such a field, called a bichromatic driver, can be obtained by mixing two laser pulses of different colors. Conservation laws constrain the allowed harmonic orders: even and every third orders are suppressed for linearly and circularly polarized HHG, respectively. This is confirmed by the experimental HHG spectra for the two polarizations. Neutral gas and plasma dispersions in an active HHG region can be compensated for by confining light in a hollow-core waveguide, and the HHG process can thus be phase-matched, which results in a significant increase in the intensity of an HHG-based tabletop source of EUV light with full polarization control. FELs produce very bright X-ray pulses by use of accelerated relativistic electron bunches but due to their complexity and cost allow very limited access to users. HHG and FEL sources can compliment one another in their respective applications in order to realize the full potential of ultrafast, coherent X-rays in the study of material, molecular, and biological systems and nanoscale devices.

Chapter 4

Extension of the EUV Magneto-Optical Spectroscopy

In this chapter, I extend the traditional magneto-optical techniques and present two approaches that are capable of measuring the full resonant EUV complex magneto-optical permittivity ϵ_{xy}, which depends on the microscopic state of a magnetic material, in a reflection geometry. In the first approach, ϵ_{xy} can be extrated from the magneto-optical reflectivity spectra measured at multiple angles of incidence in the transverse magneto-optical Kerr effect (T-MOKE) geometry. In the second, more efficient approach, the angle of incidence is kept fixed, and a series of magneto-optical spectra is taken by scanning the polarization direction of a linearly polarized EUV probe. I show that ϵ_{xy} can be unambiguously determined from this extensive data set.

The two techniques were applied in a pump-probe experiment on thin Co films in order to trace the evolution of ϵ_{xy} during the course of laser-induced ultrafast demagnetization. With the help of *ab initio* DFT simulations (carried out at Uppsala University), a connection was made to the microscopic processes, i.e., ultrafast longitudinal and transverse excitations and their role in the demagnetization process on femtosecond and picosecond timescales. The magnetization response to an ultrashort IR laser excitation was found to be dominated by transverse excitations, or magnons, with a possible smaller contribution from a transient reduction of the exchange splitting. This conclusion is supported independently by the angle- and polarization-resolved techniques.

4.1 Time-resolved EUV T-MOKE

I start by describing T-MOKE in the EUV spectral region, which has an advantage, compared to the visible one, that stems from its resonant nature because magneto-optical reflection spectra taken at the resonant absorption edges (particularly the M-edges of the ferromagnetic $3d$ metals Fe, Co, and Ni in the range of $\sim$ 50-70 eV) can provide access to the microscopic picture of magnetism and its dynamics.

The three MOKE geometries P-, L-, and T-MOKE are discussed in Chapter 2. The former two require an analysis of the polarization state of the reflected light and are thus not very well suited for the EUV photon energies, due to a lack of efficient polarization analyzers. In the transverse geometry, however, the polarization state of the reflected light remains unchanged, and the contrast is purely an amplitude one. This can be shown analytically by considering the dielectric tensor (relative to the permittivity of free space ϵ_0) for the transverse magnetization direction along the x-axis (see Fig. 2.13) in an isotropic material [121]

$$\hat{\epsilon} = \begin{pmatrix} \epsilon_{xx} & 0 & 0 \\ 0 & \epsilon_{xx} & -iQ\epsilon_{xx} \\ 0 & iQ\epsilon_{xx} & \epsilon_{xx} \end{pmatrix}, \tag{4.1}$$

where Q is the magneto-optical constant, and the off-diagonal element of $\hat{\epsilon}$ is defined as $\epsilon_{xy} = -iQ\epsilon_{xx}$.

Consider the Maxwell curl equations together with the constitutive relations (in a medium with a magnetic permeability $\mu = 1$, relative to the permeability of free space μ_0, and in the absence of current sources)

$$\begin{aligned} \vec{\nabla} \times \vec{E} &= -\frac{\partial \vec{B}}{\partial t}, \\ \vec{\nabla} \times \vec{H} &= \frac{\partial \vec{D}}{\partial t}, \\ \vec{D} &= \epsilon_0 \hat{\epsilon} \vec{E}, \\ \vec{H} &= \frac{1}{\mu_0} \vec{B}. \end{aligned} \tag{4.2}$$

By taking a curl of the first equation in (4.2) and using $c = 1/\sqrt{\epsilon_0 \mu_0}$, the following form of the wave equation can be derived

$$-\nabla^2 \vec{E} + \vec{\nabla}\left(\vec{\nabla} \cdot \vec{E}\right) = -\frac{\hat{\epsilon}}{c^2} \frac{\partial^2 \vec{E}}{\partial t^2}. \tag{4.3}$$

By inserting a plane wave solution $\vec{E} = \vec{E}_0 e^{i(\omega \vec{n} \cdot \vec{r}/c - \omega t)}$ in eq. (4.3), where the refractive index $\vec{n}$ is defined along the direction of the wavevector $\vec{k}$ as $\vec{n} = \vec{k}c/\omega$, an eigenvalue equation can be obtained [73]

$$\left(|\vec{n}|^2 - \hat{\epsilon} + \vec{n} \otimes \vec{n}\right) \cdot \vec{E}_0 = 0, \tag{4.4}$$

where $\otimes$ denotes an outer product of two column vectors. The eigenvalues are found from

$$\det\left(|\vec{n}|^2 - \hat{\epsilon} + \vec{n} \otimes \vec{n}\right) = 0, \tag{4.5}$$

and the corresponding eigenvectors $\vec{E}_0$ are found from eq. (4.4).

For the dielectric tensor in the T-MOKE geometry, defined by eq. (4.1), the eiegenvectors correspond to the s- and p-polarizations, and the respective eigenvalues of the refractive index are

$$\begin{aligned} n_s^2 &= \epsilon_{xx}, \\ n_p^2 &= \epsilon_{xx} + \frac{\epsilon_{xy}^2}{\epsilon_{xx}}. \end{aligned} \tag{4.6}$$

Therefore, in the T-MOKE geometry, only the p-polarization is affected by magneto-optical changes to the refractive index. Taking eqs (4.6) into account, the Fresnel reflections in the transverse geometry at an interface of a semi-infinite magnetic layer are [121]

$$\begin{aligned} r_{pp} &= \frac{n_s \cos\phi_i - \cos\phi_t}{n_s \cos\phi_i + \cos\phi_t} + iQ \frac{2 n_s \cos\phi_i \sin\phi_t}{\left(n_s \cos\phi_i + \cos\phi_t\right)^2}, \\ r_{ss} &= \frac{\cos\phi_i - n_s \cos\phi_t}{\cos\phi_i + n_s \cos\phi_t}, \end{aligned} \tag{4.7}$$

where ϕ_i and ϕ_t are the incident and refracted angles, and r_{pp} and r_{ss} are the reflections for the p- and s-polarizations, respectively. Generally speaking, the polarization can rotate from s to p and vice versa, upon reflection from a surface magnetized in an arbitrary direction. For that reason, it is convenient to add reflection coefficients r_{sp} and r_{ps}, which vanish in the transverse geometry [121].

Typically, in an experiment, a reflected intensity is measured $I_r = I_0|r_{pp}|^2$, where I_0 is the incident intensity, and thus the information about the phase of the complex reflection coefficient r_{pp} is lost. For brevity, I define the parameters $r_{pp}^{(0)} = \frac{n_s \cos\phi_i - \cos\phi_t}{n_s \cos\phi_i + \cos\phi_t}$ and $r_{pp}^{(1)} = i\frac{2n_s \cos\phi_i \sin\phi_t}{(n_s \cos\phi_i + \cos\phi_t)^2}$, and rewrite the p-polarization reflection coefficient as

$$r_{pp} = r_{pp}^{(0)} + Q r_{pp}^{(1)}. \tag{4.8}$$

To a first order in Q, the reflected intensity is

$$I_r = I_0 \left(|r_{pp}^{(0)}|^2 + 2\mathrm{Re}\left(Q r_{pp}^{(1)} r_{pp}^{(0)} \right) \right). \tag{4.9}$$

For a source with a fluctuating I_0, it can be difficult to distinguish the magnetic contribution to the total reflected intensity. For that reason, a differential measurement is usually performed by magnetically saturating the sample in a positive direction, measuring the reflected intensity $I_r^{(+)}$, and then reversing the magnetization direction, upon which the sign of Q in eq. (4.9) is also reversed, and measuring the reflected intensity $I_r^{(-)}$. From the two measurements, a quantity called the magneto-optical asymmetry is constructed

$$A = \frac{I_r^{(+)} - I_r^{(-)}}{I_r^{(+)} + I_r^{(-)}}. \tag{4.10}$$

Using eqs. (4.7) and (4.9) and Snell's law $\sin\phi_t = \sin\phi_i / n_s$, an explicit expression for A can be derived

$$A = 2\mathrm{Re}\left(\frac{Q r_{pp}^{(1)} r_{pp}^{(0)}}{|r_{pp}^{(0)}|^2} \right) = 2\mathrm{Re}\left(\frac{iQ \sin 2\phi_i}{n_s^2 \cos^2\phi_i - 1 + \frac{\sin^2\phi_i}{n_s^2}} \frac{r_{pp}^{(0)}}{\left(r_{pp}^{(0)}\right)^*} \right). \tag{4.11}$$

With an approximation $r_{pp}^{(0)} / \left(r_{pp}^{(0)}\right)^* \approx 1$, which holds relatively well for materials' refractive indices in the EUV spectral range, and given that $\epsilon_{xy} = -iQn_s^2$, the asymmetry can be expressed as (up to an overall sign, which depends on an arbitrary definition of the positive and negative magnetization)

$$A \approx 2\mathrm{Re}\left(\frac{\epsilon_{xy} \sin 2\phi_i}{n_s^4 \cos^2\phi_i - n_s^2 + \sin^2\phi_i} \right). \tag{4.12}$$

It is important that $A \propto Q$, which allows one to access the magnetic state by performing a magneto-optical differential measurement. An advantage of T-MOKE measured with an HHG source is

that the HHG spectrum is so broad that it can access the absorption edges of multiple elements simultaneously and thus probe laser-induced magnetization dynamics of alloys and multilayer films with elemental specificity. The asymmetry is maximized at the Brewster angle, which, for a typical metal, is near 45°. An example magneto-optical asymmetry spectrum taken with an HHG source at the M-edge of Co is shown in Fig. 4.1. The figure clearly shows a difference between the spectra measured at the opposite magnetization directions (blue). The difference results in an EUV spectrum of the magneto-optical asymmetry shown in orange.

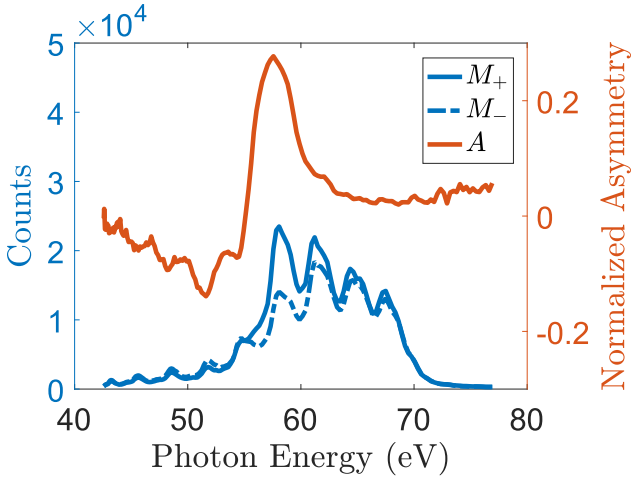

Figure 4.1: An example T-MOKE asymmetry spectrum (orange) at the M-edge of Co. The HHG spectra reflected from the sample when it was positively (solid) and negatively (dashed) magnetized are shown in blue.

The spectra in Fig. 4.1 were measured with a pump-probe T-MOKE setup shown in Fig. 4.2. In the setup, an IR laser pulse train is delivered by a KMLabs Dragon Ti:Sapphire laser amplifier producing 20 fs pulses at a ∼795 nm central wavelength with an energy of 2 mJ/pulse at a repetition rate of 4 kHz. This pulse train is split into two beams: 10% of the original beam goes into the pump arm, which has a delay stage in it to control the arrival time of pump pulses on the sample, while 90% is focused into a hollow-core waveguide where a Ne gas flows under a pressure of ∼630 Torr. In the waveguide, the IR laser drives a phase-matched HHG process, which produces broadband EUV light whose spectrum is shown in Fig. 4.1. A toroidal mirror with an imaging distance of

60 cm re-images the output of the waveguide onto a CCD camera (Andor Newton 920), which is operated in a full vertical binning mode, to increase the readout rate. Before reaching the CCD, an EUV beam impinges on a magnetic sample that has grooves etched throughout its thickness with a line spacing of 500 lines/mm in order to achieve spectral resolution and thus simultaneously acts as a spectrometer diffraction grating. The magnetic field at the sample is controlled by an electromagnet. Thin film Al filters are placed right after the waveguide and right in front of the CCD camera to block any residual IR light coming from the waveguide and reflected from the sample, respectively. The pump and the probe beams are combined on a mirror with an aperture at the center. The EUV beam is transmitted through the aperture while the pump beam is reflected from the mirror as close to the aperture as possible to minimize the angle between the two beams and thus improve the time resolution. The angle of the goniometer arm, that includes both the sample and the CCD, can be adjusted, which allows a measurement of the T-MOKE response at multiple angles of incidence. The importance of such a measurement is discussed below.

The diagram in Fig. 4.3 below shows the data collection flow of the T-MOKE setup. The synchronization of the instruments and the data acquisition was implemented in LabView.

Fig. 4.4 shows an example ultrafast demagnetization and recovery trace in pure cobalt measured with the setup in Fig. 4.2 and the data collection procedure in Fig. 4.3. While the demagnetization trace in Fig. 4.4 represents an average response of the material's magnetization to an ultrafast laser pulse, it, nonetheless, is of limited utility because the T-MOKE asymmetry defined by eq. (4.12) and measured at a fixed angle does not allow the separation of the real and imaginary parts of ϵ_{xy}. Knowledge of the evolution of the full resonant complex ϵ_{xy} is important because it would allow one, through first principles calculations, to make a connection to the microscopic mechanisms that drive the magnetization response in Fig. 4.4. Specifically, Ref. [70] makes a prediction that longitudinal Stoner excitations will have a different effect on the magneto-optical spectrum than transverse magnon excitations (see Chapter 2 for details). Namely, longitudinal excitations change the spectral shape of ϵ_{xy}, while transverse excitations simply lead to a uniform reduction of its magnitude across the entire spectrum. It is, therefore, important to have a technique

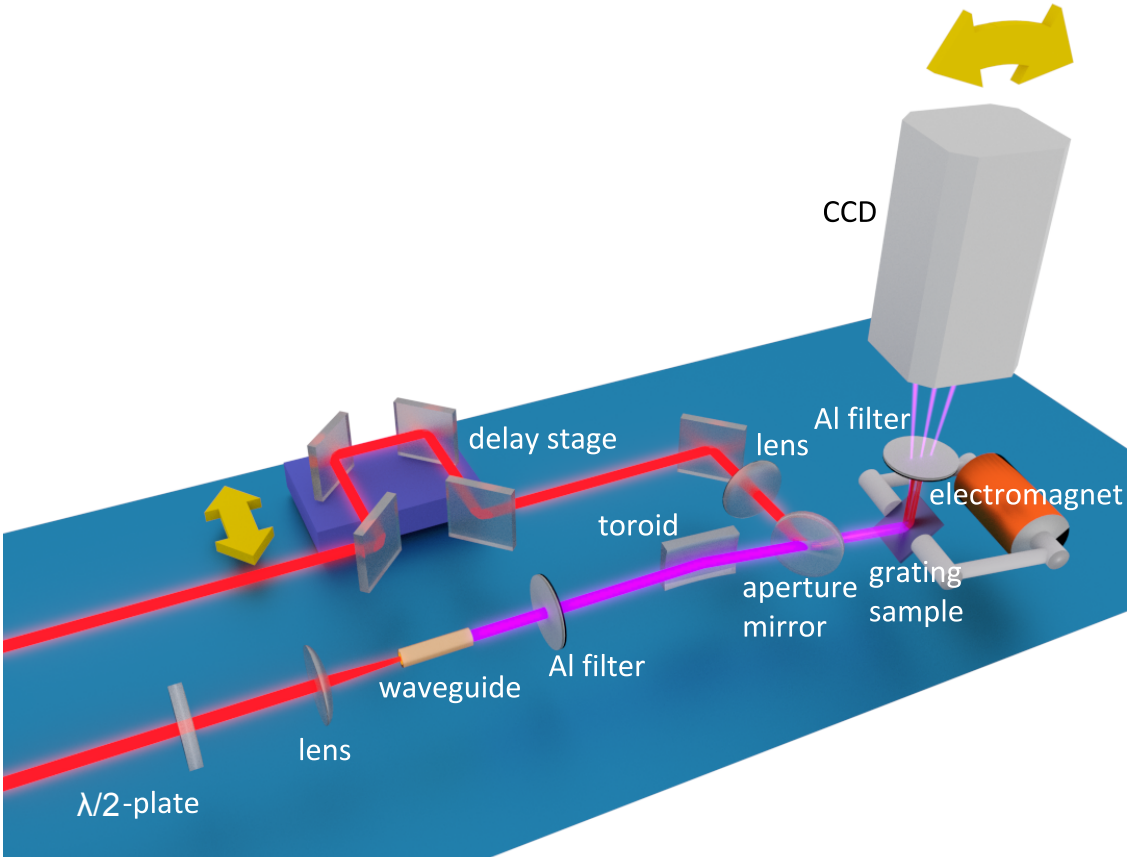

Figure 4.2: Time-resolved EUV T-MOKE setup. Laser-driven HHG in the waveguide produces a train of EUV pulses that are inherently synchronized with the IR laser pulses in the pump arm, which has a delay stage in it to control the delay time between the pump and the probe at the sample. The toroidal mirror re-images the output of the waveguide onto the CCD camera, which collects the EUV light diffracted by the grating sample. The projection-field electromagnet applies a magnetic field to the sample. The CCD and the sample can be tilted simultaneously, and thus the T-MOKE response can be measured at various angles of incidence.

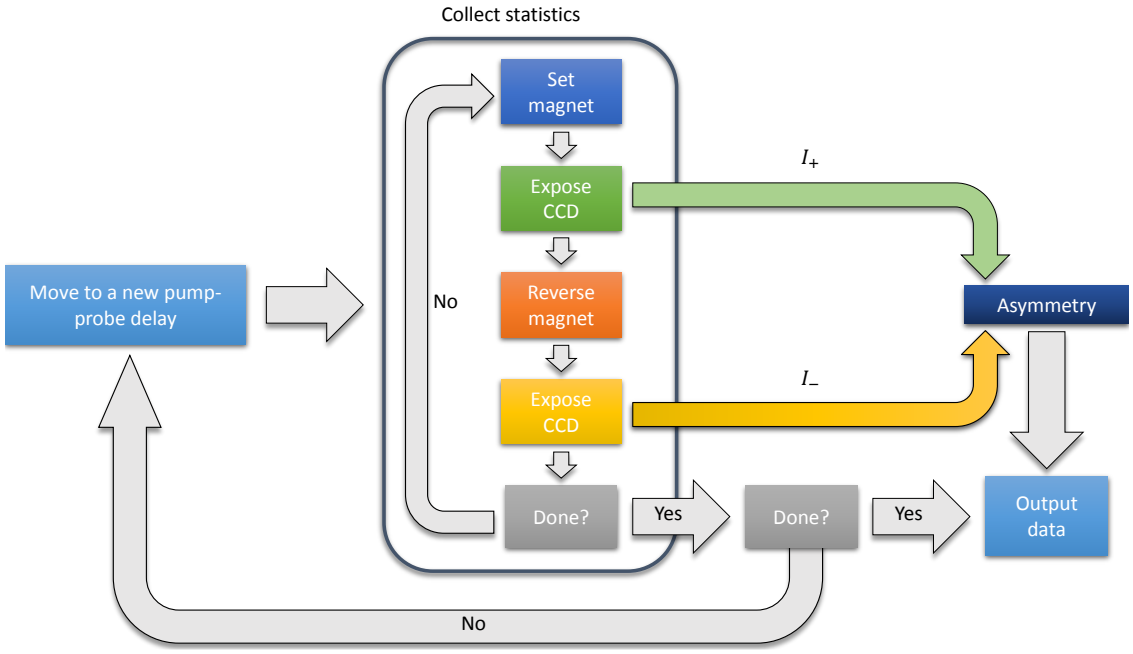

Figure 4.3: Time-resolved EUV T-MOKE data collection flow.

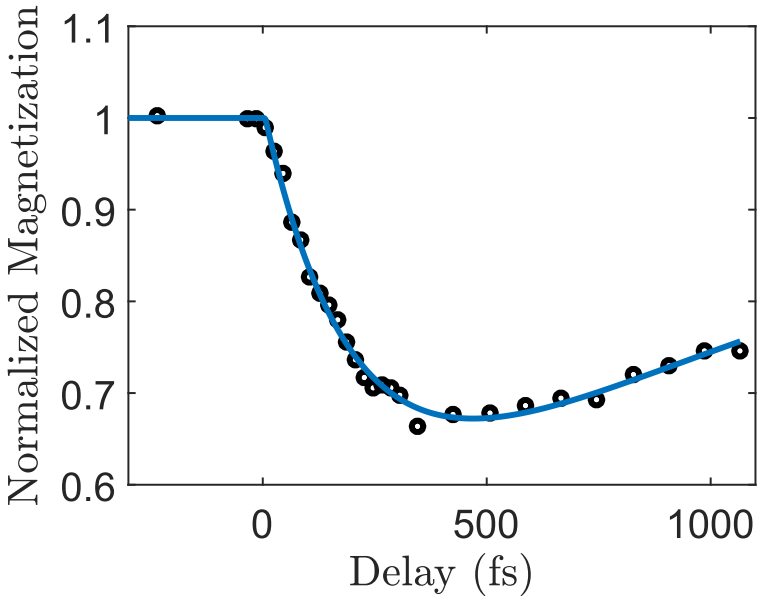

Figure 4.4: An example ultrafast demagnetization curve measured from the T-MOKE signal at the M-shell absorption edge in pure Co.

that would allow a direct extraction of ϵ_{xy}.

4.2 Measurement of the full complex magneto-optical permittivity

Such an extraction can be preformed in two ways—by adding an angle resolution to T-MOKE or by setting the magnetization direction at an angle to its transverse orientation and performing a scan of the polarization angle of a linearly polarized EUV probe. I outline both approaches below.

4.2.1 Angle-resolved T-MOKE

I start with the angle-resolved T-MOKE approach as it is a straightforward extension of the conventional T-MOKE given by expression (4.12) [122]. I define an angle-dependent factor $p(\phi_i) = \frac{\sin 2\phi_i}{n_s^4 \cos^2 \phi_i - n_s^2 + \sin^2 \phi_i}$ and rewrite eq. (4.12) as

$$A = p(\phi_i)\epsilon_{xy} + p^*(\phi_i)\epsilon_{xy}^*. \tag{4.13}$$

For two different angles of incidence, eq. (4.13) yields a linear system with two equations and two unknowns ϵ_{xy} and ϵ_{xy}^*, which can be solved uniquely to find both the real and imaginary parts of ϵ_{xy}. The factor $p(\phi_i)$ depends on the refractive index, which might change when the sample is pumped by a femtosecond IR laser pulse. However, it has been shown that the non-magnetic contribution to the EUV T-MOKE asymmetry from ultrafast changes in the refractive index is two orders of magnitude smaller than the magnetic one and can thus be neglected [123, 124]. In practice, due to experimental uncertainties and noise in the data, more than two angles of incidence are required in order to solve for ϵ_{xy}. An angle-resolved T-MOKE measurement can be carried out with the setup shown in Fig. 4.2 by titlting the sample and, correspondingly, the CCD camera. A static angle-resolved T-MOKE asymmetry measured at the M-edge of Co is shown in Fig. 4.5

4.2.2 Diagonal magneto-optical effect

I now discuss the second approach that allows a direct measurement of ϵ_{xy} [125]. In this approach, the magnetization is set "diagonally", i.e. it has both a transverse and a longitudinal

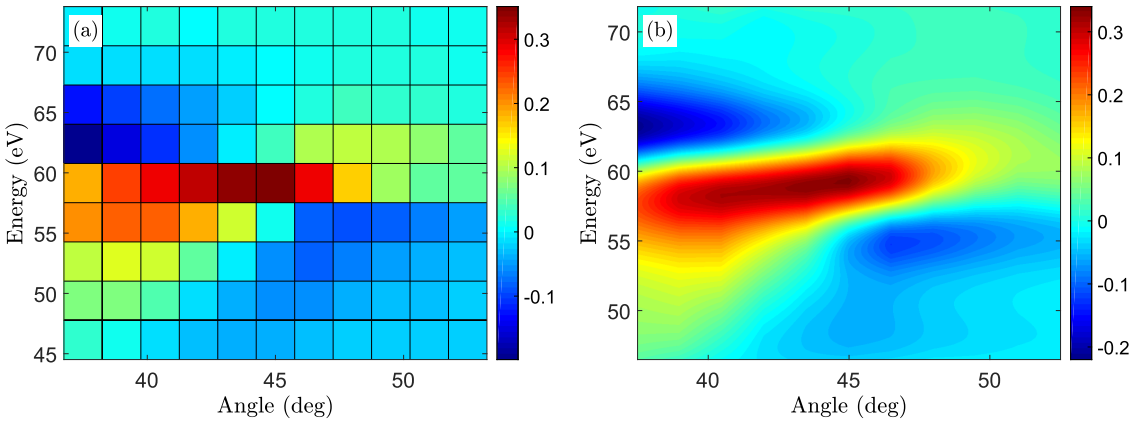

Figure 4.5: Static angle-resolved T-MOKE signal from a Co film: (a) Raw, (b) Interpolated

component, as shown in Fig. 4.6, and, for that reason, the effect is called a diagonal magneto-optical effect or D-MOE.

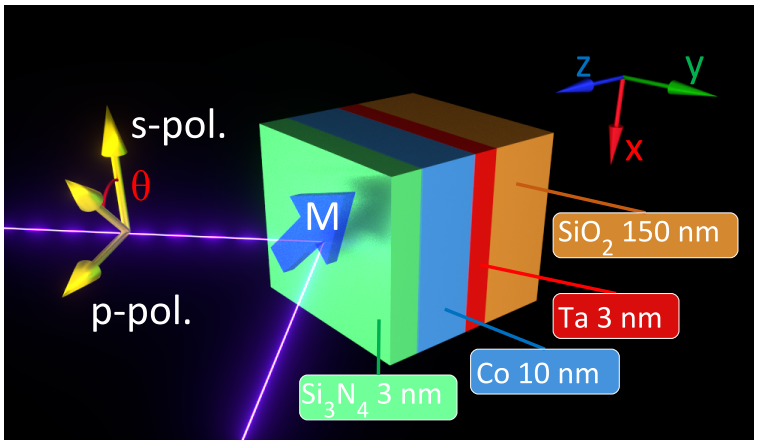

Figure 4.6: D-MOE geometry. The magnetization is set in-between the longitudinal and transverse orientations and the polarization angle is rotated. An example multilayer structure of a Co sample is also shown. θ is the polarization angle with repsect to s-polarization.

I start the derivation of the D-MOE asymmetry at the interface of a semi-infinite magnetic layer by expanding the amplitude of an incident linearly polarized field $\vec{E}_i$ in the basis of s- and p-polarizations (E_s, E_p)

$$\vec{E}_i = \begin{pmatrix} E_s \\ E_p \end{pmatrix} = \begin{pmatrix} \cos\theta \\ \sin\theta \end{pmatrix} E_0, \tag{4.14}$$

where θ is a polarization angle relative to s-polarization, as shown in Fig. 4.6, and E_0 is the magnitude of the incident field, which I set to 1 in the derivation below without loss of generality. It is convenient to assemble the Fresnel reflection coefficients similar to the ones in eqs. (4.7) into a 2×2 Fresnel reflection matrix $\hat{\mathbf{r}}$. The relationship between the incident and reflected fields then becomes

$$\vec{E}_r = \hat{\mathbf{r}}\vec{E}_i = \hat{\mathbf{r}} \begin{pmatrix} \cos\theta \\ \sin\theta \end{pmatrix}, \tag{4.15}$$

where $\hat{\mathbf{r}}$ depends on the magnetization $\vec{m}$ [121, 126]. For an in-plane magnetization direction, to a

first order in magneto-optical Voigt parameter $Q = i\epsilon_{xy}/\epsilon_{xx}$, $\hat{\mathbf{r}}$ can be written as

$$\hat{\mathbf{r}}(\vec{m}) = \begin{pmatrix} r_{ss} & r_{sp} \\ r_{ps} & r_{pp} \end{pmatrix} \simeq \begin{pmatrix} r_{ss}^{(0)} & r_{sp}^{(1)} m_y Q \\ -r_{sp}^{(1)} m_y Q & r_{pp}^{(0)} + r_{pp}^{(1)} m_x Q \end{pmatrix}, \tag{4.16}$$

where the superscripts (0) and (1) denote non-magnetic and magnetic first order contributions to the reflection coefficients, respectively. Note that $r_{ss}^{(0)} \equiv r_{ss}$. With eq. (4.10) and expressions (4.15) and (4.16), the magneto-optical asymmetry for a sample magnetized in-plane with magnetization components m_x and m_y along the x- and y-axis, respectively, can be derived (again, keeping only terms up to first order in Q)

$$A = \frac{m_y \sin 2\theta \, \Re\left((r_{ss} - r_{pp}^{(0)})^* r_{sp}^{(1)} Q\right) - m_x \left(1 - \cos 2\theta\right) \Re\left(r_{pp}^{(0)*} r_{pp}^{(1)} Q\right)}{|r_{pp}^{(0)}|^2 \sin^2\theta + |r_{ss}|^2 \cos^2\theta}. \tag{4.17}$$

For transverse ($m_x = 1$, $m_y = 0$) and longitudinal ($m_x = 0$, $m_y = 1$) configurations, the familiar expressions for the asymmetries A_T and A_L are recovered [127, 128]

$$A_T := A(m_x = 1; m_y = 0) = \frac{\left(\cos 2\theta - 1\right) \Re\left(r_{pp}^{(0)*} r_{pp}^{(1)} Q\right)}{|r_{pp}^{(0)}|^2 \sin^2\theta + |r_{ss}|^2 \cos^2\theta}, \tag{4.18}$$

$$A_L := A(m_x = 0; m_y = 1) = \frac{\sin 2\theta \, \Re\left((r_{ss} - r_{pp}^{(0)})^* r_{sp}^{(1)} Q\right)}{|r_{pp}^{(0)}|^2 \sin^2\theta + |r_{ss}|^2 \cos^2\theta}. \tag{4.19}$$

Note that the T-MOKE asymmetry A_T maximizes when $\theta = \pi/2$, i.e. for p-polarization, and $A_L = 0$ for $\theta = \pi/2$ and $\theta = 0$, which means that a mixed polarization is required to measure an asymmetry in the longitudinal configuration.

In the diagonal geometry, $|m_x| = m_y = 1/\sqrt{2}$, and the D-MOE asymmetry is

$$A_D := A\left(m_x = -\frac{1}{\sqrt{2}}; m_y = \frac{1}{\sqrt{2}}\right) = F_D(\theta) Q + F_D^*(\theta) Q^*, \tag{4.20}$$

where the complex factor $F_D(\theta)$ has been defined as

$$F_D(\theta) = \frac{\sin 2\theta (r_{ss} - r_{pp}^{(0)})^* r_{sp}^{(1)} + \left(1 - \cos 2\theta\right) r_{pp}^{(0)*} r_{pp}^{(1)}}{2\sqrt{2}\left(|r_{pp}^{(0)}|^2 \sin^2\theta + |r_{ss}|^2 \cos^2\theta\right)}. \tag{4.21}$$

Note that eq. (4.20) would hold for any other in-plane orientation of $\vec{m}$, as long as both the x and y magnetization components are non-zero. Here a symmetric configuration $|m_x| = m_y = 1/\sqrt{2}$ is chosen for simplicity and without loss of generality.

I now show that eqs. (4.20) and (4.21) can be used to uniquely determine Q, and thus ϵ_{xy} from measurements taken at multiple polarization angles, while the transverse and longitudinal geometries are not suited for that purpose. I rewrite A_T and A_L in a form similar to eq. (4.20)

$$A_T = F_T(\theta)Q + F_T^*(\theta)Q^* \equiv f_T(\theta)\left(r_{pp}^{(0)*}r_{pp}^{(1)}Q + r_{pp}^{(0)}r_{pp}^{(1)*}Q^*\right), \tag{4.22}$$

$$A_L = F_L(\theta)Q + F_L^*(\theta)Q^* \equiv f_L(\theta)\left((r_{ss} - r_{pp}^{(0)})^* r_{sp}^{(1)}Q + (r_{ss} - r_{pp}^{(0)})r_{sp}^{(1)*}Q^*\right), \tag{4.23}$$

where the parameters $f_T(\theta)$ and $f_L(\theta)$—as well as $F_T(\theta)$ and $F_L(\theta)$ implicitly—are defined as

$$f_T(\theta) \equiv \frac{F_T(\theta)}{r_{pp}^{(0)*}r_{pp}^{(1)}} = \frac{(\cos 2\theta - 1)}{2\left(|r_{pp}^{(0)}|^2 \sin^2\theta + |r_{ss}|^2\cos^2\theta\right)}, \tag{4.24}$$

$$f_L(\theta) \equiv \frac{F_L(\theta)}{(r_{ss} - r_{pp}^{(0)})^* r_{sp}^{(1)}} = \frac{\sin 2\theta}{2\left(|r_{pp}^{(0)}|^2 \sin^2\theta + |r_{ss}|^2\cos^2\theta\right)}. \tag{4.25}$$

A system of two linearly independent equations is required in order to find a unique solution for Q and Q^*. Such a system can be obtained by measuring the magnetic asymmetry spectrum at two different polarization angles θ_1 and θ_2 and, in the most general form, can be written as

$$\begin{pmatrix} a_x & b_x \\ c_x & d_x \end{pmatrix}\begin{pmatrix} Q \\ Q^* \end{pmatrix} = \begin{pmatrix} A_x(\theta_1) \\ A_x(\theta_2) \end{pmatrix}, \tag{4.26}$$

where the subscript $x = T, L$ or D. From eqs. (4.22), (4.23), and (4.20), for the transverse, longitudinal, and diagonal geometries, the system matrix $\mathbf{\Lambda_x}$ has the following explicit expressions

$$\mathbf{\Lambda_T} := \begin{pmatrix} a_T & b_T \\ c_T & d_T \end{pmatrix} = \begin{pmatrix} f_T(\theta_1)r_{pp}^{(0)*}r_{pp}^{(1)} & f_T(\theta_1)r_{pp}^{(0)}r_{pp}^{(1)*} \\ f_T(\theta_2)r_{pp}^{(0)*}r_{pp}^{(1)} & f_T(\theta_2)r_{pp}^{(0)}r_{pp}^{(1)*} \end{pmatrix}, \tag{4.27}$$

$$\mathbf{\Lambda_L} := \begin{pmatrix} a_L & b_L \\ c_L & d_L \end{pmatrix} = \begin{pmatrix} f_L(\theta_1)(r_{ss} - r_{pp}^{(0)})^* r_{sp}^{(1)} & f_L(\theta_1)(r_{ss} - r_{pp}^{(0)})r_{sp}^{(1)*} \\ f_L(\theta_2)(r_{ss} - r_{pp}^{(0)})^* r_{sp}^{(1)} & f_L(\theta_2)(r_{ss} - r_{pp}^{(0)})r_{sp}^{(1)*} \end{pmatrix}, \tag{4.28}$$

$$\mathbf{\Lambda_D} := \begin{pmatrix} a_D & b_D \\ c_D & d_D \end{pmatrix} = \begin{pmatrix} F_D(\theta_1) & F_D^*(\theta_1) \\ F_D(\theta_2) & F_D^*(\theta_2) \end{pmatrix}. \tag{4.29}$$

The determinants of the system matrices are

$$\det \mathbf{\Lambda_T} = f_T(\theta_1)f_T(\theta_2)\left(\left|r_{pp}^{(0)}\right|^2\left|r_{pp}^{(1)}\right|^2 - \left|r_{pp}^{(0)}\right|^2\left|r_{pp}^{(1)}\right|^2\right) \equiv 0, \tag{4.30}$$

$$\det \mathbf{\Lambda_L} = f_L(\theta_1) f_L(\theta_2) \left(\left| r_{ss} - r_{pp}^{(0)} \right|^2 \left| r_{sp}^{(1)} \right|^2 - \left| r_{ss} - r_{pp}^{(0)} \right|^2 \left| r_{sp}^{(1)} \right|^2 \right) \equiv 0, \tag{4.31}$$

$$\det \mathbf{\Lambda_D} = F_D(\theta_1) F_D^*(\theta_2) - F_D^*(\theta_1) F_D(\theta_2) \neq 0. \tag{4.32}$$

The only non-trivial determinant (when $\cos(\theta_1)\sin(\theta_2) \neq \sin(\theta_1)\cos(\theta_2)$, which is satisfied when $\theta_{1,2} \neq 0$ and $\theta_1 \neq \theta_2$) is the one that corresponds to the diagonal geometry, which means that this geometry can be used for a unique determination of Q and ϵ_{xy} by scanning the polarization angle, while the transverse and longitudinal geometries are not suited for that purpose.

The experimental setup in Fig. 4.2 needs to be adapted for D-MOE measurements. The rotation of the polarization of the EUV probe is easily achieved by simply rotating the polarization of the IR driving laser with a half-wave plate placed before the waveguide in which the HHG process takes place. The direction of the linear polarization of HHG pulses follows that of the laser driver [88, 82]. Therefore, no modification to the HHG source part of the setup is required, other than replacing a manual rotation stage for the half-wave plate with a motorized one, so that the polarization scans could be integrated into an automated data acquisition procedure in Fig. 4.3. In order to apply a magnetic field in a diagonal direction, the sample mount needs to be redesigned because with the mount in Fig. 4.2 the field can only be applied in the transverse direction. The spectrometer arm of the setup adapted for D-MOE measurements is shown in Fig. 4.7. Because scanning the angle of incidence is no longer required, the spectrometer can be positioned horizontally, which has an added benefit of increased stability. Moreover, the diffraction grating can now be separated from the sample. Not only does this design simplify the sample making process by eliminating the need to pattern a grating on top of the film, but it also improves the diffraction efficiency as the grating can now be blazed and positioned in a conical mount [129]. Additionally, the separation of the grating from the sample removes any ambiguity in the sample's response as it can be attributed to the sample itself without the need to consider the effects of the grating deposited on the sample. Below, I do consider the polarization sensitivity of the grating response, nonetheless, in order to confirm that it does not affect the D-MOE signal. A different Ti:Sapphire amplifier, a KMLabs Wyvern, was used in the D-MOE experiment. The laser was

operated at a 5 kHz repetition rate, with a pulse duration of ∼40 fs, and a pulse energy of 2 mJ.

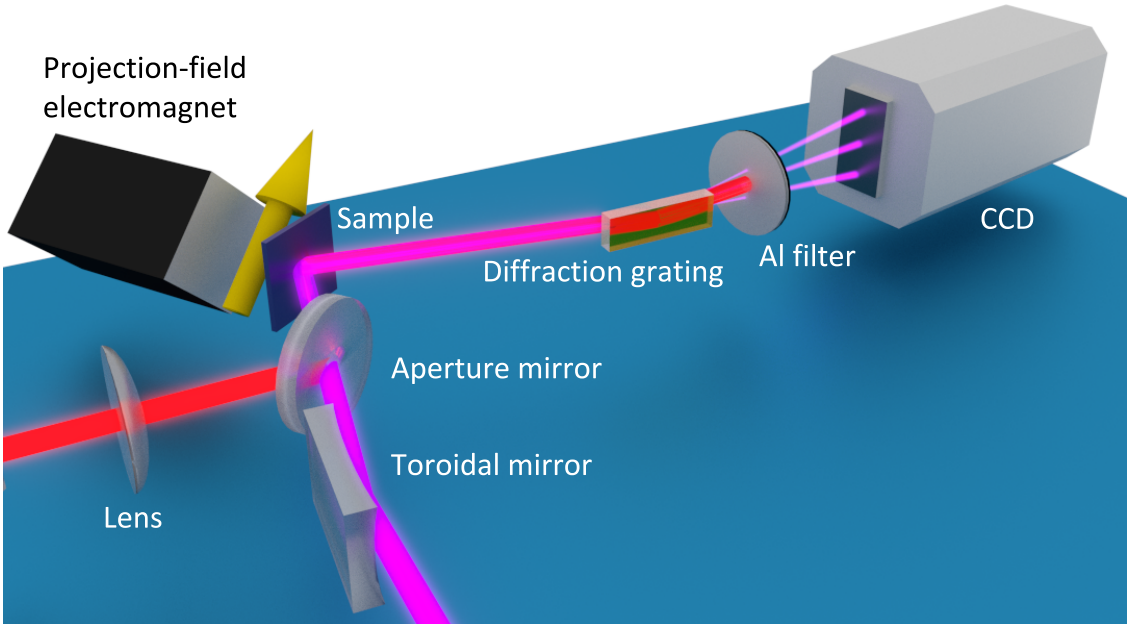

Figure 4.7: Spectrometer part of the D-MOE setup. A projection-field electromagnet is placed behind the sample. The diffraction grating is separated from the sample and is oriented in a conical mount, with the grating lines parallel to the plane of incidence for higher diffraction efficiency.

A static polarization-resolved D-MOE asymmetry is shown in Fig. 4.8, as measured at the harmonic peaks. Note that overall, the amount of data in Fig. 4.8 is greater than that in Fig. 4.5 because it is easier to take finer steps in the polarization angle than in the angle of incidence. In addition, when the angle of incidence is changed the amount of the absorbed IR pump light also changes slightly. That is not the case for time-resolved D-MOE since it keeps the angle of incidence constant.

4.2.3 Magneto-optical multilayer formalism

For thick samples, expressions (4.12) and (4.20) could be applied directly to the data in Figs. 4.5 and 4.8, respectively, to extract ϵ_{xy}. However, the data in the figures were taken with multilayer thin films, which can significantly modify the Fresnel reflections. A formalism describing the propagation of light in magnetic multilayers was developed in Ref. [130], and I outline it below.

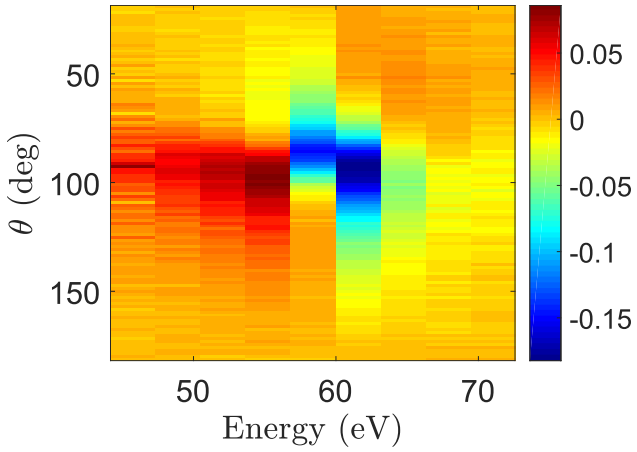

Figure 4.8: Static polarization-resolved D-MOE asymmetry at the M-edge of Co measured at the harmonic peaks.

Within this formalism, each layer in a multilayer stack is represented by a set of matrices: the boundary matrix L that describes the reflection from and transmission through the boundary of two layers and the propagation matrix $\bar{D}$ that describes the propagation of light through a given layer. The entire multilayer stack then is represented by a combination of those matrices for each layer.

The medium boundary matrix L is derived from the Maxwell boundary conditions. Consider an interface between two semi-infinite media, as in Fig. 4.9. In each half-space, there are forward (incident) and backward (reflected) propagating fields marked by the superscripts (i) and (r), respectively. The medium above the boundary is denoted with an index 1, and the one below with an index 2. The medium boundary matrix L is defined as a matrix that relates two 4-element

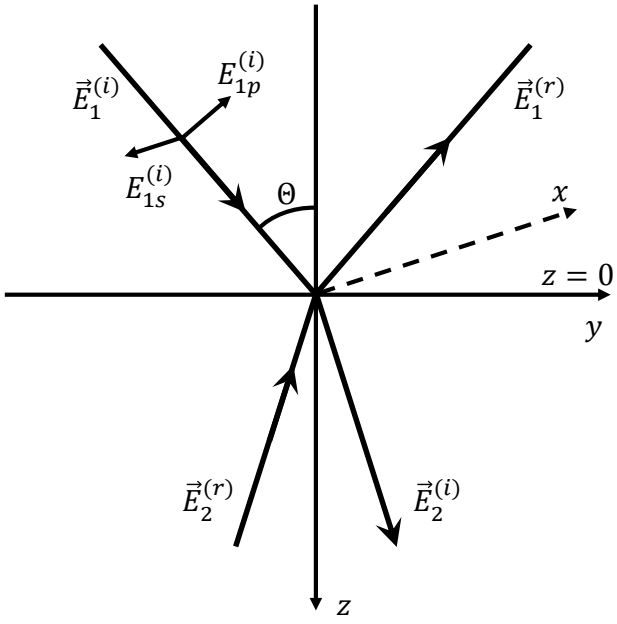

Figure 4.9: Fields at an interface between two media. The x- and y-axes are in the plane of the interface, and the z axis is normal to it. Adapted from [130].

vectors

$$F = LP, \tag{4.33}$$

where vectors F and P contain the x- and y-components of the E and H fields and the incident

and reflected s- and p-components of the E-field, respectively, all in a given medium

$$F = \begin{pmatrix} E_x \\ E_y \\ H_x \\ H_y \end{pmatrix}, \quad P = \begin{pmatrix} E_s^{(i)} \\ E_p^{(i)} \\ E_s^{(r)} \\ E_p^{(r)} \end{pmatrix}. \tag{4.34}$$

At the boundary between media 1 and 2, $F_1 = F_2$, and from eq. (4.33), matrix L for a medium with

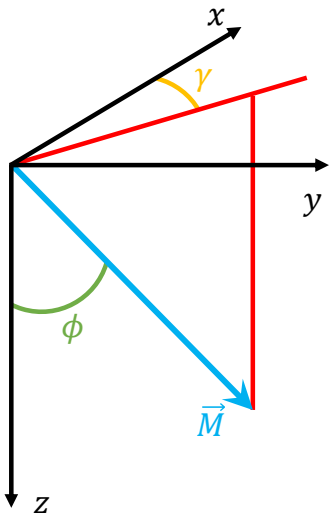

Figure 4.10: Azimuthal and polar angles for the magnetization vector. For a yz plane of incidence, the polar geometry corresponds to $\phi = 0$; transverse $\phi = \pi/2$, $\gamma = 0$; longitudinal $\phi = \pi/2$, $\gamma = pi/2$, and diagonal $\phi = \pi/2$, $0 < \gamma < \pi/2$.

a refractive index N and a magnetization direction determined by the polar angle ϕ and azimuthal angle γ (see Fig. 4.10) can be obtained (details can be found in Ref. [130])

$$L = \begin{pmatrix} 1 & 0 & 1 & 0 \\ \frac{i}{2}\frac{\alpha_y}{\alpha_z} Q\left(\alpha_y g_i - 2S_{\phi,\gamma}\right) & \alpha_z + i\alpha_y C_{\phi,\gamma} Q & -\frac{i}{2}\frac{\alpha_y}{\alpha_z} Q\left(\alpha_y g_r - 2S_{\phi,\gamma}\right) & -\alpha_z + i\alpha_y C_{\phi,\gamma} Q \\ \frac{i}{2} N g_i Q & -N & \frac{i}{2} N g_r Q & -N \\ N\alpha_z & \frac{iN}{2\alpha_z} g_i Q & -N\alpha_z & -\frac{iN}{2\alpha_z} g_r Q \end{pmatrix}. \tag{4.35}$$

In the expression above, the following definitions have been introduced

$$\begin{aligned} S_{\phi,\gamma} &= \sin\phi\sin\gamma, \quad C_{\phi,\gamma} = \sin\phi\cos\gamma, \\ \alpha_y &= \sin\Theta, \quad \alpha_z = \cos\Theta, \\ g_i &= \alpha_z\cos\phi + \alpha_y S_{\phi,\gamma}, \quad g_r = -\alpha_z\cos\phi + \alpha_y S_{\phi,\gamma}, \end{aligned} \tag{4.36}$$

where Θ is the angle of incidence.

The propagation matrix $\bar{D}$ relates the fields at the top of a layer with the fields at a depth z in the layer and is defined by

$$P(0) = \bar{D}(z)P(z). \tag{4.37}$$

This matrix takes into account phase shifts, absorption, and polarization rotation of the light propagating through a given layer. For a layer of thickness d, the medium propagation matrix can be written explicitly as

$$\bar{D} = \begin{pmatrix} U & U\delta_i & 0 & 0 \\ -U\delta_i & U & 0 & 0 \\ 0 & 0 & U^{-1} & -U^{-1}\delta_r \\ 0 & 0 & U^{-1}\delta_r & U^{-1} \end{pmatrix}, \tag{4.38}$$

where the elements U, δ_i, and δ_r are defined as follows

$$\begin{aligned} U &= \exp\left(-i\frac{2\pi}{\lambda}Nd\alpha_z\right), \\ \delta_i &= \frac{\pi}{\lambda}Nd\frac{Q}{\alpha_z}g_i, \\ \delta_r &= \frac{\pi}{\lambda}Nd\frac{Q}{\alpha_z}g_r, \end{aligned} \tag{4.39}$$

where λ is the free-space wavelength of the light propagating in the layer. Here, it is important to note that a convention where a forward propagating wave is given by $E = E_0\exp\left(i(N\vec{k}_0\cdot\vec{z} - \omega t)\right)$ is used. It requires a positive imaginary part of the refractive index, i.e. $N = 1 - \delta + i\beta$. It also determines the sign of the Kramers-Kronig transform, which I describe below.

The action of an entire multilayer stack on an initial 4-element vector P_i containing forward and backward propagating waves (zero for an incident wave) for s- and p-polarizations is described

by a single 4×4 matrix M defined as

$$P_i = MP_f, \tag{4.40}$$

where P_f is the final 4-element vector, and M is equal to a product of the medium propagation and boundary matrices and their inverses for all the layers [130]

$$M = L_i^{-1} \prod_m L_m \bar{D}_m L_m^{-1} L_f. \tag{4.41}$$

M can be written in a block-diagonal form as

$$M = \begin{pmatrix} G & H \\ I & J \end{pmatrix}, \tag{4.42}$$

where G, H, I, J are 2×2 matrices. The Fresnel transmission and reflection matrices (as in eq. (4.16)) can then be identified as [130]

$$\begin{aligned} \hat{\mathbf{t}} &= \begin{pmatrix} t_{ss} & t_{sp} \\ t_{ps} & t_{pp} \end{pmatrix} = G^{-1}, \\ \hat{\mathbf{r}} &= \begin{pmatrix} r_{ss} & r_{sp} \\ r_{ps} & r_{pp} \end{pmatrix} = IG^{-1}. \end{aligned} \tag{4.43}$$

With the expressions above, the following procedure can be used to compute magneto-optical reflections and transmissions for a magnetic multilayer stack

(1) Set the angle of incidence and the polarization state of an incident beam

(2) Set the magnetization directions for all layers

(3) For each layer, determine the refractive index N and the magneto-optical Voigt parameter Q at the wavelength of interest

(4) For each layer, compute the medium boundary and propagation matrices according to eqs. (4.35) and (4.38), respectively

(5) Compute the total matrix M for an entire stack according to (4.41)

(6) Compute the Fresnel transmission and reflection matrices $\hat{\mathbf{t}}$ and $\hat{\mathbf{r}}$ using eqs. (4.42) and (4.43)

(7) Compute the transmitted and reflected fields as $\vec{E}_t = \hat{\mathbf{t}}\vec{E}_i$ and $\vec{E}_r = \hat{\mathbf{r}}\vec{E}_i$, respectively

Sometimes, it can be advantageous to use a slightly different procedure in the interest of computational expediency. One example is when a large parameter space of wavelengths and incidence angles needs to be swept. In that case, the code would be easier to parallelize if reflections and transmissions at each boundary were calculated explicitly from the boundary condition $L_{i-1}P_{i-1} = L_iP_i$. For the most general case of arbitrary magnetization directions in the adjacent layers, the expressions are too unwieldy to provide here, but such a calculation was, nonetheless, performed in Mathematica. With known boundary reflections and transmissions, a wave can be propagated through a multilayer stack until a convergence condition (e.g. an error tolerance) is reached. An added benefit of such an approach is that it allows a calculation of the fields throughout an entire sample. This is useful when, for example, the pump absorption profile needs to be calculated, or an estimation of the depth sensitivity of an EUV probe needs to be performed. I discuss the latter estimation in Appendix A.

4.2.3.1 Effect of optical elements on the magneto-optical signal

With the multilayer formalism, the extraction of ϵ_{xy} from the angle-resolved and polarization-resolved data sets is performed by a fitting procedure, i.e., ϵ_{xy} is adjusted in order to minimize a root mean square (rms) error between the experimental data and the calculated angle-resolved T-MOKE or polarization-resolved D-MOE signals.

In the case of the angle-resolved T-MOKE, a 500 lines/mm diffraction grating was lithographically patterned on the sample (see Fig. 4.11). Because the diffraction grating is patterned directly on the sample, it might reduce the T-MOKE asymmetry because the Si substrate is non-magnetic and has a higher reflectivity. Upon diffraction from the grating, it is mixed with the light reflected from the magnetic part and, therefore, needs to be taken into account. This is done by calculating

the Fresnel reflections for both the grooves and ridges of the grating using the multilayer approach. This gives a spatially varying distribution of the reflection coefficient $r(y)$. The reflected field at the detector is equal to a Fourier transform of a product of the incident probe and $r(y)$

$$\tilde{E}(k_y) \propto \mathcal{F}\{r(y)E_i(y)\}, \tag{4.44}$$

where $E_i(y)$ is a Gaussian illuminating approximately 50 grating lines. The calculated intensity is taken at the first order diffraction peak position k_1, for a given wavelength

$$I_r = \left|\tilde{E}(k_y = k_1)\right|^2. \tag{4.45}$$

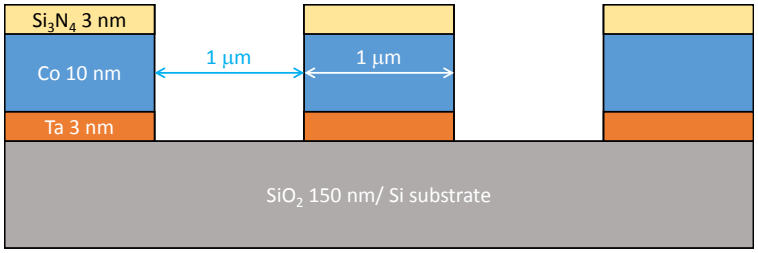

Figure 4.11: Sample structure for angle-resolved T-MOKE. A 10 nm Co film is grown on a Si wafer with a 3 nm Ta seed layer and a 3 nm Si_3N_4 cap. The sample was lithographically patterned to form a 500 lines/mm grating.

For the D-MOE experiment, the effect of the toroidal mirror on the polarization of the probe and the effect of the spectrometer grating on the D-MOE asymmetry must be examined. I will first consider the effect of the toroidal mirror. Because the measurement is polarization sensitive, one might expect that, upon reflection from the toroid, the linear polarization of the probe becomes elliptical. I confirm that the ellipticity of the reflected EUV probe is very small. The polarization ellipse is uniquely described by a set of four parameters known as the Stokes parameters [131]. The Stokes parameter S_3 is related to the ellipticity, and $S_3 = 0$ for linear polarization and $S_3 = \pm 1$ for circular. By calculating multilayer reflections at a 6° grazing incidence angle for different polarization angles ranging from s- to p-polarization from a toroid made out of

Pyrex glass and coated with a 100 nm of B_4C, I find that $S_3 \leq 0.11$. This means that approximately 95% of the reflected field maintains the original incident polarization, while only ∼5% is rotated perpendicularly to that direction. In other words, the ratio of the minor and major semi-axes of the reflected elliptical polarization is 0.055. This ellipticity is rather small and thus can be neglected for the purposes of the D-MOE experiment.

A diffraction grating could also introduce artifacts in the D-MOE signal. The reason for this is a possible difference in diffraction efficiencies for the light reflected from the positively and negatively magnetized sample. This is because the D-MOE configuration in Fig. 4.6 is not symmetric, which leads to a difference in the polarization states of the probe reflected from the sample when its magnetized in the $+\vec{m}$ and $-\vec{m}$ directions. Because the spectrometer grating is a sawtooth grating and is mounted in a conical configuration, it breaks the symmetry further, which could result in different diffraction efficiencies for different polarizations. The calculation in Fig. 4.12 was carried out for different polarization angles of EUV light incident on a thin Co film with a multilayer composition of $Si/SiO_2(150)/Ta(3)/Co(10)/Si_3N_4(3)$, where all layer thicknesses are in nm. First, I calculate the magneto-optical reflections from this sample for opposite magnetization

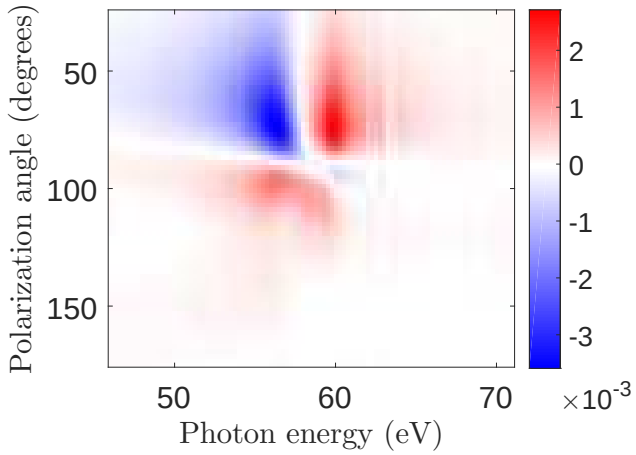

Figure 4.12: Difference in diffraction efficiencies in the D-MOE geometry for the two opposite magnetization directions. Complex magneto-optical reflections from a Co multilayer were calculated and used as inputs for an RCWA model (see Appendix B) in order to compute diffraction efficiencies from a blazed grating mounted in a conical configuration. The difference is small and does not exceed 0.35%.

directions in the D-MOE geometry at a 52° incidence using the multilayer approach described above. Next, I use the calculated complex reflected fields as inputs for a diffraction efficiency calculation. The latter is performed using the rigorous coupled-wave analysis (RCWA) formalism described in Appendix B. The sawtooth grating used in the calculation was made of Zerodur glass with a 30 nm B_4C coating. The periodicity of the grating was 2 μm, and the blaze angle was 4.7°. It was mounted in a conical configuration at a 5° grazing incidence, and the grating vector was turned by 2° with respect to the normal to the plane of incidence, to allow for any possible misalignment. The difference in the calculated diffraction efficiencies in Fig. 4.12 does not exceed 0.35%, and, therefore, the effect of the spectrometer grating on the D-MOE asymmetry is negligible.

4.3 Understanding the microscopic picture of ultrafast demagnetization

Despite the active interest in the phenomenon of ultrafast demagnetization over the past two decades and a large volume of experimental data [57, 132, 133, 123, 134, 135, 136] the consensus as to the microscopic picture of laser-driven magnetization dynamics is still lacking in the scientific community [137, 138, 139, 140, 141]. There are several reasons for this. First, as discussed in Chapter 2, our understanding of ferromagnetism in transition metals is incomplete due to the itinerant nature of $3d$ electrons in those metals, i.e. they exhibit both localized and delocalized behavior. Second, measurements are often performed on one material, e.g. Ni, and the conclusions are sometimes extrapolated to other materials, such as Co and Fe. Even though they are all transition metals, they are quite different from one another and such an extrapolation is not always correct. Third, measurements often employ different techniques, such as visible MOKE, EUV T-MOKE, spin-resolved photoemission, or XMCD. These techniques have inherent limitations, and, in general, they measure different aspects of the phenomenon. For example, photoemission is sensitive to the first few monolayers near the surface of the sample, and the measurement is performed along a specific direction in the Brillouin zone. EUV T-MOKE, on the other hand, is capable of measuring polycrystalline materials, which gives an average signal across the entire Brillouin zone, and the T-MOKE response is a convolution of the magnetization profile throughout

the thickness of the sample with the T-MOKE depth sensitivity function (see Appendix A), which can extend up to a few tens of nm into the sample. Due to a non-uniform absorption of the IR pump light, the conditions at the surface and in the bulk of the film can be quite different, and care must be taken while comparing the results of photoemission experiments with those of visible or EUV T-MOKE [142, 143]. For example, such a comparison was made for a single crystal bulk (400 nm) Ni film, and the difference in the T-MOKE and photoemission data was attributed to a depth dependence of the demagnetization process [144, 145]; additionally, in these references, an ultrafast phase transition from the ferromagnetic to the paramagnetic state was reported.

The following processes have been reported in the literature as potential microscopic drivers of ultrafast demagnetization, in the absence of a phase transition:

- Ultrafast magnon generation, or transverse spin excitations [146, 147, 148, 149, 150, 151].
- Longitudinal spin-flips driven by the spin-orbit interaction in the valence band [152] through the Elliott-Yafet electron-phonon scattering process [153]. In the context of the microscopic three-temperature model, these lead to a reduction of the exchange splitting Δ_{ex} (see Fig. 2.2) [58].
- Superdiffusive spin currents [154, 155, 156].

The former two items are known as the local demagnetization mechanisms because they lead to a local reduction of the magnetization, while the superdiffusive spin currents are non-local because they involve transport of the spin polarization from one part of the film to another. Because the films studied here are grown on insulating substrates and are rather thin, the non-local demagnetization channel is blocked, and only the local excitations are considered. Longitudinal spin fluctuations exist within the framework of the Stoner model of ferromagnetism, and transverse fluctuations are based on the Heisenberg model. More details on the two models and the types of spin excitations within them can be found in Chapter 2. It should be noted that very short-wavelength magnons overlap with the Stoner continuum of spin-flip excitations, and they have very short lifetimes

[157, 158], on the order of femtoseconds for Co, and, therefore, such short wavelength magnons can contribute to ultrafast magnetization dynamics.

As mentioned above, transverse and longitudinal spin fluctuations affect the magneto-optical permittivity ϵ_{xy} differently: transverse excitations lead to a uniform reduction of ϵ_{xy} across all photon energies, while longitudinal excitations change its spectral shape [70]. This was confirmed by first principles DFT calculations of the DOS for hcp Co. The calculations were carried out at Uppsala University, Sweden, and Charles University, Czech Republic, using the WIEN2k DFT code [159]. The dielectric tensor was computed from the linear response theory [73]. More details regarding the calculations can be found in Ref. [122] and its Supplementary Information. These calculations confirmed that if the magnetization was tilted by an angle of up to 22°, the amplitude of ϵ_{xy} would decrease uniformly without a change in its spectral shape. On the other hand, if a decrease in magnetization was due to, at least in part, a reduction in the exchange splitting, the spectral shape of ϵ_{xy} would be affected, as shown in Fig. 4.13. This provides a

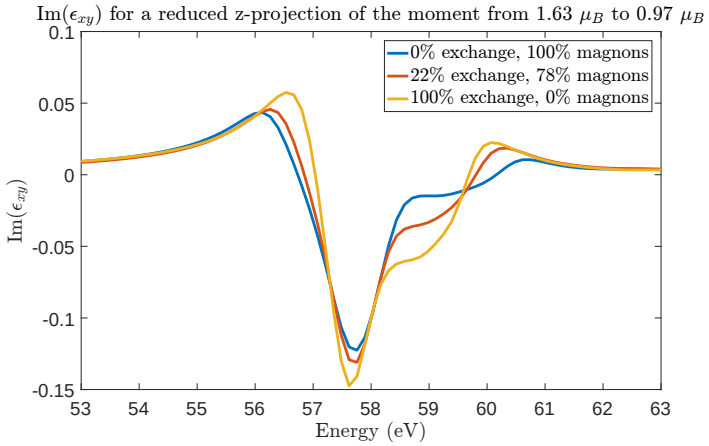

Figure 4.13: Im (ϵ_{xy}) at the M-edge of Co with a reduced magnetization calculated from first principles for different values of exchange splitting Δ_{ex}. Note the changes in the spectral shape as the exchange splitting is reduced.

means of distinguishing between longitudinal and transverse excitations in a material following a femtosecond optical pump, i.e., tracing the transient evolution of the measured full complex resonant magneto-optical permittivity ϵ_{xy}. Such tracing was carried out using the angle-resolved EUV

T-MOKE and polarization-resolved D-MOE techniques discussed above. In the following, I present the experimental results obtained using the two methods and the respective conclusions.

4.4 Ultrafast demagnetization with angle-resolved T-MOKE

First, with a 10 nm Co thin film whose composition is shown in Fig. 4.11, a T-MOKE demagnetization curve was measured (see Fig. 4.14) at the M-edge of Co at a 45° incidence using the setup in Fig. 4.2. Because the experimental procedure for angle-resolved T-MOKE involves

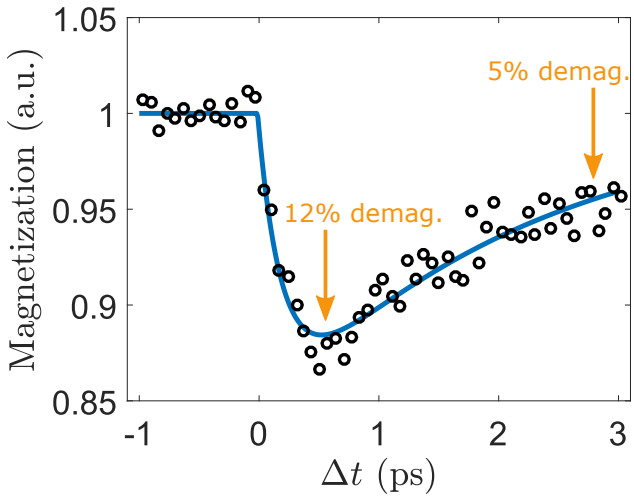

Figure 4.14: Ultrafast demagnetization in a 10 nm Co film. The maximum demagnetization is 12% (at 700 fs) and the demagnetization at 3 ps is 3%. The absorbed pump fluence is estimated at 1.3 mJ/cm^2.

a manual adjustment of the angle of incidence, which is rather cumbersome and time consuming, only two time points on the curve in Fig. 4.14 were chosen for an angle-resolved scan (from 37.5° to 52.5°): at the time of maximum demagnetization at 700 fs, and at 3 ps, when the system has reached thermal equilibrium and is in the recovery phase. Transient changes to the static angle-resolved T-MOKE scan (Fig. 4.15(a)) at these times are shown in Fig. 4.15(b) and (c). The static data and the dynamic changes to it can now be analyzed to determine the relative contributions of the longitudinal and transverse spin fluctuations. Note that a dissipation channel through spin-polarized currents is blocked because the ferromagnetic films are grown on insulating substrates.

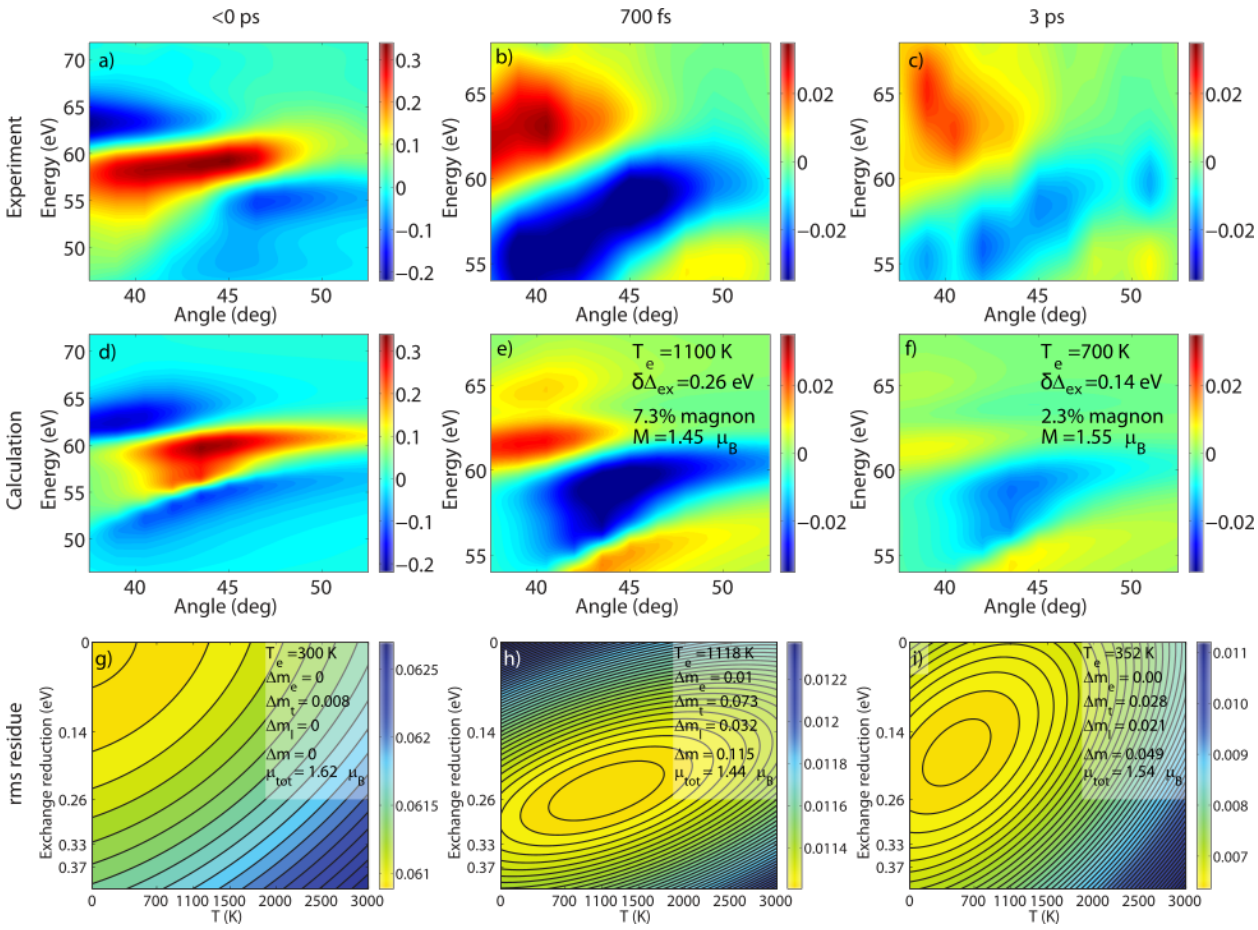

Figure 4.15: Time-resolved data and analysis of angle-resolved T-MOKE. The top row is the experimental data, the second row is the simulations that correspond to the best fit to the experimental data, and the bottom row is the rms analysis. The columns (from left to right) correspond to the times of < 0 ps, 0.7 ps, and 3 ps. (a) Static angle-resolved T-MOKE asymmetry. (b), (c) Differential changes to the static asymmetry at 0.7 and 3 ps, respectively. (d), (e), (f) are the static angle-resolved T-MOKE and the differential changes to it at 0.7 ps and 3 ps, respectively, calculated based on the theoretical values of ϵ_{xy}. (g), (h), (i) are quadratic surface fits to the rms residue calculated by fitting the experimental data with calculated T-MOKE signals based on different theoretical values of ϵ_{xy} calculated at various electron temperatures and exchange splittings.

The analysis involves fitting the data with simulated angle-resolved T-MOKE signals that are based on ϵ_{xy}'s calculated for different electron temperatures and exchange splittings in a self-consistent manner (see Ref. [122] for details on the calculation of ϵ_{xy}). This is preferable to a direct extraction of ϵ_{xy} from the experimental data because a robust extraction would require a lot more points in the incidence angle than were actually measured. In the first step of the analysis, a fit to the static data in Fig. 4.15(a) is found. This is done by applying a Gaussian broadening and an energy shift to the *ab initio* calculated ϵ_{xy} at a zero electron temperature $T_e = 0$ K and exchange splitting $\Delta_{ex} = 1.672$ eV, which corresponds to the ground-state magnetic moment of Co of 1.63 μ_B. These transformations are necessary in order to include the effects that the theoretical calculations do not take into account, such as a finite lifetime of electrons that are optically excited from the $3p$ core states to the conduction band of Co, which requires a Gaussian broadening, an energy offset of the theoretical $3p$ levels relative to the experiment (requires an energy shift), and an overestimation of the magnitude of ϵ_{xy} as well as magnon excitations present at 300 K (requires an application of a scaling factor of < 1). Additionally, a small offset of $< 1^\circ$ in the incidence angle as well as a 2% s-polarized component of the probe were included in order to allow for a misalignment of the EUV probe with respect to a purely horizontal direction and its depolarization on optical surfaces (e.g. the toroid). An additional broadening by a Gaussian kernel with a FWHM of 1.28 eV was applied to the simulated angle-resolved T-MOKE asymmetry in order to take into account the fact that an EUV probe illuminated only ∼50 grating lines, which lowered the spectral resolution. The optimal energy shift δE, the width of the Gaussian broadening kernel w, and the scaling factor G are found by minimizing a mean square difference between the calculated asymmetry and the experimental one in Fig. 4.15(a) $\sum_{\Theta,E} \left[A_{exp}(\Theta, E) - A_{calc}\left(\Theta, E, \epsilon_x y\left(w, G, \delta E\right)\right)\right]^2 = min$, where the sum is taken over all measured incidence angles Θ and harmonic energies E(see Fig. 4.5(a)). The optimal parameters w, δE, and G are then applied to the rest of ϵ_{xy}'s calculated for all other electron temperatures T_e and exchange splittings Δ_{ex}.

In the next step, a fit to the time-resolved experimental data in Fig. 4.15(b) and (c) is performed. This is done by minimizing an rms residue r between the experimental transient change

in asymmetry ΔA_{exp} (both at 0.7 ps and 3 ps) and one calculated for a given theoretical $\epsilon_{xy}(T_e, \Delta_{ex})$ at a specific T_e and Δ_{ex}. The only fitting parameter that minimizes r is the magnon contribution to the total demagnetization $\Delta m_t = \Delta\mu_t/\mu$, where $\mu = 1.63\ \mu_B$ is the ground state magnetic moment of Co, and $\Delta\mu_t$ is a reduction of its projection on the axis of average magnetization due to transverse excitations. The effect of transverse excitations is included by multiplying ϵ_{xy} by a factor $(1 - \Delta m_t)$. The rms residue mentioned above is expressed as

$$r(\Delta t, T_e, \Delta_{ex}, \Delta m_t) = \sqrt{\frac{1}{N}\sum_{\Theta,E}\left[\Delta A_{exp}^{(\Theta,E)}(\Delta t) - \Delta A_{calc}^{(\Theta,E)}\left((1-\Delta m_t)\epsilon_{xy}(T_e, \Delta_{ex})\right)\right]^2}, \qquad (4.46)$$

where Δt is a delay time between the pump and the probe, which is equal to either 0.7 ps or 3 ps, and N is the total number of experimental data points in the energy-angle parameter space (see Fig. 4.5). In addition to the transverse contribution to demagnetization Δm_t, the fitting procedure yields an rms residue, calculated according to eq. (4.46), as a function of the electron temperature T_e and the exchange splitting Δ_{ex} (or rather its reduction $\delta\Delta_{ex}(t) = \Delta_{ex}(t=0) - \Delta_{ex}(t)$).

The smaller the rms residue defined by eq. (4.46) the better the fit. For a theoretical ϵ_{xy} calculated for certain T_e and Δ_{ex}, $r(\Delta t, T_e, \Delta_{ex}, \Delta m_t)$ would be minimized, and thus the optimal values $T_e^{(min)}$ and $\Delta_{ex}^{(min)}$ of the electron temperature and the exchange splitting can be determined. Because ϵ_{xy}'s were calculated on a discrete grid of temperatures and exchange splittings, the rms residues calculated on the same grid through the fitting procedure described above are fitted with a parabolic surface given by

$$f(T_e, \Delta_{ex}) = A + B\left(\left(\Delta_{ex} - \Delta_{ex}^{(min)}\right) + C\left(T_e - T_e^{(min)}\right)\right)^2 + D\left(T_e - T_e^{(min)}\right)^2, \qquad (4.47)$$

where $A, B, C, D, T_e^{(min)}, \Delta_{ex}^{(min)}$ are fitting parameters. The parabolic fitting function (4.47) is justified because this is the lowest order approximation to a function around its minimum. The parabolic fits to the rms residues calculated at 0, 0.7, and 3 ps are shown in Fig. 4.15(g), (h), and (i), respectively. The minimum of the parabolic surface moves from the upper left corner, corresponding to the ground state with zero exchange splitting reduction $T_e = 300$ K, towards the center at 0.7 ps, indicating an increase in T_e and a reduction in Δ_{ex}, and then at 3 ps, as the system recovers, back to the upper left corner.

According to eq. (2.9), with a reduced exchange splitting $\Delta_{ex}^{(min)}$, the magnetic moment per atom also becomes reduced by an amount $\Delta\mu_l$, and a longitudinal contribution to the total demagnetization $\Delta m_l = \Delta\mu_l/\mu$ can be found. In addition, at an elevated electron temperature, the thermal filling of the spin-up and spin-down bands changes, and the magnetic moment is reduced by an additional amount $\Delta m_e(T_e) = 1 - \mu(T_e)/\mu(T_e = 0)$. The temperature dependence of $\mu(T_e)$ is shown in Fig. 2.3 in orange. Thus the total demagnetization Δm is a sum of the transverse Δm_t, longitudinal Δm_l, and thermal smearing Δm_e contributions

$$\Delta m = \Delta m_t + \Delta m_l + \Delta m_e. \tag{4.48}$$

Δm_l and Δm_e are determined from $\Delta_{ex}^{(min)}$ and $T_e^{(min)}$, respectively, which are found from fitting a parabolic surface (4.47) to the rms residues calculated using eq. (4.46). The procedure of calculating the rms residues also yields a dependence of Δm_t on Δ_{ex} and T_e, and, once the optimal values for the exchange splitting and electron temperature at the minimum of the parabolic surface are found, the corresponding Δm_t can also be determined.

The results of the analysis are summarized in Table 4.1 According to this table, at 0.7 ps,

Table 4.1: Summary of the analysis of the angle-resolved T-MOKE data.

	< 0 ps	0.7 ps	3 ps
T_e (K)	300	1018	352
Measured Δm	0	0.12 ± 0.01	0.05 ± 0.01
Fitted Δm	0	0.115 ± 0.014	0.049 ± 0.012
Fitted net moment (μ_B/atom)	1.62	1.44 ± 0.02	1.54 ± 0.02
Δm_l	0	0.032 ± 0.013	0.021 ± 0.011
$\Delta\mu_l$ (μ_B/atom)	0	0.05 ± 0.02	0.03 ± 0.02
Δm_t	0.008 [38]	0.073 ± 0.006	0.028 ± 0.004
$\Delta\mu_t$ (μ_B/atom)	0.013	0.12 ± 0.01	0.05 ± 0.01
Δm_e	0	0.01	0
$\Delta\mu_e$ (μ_B/atom)	0	0.016	0

approximately 2/3 of the total 12% magnetization reduction comes from transverse excitations Δm_t, about 10% of the signal is due to thermal repopulation of the bands Δm_e, and the rest

is from longitudinal excitations Δm_l. At 3 ps, longitudinal and transverse excitations contribute approximately 40% and 60% to the total demagnetization, respectively.

In order to confirm that both types of excitations drive the demagnetization process simultaneously, the above analysis was repeated for two additional cases where, in addition to the thermal repopulation of the bands Δm_e, only a single type of excitation was allowed (either transverse or longitudinal). The results are summarized in Tables 4.2 and 4.3

Table 4.2: Summary of the analysis of the angle-resolved T-MOKE data with longitudinal excitations only.

	< 0 ps	0.7 ps	3 ps
T_e (K)	300	3225	796
Measured Δm	0	0.12 ± 0.01	0.05 ± 0.01
Fitted Δm	0	0.082 ± 0.025	0.034 ± 0.009
Fitted net moment (μ_B/atom)	1.62	1.49 ± 0.04	1.56 ± 0.04
Δm_l	0	0.032 ± 0.025	0.029 ± 0.009
$\Delta \mu_l$ (μ_B/atom)	0	0.052 ± 0.041	0.047 ± 0.014
Δm_t	0.008	0.008	0.008
$\Delta \mu_t$ (μ_B/atom)	0.013	0.013	0.013
Δm_e	0	0.05	0.005
$\Delta \mu_e$ (μ_B/atom)	0	0.08	0

In both Tables 4.2 and 4.3, the predicted net demagnetization Δm at 0.7 ps as well as 3 ps is below the experimentally measured values. It should be noted that in Table 4.3, only the lower limit of Δm is estimated because ϵ_{xy}'s calculated for higher electron temperatures were required to minimize the rms residue. In addition, both analyses predict very high electron temperatures. For the experimental value of absorbed fluence of $F = 1.3$ mJ/cm^2, the upper and lower temperature limits can be estimated by solving for T from

$$F/d = \int_{300}^{T} C(\tau) d\tau, \tag{4.49}$$

where d is the thickness of the film, and $C(T)$ is the temperature dependent specific heat. Here, a uniform distribution of the absorbed fluence throughout the sample thickness is assumed. Because only an average temperature needs to be estimated, such an approximation is acceptable. The

Table 4.3: Summary of the analysis of the angle-resolved T-MOKE data with transverse excitations only.

	< 0 ps	0.7 ps	3 ps
T_e (K)	300	3500	1136
Measured Δm	0	0.12 ± 0.01	0.05 ± 0.01
Fitted Δm	0	> 0.087	0.033 ± 0.008
Fitted net moment (μ_B/atom)	1.62	< 1.48	1.57 ± 0.012
Δm_l	0	0	0
$\Delta \mu_l$ (μ_B/atom)	0	0	0
Δm_t	0.008	> 0.037	0.025 ± 0.008
$\Delta \mu_t$ (μ_B/atom)	0.013	> 0.06	0.041 ± 0.012
Δm_e	0	0.05	0.008
$\Delta \mu_e$ (μ_B/atom)	0	0.016	0.012

upper electron temperature limit corresponding to the 0.7 ps delay time is found when all of the absorbed energy goes into the electron system, which means that $C = C_e$. With the electron heat capacity of Co (see Appendix C), eq. (4.49) yields an upper limit of 2295 K for T_e. Similarly, a lower limit of 620 K, which corresponds to 3 ps, is found when the total specific heat includes all three energy baths: electrons, lattice, and spins, and so the total heat capacity $C = C_e + C_l + C_s$ (see Appendix C). The temperatures in Tables 4.2 and 4.3 at 0.7 ps exceed the upper limit. Even though they are within the limits at 3 ps, the values of Δm disagree with the experimental ones. This supports the conclusion that both longitudinal and transverse excitations, rather than a single type of excitation, contribute to the total demagnetization at both delay times.

These results must interpreted with caution because of the rather low temperature sensitivity of the method, which leads to a large uncertainty of the temperatures derived from the fitting procedure. This can be seen from Figs. 4.15(h) and (i), where the iso-contours are stretched in the horizontal direction, indicating a shallow minimum along T_e. For that reason, the analysis was repeated with the coefficients C and D in eq. (4.47) set to zero, which yields a temperature dependence of both Δm_l and Δm_t. The analysis confirms that regardless of the temperature, both types of excitations are required in order to explain the net amount of demagnetization observed

in the experiment, albeit with different ratios of longitudinal to transverse contributions depending on the temperature.

4.5 Ultrafast demagnetization with D-MOE

Unlike angle-resolved T-MOKE, D-MOE is a very efficient technique, which allows one to collect a sufficient amount of data relatively quickly, thus making possible a direct measurement of the full resonant complex ϵ_{xy}.

First, I validate D-MOE by extracting ϵ_{xy} of Co from a static polarization scan (shown in Fig. 4.8) performed on a Co multilayer with a composition of Si/SiO2(150)/Ta(3)/Co(10)/Si3N4(3) (all layer thicknesses are in nm) shown in Fig. 4.6. The extraction is performed by fitting the D-MOE data in Fig. 4.8 with a multilayer model of the sample based on the multilayer formalism introduced above. Material refractive indices used in the model were taken from Ref. [160]. ϵ_{xy} is found, independently at different photon energies, from the best fit of the simulated D-MOE signal to the experimental data. In order to validate the technique, the extracted ϵ_{xy} is then used to successfully reproduce the polarization-resolved asymmetries measured in the transverse and longitudinal geometries. A comparison of the experimental D-MOE, T-MOKE, and L-MOE signals with the calculated ones based on the ϵ_{xy} extracted from D-MOE is shown in Fig. 4.16. The abbreviation L-MOE introduced here stands for longitudinal magneto-optical effect, which is given by eq. (4.19). It should not be confused with L-MOKE, as the latter requires a polarization analysis whereas the former simply results in a magneto-optical asymmetry. The agreement between the experimental data and the reconstructions based on the extracted ϵ_{xy} in Fig. 4.16 demonstrates the validity of the D-MOE technique.

An additional test was also performed where the same extraction procedure was applied to the T-MOKE and L-MOE data. The results are summarized in Fig. 4.17. Importantly, the reconstructions are successful only for the geometries from which ϵ_{xy} was extracted, but not for the other ones. This confirms the conclusion of eqs. (4.31), (4.30), and (4.32), which states that only the diagonal geometry can provide a unique ϵ_{xy} by use of polarization scanning, while the

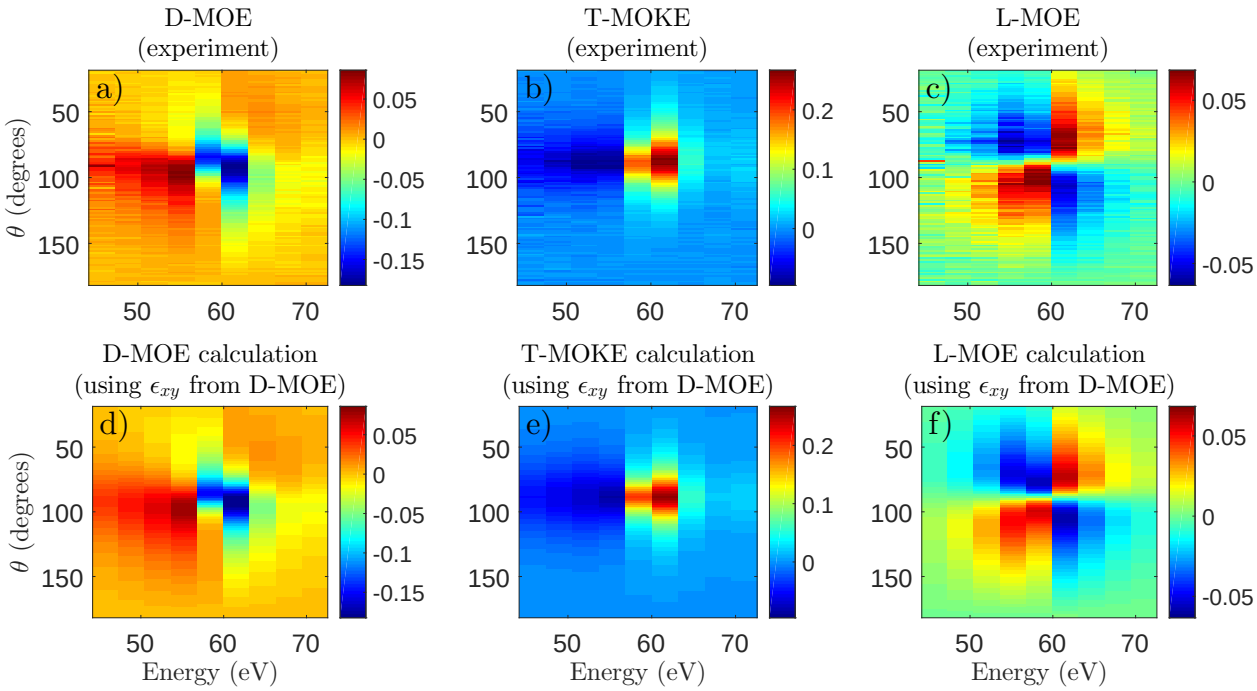

Figure 4.16: Comparison of the experimental (a)-(c) and reconstructed (d)-(f) D-MOE, T-MOKE, and L-MOE polarization angle-resolved spectra. The experimental data points are taken at the discrete HHG peaks of the probe. $\theta = 90°$ corresponds to p-polarization; $\theta = 0°$ corresponds to s-polarization. The reconstructions are based on the $\epsilon_{xy}(\omega)$ extracted from (a).

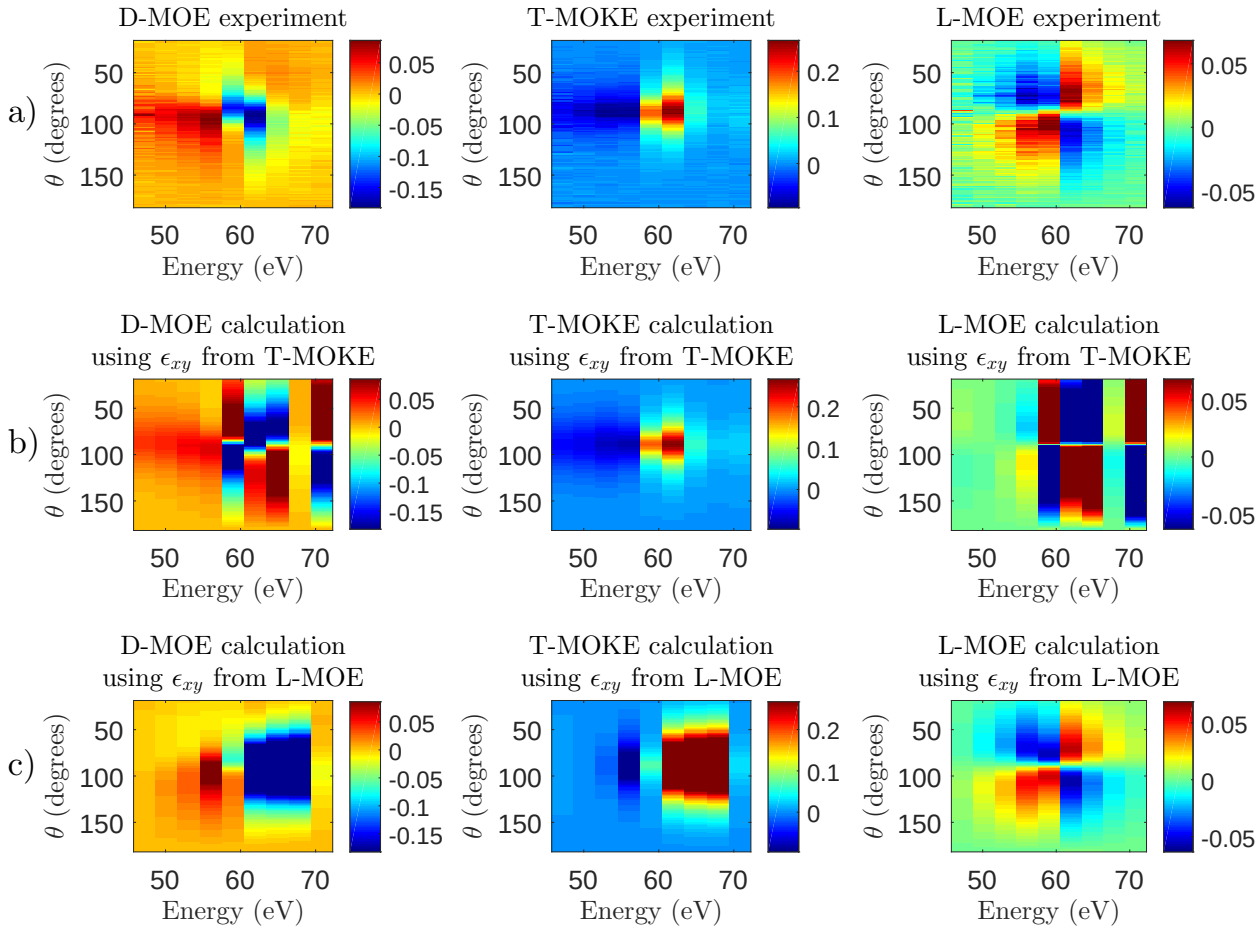

Figure 4.17: Comparison of the experimental and calculated polarization scans based on ϵ_{xy} extracted from the T–MOKE and L-MOE scans. (a) experimental signals, (b) reconstructions based on the ϵ_{xy} extracted from T-MOKE, (c) reconstructions based on the ϵ_{xy} extracted from L-MOE. The reconstructions can successfully reproduce only the signals in their respective experimental geometries, which the extraction of ϵ_{xy} was based on, but not the other two.

transverse and longitudinal geometries cannot.

Another verification of the D-MOE method is done by checking the consistency of the extracted ϵ_{xy} with the Kramers-Kronig relations [161]. Because ϵ_{xy} arises as a material's response to an electromagnetic wave [73, 161], which is causal, it must be analytic [161, 162]. As such, it must satisfy the Kramers-Kronig relations, which are written as [73]

$$\begin{aligned} \mathrm{Re}(\epsilon_{xy}) &= \frac{2}{\pi\omega}\mathrm{P}\int_0^\infty d\omega' \frac{\omega'^2}{\omega'^2-\omega^2}\mathrm{Im}(\epsilon_{xy}), \\ \mathrm{Im}(\epsilon_{xy}) &= -\frac{2}{\pi}\mathrm{P}\int_0^\infty d\omega' \frac{\omega'}{\omega'^2-\omega^2}\mathrm{Re}(\epsilon_{xy}), \end{aligned} \tag{4.50}$$

where P indicates the principal value of the integral. Note that the sign of the second expression depends on the sign convention for the absorptive part of the refractive index n. Expressions (4.50) are defined for the positive absorptive part of n. An extracted experimental ϵ_{xy} for a 5 nm Co film, which was also used for dynamic measurements, is shown in Fig. 4.18, along with the Kramers-Kronig transform of an interpolated $\mathrm{Im}(\epsilon_{xy})$ and a comparison with a theoretical ϵ_{xy}. The experimental ϵ_{xy} satisfies the Kramers-Kronig relations and agrees well with the theoretical

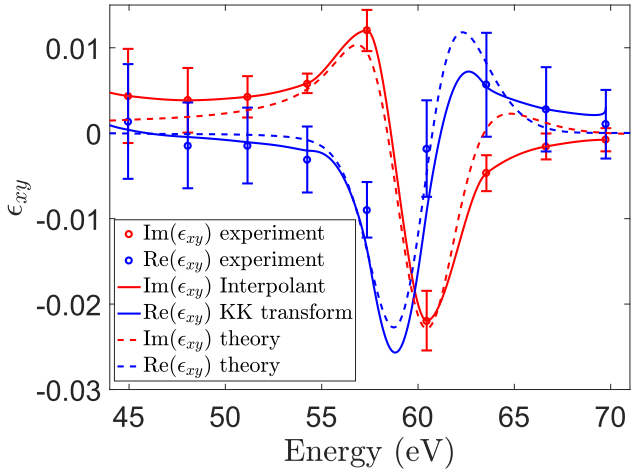

Figure 4.18: Static experimental ϵ_{xy} of Co measured on a Si/SiO2(150)/Co(5)/GeO2(3) multilayer. The data satisfy the Kramers-Kronig relations and compare well with the theoretical values [122].

calculations of Ref. [122].

An experimental uncertainty in the measured ϵ_{xy} shown as the errorbars in Fig. 4.18 was estimated based on the measured standard deviation of the intensity of the EUV probe. Uncertain-

ties in the reflected intensities were propagated into the measured asymmetry, for each polarization according to

$$\Delta A = \sqrt{\left(\frac{\partial A}{\partial R_+}\Delta R_+\right)^2 + \left(\frac{\partial A}{\partial R_-}\Delta R_-\right)^2} = \frac{2\sqrt{R_-^2\Delta R_+^2 + R_+^2\Delta R_-^2}}{(R_+ + R_-)^2}, \tag{4.51}$$

where ΔR_+ and ΔR_- are the standard deviations of the reflected intensities R_+ and R_- for the positive and negative magnetization directions, respectively. ΔR_+ and ΔR_- were measured at each HHG peak independently. In principle, ΔA could be determined from the experimental data, however, only HHG spectra averaged over 100 acquisitions were saved, which streamlined the data acquisition process and reduced data storage requirements. Therefore, in order to estimate an uncertainty in ϵ_{xy}, a series of Gaussian-distributed D-MOE polarization scans was simulated with an average D-MOE asymmetry over the series equal to the experimentally measured value and a standard devition ΔA calculated according to eq. (4.51). For each element of the series, an extraction of ϵ_{xy} was performed, which yielded a series of ϵ_{xy}. $\Delta\epsilon_{xy}$ was calculated as a standard deviation of that series.

In the next step, time-resolved D-MOE polarization scans were taken. The polarization angle was scanned from 30° to 150° in steps of 6.7°, and the delay times were scanned in the range from -0.5 ps to 2 ps with 25 fs time steps. It should be noted that such fine time steps, which effectively amount to measuring ϵ_{xy} as a continuous function of time, were made possible due to the efficiency of the D-MOE method. Other methods that are, in principle, capable of directly measuring ϵ_{xy} have certain challenges in the EUV and X-ray spectral regions associated with them, which precludes the use of such methods for dynamic measurements with fine time steps. In the case of angle-resolved T-MOKE [122], XMCD in transmission [163, 8] and reflection [164], or polar MOKE [165, 166], one has to vary the angle of incidence. A polarization analysis is required in the case of longitudinal MOKE [167, 165, 166] and Faraday and Voigt rotation [168, 169, 170]. The data were taken on a 5 nm Co film grown directly on an insulating substrate with a composition of Si/SiO_2(150 nm)/Co(5 nm)/GeO_2(3 nm). Such a sample structure was used in order to exclude any possible non-local microscopic demagnetization mechanisms, e.g. superdiffusive spin currents, and

thus isolate the contributions of local processes, e.g. magnons, spin-flips, and exchange splitting reduction, to the total demagnetization. Average demagnetization curves measured from raw D-MOE data and based on extracted $\epsilon_{xy}(t)$ are shown in Fig. 4.19. Both curves in the figure agree

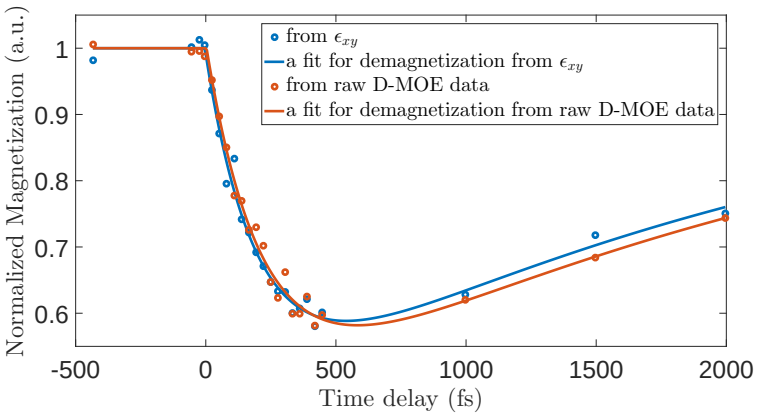

Figure 4.19: Average magnetization response of a 5 nm Co film on an insulator based on raw D-MOE data as well as extracted time-dependent $\epsilon_{xy}(t)$.

well. The signal measured from the raw D-MOE data was averaged over multiple harmonic peaks and all of the polarization angles in the scanned range. To improve the signal-to-noise ratio, a threshold of 0.12 was applied to the D-MOE asymmetry before time-zero. For the blue curve, an average response of $\mathrm{Im}(\epsilon_{xy}(E,t))$ was taken in the energy range from 55 to 63 eV. Based on double-exponential fits [171] of the two experimental data sets, the demagnetization τ_D and recovery τ_R times were $\tau_D = 224 \pm 53$ fs and $\tau_D = 242 \pm 58$ fs and $\tau_R = 2302 \pm 623$ fs and $\tau_R = 2417 \pm 686$ for the blue and orange curves in Fig. 4.19, respectively.

Using the method described above, values of ϵ_{xy} were extracted at each delay time between an IR laser pump pulse and an EUV probe. A time dependent change $\Delta\epsilon_{xy}(E,t) = \epsilon_{xy}(E,t) - \epsilon_{xy}(E, t<0)$ is shown in Fig. 4.20. The data in the figure show a transient reduction and recovery of ϵ_{xy}. This direct time-resolved measurement of an evolving ϵ_{xy} allows an analysis of the relative contributions of the local transverse and longitudinal excitations to the total demagnetization, according to Ref. [70], at various time steps. The non-local mechanisms, i.e. spin-polarized currents are not allowed in the sample structure considered here.

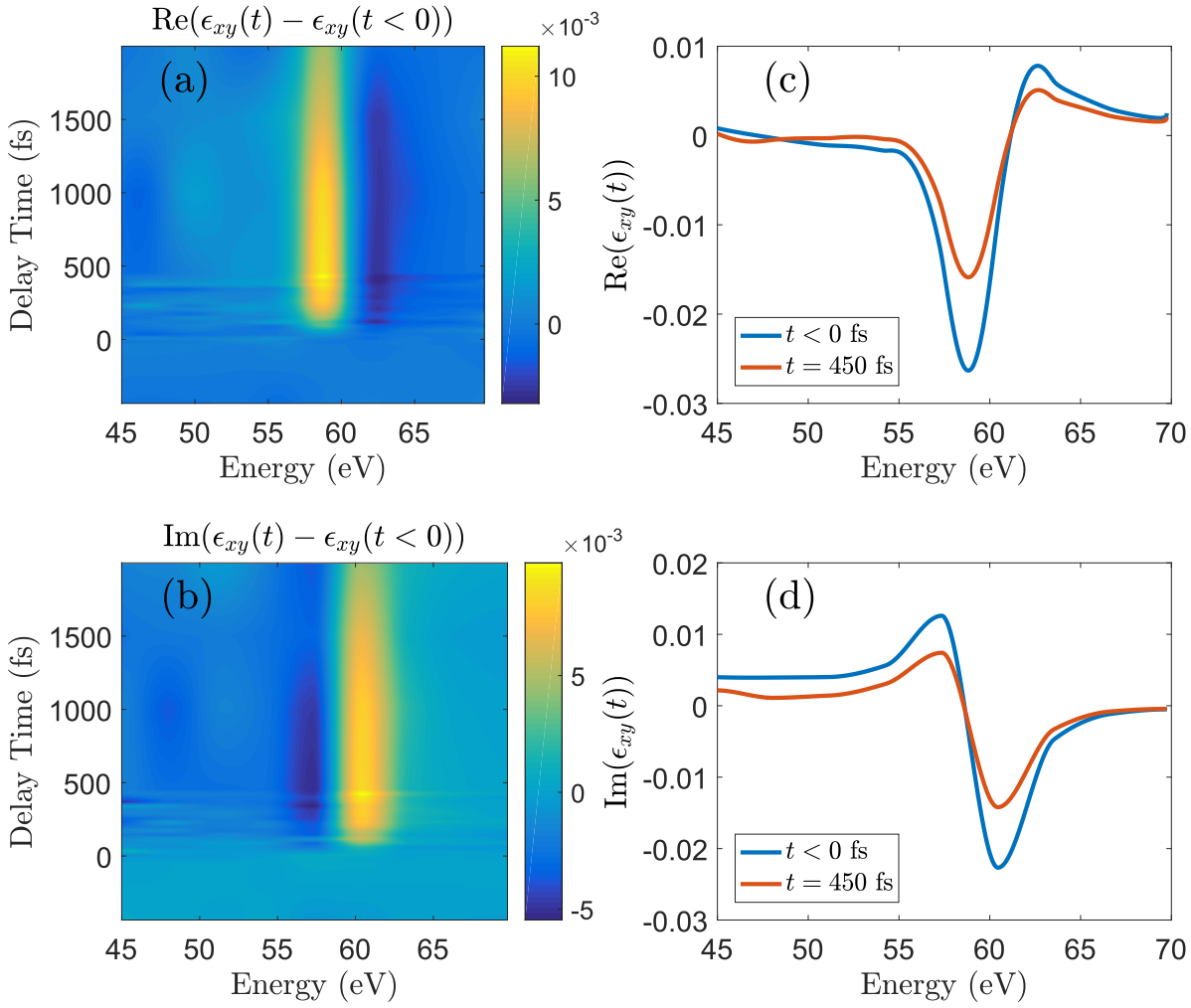

Figure 4.20: Transient changes in ϵ_{xy} measured with time-resolved D-MOE: (a) $\mathrm{Re}(\Delta\epsilon_{xy}(E,t)) = \mathrm{Re}(\epsilon_{xy}(E,t) - \epsilon_{xy}(E,t<0))$, (b) $\mathrm{Im}(\Delta\epsilon_{xy}(E,t)) = \mathrm{Im}(\epsilon_{xy}(E,t) - \epsilon_{xy}(E,t<0))$. Also shown is a comparison of the (c) real and (d) imaginary parts of ϵ_{xy} at the time of maximum demagnetization $t = 450$ fs with the unperturbed state at $t < 0$.

With the angle-angle resolved T-MOKE technique described above, such an analysis was performed by comparing experimental and theoretical angle-resolved T-MOKE spectra. The D-MOE technique allows a direct comparison of the experimental and theoretical values of ϵ_{xy}, which is shown in Fig. 4.21. The comparison is done between the imaginary parts. In panel (a) of the

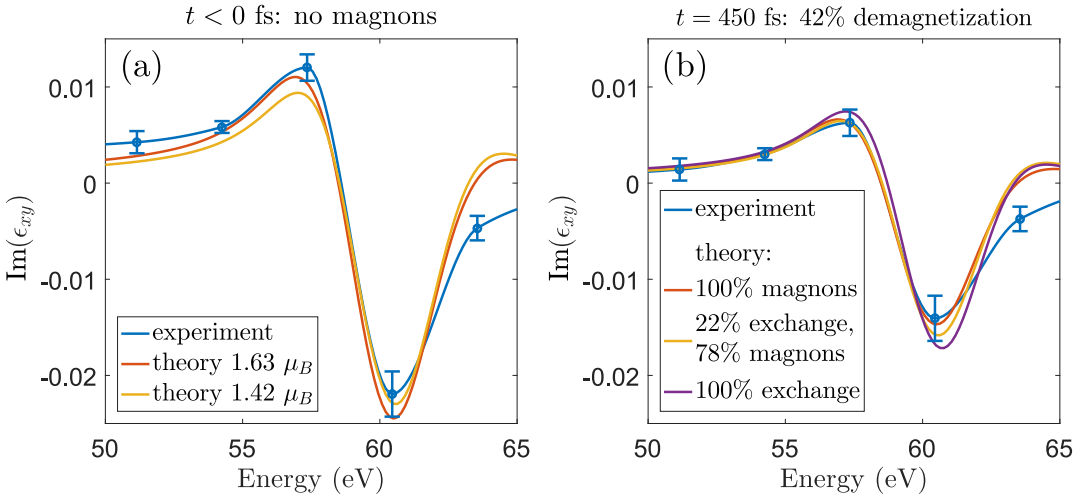

Figure 4.21: Direct comparison between theory and experiment for the static and transient ϵ_{xy} of Co. (a) The ground-state case $t \leq 0$. The red and yellow theoretical curves do not include any magnon excitation. A reduction in the magnetic moment from 1.63 μ_B (red) to 1.42 μ_B (yellow) is entirely due to a reduced exchange splitting. For the ground state, the theoretical ϵ_{xy} corresponding to an unperturbed exchange splitting (red) is in better agreement with the experiment (blue). (b) $t = 450$ fs. The theoretical ϵ_{xy}'s are calculated for varying relative contributions (see the legend) of the longitudinal and transverse excitations to the total demagnetization of 42 %.

figure, the ground state is considered. An *ab initio* calculated ϵ_{xy} corresponding to a magnetic moment of 1.63 μ_B per atom (red) is a better fit to the experimental data (blue) than the 1.42 μ_B per atom (yellow) obtained with a reduced exchange splitting. At $t = 450$ fs, in panel (b), several *ab initio* calculations are compared with the experimental result. For each of those cases, the relative contributions to the total demagnetization of 42 % from transverse excitations and exchange splitting reduction are varied. For the red curve, it was assumed that the entire 42 % reduction in magnetization is driven by magnon generation; whereas for the purple curve it is purely due to a decrease in the exchange splitting. The yellow curve is an intermediate case, for which about 3/4 of the demagnetization comes from magnons and the rest is from the exchange splitting reduction.

Because the highest signal-to-noise ratio is at the peak of $\mathrm{Im}(\epsilon_{xy})$, which is around 60.5 eV, a comparison between theory and experiment is more reliable at that energy. The red and yellow curves are within the experimental uncertainty indicated by the errorbars in the figure, while the purple curve is outside the error bars. This helps estimate an upper limit on the relative contribution from the exchange splitting reduction to the total demagnetization at $\sim$25 %. Thus a reduction of ϵ_{xy} is predominantly uniform across the spectrum, and at least 75 % of the demagnetization in Co is driven by magnons, or transverse excitations, which compares well with the result obtained with the angle-resolved T-MOKE reported above as well as the recent time- and spin-resolved photoemission measurements [172].

The spectral resolution of D-MOE is limited by the spectrum of the HHG source, which is a comb of harmonic peaks separated by approximately 3.1 eV. More information about the transient evolution of ϵ_{xy} can be obtained using a source with a continuous spectrum. Such an HHG spectrum can be achieved by generating isolated attosecond pulses[173, 174, 175].

4.6 Conclusions

In this chapter, I presented two new magneto-optical techniques, an angle-resolved T-MOKE and a polarization-resolved diagonal magneto-optical effect, which extend the capabilities of the traditional transverse, longitudinal, and polar magneto-optical geometries and can be used to unambiguously determine the full resonant complex magneto-optical permittivity of materials ϵ_{xy}. The permittivity depends on the microscopic state of a given material, i.e., on the number of longitudinal spin fluctuations, which lead to a reduction of the exchange splitting, and the number of transverse spin fluctuations, or magnons. A connection between the measured ϵ_{xy} and the relative amounts of longitudinal and transverse excitations is made via first principles DFT calculations, which confirm that magnons result in a uniform reduction of ϵ_{xy} across an entire spectrum, while a decrease in exchange splitting changes the spectral shape of ϵ_{xy}, in agreement with previous work. The two techniques were used to study laser-induced magnetization dynamics on sub-picosecond timescales of thin Co films, namely, the role of transverse and longitudinal excitations in the ul-

trafast demagnetization process driven by a near-infrared laser pulse. By tracing the dynamical changes in ϵ_{xy} and comparing them with theory, it was found that the demagnetization response of Co is dominated by magnons, with a possible smaller contribution from an exchange splitting reduction. The findings obtained independently with both the angle-resolved T-MOKE and the polarization-resolved D-MOE methods are in agreement.

The character of the microscopic demagnetization mechanisms discussed in this chapter is likely not universal for all $3d$ ferromagnets, and could be unique for Co because of its rather large exchange splitting compared to the exchange interaction energy. This could make the microscopic demagnetization channel by means of magnon generation energetically more favorable. Recent work comparing photoemission and T-MOKE measurements suggests that the situation is different in Ni, where the values of the exchange splitting and exchange interaction energies are much closer. A similar comparison of photoemission and EUV magneto-optical measurements for Co and Fe would be very useful in the future. In addition, an EUV source with a continuous HHG spectrum will be able to provide much more magneto-optical information than a source with a rather sparse HHG comb.

Chapter 5

EUV Magneto-Optics with Spatial Resolution

This chapter is dedicated to a coherent resonant magnetic scattering (RMS) experiment with a tabletop EUV HHG light source. Unlike spectroscopic approaches, scattering experiments provide important information about spatial variations of the magnetization and are capable of capturing nanoscale magnetic features.

Magneto-optical phenomena, such as the Kerr and Faraday effects, have been known since the nineteenth century, and a quantum theory of the interaction of electron magnetic moments with polarized photons was developed in 1929 [176]. The interaction of X-rays with magnetic materials had not been discovered until the 1970's, when a theoretical paper predicted relativistic corrections to the Compton and Bragg scattering cross-sections due to magnetic moments [177]. The first observation of X-ray magnetic diffraction from an antiferromagnetic NiO crystal was made in 1972 with a cathode tube used as a source of incoherent X-rays [178], and later measurements on ferro- and ferrimagnetic compounds were reported along with detailed relativistic quantum calculations [179]. The development of bright X-ray sources, such as synchrotrons, turned magnetic scattering into a reliable measurement technique by compensating for a low scattering cross-section with a bright photon flux and thus boosting the signal [180]. An enhancement of magnetic scattering at elemental absorption edges was observed in 1988 [181].

Tabletop EUV light sources have an advantage over synchrotron facilities in that they bring coherent RMS experiments to a laboratory setting and thus provide more flexibility and cost efficiency. Additionally, with such sources, RMS could be performed in a time-resolved manner with

femtosecond temporal resolution [182]. The first demonstration of coherent RMS with a tabletop source at the $M_{2,3}$ absorption edge of Co was reported in Ref. [183], and with a bright phase-matched high harmonic source at the $M_{2,3}$ absorption edge of Fe in Ref. [184].

Given that the magnetic scattering efficiency is very weak, the design of the experiment reported here makes use of the resonant nature of RMS and employs efficient grazing incidence broadband EUV focusing optics, instead of multilayer coatings as in Refs. [183] and [184], in order to maximize the photon flux at the sample.

In this chapter, I develop a theoretical description of RMS with linearly and circularly polarized light and show that the contrast mechanism for the scattering with a linearly polarized probe is entirely due to Faraday rotation. I also derive an optimal sample thickness that maximizes the RMS signal. I design an RMS experiment on a tabletop and apply it to study field-dependent skyrmion formation in a sample with perpendicular magnetic anisotropy. I report an observation of a transition from a disordered domain phase to an ordered hexagonal lattice of skyrmions accompanied by an increase in the size of magnetic features.

5.1 Resonant magnetic scattering with linearly and circularly polarized light

As mentioned in Chapter 2, the interaction of light with a magnetized material can be described using the material's dielectric tensor $\hat{\epsilon}$. The off-diagonal elements of the tensor depend on the magnetization direction. For an arbitrary direction, all three off-diagonal elements ϵ_{xy}, ϵ_{xz}, and ϵ_{yz} are, in general, non-zero, and an electromagnetic wave transmitted through or reflected from such a material will have magneto-optical changes to its amplitude, phase and polarization. However, in most cases, the magnetization direction is either strictly parallel or perpendicular to the surface of the sample, which introduces additional symmetries and helps simplify the problem. In particular, a significant simplification is achieved in the case of magnetic films with perpendicular magnetic anisotropy. In these films, the magnetization predominantly points into or out of the plane of the film, and the perpendicular magnetic anisotropy leads to a variety of magnetic textures ranging from networks of nanoscale domains to magnetic bubbles and vortices, known as skyrmions,

depending on the composition of the film.

For an out-of plane magnetization, the dielectric tensor becomes

$$\hat{\epsilon} = \begin{pmatrix} \epsilon_{xx} & \epsilon_{xy} & 0 \\ -\epsilon_{xy} & \epsilon_{yy} & 0 \\ 0 & 0 & \epsilon_{zz} \end{pmatrix}, \tag{5.1}$$

where z is the axis orthogonal to the surface of the sample. Note that $\epsilon_{yx} = -\epsilon_{xy}$ [185, 186]. With the $\hat{\epsilon}$ defined by eq. (5.1), from eq. (4.4), it can be shown that for left (+) and right (−) circularly polarized incident fields, the refractive indices in a material uniformly magnetized in an out-of-plane direction satisfy [73]

$$n_{\pm}^2 = \epsilon_{xx} \pm i\epsilon_{xy} \cos\phi, \tag{5.2}$$

where ϕ is the angle of refraction. For normal incidence, $\phi = 0$, and by taking a square root of eq. (5.2), and Taylor expanding it up to a first order in ϵ_{xy}, the expression for the refractive index can be simplified to

$$n_{\pm} = \sqrt{\epsilon_{xx}} \left(1 \pm i\frac{\epsilon_{xy}}{\epsilon_{xx}}\right) = n_0 \pm \delta n_s, \tag{5.3}$$

where $n_0 = \sqrt{\epsilon_{xx}}$ is the non-magnetic part of the refractive index, and $\delta n_s = i\epsilon_{xy}/\sqrt{\epsilon_{xx}}$ is its magnetic variation. For convenience, I write δn_s in terms of its real ($\Delta\delta$) and imaginary ($\Delta\beta$) parts

$$\delta n_s = -\Delta\delta + i\Delta\beta. \tag{5.4}$$

Equation (5.3) can be viewed as a difference between the refractive indices for left and right circularly polarized fields for a fixed out-of-plane magnetization direction, or as a difference in refractive indices upon magnetization reversal for a field of fixed helicity.

I now consider the transmission of a plane wave with a wavenumber k through a magnetized film of thickness d. I define the basis vectors for the linear s and p and circular (+) and (−)

polarizations in terms of the x and y field components as

$$\begin{aligned} \vec{E}_s &= \begin{pmatrix} 1 \\ \\ 0 \end{pmatrix}, \quad \vec{E}_p = \begin{pmatrix} 0 \\ \\ 1 \end{pmatrix}, \\ \vec{E}_+ &= \frac{1}{\sqrt{2}} \begin{pmatrix} 1 \\ \\ i \end{pmatrix}, \quad \vec{E}_- = \frac{1}{\sqrt{2}} \begin{pmatrix} 1 \\ \\ -i \end{pmatrix}. \end{aligned} \tag{5.5}$$

Starting with a simpler case of circular polarization, the transmitted field is

$$\begin{aligned} \vec{E}_+^{(t)} &= \frac{1}{\sqrt{2}} \begin{pmatrix} 1 \\ \\ i \end{pmatrix} e^{ikn_+ d} = \frac{1}{\sqrt{2}} \begin{pmatrix} 1 \\ \\ i \end{pmatrix} e^{ikn_0 d} e^{-ik\Delta\delta d} e^{-k\Delta\beta d}, \\ \vec{E}_-^{(t)} &= \frac{1}{\sqrt{2}} \begin{pmatrix} 1 \\ \\ -i \end{pmatrix} e^{ikn_- d} = \frac{1}{\sqrt{2}} \begin{pmatrix} 1 \\ \\ -i \end{pmatrix} e^{ikn_0 d} e^{ik\Delta\delta d} e^{k\Delta\beta d}, \end{aligned} \tag{5.6}$$

for the positive and negative magnetization directions, respectively. For a magnetic domain sample, $\vec{E}_+^{(t)}$ and $\vec{E}_-^{(t)}$ correspond to the fields transmitted through the positively and negatively magnetized domains. Between $\vec{E}_+^{(t)}$ and $\vec{E}_-^{(t)}$, there is a difference in both phase and amplitude. The difference in phase is $2k\Delta\delta d$ and the difference in amplitude is approximately $2k\Delta\beta d$. The polarization state remains circular and unchanged. The latter is especially important for holographic imaging of magnetic domains [187, 188, 189] because, in order for the beams transmitted through the domains and the reference hole to interfere, they must have identical polarizations. The disadvantage is that the non-magnetic signal, such as scattering from inhomogeneities in the film, for example, will interfere with the magnetic one making it impossible to separate the magnetic and the unwanted non-magnetic scattering.

With linear polarization, the situation is different. I choose $\vec{E}_s$ as the incident field. It can be written as a superposition of left and right circular fields

$$\vec{E}_s = \frac{1}{\sqrt{2}} \left(\vec{E}_+ + \vec{E}_- \right) = \frac{1}{2} \left[\begin{pmatrix} 1 \\ \\ i \end{pmatrix} + \begin{pmatrix} 1 \\ \\ -i \end{pmatrix} \right]. \tag{5.7}$$

For the positive magnetization direction, the transmitted field is

$$\vec{E}^{(t,+)} = \frac{1}{\sqrt{2}} \left(\vec{E}_+ e^{in_+ kd} + \vec{E}_- e^{in_- kd} \right) = \frac{1}{\sqrt{2}} e^{in_- kd} \left(\vec{E}_+ e^{-2\Delta\beta kd} e^{-2i\Delta\delta kd} + \vec{E}_- \right). \tag{5.8}$$

A similar expression can be derived for the transmitted field when the magnetization direction is reversed

$$\vec{E}^{(t,-)} = \frac{1}{\sqrt{2}}\left(\vec{E}_+ e^{in_- kd} + \vec{E}_- e^{in_+ kd}\right) = \frac{1}{\sqrt{2}} e^{in_- kd}\left(\vec{E}_+ + \vec{E}_- e^{-2\Delta\beta kd} e^{-2i\Delta\delta kd}\right). \tag{5.9}$$

I now expand eqs. (5.8) and (5.9) in the basis of the linear s- and p-polarizations using

$$\vec{E}_\pm = \frac{1}{\sqrt{2}}\left(\vec{E}_s \pm i\vec{E}_p\right). \tag{5.10}$$

Eqs. (5.8) and (5.9) then become

$$\begin{aligned}
\vec{E}^{(t,+)} &= \frac{1}{2} e^{in_- kd}\left[\left(\vec{E}_s + i\vec{E}_p\right) e^{-2\Delta\beta kd} e^{-2i\Delta\delta kd} + \left(\vec{E}_s - i\vec{E}_p\right)\right], \\
\vec{E}^{(t,-)} &= \frac{1}{2} e^{in_- kd}\left[\left(\vec{E}_s + i\vec{E}_p\right) + \left(\vec{E}_s - i\vec{E}_p\right) e^{-2\Delta\beta kd} e^{-2i\Delta\delta kd}\right].
\end{aligned} \tag{5.11}$$

Grouping the terms with $\vec{E}_s$ and $\vec{E}_p$, these expressions yield

$$\vec{E}^{(t,\pm)} = \frac{1}{2} e^{in_- kd}\left[\left(1 + e^{-2\Delta\beta kd} e^{-2i\Delta\delta kd}\right)\vec{E}_s \mp i\left(1 - e^{-2\Delta\beta kd} e^{-2i\Delta\delta kd}\right)\vec{E}_p\right]. \tag{5.12}$$

According to eq.(5.12), for the case of a linearly polarized incident field, the light transmitted through a material magnetized out-of-plane becomes elliptically polarized and the axes of the ellipse are rotated. Such rotation is known as the Faraday effect; the amount of rotation is the same for both the positive and negative magnetization directions, but the rotation directions are opposite. When decomposed into the s- and p-polarization components, the transmitted fields for the two magnetization directions have identical s-polarization components (for the incident s-polarized field), and the p-polarization components have equal magnitudes but opposite signs, which effectively amounts to a π phase shift between them since $-1 = e^{i\pi}$. For a network of up and down magnetic domains, this phase shift maps out the transverse magnetization profile and causes the incident light to scatter. An important consequence of eq. (5.12) is that the light scattered from magnetic feastures is polarized orthogonally to the incident linearly polarized field. Since any non-magnetic scattering preserves the polarization state, the photons scattered magnetically and non-magnetically will have orthogonal polarizations and thus will not interfere. This makes the separation of the magnetic and non-magnetic scattering signals possible by magnetically saturating

the sample and subtracting the scattered intensity from the signal measured with an unsaturated sample. On the other hand, any holographic imaging techniques that rely on an interference of the scattered light with a reference beam are not possible with linear polarization.

5.1.1 Maximization of the scattered intensity

From eq. (5.12), the magnetically scattered fraction of the incident flux is

$$\begin{aligned}\rho_{RMS} &= \left|\frac{i}{2}e^{in_-kd}\left(1-e^{-2\Delta\beta kd}e^{-2i\Delta\delta kd}\right)\right|^2 = \\ &= \frac{1}{4}\left|e^{in_0kd}\left(e^{\Delta\beta kd}e^{i\Delta\delta kd}-e^{-\Delta\beta kd}e^{-i\Delta\delta kd}\right)\right|^2,\end{aligned} \tag{5.13}$$

where the non-magnetic part of the refractive index is defined as $n_0 = 1-\delta+i\beta$. The goal now is to find the optimal sample thickness d that maximizes the RMS signal ρ_{RMS}. By Taylor expanding the exponents of the factor in parentheses in powers of $\Delta\delta$ and $\Delta\beta$ and keeping the terms only up to a first order in $\Delta\delta$ and $\Delta\beta$, I obtain

$$\rho_{RMS} \approx \frac{1}{4}e^{-2\beta kd}\left|(2\Delta\beta kd + 2i\Delta\delta kd)\right|^2. \tag{5.14}$$

After expanding the square eq. (5.14) is simplified to

$$\rho_{RMS} = k^2d^2e^{-2\beta kd}\left(\Delta\beta^2+\Delta\delta^2\right). \tag{5.15}$$

For the optimal sample thickness, $\partial\rho_{RMS}/\partial d = 0$. Taking a derivative of eq. (5.15) with respect to d yields

$$\frac{\partial\rho_{RMS}}{\partial d} = -2\beta e^{-2\beta kd}k^3d^2\left(\Delta\beta^2+\Delta\delta^2\right) + 2k^2de^{-2\beta kd}\left(\Delta\beta^2+\Delta\delta^2\right) = 0, \tag{5.16}$$

which leads to an equation for d

$$-\beta kd^2 + d = 0. \tag{5.17}$$

The non-trivial solution of eq. (5.17) is

$$d = \frac{1}{\beta k}. \tag{5.18}$$

Given that $\beta k = 1/2a$, where a is an absorption length, according to eq. (5.18), the optimal thickness of the sample that maximizes the total magnetically scattered intensity is equal to twice

the absorption length of a given material at the wavelength of the X-ray or EUV probe. This is a result of the fact that the Faraday rotation, which leads to the magnetic contrast, increases linearly with d, while the overall transmittance of light by the sample decreases exponentially with d.

An important consequence of eq. (5.18) for EUV and soft X-ray scattering experiments has to do with the typical absorption lengths at the M and L absorption edges of metals. Absorption lengths at the M-edges are on the order of $\sim$ 20 nm while at the L-edges they are $\sim$ 10 times greater. This means that the optimal sample thicknesses of $\sim$ 40 nm for EUV experiments agree well with the typical thicknesses of several tens of nm of magnetic multilayer films with perpendicular magnetic anisotropy. Soft X-ray experiments, on the other hand, operate far away from the optimal conditions. This can be partially compensated for by a high photon flux at synchrotrons or free-electron lasers. In addition, sample surface quality typically improves as its thickness is reduced, and, in that respect, the situation is more favorable for HHG sources.

5.1.2 Estimation of the RMS efficiency

With the result of eq. (5.18), the maximum scattering efficiency can be computed from eq. (5.15) as

$$\rho_{RMS}^{(max)} = \frac{1}{\beta^2} e^{-2} \left(\Delta\beta^2 + \Delta\delta^2 \right). \tag{5.19}$$

With the typical magnitudes of β, $\Delta\beta$, and $\Delta\delta$ of 0.1, 10^{-2}, and 10^{-2}, respectively, at the M-edges of Fe, Co, and Ni [168], the highest possible fraction of magnetically scattered flux relative to the incident intensity can be estimated at $\sim 10^{-3}$. In reality, it is even lower because films with perpendicular magnetic anisotropy are usually composed of multiple layers, which might effectively reduce $\Delta\beta$ and $\Delta\delta$. In addition, given that the diffraction efficiency depends on the transverse magnetization profile of a particular sample, the actual ρ_{RMS} will decrease even further. Thus RMS experiments are very demanding with respect to the photon flux, and great care must be taken to generate a high number of photons at the resonance energy of the sample of interest as well as to preserve it as the probe beam is transported down the beamline.

5.2 Resonant magnetic scattering on a tabletop

In order to generate a high photon flux at EUV wavelengths, laser driven phase-matched high harmonics were used [104]. The phase matching process is critical for the HHG brightness and is described in more detail in Chapter 3. In order to preserve the photon flux, broadband grazing incidence optics rather than wavelength-selective multilayer EUV mirrors were used. This approach relies on the resonant nature of the EUV magnetic scattering: in eq. (5.15), $\Delta\beta$ and $\Delta\delta$ depend on the photon energy and are greatly enhanced at the resonant energy of the absorption edge for a given material. Therefore, on resonance, ρ_{RMS} is much greater than off resonance, and only the photons at the resonant photon energy will scatter. A caveat with this approach is that it puts constraints on the sample composition, i.e., the sample cannot contain multiple elements whose absorption edges lie within the bandwidth of the EUV source because this will create an overlay of multiple scaled versions of the scattering pattern, each corresponding to the absorption edge of a given element within the sample, and will ultimately lead to decoherence effects. For example, if the photon energies of the EUV beam range from ∼30 to 72 eV (absorption edge of Al filters), and the sample contains approximately equal amounts of Fe and Co whose M-shell absorption edges are at ∼53 eV and ∼59 eV, respectively, the scattered intensity at 53 eV will overlap with that at 59 eV, and the total scattered intensity will be smeared because of this. Note that for uniform transverse distributions of the Fe and Co atomic species, the scattering pattern is determined purely by the magnetic texture of the sample, and will have the same profile at both photon energies, but because higher energy photons scatter at smaller angles, it will appear smaller at the Co edge than at the Fe. However, if only one element with an absorption edge within the bandwidth of the EUV source is present in the sample, which was the case with the Fe-Gd magnetic film studied here, this concern is alleviated, and broadband optics are safe to use.

Fig. 5.1 illustrates the concept of an EUV RMS experiment. Instead of multilayer EUV mirrors, more efficient broadband optics are used, which increased the photon flux incident on the sample. A toroidal mirror focuses the beam, and the flat mirror directs it through the sample.

In addition, it allows small adjustments of the beam pointing. A permanent ring magnet can be moved along the beam, and thus magnetic fields of up to 270 mT can be applied to the sample. A beam block placed in front of the CCD which collects diffraction patterns prevents the undiffracted light from saturating it. This is necessary because a direct transmitted beam carries no magnetic information and is several orders of magnitude more intense than the magnetic scatter. I outline

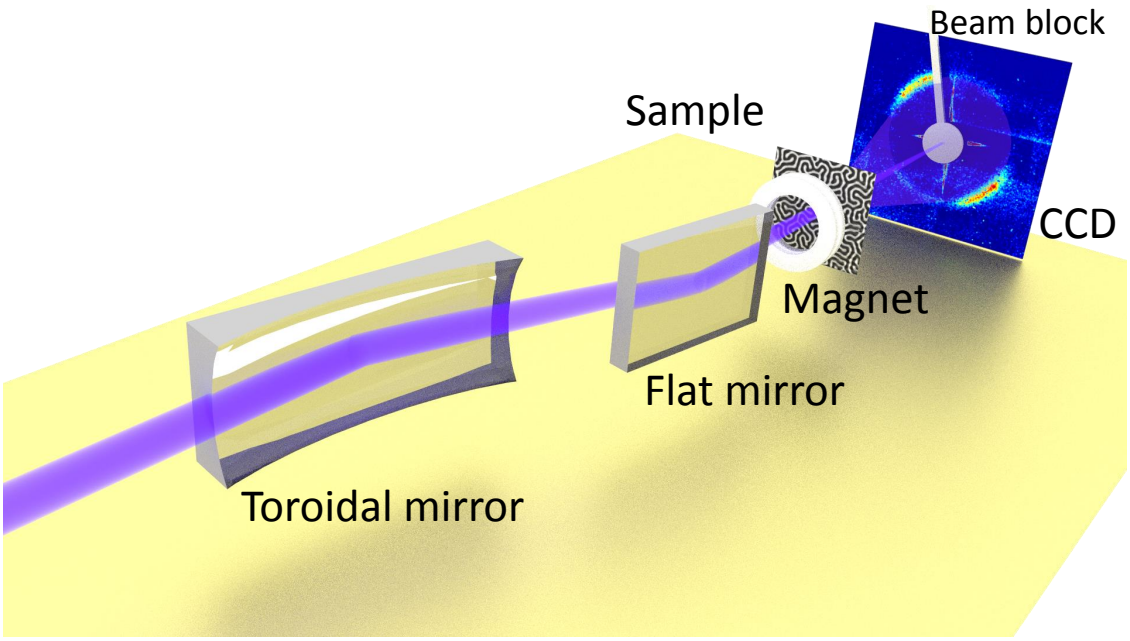

Figure 5.1: The concept of an EUV RMS experiment. Broadband grazing incidence optics are more efficient than wavelength-selective multilayers. A permanent ring magnet applies a field to the sample. The CCD placed behind the sample is used to collect the scattered intensity.

the design considerations in more detail below.

5.2.1 Experimental Design

The design of the tabletop RMS setup is concerned with optimizing the brightness and the beam profile of the EUV source as well as the general layout and efficiency of the optics in the scattering chamber itself.

I start by discussing the design of the EUV source. A schematic of the source is shown in Fig. 5.2. EUV light is obtained by driving the process of high harmonic generation with an infrared

amplified Ti:Sapphire laser at the central wavelength of 795 nm. The repetition rate of the laser was 5 kHz, and the pulse energy was 1.9 mJ. The pulse duration was intentionally stretched in order to minimize the B-integral [190]

$$B(\vec{r},t) = \frac{2\pi}{\lambda}\int n_2\,|E(\vec{r},t)|^2\,dz, \tag{5.20}$$

where n_2 is the second-order nonlinear component of the refractive index. The quantity in eq. (5.20) corresponds to a nonlinear phase accumulation during the propagation of a laser pulse, which can interrupt the phase-matched HHG process and thus cause instabilities of the EUV pulses. $B(\vec{r},t)$ can be minimized by reducing the magnitude of the electric field $|E(\vec{r},t)|$, which can be achieved by stretching the laser pulse.

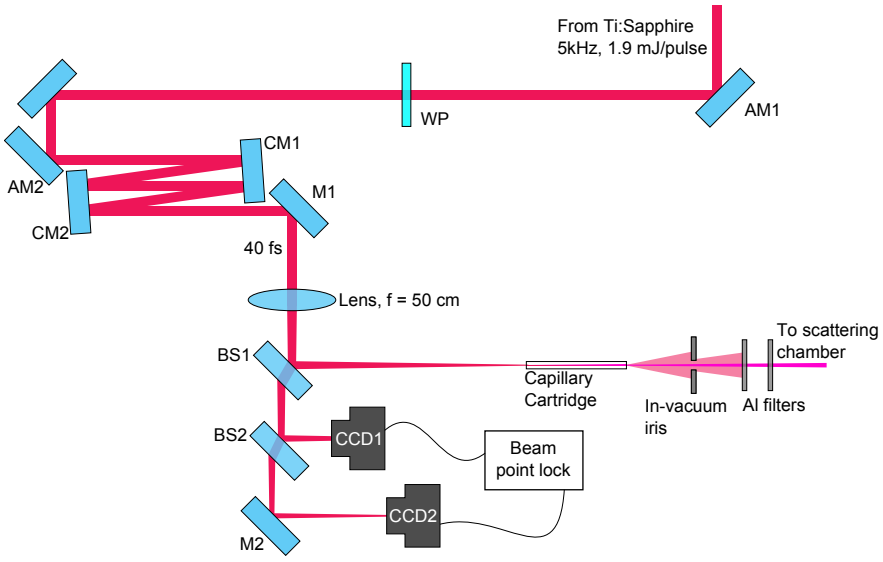

Figure 5.2: Schematic of the EUV source. Amplified 40 fs pulses from a Ti:Sapphire laser (KMLabs Wyvern) at the central wavelength of 795 nm are converted into bright EUV pulses in a hollow-core glass waveguide filled with He. The pointing of the infrared beam into the fiber is stabilized. Any residual infrared light emitted from the fiber is blocked by an in-vacuum aperture and a series of Al filters.

HHG, however, requires a high-intensity laser driver, and for that reason, laser pulses need to be compressed before they enter the gas filled capillary in Fig. 5.2. The compression is performed with a pair of chirped mirrors CM1 and CM2, which compensate for the quadratic spectral phase introduced into the pulse for the purpose of increasing its duration and thus compress the pulse

back to its nearly transform-limited length of ∼40 fs. Because this pulse compression is performed relatively close to the HHG region, it accomplishes the goal of minimizing the B-integral by optimizing the long pulse vs. short pulse propagation distance while delivering short pulses to the gas-filled capillary.

A CaF_2 lens with a focal length of 50 cm is used to focus the beam into the hollow-core waveguide. The material of the lens has a low group velocity dispersion, which allows one to minimize the stretching of laser pulses as they travel through the lens. The laser spot size at the focus of the lens is matched with the inner diameter of the fiber of 150 μm in order to optimize the coupling of the laser light into the lowest order mode of the fiber. The fiber entrance is placed close to the focus of the lens.

The beam splitter immediately after the lens (BS1) in Fig. 5.2 reflects 99% of the IR beam into the fiber, and 1% goes into the beam stabilization system composed of a 50/50 beam splitter BS2, a mirror M2, two CCD cameras CCD1 and CCD2, control software, and two actuated mirrors AM1 and AM2. The purpose of the beam stabilization system is to lock the position and angle of the IR laser beam at the entrance of the fiber as they may change due to thermal drifts in the laser amplifier and, therefore, can cause a reduction in the coupling efficiency into the fiber, which, in turn, may lead to instabilities and decreased efficiency of the HHG process and result in a low total photon flux. The cameras track the centroids of non-focused (CCD1) and focused (CCD2) beams and the control software makes adjustments to the actuated mirrors AM1 and AM2 based on the feedback from the cameras. The two actuated mirrors are placed before the pair of chirped mirrors in order to keep the incidence angle of the laser beam on CM1 and CM2 the same. Changes in the incidence angle on the chirped mirrors can result in a fluctuating pulse duration and adversely affect the HHG process. More details on the beam stabilization setup can be found in Ref. [107].

The HHG process itself takes place in a KMLabs XUUS^{TM} hollow waveguide cartridge. The waveguide is filled with He gas at ∼900 Torr. Because the end section of the waveguide is very short, an efficient pumping scheme must be used in order to evacuate any residual gas from the beamline to minimize re-absorption of high harmonics. Two Agilent TriScroll 300 roughing pumps

and a Pfieffer HiPace 300 turbo pump were used for that purpose. A pressure of 10^{-4} Torr in the beamline was reached even at the highest gas pressures in the waveguide. To maximize the amount of IR light coupled into the waveguide, a sapphire Brewster window was used in front of the waveguide at the entrance into the vacuum section of the beamline. The Brewster window was oriented such that the HHG linear polarization would be in the s-polarization direction with respect to the toroidal mirror in Fig. 5.1 in order to maximize its reflectivity. A half-wave plate WP in Fig. 5.2 was used to match the polarization of the laser to the orientation of the Brewster window and maximize the transmission through the window. After the waveguide, a 500 nm and a 200 nm Al filters were used to reject any residual IR light emitted from the waveguide. Because the divergence of the IR beam is higher than that for the EUV, an aperture was placed in front of the filters to select a small central portion of the IR beam and transmit the full EUV beam. Such an approach greatly reduces the total amount of the IR power incident on the Al filters and thus lowers the risk of their failure.

I now proceed to discussing the layout of the scattering chamber shown in Fig. 5.3. Three beam paths are implemented in the chamber. The main one is path 1 shown in purple in the figure. In this path, the EUV beam from the waveguide impinges on a toroidal mirror, which focuses it through the sample. The toroid is oriented at a $\sim 10^{\circ}$ grazing incidence, and, in order to redirect the beam onto the sample, a flat mirror M2 oriented at the same angle is used. The beam is then transmitted through a sample with a magnetic texture, and the diffracted light is collected with an imaging CCD (Andor DO-436). The beam block in front of the imaging CCD blocks the un-diffracted transmitted beam as it contains no magnetic information, and, due to its very high intensity compared to the scattered light, can saturate the camera and thus make the observation of magnetic scattering impossible. The beam block is mounted on translation stages and its position can be adjust to match the position of the un-diffracted peak on the CCD. The sample can be translated in three directions. Translating it along the x and y directions perpendicular to the normal to the sample helps align it with the incident beam, while translation along the beam adjusts the distance between the imaging CCD and the sample and thus, for a fixed scattering

angle, controls the size of the measured diffraction pattern. In the experiment reported here, the sample was placed at a distance of 36 mm away from the CCD. The sample mount was intentionally made rather big, so that it would prevent any light scattered in the chamber from illuminating the imaging CCD. A ring magnet placed in front of the sample applies a magnetic field while letting the EUV beam to go through. More details on the magnet mount are given below.

In path 2, shown in yellow in Fig. 5.3, a 45° gold coated mirror M1 can be inserted in the beam before the toroid to reflect it onto the beam diagnostic CCD (Andor Newton 920). It helps ensure that the HHG process in the waveguide cartridge is phase-matched and the EUV mode is good with a symmetric Gaussian profile and low divergence as shown in Fig. 5.4. This is a critical step because the EUV photon flux depends on how well phase-matched the HHG process is, and the focusing of the beam depends on its divergence and profile. A beam with a high divergence and/or an asymmetric profile cannot be focused into a small spot by the toroid. Typically, a good mode indicates that the phase-matching is also good, and, therefore, the photon flux is high.

In path 3, shown in Fig. 5.3 in blue, mirror M2 can be moved out of the beam in order to direct it into a spectrometer that consists of a 500 lines/mm gold coated diffraction grating and a CCD (Andor DO-420 BN). The imaging CCD and the spectrometer CCD are both mounted at the focus of the toroid, which, in the case of the spectrometer, improves the spectral resolution by making the spot sizes of the diffracted beamlets small in the plane of the CCD. The spectrometer allows a small tuning of the HHG spectrum to match a harmonic peak with the resonant absorption peak of the sample. An example spectrum is shown in Fig. 5.5(a) together with the maximum estimated scattering efficiency for Fe calculated according to eq. (5.19) with the optical constants for Fe taken from Ref. [168]. As can be seen from the figure, the spectral overlap of $\rho_{RMS}^{(max)}$ and the HHG spectrum could be improved, but even with the existing overlap, the scattering predominantly occurs at a single harmonic energy, as evidenced by Fig. 5.5(b), which shows a normalized product of the two curves in (a).

Another important consideration in the design of the setup is the EUV spot size on the sample. It can be estimated by assuming that the EUV beam is a perfect Gaussian ($M^2 = 1$)

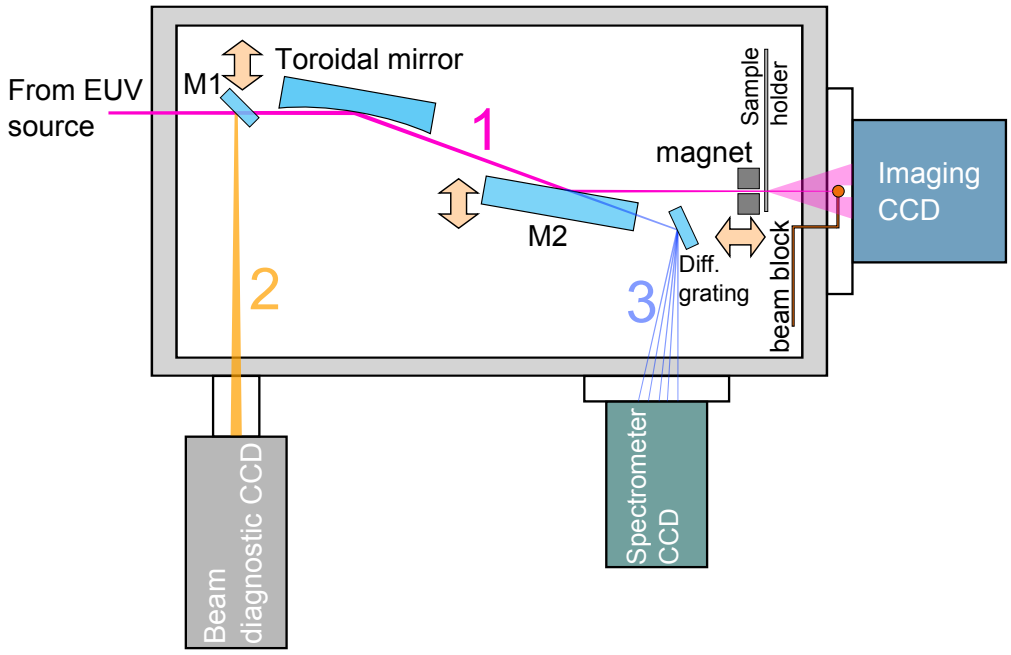

Figure 5.3: RMS chamber layout. Three beam paths are implemented in the chamber: In path 1 (purple), the EUV beam is transmitted through the sample, and the diffraction pattern is collected with the Imaging CCD; in path 2 (yellow), the beam is directed onto the Beam diagnostic CCD, which measures its spatial profile; in path 3 (blue), the beam is directed into the spectrometer.

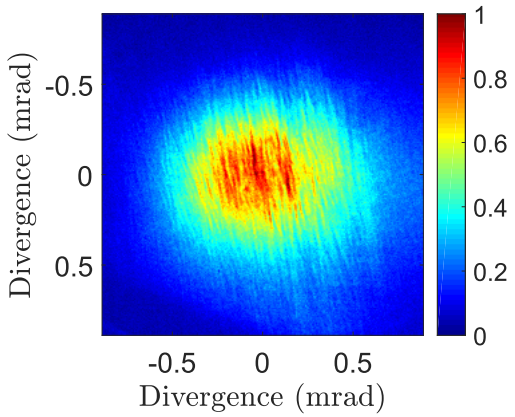

Figure 5.4: Transverse profile of a phase-matched HHG beam. The vertical streaks are from the scratches on the gold mirror.

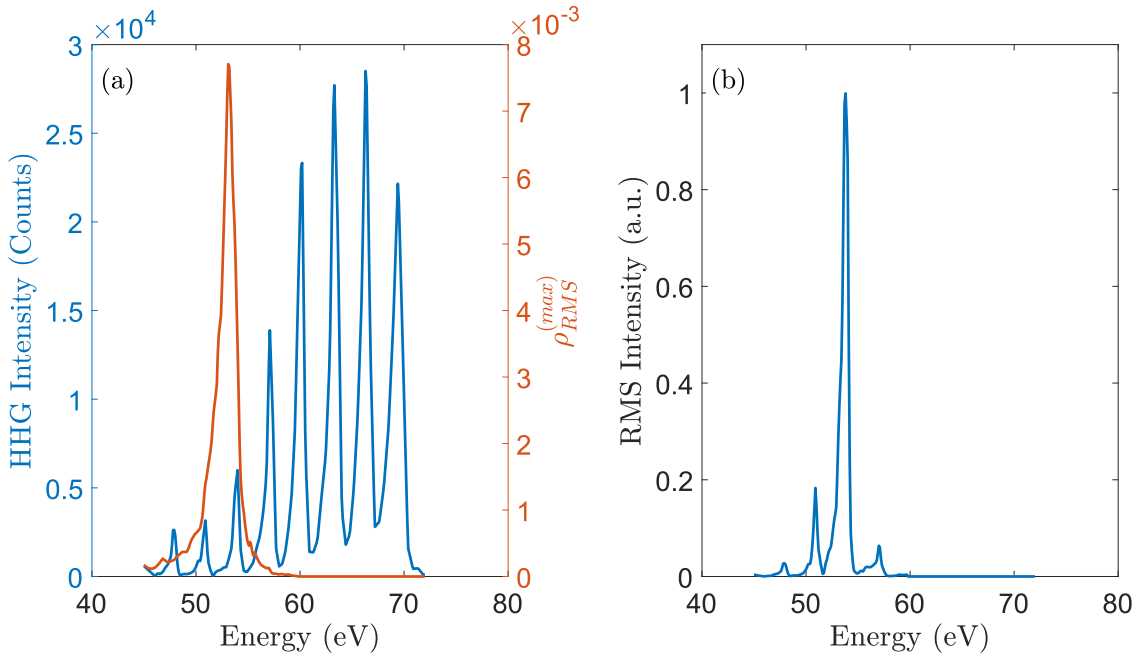

Figure 5.5: (a) An example HHG spectrum and its overlap with the scattering efficiency $\rho_{RMS}^{(max)}$. (b) The product of the spectrum and $\rho_{RMS}^{(max)}$ demonstrates that the scattering occurs predominantly at a single harmonic energy.

and propagating it through the beamline to the sample. The beam radius at the output of the waveguide can be calculated from the divergence in Fig. 5.4 as [191]

$$w_0 = \frac{\lambda}{\pi\theta}, \tag{5.21}$$

where θ is the divergence half-angle. With $\theta \approx 0.5$ mrad and $\lambda \approx 23$ nm at the M-edge of Fe, $w_0 \approx 15$ μm, and thus the spot size $2w_0$ is 30 μm. A toroid has two focal lengths—sagittal and tangential—that correspond to the sagittal and tangential radii of curvature of its surface r and R, respectively, shown in Fig. 5.6. The two focal lengths depend on the angle of incidence α and are

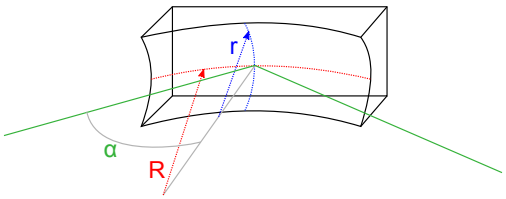

Figure 5.6: A sketch of a toroidal mirror. r and R are the sagittal and tangential radii of curvature, respectively. α is the angle of incidence with respect to the surface normal.

the same when

$$\cos\alpha = \sqrt{\frac{r}{R}}. \tag{5.22}$$

For α defined by eq. (5.22), the focal length is

$$f = \frac{1}{2}\sqrt{rR}. \tag{5.23}$$

For the toroid used in this experiment, $r = 90.5$ mm and $R = 3220$ mm, which, according to eqs. (5.22) and (5.23), yields $\alpha = 80.35°$, which is equivalent to a 9.65° grazing angle, and $f = 27$ cm.

The distance between the toroid and the EUV source is 160 cm, and with a known focal length and the size of the EUV beam at the output of the waveguide, the beam size at the sample position can be calculated with the ABCD-matrix method [191]. At the sample position 29 cm away from the toroid (and 3.6 cm from the imaging CCD), an estimated beam diameter is ∼150 μm. This is a rather large beam, compared to typical illumination spot sizes of a few μm in EUV microscopy; however, for scattering experiments this can be beneficial because an average over a bigger area is

taken. Additionally, if a magnetic texture consists of repeated features, such as worm-like domains or a skyrmion lattice, the scattering peak is sharper for a larger illumination area. This is analogous to the resolution of a diffraction grating: the resolution improves and the diffraction peaks become sharper if a larger area of the grating is illuminated.

5.2.2 Beamline efficiency

As mentioned above, a high EUV photon flux from the laser driven HHG source in Fig. 5.2 needs to be preserved in the beamline. Typical reflectivities of multilayer wavelength-selective EUV mirrors do not exceed 50%, and approximately 3/4 of the photon flux would be lost on a pair of such mirrors. For that reason, broadband grazing incidence optics were used in the chamber. Reflectivities at grazing incidence are normally quite high. Fig. 5.7 confirms that this is indeed the case for the toroidal mirror and flat mirror M2 (see Fig. 5.3). Both optics are made from Pyrex glass and coated with 30 nm of B_4C. The reflectivities in the figure are calculated for a grazing angle of 10° with the multilayer approach described in Chapter 4. For a toroid-flat mirror pair

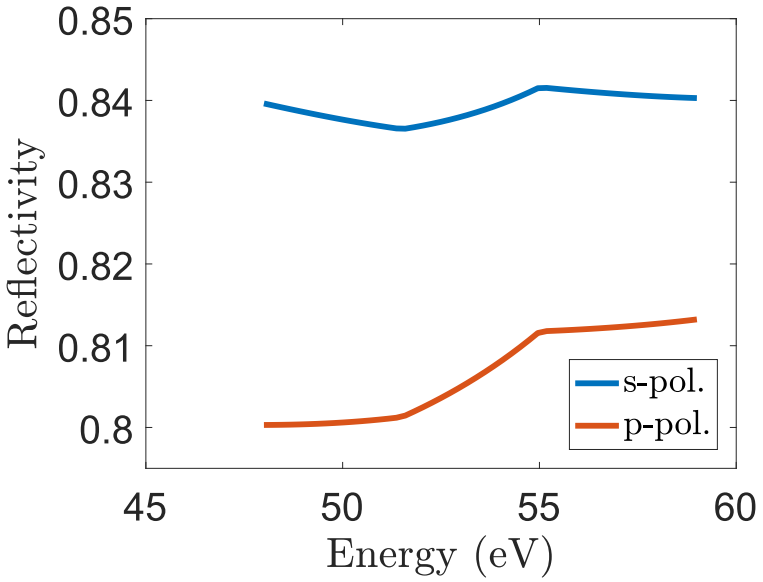

Figure 5.7: Reflectivity of a toroidal mirror made from Pyrex glass and coated with 30 nm of B_4C at a 10° grazing incidence.

in path 1 in Fig. 5.3, the total reflectivity is approximately 0.71 for s-polarization and 0.64 for p-polarization, according to the data in Fig. 5.7. In the case of an s-polarized EUV probe, there is almost a threefold improvement compared to multilayer EUV mirrors.

Two alternative designs are possible to reject the residual IR light emitted from the fiber. The first design includes a pair of rejector mirrors, typically made from Ru or another material, that are very efficient at absorbing the IR light and reflecting the EUV. After the Ru rejectors, a thin (200 nm) Al film is placed to filter out any IR light that either was not absorbed or was scattered. This design is robust in that it ensures that no damage to the camera by direct laser light will be caused should the Al film break. However, the rejectors are most efficient when the incident light is p-polarized. For example, for a pair of Ru rejectors at an 8° grazing incidence, the total reflectivity is 0.36 at the Fe absorption edge, and if the 0.72 transmissivity of the 200 nm Al filter is included, the efficiency of the Ru rejectors with an Al filter becomes 0.26. Alternatively, a series of Al filters can be used. A combination of a 500 nm and a 200 nm Al film transmits virtually no IR light, and its transmissivity at the Fe M-edge is 0.32, which is higher than the reflectivity of a pair of Ru rejectors, and, therefore, this design is preferable. Additionally, at normal incidence, these filters are not sensitive to the polarization direction. The disadvantage is that the Al filters could fail under very high thermal load from the IR laser pulses thus putting the imaging camera and the sample at risk. To mitigate this risk, an aperture is used in front of the filters (see Fig. 5.2). It blocks most of the IR beam, whose divergence is high, while transmitting a slowly diverging EUV beam. The total efficiency of the beamline includes the transmissivity of the Al filters and the reflectivities of the toroid and the flat mirror and is equal to 0.26 at the Fe absorption edge meaning that approximately 26% of the EUV light generated in the waveguide is delivered to the sample.

5.2.3 Application of an external magnetic field

An external magnetic field can either be applied to the sample with an electromagnet or a permanent magnet. For an in-vacuum experiment, the latter is preferable because it does not

require water lines in the vacuum chamber to cool the magnet. Additionally, stronger fields can be achieved with a permanent magnet, and the field at the sample can be adjusted by changing the distance to the magnet. In Fig. 5.8, the measured on-axis (a) and the calculated (b) fields of a system of two permanent ring magnets are shown. Two magnets, rather than a single magnet are required for the mounting. The maximum on-axis field magnitude is $\sim$ 280 mT, which should be sufficient to induce the skyrmion phase in the Fe-Gd sample, according to Ref. [192]. In addition, the field near the axis at $z > 8$ mm is relatively uniform and thus the experiment should not be very sensitive to a small misalignment of the magnet relative to the sample and the EUV beam.

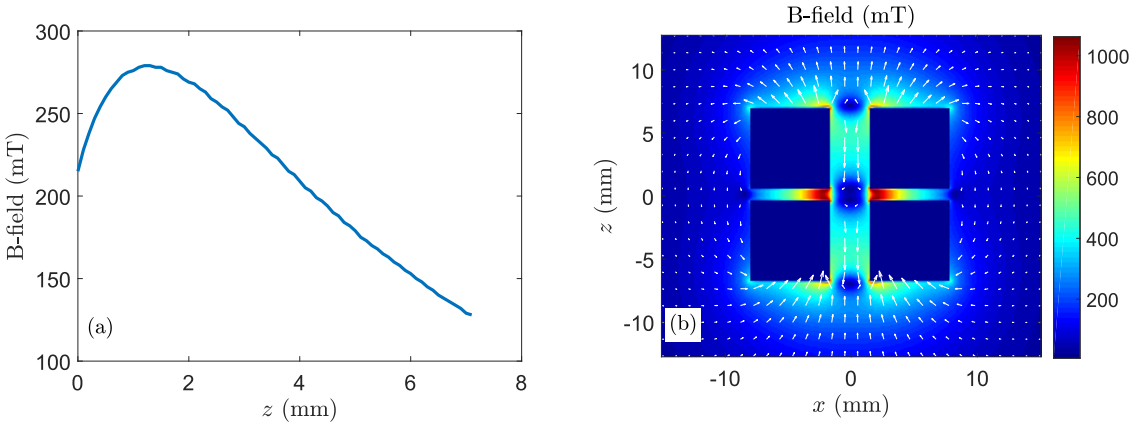

Figure 5.8: Magnetic field of a system of two permanent ring magnets (shown in dark blue) (a) measured on-axis and (b) calculated.

The calculation in Fig. 5.8(b) was carried out using a magnetostatic scalar potential approach [92]. According to this approach, the magnetic potential, in the absence of boundary surfaces, is given by

$$\Phi_M(\vec{r}) = -\int \frac{\vec{\nabla}' \cdot \vec{M}(\vec{r}')}{|\vec{r} - \vec{r}'|} d^3\vec{r}', \tag{5.24}$$

where $\vec{M}(\vec{r})$ is a spatially dependent magnetization, and the magnetic field in free space can then be computed using

$$\vec{B} = -\mu_0 \vec{\nabla} \Phi_M. \tag{5.25}$$

The magnet mount is placed on a translation stage, and the distance between the sample

and the magnet, and thus the field at the sample, can be adjusted.

5.3 Field-dependent scattering

The magnetic field dependence of resonant magnetic scattering from an Fe-Gd film was studied. The nominal structure of the sample was [Gd (0.41 nm)/Fe (0.34)nm]×80. However, due to an interdiffusion of the Fe and Gd layers, the interfaces disappeared, and the entire film could be considered an amorphous alloy. The sample was prepared at the Center for Memory and Recording Research at the University of California San Diego, and more details about it can be found in Refs. [192] and [53]. The magnetic film was grown on a 50 nm Si_3N_4 membrane, and 5 nm Ta films were used as a seed and cap layers.

Since the scattering experiment is performed at the Fe M-edge, the total thickness of the Fe layers needs to be optimized in order to improve the magnetic contrast, according to eq. (5.18). With an attenuation length of Fe equal to ∼15 nm at 54 eV, the optimal thickness is 30 nm, which is very close to the sample's total thickness of the Fe layers of 27.2 nm.

In the sample studied here, skyrmions are formed due to a competition between long-range magnetic dipolar interactions and the energy of domain walls [54, 52, 193]. Such skyrmions are also called dipole-stabilized skyrmions to emphasize the fact that, although they are topologically similar to the more common skyrmions stabilized by the chiral Dzyaloshinskii-Moriya interaction [194, 195, 196], the mechanism that leads to their formation is different from the latter. The sample was designed to form a hexagonal lattice of dipole-stabilized skyrmions in a magnetic field. Here, I study a transition from a disordered stripe-domain phase to an ordered skyrmion phase by measuring RMS patterns at various applied magnetic fields.

An example RMS pattern is shown in Fig. 5.9. The pattern was taken at zero applied field and shows two intensity lobes around $q \approx 0.03$ nm^{-1}, where q is the momentum-transfer vector defined as $q = 4\pi \sin(\theta/2)/\lambda$ (with $\lambda = 23.16$ nm) and θ are the wavelength and scattering angle, respectively. This is a signature of a disordered nanoscale worm-like domain network commonly seen in thin films with perpendicular magnetic anisotropy. At $q \approx 0.06$ nm^{-1}, additional lobes

can be seen. They correspond to second-order scattering and indicate that there is an asymmetry between up and down domains. To understand this, consider a Fourier series expansion of a square wave. If the wave is perfectly symmetric, only odd harmonics will be present in the expansion [1] . If the duty cycle is not equal to 50%, or the shape of the wave deviates from a perfect square wave, e.g. becomes a sawtooth wave, even harmonics will appear in the expansion. In the case considered here, those are manifested as two additional intensity lobes.

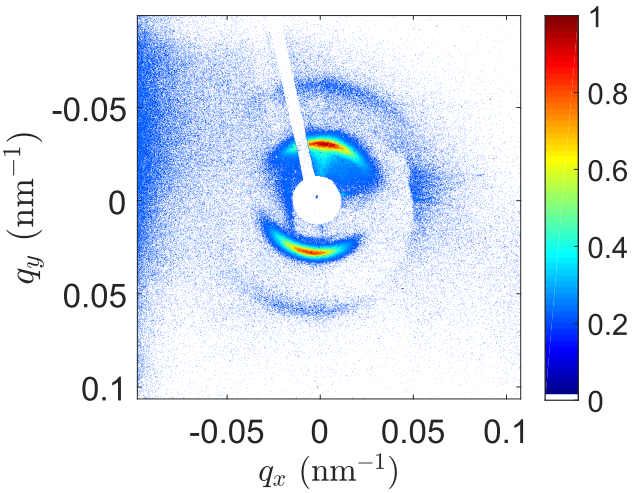

Figure 5.9: Example RMS pattern from an Fe-Gd multilayer alloy at zero field. Notice a weak second order scattering ring at $q \approx 0.06$ nm^{-1}.

Fig. 5.10 shows RMS patterns taken as the field was increased from 0 to 180 mT. The intensity in all of the images is normalized to 1. The patterns in the figure change from large lobes at low fields to more concentrated intensity distributions in q-space at higher fields. This indicates a transition from a disordered network of worm-like domains to a more ordered phase of stripe domains. For a perfectly ordered stripe domain phase, the scattering pattern has two concentrated peaks at $\vec{q}_0$ and $-\vec{q}_0$, as shown in Fig. 5.11. The magnitude of q_0 corresponds to the periodicity of the domain pattern, and its direction is orthogonal to the direction of the stripes. At $B > 100$ mT, the RMS patterns look like an overlay of an RMS pattern from perfectly ordered stripe-domains and that from a more disordered domain distribution. This is likely due to a co-existence of an

[1] `http://mathworld.wolfram.com/FourierSeriesSquareWave.html`

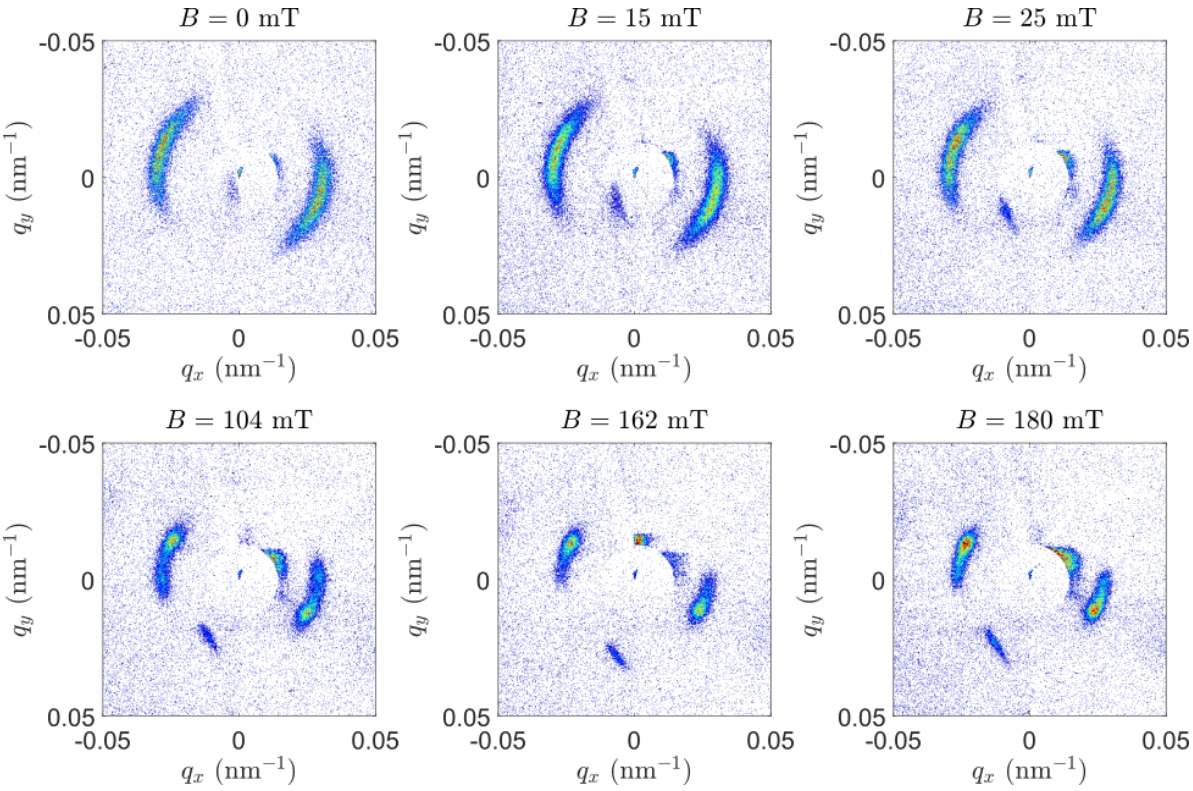

Figure 5.10: Field-dependent RMS patterns. The film transitions from a disordered worm-like domain phase at low fields to a more ordered mixed phase of stripe domains at high fields.

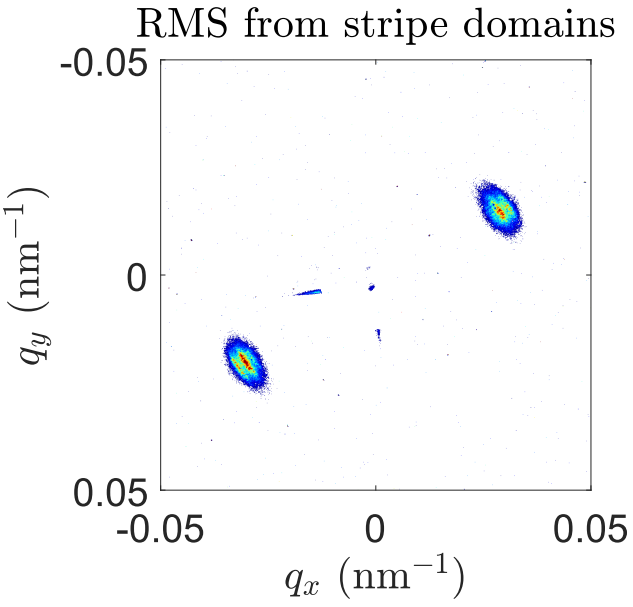

Figure 5.11: RMS from ordered stripe domains in Fe-Gd (taken at 54 eV, $B = 0$ mT).

ordered and disordered domain phases within the illuminated area.

The domain periodicity at a given field can calculated from the RMS patterns. For small scattering angles, $2\sin(\theta/2) \approx \sin\theta = m\lambda/p$, where p is the periodicity, and m is a diffraction order. In Fig. 5.10, $m = 1$. The domain size $d = p/2$, and, given the definition of the scattering vector q, an expression for the domain size is

$$d = \frac{\pi}{q}. \tag{5.26}$$

In order to obtain an accurate estimate of the position of diffraction peaks in q-space, the diffraction patterns in Fig. 5.10 are averaged in the azimuthal direction. The averaging must exclude areas of the detector with pixels that do not carry any scattering information because they were either obscured by the beam block (see the white shadow in Fig. 5.9) or exposed to scattered light (see the left edge of Fig. 5.9). Such a map of bad pixels is shown in Fig. D.1 in Appendix D. A detailed description of the averaging procedure is given in Chapter 6. An example azimuthally averaged intensity distribution for $B = 25$ mT in Fig. 5.10 is shown in Fig. 5.12. In the figure, the peak

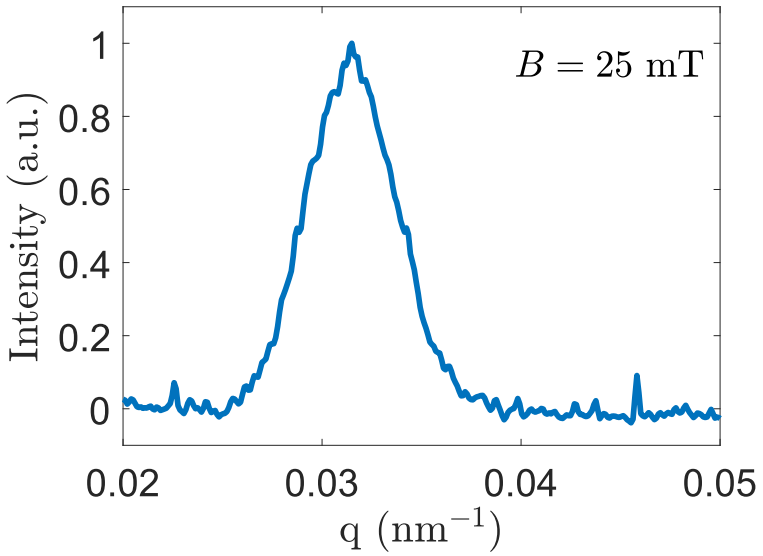

Figure 5.12: Azimuthally averaged RMS pattern for the Fe-Gd sample at $B = 25$ mT.

is located at $q = 0.0315$ nm^{-1}, which corresponds to a domain size $d = 99.7$ nm, according to eq. (5.26). By performing the averaging procedure for each field value in Fig. 5.10, the dependence

of the diffraction peak position, and thus of the domain size, on the field can be obtained. The results are shown in Fig. 5.13. As the field increases, the scattering peak in (a) shifts towards lower q-values, and the domain size in (b) increases, accordingly.

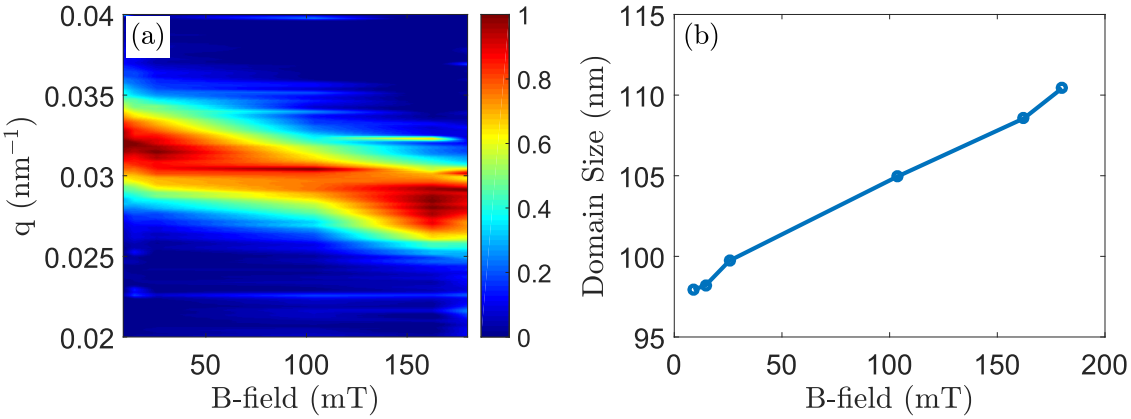

Figure 5.13: The dependence of the (a) angular RMS spectrum and (b) domain size of the Fe-Gd sample on the applied magnetic field.

Upon further increase of the magnetic field to 220mT, a hexagonal lattice of dipole-stabilized skyrmions formed in the film, which is reflected in the hexagonal shape of the scattering pattern shown in Fig. 5.14, in agreement with Ref. [192]. The lattice constant, as determined from the figure, is $a = 228$ nm. Assuming that the lattice is two-dimensional and close-packed, as illustrated in Fig. 5.15, the radius of the skyrmions is $r_s = 124$ nm. This result is a first demonstration of resonant magnetic scattering from a skyrmion lattice on a tabletop.

5.4 Conclusions

This chapter presented the design of a resonant magnetic scattering experiment on a tabpletop and its implementation for studying field-dependent scattering from a Fe-Gd magnetic film, as well as some general theoretical considerations pertaining to the scattering process with linearly and circularly polarized probes.

I showed analytically that the contrast mechanism of resonant magnetic scattering with linearly polarized light arises from the Faraday rotation, which is mapped onto the magnetic texture,

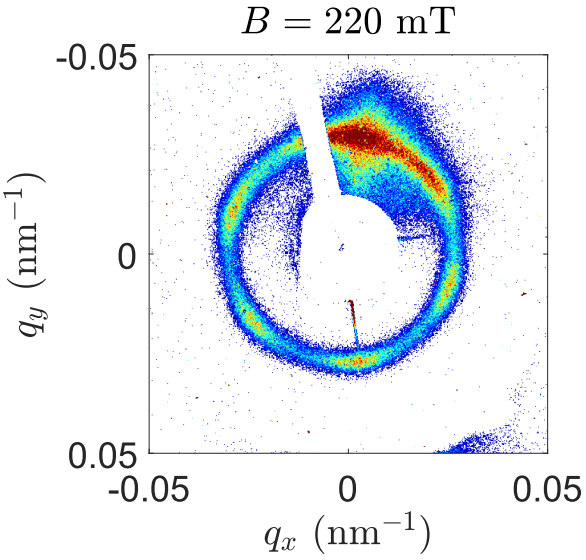

Figure 5.14: RMS from a hexagonal skyrmion lattice.

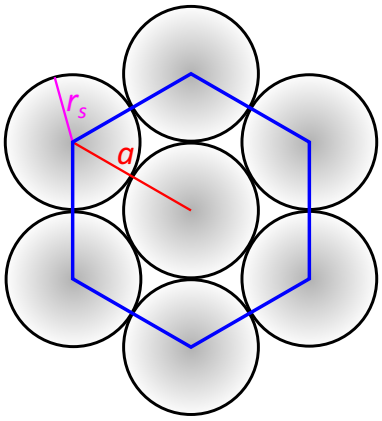

Figure 5.15: Two-dimensional hexagonal close-packed lattice of skyrmions. a is the lattice constant $r_s = a/2$ is the skyrmion radius.

and derived the optimal sample thickness, equal to twice the attenuation length, that maximizes the scattered flux.

A high photon flux at the M-shell absorption edge of Fe was achieved with a phase-matched laser-driven HHG process. The resonant nature of magnetic scattering in the EUV spectral region allowed an improvement of the beamline efficiency through the use of efficient broadband grazing incidence optics instead of multilayer mirrors. Even though the spectrum of the EUV probe incident on the sample is broad, only the photons whose energy is on resonance with the absorption edge of a given magnetic material are scattered.

The tabletop RMS setup was employed to study the field dependence of magnetic textures in a Fe-Gd multilayer alloy with perpendicular magnetic anisotropy. At low fields, the sample exhibited disordered domain networks. As the field increased, the domain size also increased, and the domains themselves became more ordered. At $B = 220$ mT, an RMS pattern with a hexagonal symmetry was observed. It was attributed to a formation of a two-dimensional hexagonal close-packed lattice of dipole-stabilized skyrmions. This constituted the first observation of magnetic skyrmions with a tabletop EUV source.

Chapter 6

Laser-Induced Spin Dynamics in a Network of Magnetic Domains

In this chapter, I report the results of an RMS experiment performed at LCLS. The goal of the experiment was to study optically-induced dynamics of nanoscale magnetic domains and domain walls in a ferromagnetic multilayer film by use of resonant soft X-ray (SXR) magnetic scattering. In the experiment, photons at high scattering angles were captured, which allowed access to fine spatial features such as domain walls. I develop a method of reconstructing dynamic changes to magnetic domains in real space by applying the experimental time-resolved scattering data to a simulated domain pattern whose Fourier spectral intensity agrees well with the static experimental scattering intensity. The reconstructed changes in the domain pattern reveal feature-dependent non-uniform demagnetization. I develop a phenomenological spin transport model and apply it to the same simulated domain pattern and find that the model predictions agree well with the experimental reconstructions. I, therefore, attribute the observed spatially resolved dynamics to a transient exchange of angular momentum between magnetic domains of opposite magnetization. I also find that, on short timescales, domain walls remain sharp and demagnetize less than the domains themselves, but their demagnetization and broadening proceed even on long timescales. I perform thermal transport simulations and correlate this behavior with the heat diffusion through the crystal lattice throughout the depth of the sample, which affects the total magnetic anisotropy of the film and thus the width of the domain walls.

6.1 Overview of previous work

RMS is a very powerful technique because it allows one to access spatial variations of magnetic properties with light. This is especially important in time-resolved studies since additional non-local demagnetization channels, such as superdiffusive spin currents [154], can arise due to magnetic inhomogeneities, e.g. in a network of magnetic domains, and contribute to the demagnetization process. Because of this and the nanometer magnetic correlation lengths involved, laser-induced evolution of a magnetic texture can be substantially different from that of a uniformly magnetized film. To date, most studies of ultrafast demagnetization have either adopted a spatially averaged approach [197, 172, 144] or used uniformly magnetized samples [127, 57, 122, 133, 125, 198, 199]. They have been able to uncover the role of Stoner excitations and ultrafast magnon generation in ultrafast demagnetization [122, 125], as described in Chapter 4, and also reported an observation of an ultrafast phase transition from the ferromagnetic to the paramagnetic state [144, 172]. In the absence of spatial resolution, however, observation of lengthscale-dependent ultrafast magnetic phenomena would be impossible without specifically tailoring the design of the sample, as was done in Refs. [200, 201, 156, 202], where the authors observed ultrafast spin transport by carefully designing the magnetic multilayer stacks and measuring a spectroscopic time-resolved MOKE response in the EUV or visible spectral range. An ability to perform measurements with both a high temporal and spatial resolution is critical not only for gaining insight into the fundamental aspects of materials' magnetism but also from the practical standpoint when, for instance, fast switching of a nanoscale magnetic device needs to be observed.

I reviewed the tools for studying materials systems and their respective temporal and spatial resolution in Fig. 1.1 in Chapter 1. FELs and laser-driven tabletop HHG sources are best suited for the task of capturing magnetization dynamics with a high temporal and spatial resolution by means of time-resolved resonant magnetic scattering. Such experiments have been performed to study ultrafast spatially resolved magnetization dynamics in real space in patterned [203] and disorded [204] systems by use of X-ray holography at an FEL. Time-resolved experiments in reciprocal space

have been carried out using both FEL [205, 206, 207] and HHG [182] sources. Refs. [206, 207] report on magnetization dynamics in granular media, which are quite different from the domain sample studied here. Relevant results concerning the evolution of a pattern of disordered magnetic domains are reported in Refs. [182, 204, 205], where evidence of ultrafast spin-polarized transport between domains is observed. While Ref. [182] does not make any claims regarding the dynamics of domain walls, Refs. [205, 204] state that the the domain walls are softened in a laser-excited sample. This softening is attributed to the effect of spin currents. However, in all of the references above, the spatial resolution was limited by the relatively low scattering angles, which included only the first order scattering ring. Therefore, the interpretation of the results is based on an extrapolation of the experimental signals to higher scattering angles.

In the experiment reported here, in addition to the first order ring, third and fifth orders were measured, which allowed an extraction of the dynamics of very small magnetic features including domain walls. In contrast with Refs. [204, 205], I observe that domain walls demagnetize less and remain sharp on short timescales, and only start to broaden at longer times. In this chapter, I discuss possible sources of this disagreement with the previous results in the literature.

6.2 Soft X-ray scattering experiment at LCLS

The experiment was performed at the SXR beamline at LCLS, and the setup is shown in Fig. 6.1. Soft X-ray pulses with a 60 fs pulse length were produced by the FEL at a repetition rate of 120 Hz. The energy of the photons in the pulse was set to 852.7 eV to match the L_3 absorption edge of nickel. The linear polarization of the soft X-ray pulses was converted to circular in the Delta-undulator [208]. The X-rays were scattered by a domain sample whose multilayer composition was Si_3N_4(50)/ Ta(3)/ Cu(5)/ (Co90Fe10(0.2)/ Ni(0.6))x50/ CoFe(0.2)/ Cu(3)/ Ta_2O_5(3), where the layer thicknesses in parentheses are in nm. Such a sample structure generated perpendicular magnetic anisotropy (PMA), which lead to a formation of worm-like magnetic domains with a periodicity of 160 nm. The multilayer structure of the sample and its magnetic force microscopy image are shown in Fig. 6.2. As discussed in Chapter 5, the magnetic contrast mechanism with

circularly polarized X-rays is due to the X-ray Magnetic Circular Dichroism (XMCD), which is manifested as a dichroism in the X-ray absorption of light with a well defined helicity by domains with opposite magnetization directions. XMCD thus maps the domain pattern to a difference in X-ray absorption. In the far field, the X-rays scattered by the domain sample produce a series of concentric rings corresponding to odd orders of diffraction. This scattering pattern was recorded with a pnCCD detector placed 275.3 mm away from the sample. The detector consisted of four 512×512 pixel independent panels with adjustable positions, and the pixel size was 75 μm. Such an experimental geometry allowed detection of X-rays scattered at angles of up to $\sim 8°$. The pnCCD

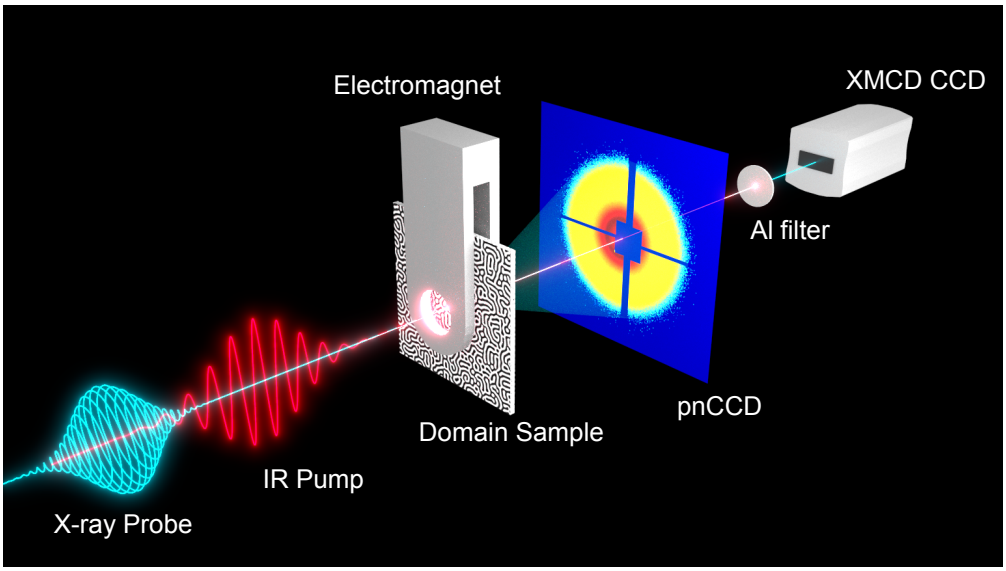

Figure 6.1: Experimental setup for time-resolved soft X-ray resonant magnetic scattering. The pnCCD is used to detect scattered X-rays at different delay times between an IR pump and an X-ray probe, and the detector behind the pnCCD is used for XMCD measurements. The electromagnet allows one to control an external magnetic field at the sample.

had an opening at the center to allow the unscattered X-rays propagate through. These X-rays were detected with an Andor Newton CCD camera placed behind the pnCCD. An Al filter in front of the Andor CCD suppressed the IR light from the pump laser. An electromagnet could apply up to 0.6 T of external magnetic field perpendicularly to the surface of the sample. In addition to zero-field RMS measurements, both the scattering (with the pnCCD) and XMCD (with the Andor

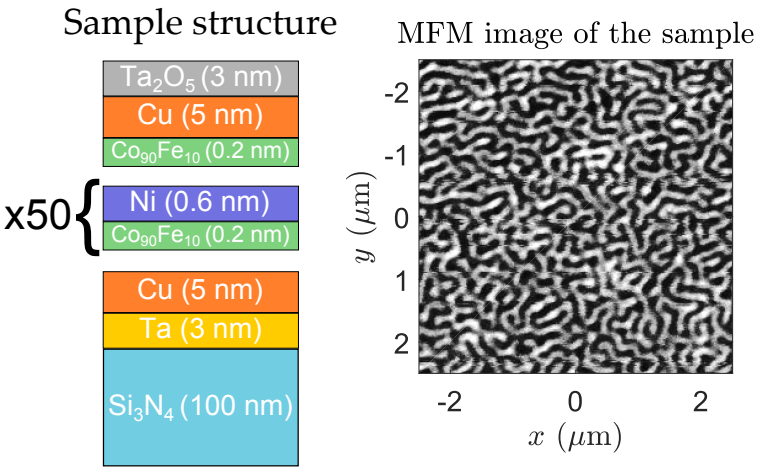

Figure 6.2: Sample structure and MFM image of domains. The domains are disordered, and their periodicity is ∼160 nm.

CCD) signals were taken when the sample was magnetically saturated. Those data were used to remove any non-magnetic contributions from the zero-field scattering data. I describe the details of this removal procedure in Section 6.4.

An X-ray probe pulse arrived at the sample with a time delay relative to an IR pump pulse from an amplified Ti:Sapphire laser at 795 nm. The pump pulses were 60 fs long, and the average incident pump fluence was $\sim$23 mJ/cm^2. The pump laser was time-locked to the FEL. However the FEL had an intrinsic jitter associated with an uncertainty in the emission time, energy, and intensity of individual electron bunches, which was manifested as fluctuations in the arrival time, energy, and brightness of X-ray pulses. The delay time between the IR pump and the X-ray probe was scanned in the range from -3 ps (to probe an unperturbed sample at negative delays) to 20 ps. Scattering patterns at each delay time were taken in a signle-shot manner. Because of the jitter in the arrival time of the probe, the position of the delay stage in the pump arm does not correspond to a fixed pump-probe delay from pulse to pulse. However, a correlation method used to time stamp the X-ray pulses at LCLS allows one to correct for such jitter. If both the position of the delay stage and the arrival time of the probe pulse are known, then the total delay between the pump and the probe can be calculated. For this reason, the delay stage is moved continuously in order to improve the statistics. In the next step, all of the collected scattering patterns are sorted according to their delay, and the pattern at a requested delay is computed as an average of all the patterns recorded within a specified time window (400 fs for this experiment) centered at that delay. Such a binning procedure, while lowering the temporal resolution, leads to a significantly improved signal-to-noise ratio.

6.3 Data processing considerations

With the experimental setup in Fig. 6.1, two-dimensional RMS intensity distributions $S_q^2(q_x, q_y)$ shown in Fig. 6.3(a) were measured. Because of the azimuthal symmetry of $S_q^2(q_x, q_y)$,

the dimensionality of the data set can be reduced by computing an azimuthal average of $S_q^2(q_x, q_y)$

$$\langle S_q^2 \rangle(q) = \frac{1}{2\pi} \int_0^{2\pi} S_q^2(q\cos\phi, q\sin\phi) d\phi, \tag{6.1}$$

where the scattering vector q is defined as $q = 4\pi \sin(\theta/2)/\lambda$ (λ is the incident wavelength and θ is the scattering angle). An azimuthally averaged RMS intensity distribution is shown in Fig. 6.3(b). Prior to computing $\langle S_q^2 \rangle$ with eq. (6.1), it is important to ensure that several aspects are properly

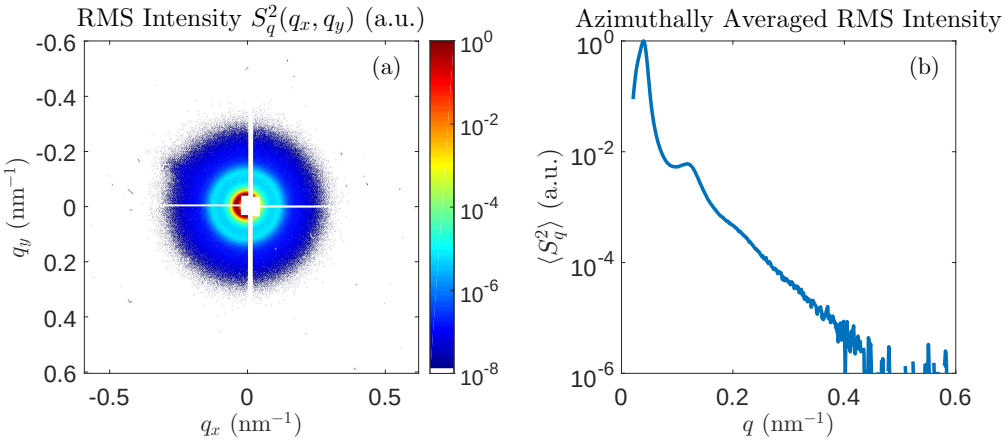

Figure 6.3: RMS intensity distribution from an unperturbed domain sample at $t = 0$: (a) as measured by the pnCCD, (b) averaged in the azimuthal direction. In (b), the first and third order scattering peaks are clearly visible at 0.04 and 0.12 nm^{-1}, respectively. A small fifth order peak is discernable at 0.2 nm^{-1}.

accounted for.

First, the panels of the pnCCD must be aligned correctly. The spacing in pixels between the panels seen as white lines cutting through the data in Fig. 6.3(a) represents the actual physical spacing between the panels. If this distance-to-pixel calibration is incorrect, the azimuthally averaged signal will be distorted.

Second, the center of the scattering pattern must be determined accurately. This is important for the correct computation of $\langle S_q^2 \rangle$, especially at low q-values. For a continuous detector this can be done simply by finding the centroid of the image. For the pnCCD detector consisting of four separate panels, the centroid does not give the true position of the center of the scattering pattern because of the missing pixels in between the panels. I, therefore, threshold the data and fit a circle

to the pixels whose values are above the specified threshold. A function that performs the fitting can be found online.[1]

Third, the missing pixels in between the pnCCD panels (as well as pixels at the edges of the pnCCD that are saturated by the pump) must be properly accounted for. Eq. (6.1) assumes that on a circle of radius q, there are $2\pi q$ pixels. However, in the case considered here, data on some pixels might be missing, so the total number of pixels with data is less than $2\pi q$. This is illustrated with the pixel mask in Fig. 6.4, where the pixels with missing or bad data are shown in black, and a circle of constant q is shown in blue. The intersection of the circle with the black pixels should not contribute to the total average. Assuming that the scatter pattern is azimuthally symmetric the missing data can be accounted for by multiplying $\langle S_q^2 \rangle(q)$ defined by eq. (6.1) by a correction factor $f_c(q) = \left(\int_0^{2\pi} m(q,\phi) d\phi \right)^{-1}$, where $m(q,\phi)$ is a mask of pixels with bad data shown in Fig. 6.4, such that $m(q,\phi) = 1$ for good pixels (white) and $m(q,\phi) = 0$ otherwise (black).

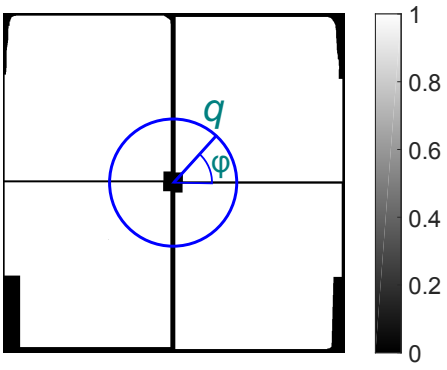

Figure 6.4: Mask of bad pixels m and a circle of constant q. $m(q,\phi) = 1$ for good pixels (white) and $m(q,\phi) = 0$ otherwise (black).

With the procedure described above, an azimuthally averaged spectrum is obtained (see Fig. 6.3(b)). The procedure is repeated for each delay time between the pump and the probe and yields a time-dependent azimuthally averaged dataset $\langle I_q \rangle(t)$ shown in Fig. 6.5 as a density plot of the time-resolved data normalized by the static signal $\langle I_q \rangle(0)$. Here, I have changed the notation

[1] https://blogs.mathworks.com/pick/2008/03/14/fitting-a-circle-easily/

for the scattered intensity from S_q^2 to I_q to emphasize the fact that the measured scattering is not necessarily purely magnetic (which will be denoted by S_q^2 further in the text) but also has a charge component C_q^2 contributing to the total scattered intensity I_q. In Section 6.4, I show that the oscillations seen in Fig. 6.5 around $q \approx 0.3$ nm^{-1} come from the charge scattering and develop a method of isolating the purely magnetic component of the scattered intensity S_q^2.

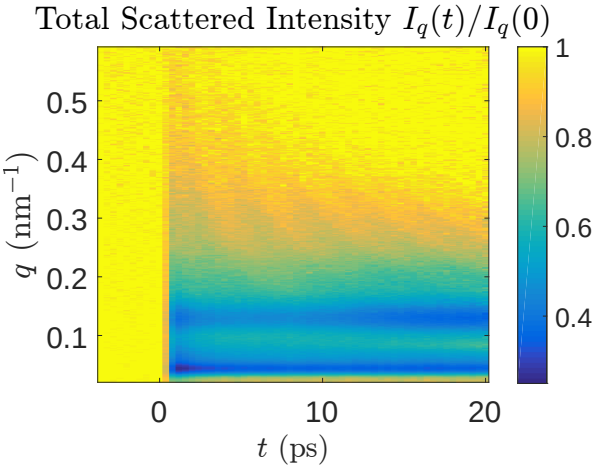

Figure 6.5: Time-resolved azimuthally averaged scattered intensity normalized by the static signal $\langle I_q \rangle(t)/\langle I_q \rangle(0)$. Note the oscillations at $q \approx 0.3$ nm^{-1}.

6.4 Separation of magnetic and electronic scattering

6.4.1 Mathematical basis

In the following, I derive the intensity of the probe beam at the pnCCD after it is scattered by a sample with some real-space distribution of the magnetization (or spin) $s(\vec{r})$ and charge $c(\vec{r})$. I employ the refractive index formalism to describe X-ray interactions with matter, which is equivalent to the scattering factor formalism often used for that purpose [160]. The derivation takes into account contributions from both the charge distribution $c(\vec{r})$, as well as two types of spin distribution—one that is uncorrelated ($s(\vec{r})$) and one that is correlated ($\alpha c(\vec{r})$) with the charge, where α is a scalar that represents the magnitude of the charge-correlated spin distribution. Because the sample is probed with circularly polarized X-rays, the magnetic and charge scattering

components have the same polarization and can interfere in the detector plane. Therefore, care must be taken while separating the two scattering components.

6.4.1.1 General case

A wave transmitted through the sample is called the exit surface wave (ESW). If the electric field of the incident wave is E_0, the exit surface wave is

$$E = E_0 \exp\left[ikd\left(n_0 + \delta n_s s(\vec{r}) + \delta n_c c(\vec{r}) + \alpha \delta n_s s(\vec{r})\right)\right], \tag{6.2}$$

where d is the sample thickness, δn_c is the magnitude of the refractive index variation due to charge, δn_s is the magnetic refractive index variation, i.e. it is defined by the difference in the refractive index between the positive (+) and negative (−) magnetization directions $\delta n_s = \frac{1}{2}(n_+ - n_-)$, $k = 2\pi/\lambda$. $s(\vec{r})$ is determined by, for example, the magnetic domain topography of a given sample and is equal to the spatial dependence of the out-of-plane component of the magnetization $s(\vec{r}) = M_z(\vec{r})$. $c(\vec{r})$ is determined by spatial variations of the charge distribution that arise due to, e.g., inhomogeneities in the chemical composition and/or sample roughness. In the most general case, there is a charge-correlated spin distribution $\alpha c(\vec{r})$, which depends on how strongly the magnetization is sensitive to local charge variations $c(\vec{r})$. In the case of granular media [206, 207], such correlation is indeed very strong. In the case considered here, it is expected to be negligible because the sample is relatively flat and homogeneous. Nonetheless, I shall keep the $\alpha c(\vec{r})$ term in order to develop a rigorous approach. Note that $c(\vec{r})$, $s(\vec{r})$, and α can all be time-dependent, and the time dependencies of these terms are not necessarily the same.

The spot size of the X-ray probe is on the order of 100 μm in the experiment, which is much bigger than the characteristic lengths of the domain sample. Hence, I assume that the incident beam is a plane wave, and, in eq. (6.2), $E_0 = 1$. Additionally, I divide out the factor $\exp\left[ikdn_0\right]$ because it does not contribute to the scattered intensity. For brevity, I define $C_r = ikd\delta n_c c(\vec{r})$ and $S_r = ikd\delta n_s s(\vec{r})$. With these definitions and the assumptions made above, eq. (6.2) simplifies to

$$E = \exp\left[S_r + C_r + \alpha \frac{\delta n_s}{\delta n_c} C_r\right]. \tag{6.3}$$

I Taylor expand this expression up to second order

$$E = 1 + C_r + S_r + \alpha\frac{\delta n_s}{\delta n_c}C_r + \frac{1}{2}C_r^2 + \frac{1}{2}S_r^2 + \frac{1}{2}\alpha^2\left(\frac{\delta n_s}{\delta n_c}\right)^2 C_r^2 + \alpha\frac{\delta n_s}{\delta n_c}C_r^2 + \alpha\frac{\delta n_s}{\delta n_c}C_rS_r + C_rS_r. \quad (6.4)$$

The complex electric field of the scattered wave at the detector is obtained by Fourier transforming expression (6.4)

$$\begin{aligned} E_q = \delta(\vec{q}) + \left(1 + \alpha\frac{\delta n_s}{\delta n_c}\right)C_q + S_q + \frac{1}{2}\left(1 + 2\alpha\frac{\delta n_s}{\delta n_c} + \alpha^2\left(\frac{\delta n_s}{\delta n_c}\right)^2\right)\mathcal{F}\{C_r^2\} + \\ + \frac{1}{2}\mathcal{F}\{S_r^2\} + \left(1 + \alpha\frac{\delta n_s}{\delta n_c}\right)\mathcal{F}\{C_rS_r\}, \end{aligned} \quad (6.5)$$

where I defined $C_q = \mathcal{F}\{C_r\}$ and $S_q = \mathcal{F}\{S_r\}$. This expression can be simplified by introducing $a = \left(1 + \alpha\frac{\delta n_s}{\delta n_c}\right)$ and canceling the Dirac-Delta $\delta(\vec{q})$, as it is only non-zero at $\vec{q} = 0$, i.e. for the unscattered light, which I am not considering here. Eq. (6.5) now simplifies to

$$E_q = aC_q + S_q + \frac{1}{2}a^2\mathcal{F}\{C_r^2\} + \frac{1}{2}\mathcal{F}\{S_r^2\} + a\mathcal{F}\{C_rS_r\}, \quad (6.6)$$

The scattered intensity is $I_q = |E_q|^2$. Using eq. (6.6) and neglecting the third order terms, an expression for the scattered intensity can be derived

$$\begin{aligned} I_q = &\left|a^2C_q^2\right| + \left|a^3C_q\mathcal{F}\{C_r^2\}\right|\cos\left(\xi_{aC_q} - \xi_{a^2\mathcal{F}\{C_r^2\}}\right) + \\ &+ 2\left|a^2C_q\mathcal{F}\{C_rS_r\}\right|\cos\left(\xi_{aC_q} - \xi_{a\mathcal{F}\{C_rS_r\}}\right) + \left|aC_q\mathcal{F}\{S_r^2\}\right|\cos\left(\xi_{aC_q} - \xi_{\mathcal{F}\{S_r^2\}}\right) + \\ &+ 2\left|aC_qS_q\right|\cos\left(\xi_{aC_q} - \xi_{S_q}\right) + \left|a^2\mathcal{F}\{C_r^2\}S_q\right|\cos\left(\xi_{a^2\mathcal{F}\{C_r^2\}} - \xi_{S_q}\right) + \\ &+ 2\left|a\mathcal{F}\{C_rS_r\}S_q\right|\cos\left(\xi_{S_q} - \xi_{a\mathcal{F}\{C_rS_r\}}\right) + \left|\mathcal{F}\{S_r^2\}S_q\right|\cos\left(\xi_{S_q} - \xi_{\mathcal{F}\{S_r^2\}}\right) + \left|S_q^2\right|, \end{aligned} \quad (6.7)$$

where ξ_x are the phases of the respective terms indicated by the subscript x. The expression above is very unwieldy, but it is simplified upon azimuthal integration because, for disordered and uncorrelated distributions $s(\vec{r})$ and $c(\vec{r})$, many of the cosines average out to zero. The phases in the following pairs are random and uncorrelated ξ_{aC_q} and ξ_{S_q}, $\xi_{a^2\mathcal{F}\{C_r^2\}}$ and ξ_{S_q}, $\xi_{\mathcal{F}\{S_r^2\}}$ and ξ_{aC_q}. Therefore $\left\langle\cos\left(\xi_{aC_q} - \xi_{\mathcal{F}\{S_r^2\}}\right)\right\rangle = 0$, $\left\langle\cos\left(\xi_{aC_q} - \xi_{S_q}\right)\right\rangle = 0$, and $\left\langle\cos\left(\xi_{a^2\mathcal{F}\{C_r^2\}} - \xi_{S_q}\right)\right\rangle = 0$, where $\langle X\rangle = 1/2\pi\int_0^{2\pi} X(\phi)d\phi$ is an azimuthal average.

The terms with the factors $\left|a^3C_q\mathcal{F}\{C_r^2\}\right|$ and $\left|\mathcal{F}\{S_r^2\}S_q\right|$ are vanishingly small and, as such, can be eliminated. The reason for this is that C_q and $\mathcal{F}\{C_r^2\}$, and S_q and $\mathcal{F}\{S_r^2\}$ have a different

q-dependence. To illustrate this, consider a one-dimensional example $f(x) = e^{i\omega x}$. The Fourier transforms of $f(x)$ and $f^2(x)$ are $\mathcal{F}\{f(x)\} = \delta(\omega)$ and $\mathcal{F}\{f^2(x)\} = \mathcal{F}\{e^{i2\omega x}\} = \delta(2\omega)$. The product of the two Dirac-Deltas is zero $\delta(\omega)\delta(2\omega) = 0$. Similarly, if the Fourier transform of S_r is a ring of a certain diameter, then the Fourier transform of S_r^2 is a ring of twice the diameter, and the product of the two rings is negligible if the widths of the rings are smaller than their radii, which is the case for the data set being considered. The same argument applies to C_r. With these approximations and the fact the, from the convolution theorem, $\mathcal{F}\{C_r S_r\} = C_q \otimes S_q$, where the symbol $\otimes$ denotes the convolution operation, the final expression for the azimuthally averaged scattering intensity is

$$\begin{aligned}\langle I_q \rangle = &\left|1 + \alpha\frac{\delta n_s}{\delta n_c}\right|^2 \left\langle |C_q|^2 \right\rangle + 2\left|1 + \alpha\frac{\delta n_s}{\delta n_c}\right|^2 \left\langle |C_q|\,|C_q \otimes S_q| \cos\left(\xi_{aC_q} - \xi_{aC_q \otimes S_q}\right)\right\rangle + \\ &+ 2\left|1 + \alpha\frac{\delta n_s}{\delta n_c}\right| \left\langle |C_q \otimes S_q|\,|S_q| \cos\left(\xi_{S_q} - \xi_{aC_q \otimes S_q}\right)\right\rangle + \left\langle |S_q|^2 \right\rangle .\end{aligned} \tag{6.8}$$

This expression is valid in the general case and can be simplified for the special cases of zero and near-saturation applied magnetic field B.

6.4.1.2 Zero applied field

Without an external magnetic field, C_r and S_r are random an uncorrelated, and, therefore $\left\langle \cos\left(\xi_{aC_q} - \xi_{aC_q \otimes S_q}\right)\right\rangle = \left\langle \cos\left(\xi_{S_q} - \xi_{aC_q \otimes S_q}\right)\right\rangle = 0$. The measured azimuthally averaged intensity then becomes

$$\langle I_q(B=0) \rangle = \left|1 + \alpha\frac{\delta n_s}{\delta n_c}\right|^2 \left\langle |C_q|^2 \right\rangle + \left\langle |S_q|^2 \right\rangle . \tag{6.9}$$

If $\alpha = 0$, the signal is simply the sum of the magnetic and charge scattering intensities.

6.4.1.3 Near-saturation applied field

I have assumed above that the magnetic part has two components—a non-uniform charge-correlated $\pm\alpha\frac{\delta n_s}{\delta n_c} C_r$ and a uniform charge-uncorrelated $s(\vec{r}) = \pm 1$, so that $S_r = \pm idk\delta n_s$ when the sample is magnetically saturated by an external field. The Fourier transform of S_r, in this case, is a delta-function $S_q = \mathcal{F}\{S_r\} = \pm idk\delta n_s \delta(\vec{q})$. Therefore, $S_q(\vec{q} \neq 0) = 0$, and $S_q \otimes C_q = \pm idk\delta n_s C_q$.

Note that I am not assuming the existence of a non-uniform and charge-uncorrelated magnetization component because, in the experiment, only scattering into q-vectors corresponding to the charge scattering was observed with a saturating applied field without any additional time-dependent scattering into any other q-vectors. It would be an improbable coincidence if a charge-uncorrelated magnetic component would scatter X-rays into the same cone of angles as the C_r. The assumption employed here can, therefore, be considered reasonable.

Under these conditions, only the first two terms in eq. (6.8) remain and the expression for $\langle I_q \rangle$ is simplified to

$$\langle I_q(B \neq 0) \rangle = \left| 1 + \alpha \frac{\delta n_s}{\delta n_c} \right|^2 \left\langle |C_q|^2 \right\rangle + 2 \left| dk \delta n_s \right| \left| 1 + \alpha \frac{\delta n_s}{\delta n_c} \right|^2 \left\langle |C_q|^2 \cos\left(\xi_{aC_q} - \xi_{\pm idk\delta n_s aC_q} \right) \right\rangle . \tag{6.10}$$

In order to compute the scattered intensity using this expression, the argument of the cosine has to be evaluated for positive and negative applied fields. This can be done using the fact that the phase of a product of two complex numbers is equal to the sum of their individual phases. The following expressions thus hold

$$\begin{aligned} \xi_{aC_q} &= \xi_a + \xi_{C_q}, \\ \xi_{\pm idk\delta n_s aC_q} &= \xi_a + \xi_{C_q} + \xi_{\pm idk\delta n_s}. \end{aligned} \tag{6.11}$$

The phase of the complex number $\pm idk\delta n_s$ for positive and negative fields, respectively, is simply

$$\begin{aligned} \xi_{+idk\delta n_s} &= \arctan\left(\frac{\mathrm{Im}(\delta n_s)}{\mathrm{Re}(\delta n_s)} \right) + \frac{\pi}{2}, \\ \xi_{-idk\delta n_s} &= \arctan\left(\frac{\mathrm{Im}(\delta n_s)}{\mathrm{Re}(\delta n_s)} \right) + \frac{\pi}{2} + \pi. \end{aligned} \tag{6.12}$$

Using eqs. (6.10), (6.11), and (6.12), I derive the final expression for the scattered intensity under a saturating applied magnetic field

$$\langle I_q(B \neq 0) \rangle = (1 \pm 2dk\mathrm{Im}(\delta n_s)) \left| 1 + \alpha \frac{\delta n_s}{\delta n_c} \right|^2 \left\langle |C_q|^2 \right\rangle . \tag{6.13}$$

Note that C_q and α can be time-dependent. Additionally, in the saturation-field case, I allow δn_s to be time-dependent in order to take into account the possibility of ultrafast demagnetization of a uniformly magnetized sample via local demagnetization mechanisms. Because of the possible

additional demagnetization channels in the zero-field case, the time dependence of δn_s in that case is not necessarily the same. Finally, in the limit of $\alpha = 0$ the total scattering intensity is simply equal to the charge scattering intensity modulated by the XMCD absorption.

6.4.1.4 Separation of the spin and charge contributions

I now use eqs. (6.9) and (6.13) to separate the magnetic and charge scattering intensities.

First, I use eq. (6.13) to solve for $\left\langle |C_q|^2 \right\rangle$. To streamline the derivation, I introduce a substitution $f = \alpha \frac{\delta n_s}{\delta n_c}$. With this substitution, I expand the term $|1 \pm f|^2$ and rewrite the intensities for the positive and negative fields

$$\begin{aligned} \langle I_q(B>0)\rangle &= (1 + 2dk\mathrm{Im}(\delta n_s)) \left|1 + |f|^2 + 2\mathrm{Re}(f)\right|^2 \left\langle |C_q|^2 \right\rangle, \\ \langle I_q(B<0)\rangle &= (1 - 2dk\mathrm{Im}(\delta n_s)) \left|1 + |f|^2 + 2\mathrm{Re}(f)\right|^2 \left\langle |C_q|^2 \right\rangle. \end{aligned} \tag{6.14}$$

I define the sum and difference intensities as and

$$\begin{aligned} \Sigma &= \frac{1}{2}\left(\langle I_q(B>0)\rangle + \langle I_q(B<0)\rangle\right), \\ \Delta &= \frac{1}{4}\left(\langle I_q(B>0)\rangle - \langle I_q(B<0)\rangle\right). \end{aligned}$$

Using eqs. (6.14), Δ and Σ can be written explicitly as

$$\begin{aligned} \Delta &= \left(dk\mathrm{Im}(\delta n_s)\left(1 + |f|^2\right) + \mathrm{Re}(f)\right) \left\langle |C_q|^2 \right\rangle, \\ \Sigma &= \left(1 + |f|^2 + 4dk\mathrm{Im}(\delta n_s)\mathrm{Re}(f)\right) \left\langle |C_q|^2 \right\rangle. \end{aligned} \tag{6.15}$$

Assuming that f is small (because α must be small in this experiment) and δn_s is small, and neglecting second order terms, these expressions are simplified to

$$\begin{aligned} \Delta &\approx \left(dk\mathrm{Im}(\delta n_s) + \mathrm{Re}\left(\alpha \frac{\delta n_s}{\delta n_c}\right)\right) \left\langle |C_q|^2 \right\rangle, \\ \Sigma &\approx \left\langle |C_q|^2 \right\rangle. \end{aligned} \tag{6.16}$$

The charge-uncorrelated (time-dependent) term $S_{xmcd} = dk\mathrm{Im}(\delta n_s(t))$ can be found from the measured XMCD signal since d and k are known, $\delta n_s(t=0)$ can be found from the CXRO database [209], and the time dependence of $\delta n_s(t)$ is given by the time dependence of the XMCD intensity $\Delta I_{xmcd}(t)$. Thus the charge-correlated (time-dependent) term $\mathrm{Re}\left(\alpha \frac{\delta n_s}{\delta n_c}\right)$ can be found from Δ.

In order to finalize this derivation and separate the charge and magnetic contributions to the scattering intensity, I Taylor-expand eq. (6.9) in powers of $\mathrm{Re}\left(\alpha\frac{\delta n_s}{\delta n_c}\right)$ up to a first order

$$\langle I_q(B=0)\rangle \approx \left(1+\mathrm{Re}\left(\alpha\frac{\delta n_s}{\delta n_c}\right)\right)\left\langle|C_q|^2\right\rangle + \left\langle|S_q|^2\right\rangle. \tag{6.17}$$

Using eqs. (6.16) and (6.17) and the definition $S_{xmcd} = dk\mathrm{Im}(\delta n_s(t))$, I now solve for $\left\langle|S_q|^2\right\rangle$ and thus completely separate the spin and charge contributions to the scattering intensity

$$\begin{aligned}\left\langle|C_q|^2\right\rangle &= \Sigma = \frac{1}{2}\left(\langle I_q(B>0)\rangle + \langle I_q(B<0)\rangle\right),\\ \left\langle|S_q|^2\right\rangle &= \langle I_q(B=0)\rangle - \left(1+\frac{\Delta}{\Sigma} - S_{xmcd}\right)\Sigma.\end{aligned} \tag{6.18}$$

Notice that in the limit of $\alpha = 0$, $\frac{\Delta}{\Sigma} - S_{xmcd} = 0$, and $\left\langle|S_q|^2\right\rangle$ simply becomes the difference between the total measured intensity and the average of intensities measured at the opposite values of an applied saturating field.

With eq. (6.18), the separation procedure can be summarized as follows

(1) Measure the scattering intensity $\langle I_q(B=0)\rangle$ at zero field.

(2) Apply a saturating magnetic field to the sample and measure the scattering intensities $\langle I_q(B>0)\rangle$ and $\langle I_q(B<0)\rangle$ for the opposite directions of the field. Simultaneously, take an XMCD signal $\Delta I_{xmcd}(t)$ with the XMCD detector in Fig. 6.1.

(3) From $\Delta I_{xmcd}(t)$ compute S_{xmcd}

(4) Using eqs. (6.18), compute $\left\langle|C_q|^2\right\rangle$ and $\left\langle|S_q|^2\right\rangle$.

6.4.2 Implementation of the separation procedure

The result of the application of the separation procedure derived above to the experimental dataset in Fig. 6.5 is shown in Fig. 6.6(c). The oscillations seen in the total scattered intensity in Fig. 6.6(a) are present in the sum intensity Σ, shown in Fig. 6.6(b), which confirms that their origin is non-magnetic. They appear due to laser-induced acoustic strain waves that originate at charge inhomogeneities and travel through the film. As can be seen from Fig. 6.6(c), the

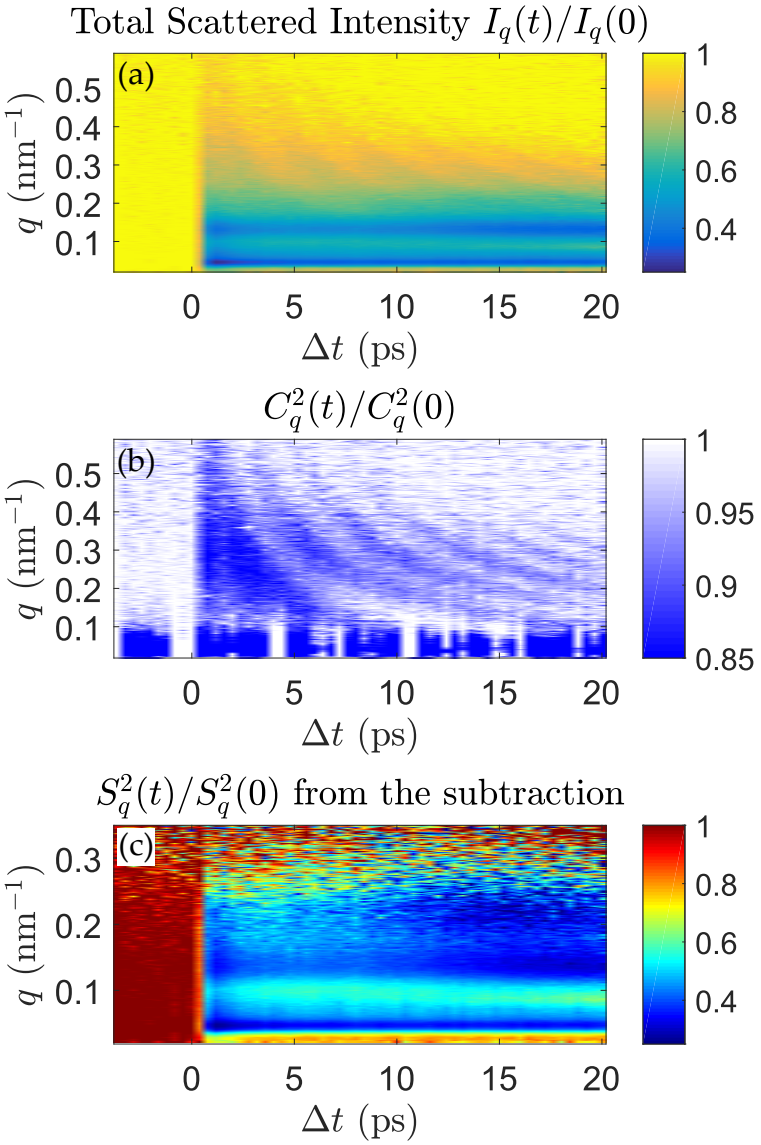

Figure 6.6: Separation of the spin and charge scattering: (a) Total measured scattering intensity $\langle I_q(B=0,t)\rangle \,/\, \langle I_q(B=0,t=0)\rangle$, (b) Charge scattering $\Sigma(t)/\Sigma(t=0)$, (c) Spin scattering $\langle S_q^2(t)\rangle \,/\, \langle S_q^2(t=0)\rangle$.

oscillations that appear in the original signal in Fig. 6.6(a) are no longer present in the magnetic scattering intensity in Fig. 6.6(c) computed according to eq. (6.18), which confirms the validity of the separation procedure. The XMCD signal used to separate out the spin contribution is shown in Fig. 6.7. While the XMCD trace is noisy its effect on the final result is small because the magnitude of the charge-correlated spin distribution represented by α is small.

6.5 Summary of the experimental RMS results

Using the purely magnetic scattering signal in Fig. 6.6(c), I can now carry out its time-resolved analysis, which is summarized in Fig. 6.7.

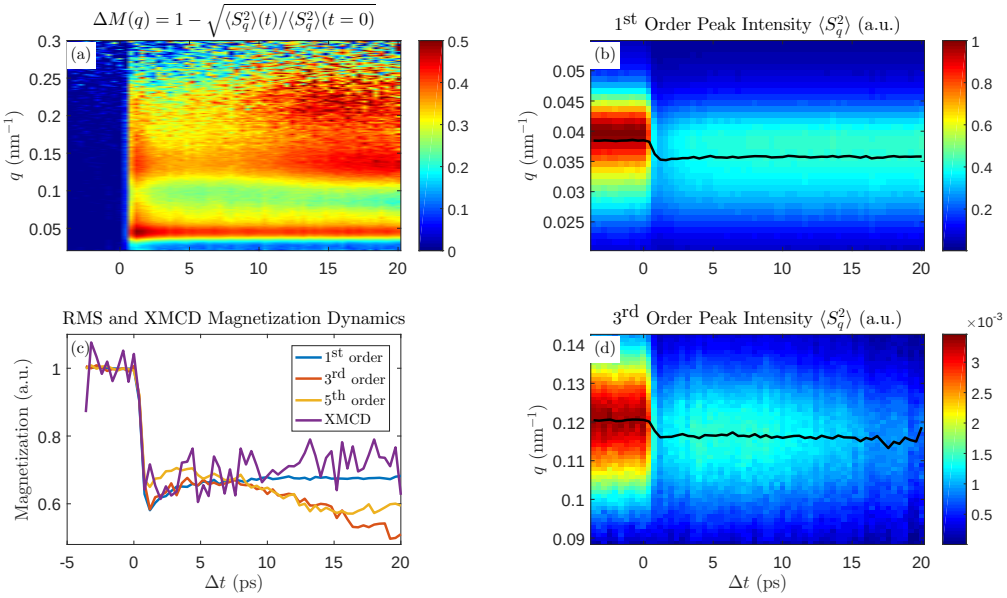

Figure 6.7: Summary of the transient RMS dynamics in the CoFe/Ni multilayer sample: (a) q-dependent relative demagnetization; (c) demagnetization as determined from the first, third, and fifth order peaks as well as the XMCD signal; dynamics of the (b) first and (d) third order scattering peaks. The solid black lines represent the center positions of the peaks.

First, I compute the magnetization dynamics in reciprocal space as a function of momentum transfer q and time t according to

$$\Delta M(q) = 1 - \sqrt{\langle S_q^2\rangle(t)/\langle S_q^2\rangle(t=0)}. \tag{6.19}$$

The result is shown in Fig. 6.7(a). Surprisingly, the magnetization behaves differently at different q's, which suggests some interesting feature-dependent spatial dynamics of magnetic domains. In order to analyze the first, third, and fifth order scattering rings separately, they need to be isolated. Because the magnitude of the first order peak is ∼2 orders of magnitude greater than that of the third order (see Fig. 6.3(b)), the first order can be considered isolated without any further processing. The fifth order peak is too small—only a few detector counts above the noise level—and a reliable background subtraction for this peak has been impossible. The third order peak is sitting on an exponential background, which is manifested as a straight line with a constant negative slope on the log scale in Fig. 6.3(b). As such, the background under the third order peak can be fitted with a decaying exponential, at each time step. An example of such fitting for $t = 0$ ps is shown in Fig.6.8.

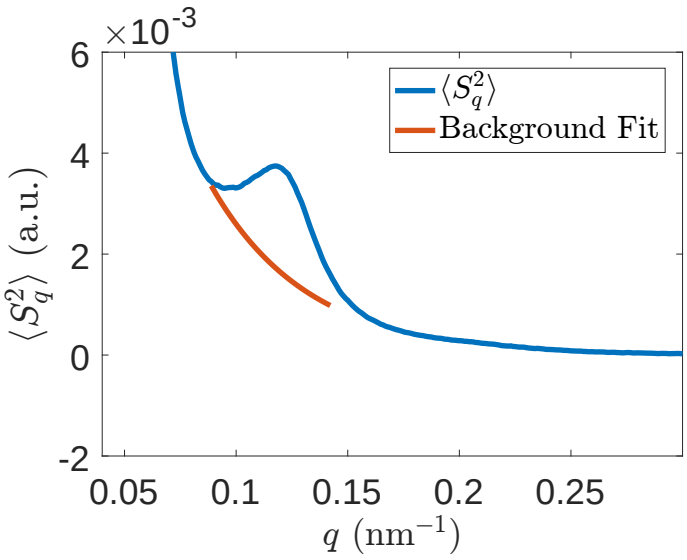

Figure 6.8: Background subtraction for scattered intensity at $t = 0$ ps in order to isolate the third order peak (blue signal above the orange background).

For the isolated scattering peaks, I track changes in their position and magnitude with time. Square roots of the peaks' magnitude correspond to changes in magnetization $M(q,t) = \sqrt{\langle S_q^2 \rangle (t) / \langle S_q^2 \rangle (t=0)}$, according to eq. (6.19). They are shown in Fig. 6.7(c). Note that the

first order demagnetization trace agrees well with the XMCD signal. The third and fifth order demagnetization traces match well with the first order at short times, but start to decay after $\sim$ 7 ps. The discrepancy between the fifth order and the rest of the data stems from the fact that the fifth order could not be properly isolated. For that reason, I did not perform a peak shift analysis for the fifth order.

I track the peak positions of the first and third order scattering peaks by separately fitting each peak with a split Pearson type VII distribution [205]

$$\langle I_q \rangle = I_0 \left(1 + \frac{(q-q_0)^2}{\alpha_1^2 m_1}\right)^{-m_1} H(q_0 - q) + I_0 \left(1 + \frac{(q-q_0)^2}{\alpha_2^2 m_2}\right)^{-m_2} H(q - q_0), \tag{6.20}$$

where I_0 is the peak amplitude, $\alpha_{1,2}$ and $m_{1,2}$ are the parameters of the distribution that account for its skewness and sharpness, q_0 is the position of the peak maximum, which I define as the center of the peak, and H is the Heaviside step function. At each time delay, the fitting of the peaks with eq. (6.20) is performed, which yields $q_0(t)$ for the first and third order peaks shown with a black line in Fig. 6.7(b) and (d), respectively. Both peaks shift rapidly towards lower q's by approximately 7% within the first 1.6 ps, after which their positions remain almost constant. A similar peak shift observed only in the first order was interpreted as evidence of a softening of domain walls caused by superdiffusive spin currents in Ref. [205]. Here, I show that the additional data provided by the third and fifth order scattering rings are inconsistent with such a scenario, and, to the contrary, domain walls remain sharp.

I summarize the main features of the time-resolved data set in Fig. 6.7 as follows:

- Demagnetization traces extracted from the first, third and fifth orders agree on short times.
- Third and fifth order magnetization starts to decay relative to the first order after $\sim$7 ps.
- First order demagnetization agrees well with the XMCD trace.
- First and third order scattering peaks shift rapidly towards lower q's within the first 1.6 ps.

6.6 Reconstruction of real-space transient domain dynamics

In order to gain insight into spatially resolved magnetization dynamics, it would be very advantageous to have the capability of time resolved real-space imaging of magnetic domains. Coherent diffractive imaging techniques are capable of reconstructing an object from its diffraction intensity distribution by use of phase retrieval methods, which rely on specialized computer algorithms [210, 211, 212, 213, 214]. However, such phase retrieval methods require that the data satisfy certain constraints. One of such constraints is oversampling [215], which requires that the diffraction amplitude is sampled at a spatial frequency exceeding the Nyquist frequency. This oversampling ratio is expressed as [107]

$$\rho = \frac{\lambda z}{pD}, \tag{6.21}$$

where λ is the wavelength of the probe, z is the distance between the sample and the detector, D is the lateral size of the object, and p is the pixel size of the detector. In order for phase retrieval algorithms to work, ρ must be greater than 2. In the experiment reported here, $\rho \approx 0.1$, which makes the reconstruction of the real-space domain pattern impossible.

Therefore, in order to observe spatially resolved transient changes to the magnetization profile, particularly to the out-of plane magnetization component $M_z(x, y)$, a different approach has to be adopted. I develop such an approach below. It involves application of the measured RMS data to a simulated domain pattern, for which the phase is known and does not need to be retrieved computationally, and thus enables the computation of transient laser-induced changes in the simulated pattern. A caveat with this approach is that the simulated domain pattern has to represent the actual domain pattern of the sample to a high degree of accuracy. The arrangement of the domains is not so important because the system is disordered, and the experimental data were averaged over multiple domain configurations due to shot-to-shot variability of the domain pattern caused by a re-nucleation of the domains after an optical pump pulse. In principle the MFM image in Fig. 6.2 could be used for the purpose of reconstruction. However, the quality and the resolution of the image are not sufficient. Instead, I use a domain pattern that was sim-

ulated using the MuMax software [216] with the first and second order magnetic anisotropy equal to the experimental values of 343 kJ/m^3 and -143 kJ/m^3, respectively. The simulation grid size was 1024×1024×8 cells, and the dimensions of each cell were 5×5×5 nm. The resulting pattern and the comparison of its scattered intensity $\langle S_q^2 \rangle$ with the experimental one are shown in Fig. 6.9 The agreement between the simulated and the experimental RMS intensities is reasonable: the

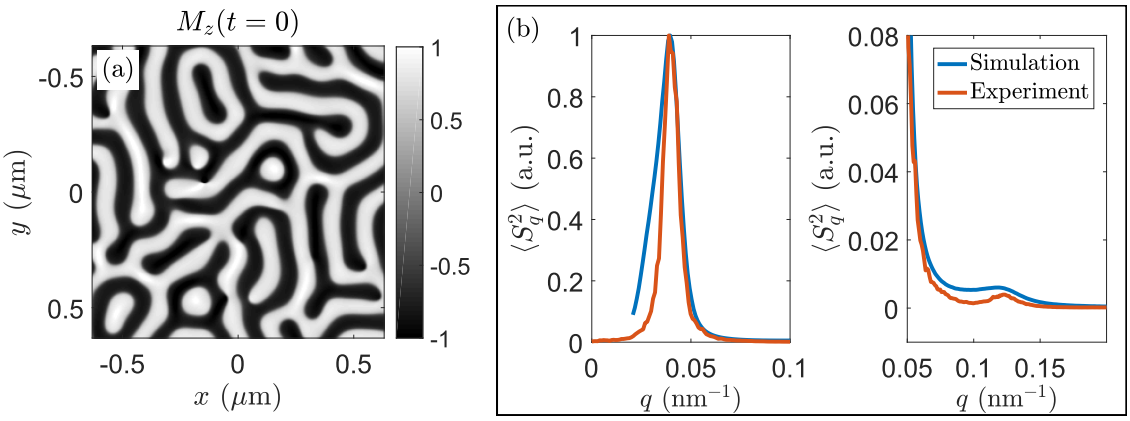

Figure 6.9: (a) Part of the simulated domain pattern and (b) comparison of the simulated and experimental scattering intensities for the first (left) and third (right) orders.

magnitudes and positions of the peaks agree well, while the experimental peaks are broader than the simulated ones. The cause for the latter is the fact that the probed area in the experiment was $\sim 100 \times 100$ μm, while the simulation window was only $\sim 5 \times 5$ μm. For perfectly regular domains, increasing the width of the window would lead to a narrowing of the scattering peaks. However, because in the FeCo/Ni sample domains are stochastic, broader areas show more domain variability and thus broaden the scattering peaks. Simulating a larger area is computationally prohibitive, and for that reason, given that the agreement between the RMS intensities is satisfactory, I use the simulated domain pattern in Fig. 6.9(a). Caution must be exercised in order not to over-interpret the results of the reconstruction procedure due to the discrepancies between the simulated and experimental scattering intensities mentioned above.

The base assumption underlying the method of reconstructing laser-induced changes in magnetic domains is that, at any given time t, the profile $M_z(x, y, t)$ can be represented by a convolution

of the original magnetization profile $M_z(x, y, t = 0)$ with a spatial filtering kernel $G(x, y, t)$

$$M_z(x, y, t) = G(x, y, t) \otimes M_z(x, y, t = 0). \tag{6.22}$$

This assumption is valid if there are no new spectral components in the Fourier spectrum of M_z at time t compared to $t = 0$ ps. Fig. 6.6 clearly demonstrates that this is indeed the case: none of the values in the figure exceed unity, and thus a Fourier spectrum at any time is just a modified original Fourier spectrum. Note that eq. (6.22) does not require a linear response of the magnetization to an optical pump in the time domain. Since the RMS intensity is related to M_z via a Fourier transform as $S_q^2 = |\mathcal{F}\{M_z\}|^2$, from the convolution theorem and eq. (6.22), it follows that the RMS intensity at time t can be expressed as a product of the unperturbed RMS intensity and a squared Fourier transform of $G(x, y, t)$

$$S_q^2(t) = \left|g_q^2(t)\right| \cdot S_q^2(t = 0), \tag{6.23}$$

where $g_q(t) = \mathcal{F}\{G(x, y, t)\}$. Eq. (6.23) can be solved to find the spatial filter in reciprocal space

$$|g_q(t)| = \sqrt{S_q^2(t)/S_q^2(t = 0)}. \tag{6.24}$$

Because of the azimuthal symmetry, eq. (6.24) holds for the azimuthal averages as well. Thus $|g_q(t)|$ is simply equal to the time-resolved RMS data set normalized by the unperturbed RMS intensity, and the quantity shown in Fig. 6.6(c) is equal to $|g_q|^2(t)$. In practice, I obtain $g_q(t)$ by fitting the square root of the normalized RMS data with a smoothing spline and extrapolating to higher q-vectors with a constant value equal to the average demagnetization at a given time step. This is illustrated in Fig. 6.10, where $g_q(t = 1.6$ ps$)$ is shown at the time of both maximum demagnetization and maximum shift in the peak positions. g_q is then rotated around $q = 0$ nm^{-1} to produce a rotationally symmetric two-dimensional Fourier filter.

In the most general case, g_q is complex and thus its phase would be lost in eq. (6.24). However, here, g_q is purely real. This is because the spatial filtering kernel $G(x, y, t)$ is even and real, and, therefore, its Fourier transform g_q is also real. The even parity of $G(x, y, t)$ follows from its azimuthal symmetry which requires that $G(x, y, t) = G(-x, -y, t)$. The azimuthal symmetry, in

turn, is based on an assumption that laser-induced changes in the magnetization profile are driven by an isotropic process because, for a disordered domain network, there should not be any preferred direction. The real-valuedness of $G(x, y, t)$ follows from the real-valuedness of the magnetization profile $M_z(x, y, t)$. Hence, as a Fourier transform of a real and even function, g_q is real. It is also positive. If g_q became negative for certain times the XMCD signal in Fig. 6.7(c) would switch sign. Such a reversal of the magnetization was not observed. If g_q crossed zero at certain q's, g_q^2 would be equal to zero at those q's. However, g_q^2 is always positive, according to Fig. 6.6(c). Therefore, g_q is real and positive, which means that its phase is zero, and that $g_q = |g_q|$.

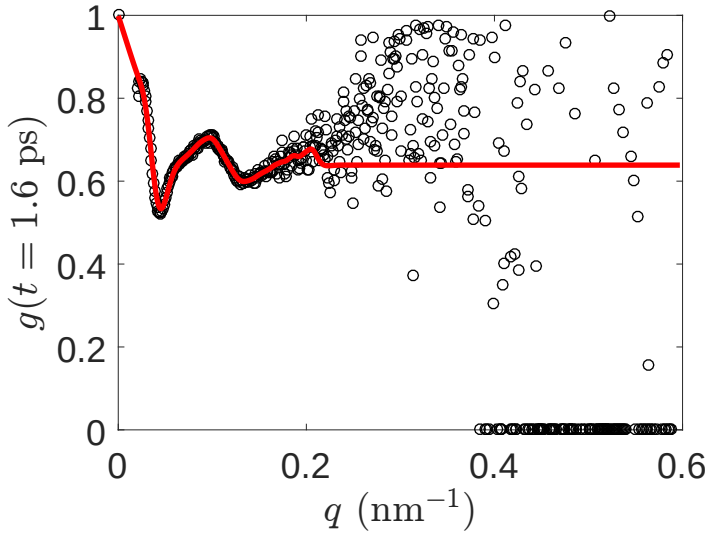

Figure 6.10: Spatial filter $g_q(t = 1.6$ ps) (red) is fitted to the data (black) with a smoothing spline. A constant value is extrapolated to high q's.

With the simulated magnetization profile $M_z(x, y, t = 0)$ and the experimentally measured spatial filter $g_q(t)$, an excited domain pattern at time t can now be found from eqs. (6.22) and (6.23) as

$$M_z(x, y, t) = \mathcal{F}^{-1}\left\{g_q(t)\mathcal{F}\left\{M_z(x, y, t = 0)\right\}\right\}. \tag{6.25}$$

At each time t, I apply eq. (6.25) and thus follow the evolution of an excited domain pattern in real-space. Fig. 6.11 shows the original simulated unperturbed domain pattern (panel (a)) and

snapshots of the relative changes to this pattern at the time of maximum demagnetization (and maximum RMS peak position shifts) of 1.6 ps (panel(b)), and at the longest time step of 20 ps (panel (d)). Fig. 6.11(c) shows the lineouts of the domain profiles along the red line in Fig. 6.11(a) at 0 ps, 1.6 ps and 20 ps.

The reconstructed domain pattern exhibits several distinct features

(1) The demagnetization process is spatially non-uniform: smaller domains and domain ends demagnetize stronger

(2) This feature-dependent asymmetric quenching causes a perceived motion of domain walls by shifting the magnetization zero-crossings. In the two-dimensional images (b) and (d) in Fig. 6.11, it is manifested as sharp color transitions from red to blue at the domain walls. In Fig. 6.11(c), the zero-crossing of the orange and yellow curves at around -0.27 μm is shifted by 2.6 nm to the right relative to the unperturbed blue curve.

(3) The domain walls themselves demagnetize less than the centers of domains.

(4) At long times, the magnetization profile becomes smoother as evidenced by the recovery of the magnetization at the domain centers of the yellow curve in Fig. 6.11(c).

To finalize the discussion of the reconstruction of laser-induced changes, I repeat the reconstruction procedure with a Gaussian spatial filter based only on the first order scattering ring in order to see the effect of the data at higher q-vectors on the reconstruction and directly compare the results with Ref. [205]. Fig. 6.12 shows both, a Gaussian fit for the filter at 1.6 ps (panel (a)) and changes to the original domain pattern that were reconstructed using this filter.

A comparison of Fig. 6.12(b) and Fig. 6.11(b) reveals that if the high q data are removed, the demagnetization process remains spatially non-uniform, but the domain walls are quenched much stronger than the domain centers. This is in agreement with Ref. [205], but contradicts the result of this experiment. Thus, discarding scattering data at high q's does not allow one to capture the persistence of domain walls and their motion in the course of ultrafast demagnetization.

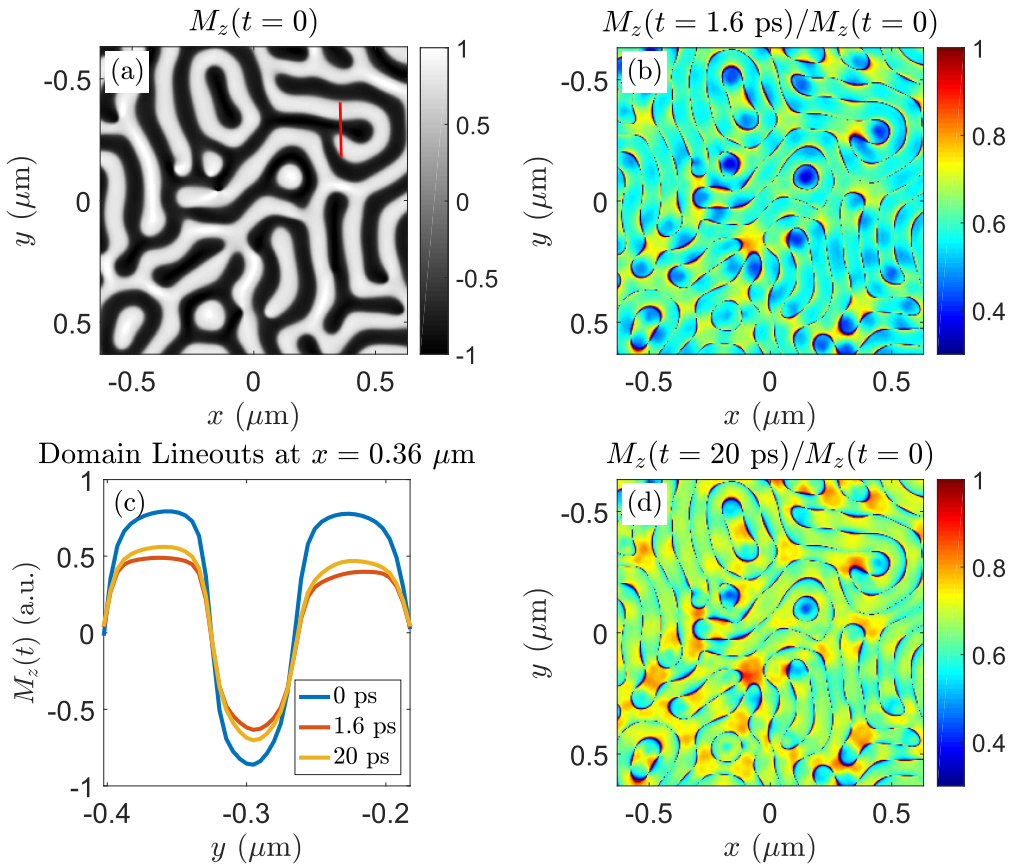

Figure 6.11: Laser-induced evolution of magnetic domains: (a) original domain pattern; changes in the domain pattern at (b) $t = 1.6$ ps (the time of maximum demagnetization and maximum peak shifts) and (d) 20 ps after the pump pulse; (c) lineouts of domain profiles at various times along the red line in (a).

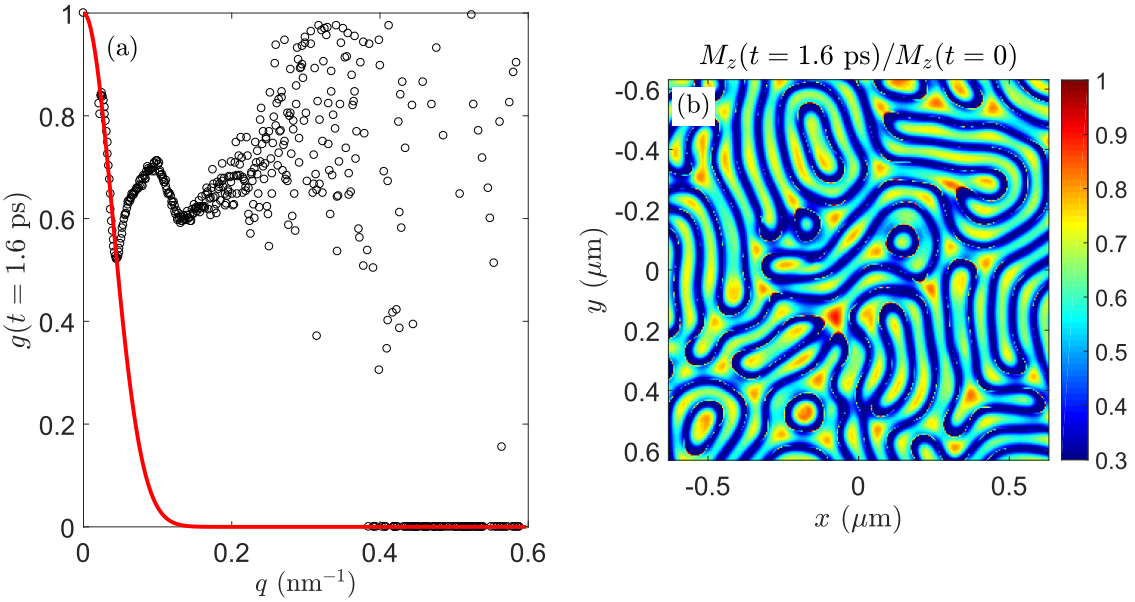

Figure 6.12: Laser-induced changes in domains with a Gaussian spatial filter according to Ref. [205]: (a) Gaussian fit to the filter; (b) Changes in the domains reconstructed with the filter in (a).

6.7 Spin transport in a laser-excited domain network

To explain the features observed in the spatially-resolved magnetization dynamics, namely, the non-uniformity of the demagnetization process, the smaller quenching of domain walls and their motion, I develop an effective model that describes two interacting spin populations: one is a cold , i.e., below the Fermi level, and stationary ground-state population $S_{cold}(x, y)$, and the other is an excited spin population $S_{hot}(x, y)$, which is hot, i.e., above the Fermi level, and mobile. The model is illustrated in Fig. 6.13. The two populations interact with one another because the cold

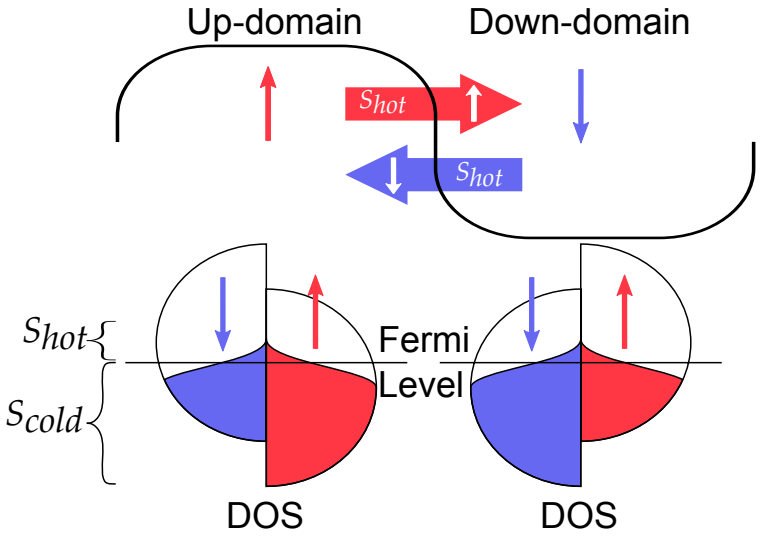

Figure 6.13: Schematic of the spin transport model.

electrons are promoted above the Fermi level by the laser pump, and the hot electrons cool down and eventually decay. Additionally, the hot electrons can move to reduce a magnetization gradient. Mathematically, the dynamics of the two spin populations are described by the following coupled equations

$$\begin{aligned}
\frac{\partial S_{cold}(x,y,t)}{\partial t} &= -\gamma(t) S_{cold}(x,y,t) + \beta(t) S_{hot}(x,y,t), \\
\frac{\partial S_{hot}(x,y,t)}{\partial t} &= \gamma(t) S_{cold}(x,y,t) - \beta(t) S_{hot}(x,y,t) + \vec{\nabla}\left(D(x,y,t)\vec{\nabla} S_{hot}(x,y,t)\right), \\
M_z(x,y,t) &= S_{cold}(x,y,t) + S_{hot}(x,y,t),
\end{aligned} \tag{6.26}$$

where $\gamma(t)$ is the rate of generation of hot electrons, $\beta(t)$ is the rate of their relaxation, the diffusion coefficient $D(x, y, t)$ determines the transport properties of hot electrons, and $M_z(x, y, t)$ is the total transverse profiles of the z-component of the magnetization.

The parameters γ, β and D are phenomenological, but they can have a microscopic origin. For example, β can be viewed as an ensemble-averaged decay rate of electrons above the Fermi level

$$\beta = \frac{1}{\int_{-\infty}^{E_F} \tau(\epsilon) g(\epsilon) f(\epsilon, T) d\epsilon}, \tag{6.27}$$

where $\tau(\epsilon)$ is the lifetime of excited electrons [217], and $g(\epsilon)$ and $f(\epsilon)$ are the density of states and the non-equilibrium electron distribution function, respectively.

The diffusion coefficient $D(x, y, t)$ is an effective parameter, which, similarly to eq. (6.27), is also an ensemble average of the hot spin population. The underlying processes of spin transport might not necessarily be diffusive, and might evolve from ballistic transport at early times after the laser pump to diffusive transport at longer times, according to Ref. [155], which refers to such transient evolution as the superdiffusion of spins. Note that this is different from the standard definition of superdiffusion, where the particle displacement $\Delta x \propto t^{p>1}$ [218]. However, since the former nomenclature has become a standard convention in the field of ultrafast magnetism, I shall refer to the transient evolution from ballistic to diffusive transport as superdiffusive spin transport. In the spin transport model described by eqs. (6.26), the superdiffusion can effectively be described through the time dependence of D.

The spin transport model presented here requires that the polarization of spin currents is preserved over hundreds of nm. Although such lengths exceed the mean free path of hot electrons, efficient spin-polarized currents mediated by hot electrons through up to 300 nm thick Cu films have been observed in ultrafast experiments [219, 220].

The results of applying eqs. (6.26) to the domain pattern in Fig. 6.11(a) are shown in Fig. 6.14. The parameter values used in the simulations were $\beta = 2.5$ ps^{-1}, γ was time-dependent $\gamma(t) = (1 - \exp(-t/\tau))10^2$ ps^{-1}, where $\tau = 100$ fs, and the diffusion coefficient D in Fig. 6.14(a)

was higher for the domains than for the domain walls $D(x,y) = 2 \cdot 10^4(0.15 + 0.85M_z^2(x,y,t = 0))$ nm^2/ps whereas in Fig. 6.14(b) it was constant $D = 10^4$ nm^2/ps. Note that the values of the parameters were chosen with the goal of reproducing the extracted changes in the domain pattern in Fig. 6.11 and are derived neither from first principles nor from a rigorous fitting procedure, so their uniqueness cannot be guaranteed. Nonetheless, the simulations do capture the main features of the experimentally extracted dynamic domain patterns and clearly demonstrate that the observed laser induced changes in the magnetization profile are driven by spin transport.

Fig. 6.14(a) simulated with a varying diffusion coefficient D agrees well with the extracted changes in the domain pattern in Fig. 6.11(b), while the result of the simulation with a constant D in Fig. 6.14(b) is in good agreement with Fig. 6.12 obtained by neglecting scattering data at high q-vectors. This leads to a conclusion that the smaller quenching of the magnetization at the domain walls is caused by a dependence of the spin transport properties on the local magnetization vector, which reduces the spin-polarized flux at the domain boundaries. The lineouts in Fig. 6.14(c) illustrate this point further. The orange curve, which corresponds to the simulation with a magnetization-dependent D, exhibits sharper domain walls, albeit not as sharp as in Fig. 6.11(c), and a clear shift of the domain wall at -0.27 μm to the right, in good agreement with the experimental domain reconstructions. For a constant D, the broadening of the domain walls is too strong.

A comparison in Fig. 6.14(d) of the azimuthally averaged scattering intensities corresponding to the simulations with a magnetization-dependent and constant D with the scattering intensity of the original domain pattern reveals that, in both cases, there is a shift of the first order peak (left panel) towards lower q's, in agreement with the experimental data in Fig. 6.7(b). However, the third order peak (right panel) disappears when D is assumed to be constant. For the magnetization-dependent D, the third order peak persists, again, in agreement with the experimental data, albeit with a somewhat decreased magnitude, and, like in the experiment, it is shifted relative to the blue curve at 0 ps. A small reduction of the simulated third order peak suggests that the dependence of the diffusion coefficient on the magnetization might be more complex than what is assumed here.

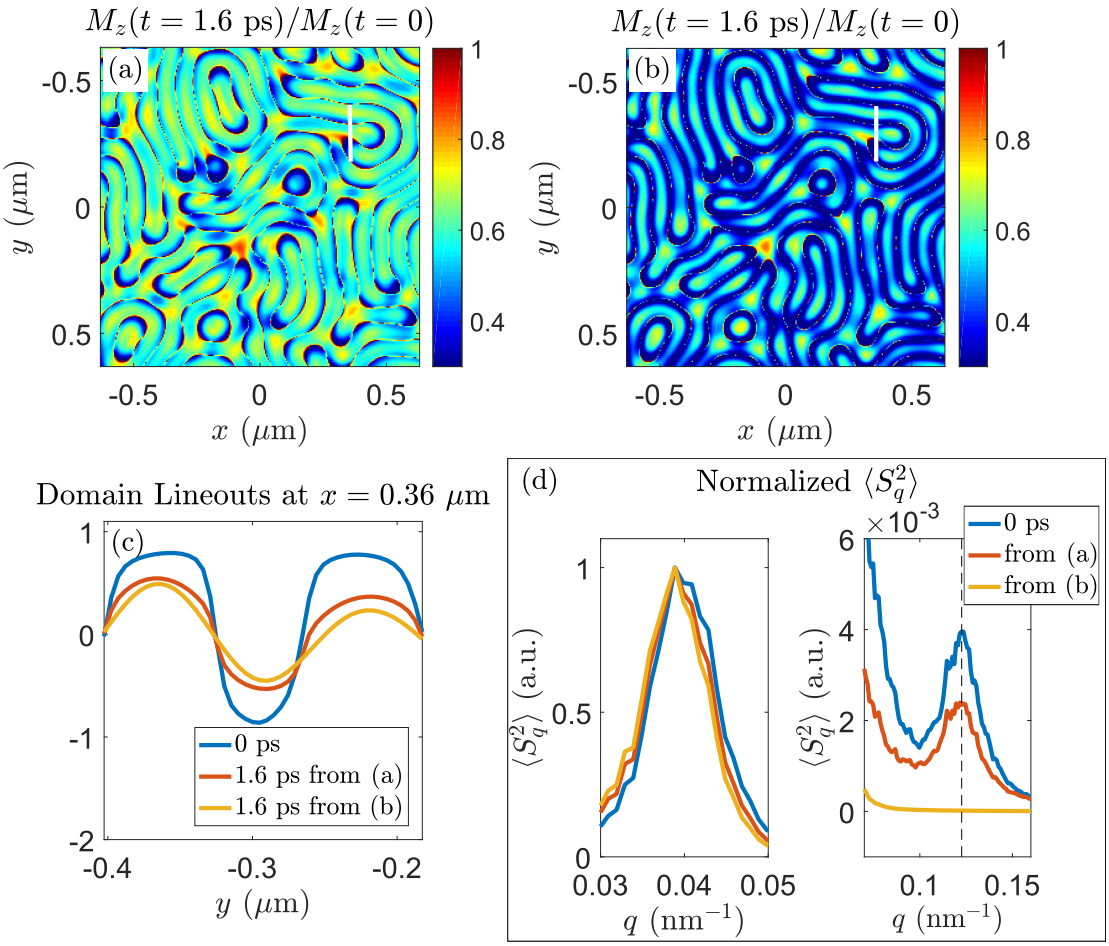

Figure 6.14: Laser-indeced changes to the ground-state of a domain pattern (Fig. 6.11(a)) simulated using eqs. (6.26) with (a) a magnetization dependent diffusion coefficient $D = 2 \cdot 10^4(0.15 + 0.85M_z^2(x, y, t = 0))$ nm^2/ps and (b) constant diffusion coefficient $D = 10^4$ nm^2/ps. The white lines in (a) and (b) indicate the paths along which (c) the lineouts of the magnetization profile are taken. (d) is a comparison of the $\langle S_q^2 \rangle$ Fourier spectra of the original domain pattern and calculated for the cases (a) and (b).

Nonetheless, the figure provides clear proof of the dependence of the spin transport properties on the magnetization.

In summary, the simulations in Fig. 6.14 demonstrate that ultrafast spin transport gives rise to the observed non-uniformity of the demagnetization in Fig. 6.11. Because the spin-polarized flux is proportional to the size of a domain boundary $\sim d^2$, where d is the characteristic domain size, and the total number of spins within a domain is proportional to its volume $\sim d^3$, the number of spins leaving the domain per unit time relative to the number of spins contained within the domain scales as $1/d$. Therefore, the smaller the domain the more it demagnetizes, which is why in Fig. 6.11, the magnetization reduction is stronger for smaller domains and domain ends. Such an asymmetry in the demagnetization leads to shifts in zero-crossings of the magnetization, which are perceived as domain wall motions. The persistence of domain walls requires a reduced transport of spins at the walls compared to the domain centers. This could either be an intrinsic property of ultrafast spin transport or it could be related to the behavior of the magnetic anisotropy. The latter is responsible for the slow decay of the magnetization measured at the third order peak in Fig. 6.7, as I show below.

6.8 Effects of temperature gradients on domain wall dynamics

The thickness of the CoFe/Ni magnetic film in Fig. 6.2 was 40 nm. Given that the absorption length of the pump at 800 nm in Ni is ∼13 nm, one could expect a significant gradient of laser excitation throughout the film. Indeed, this is the case for the sample considered here, as can be seen from Fig. 6.15. The heat source in the figure was computed as

$$S = -dF_{abs}(z)/dz,$$

where the absorbed fluence $F_{abs}(z)$ of the infrared laser pump was calculated using the full multilayer formalism described in Chapter 4. In this section, I explore how this gradient in the pump absorption affects the magnetization dynamics.

I start with the three-temperature model (3TM) proposed in the 1996 pioneering work on ul-

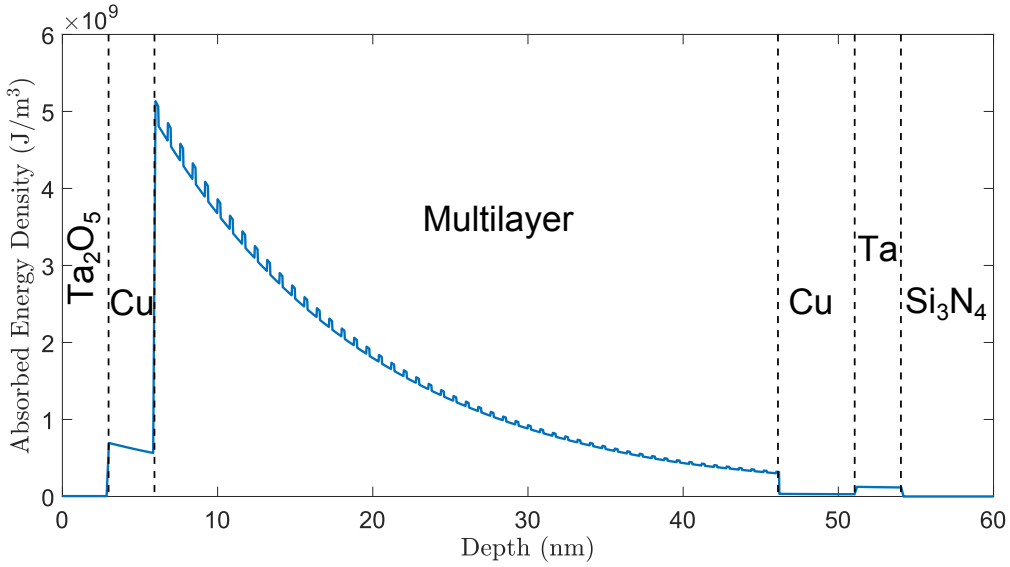

Figure 6.15: Depth gradient of the IR laser excitation in the CoFe/Ni multilayer in Fig. 6.2 for an incident pump fluence of 26.7 mJ/cm^2.

trafast magnetization dynamics [57]. The model consists of three coupled thermodynamic equations that describe the interacting electron, lattice, and spin energy baths

$$\begin{aligned} C_e(T_e)\frac{\partial T_e}{\partial t} &= \vec{\nabla}\cdot\left(\kappa_e(T_e,T_l)\vec{\nabla}T_e\right) + G_{el}(T_e)(T_l - T_e) + G_{el}(T_s - T_e) + S(z,t), \\ C_l(T_l)\frac{\partial T_l}{\partial t} &= \vec{\nabla}\cdot\left(\kappa_l(T_e,T_l)\vec{\nabla}T_l\right) + G_{el}(T_e)(T_e - T_l) + G_{ls}(T_s - T_l), \\ C_s(T_s)\frac{\partial T_s}{\partial t} &= G_{es}(T_e - T_s) + G_{ls}(T_l - T_s), \end{aligned} \tag{6.28}$$

where indices e, l, and s correspond to the electron, lattice, and spin systems; T_x is the temperature of the respective system, C_x is the specific heat, κ_x is the thermal conductivity, and G_{ij} are the coupling parameters between the electron and lattice, electron and spin, and lattice and spin energy baths. The source term in first equation in (6.28) describes the direct absorption of the pump pulse by the electron system. The details regarding the material parameters used in the 3TM simulations can be found in Appendix C.

The 3TM is fitted to the experimental XMCD signal in Fig. 6.7(c) by converting the spin temperature T_s to the magnetization using the temperature dependence of the magnetization of the sample measured with a vibrating-sample magnetometer (VSM) (see Fig. 6.16).

6.8.1 Electron, lattice, and spin temperatures

The electron, lattice, and spin temperatures for the best fit of the 3TM to the experimental XMCD data are shown in Fig. 6.17, and the corresponding calculated depth profile of the magnetization, as well as its depth average, are shown in Fig. 6.18

While the equilibrium in the electron temperature is established quickly throughout the thickness of the sample (see Fig. 6.17(a)) due to a high electron thermal conductivity κ_e, the gradients in the lattice and spin temperatures persist out to longer times. The thermal conductivity of the latter two is negligibly small (see Appendix C) and thus the equilibriation of the temperature distribution of the lattice and spin systems throughout the sample is mediated by electrons. For the case of the lattice, for example, at early times, the hot electrons at the top portion of the sample strongly couple their energy to phonons and also diffuse downward into the cooler bottom

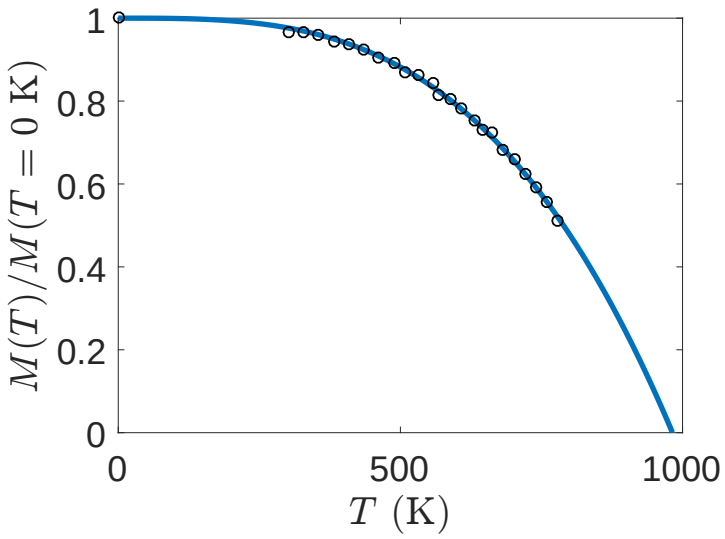

Figure 6.16: Temperature-dependent magnetization of the FeCo/Ni multilayer. The experimental data are represented by black circles, and the blue curve is a fit with $M(T) = 1 - (T/T_C)^l$ (T_C = 982.2 K and $l = 3.166$).

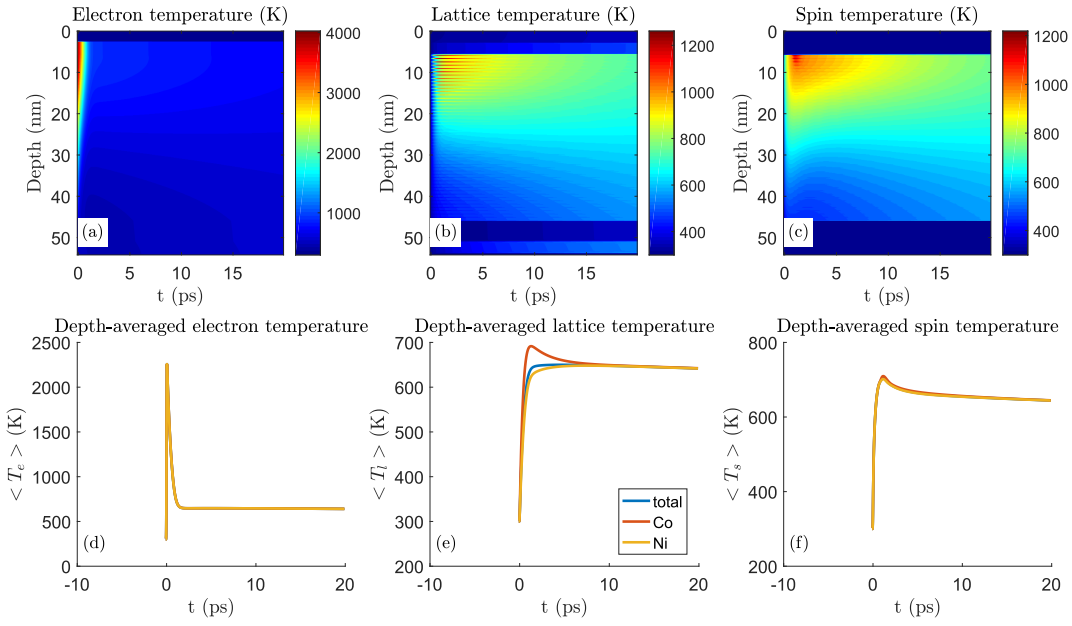

Figure 6.17: Depth-dependent (a)-(c) and depth-averaged (d)-(f) temperatures of the (a), (d) electron, (b), (e) lattice, and (c), (f) spin baths. The total averages as well as separate ones for the Ni and Co layers are shown in (d)-(f).

portion of the film where they again transfer some of their energy to the lattice. Even if the electrons and the lattice are in thermal equilibrium locally, any gradient in the lattice temperature will manifest itself as a gradient in the electron temperature through the electron-lattice coupling parameter G_{el}. The cycle of coupling-diffusion-coupling will thus continue until a full thermal equilibrium is reached. For the spins, the situation is similar. These temperature gradients result in a magnetization gradient shown in Fig. 6.18

Such a non-uniform simulated demagnetization suggests that, for a domain pattern, the dynamics could be different at different depths. It is important to understand that the scattering data provide depth-averaged information, as I show below.

6.9 Propagation of X-rays through a thick sample

Because the wavelength of the X-ray probe at 1.45 nm is much smaller than the thickness of the magnetic multilayer film of 40 nm, strictly speaking, the propagation of X-rays through such a film should be treated as a three-dimensional problem, and a gradient in the magnetization can be expected to affect the overall scattering intensity. In general terms, the propagation of an electromagnetic wave through a non-uniform medium with a spatially varying refractive index $n(x, y, z)$ is described by the Helmholtz equation [221]

$$\nabla^2 E + k_0^2 n^2(x, y, z) E = 0, \tag{6.29}$$

where E is the electric field envelope, which excludes the fast oscillating part $e^{i\omega t}$, and k_0 is the wavenumber in vacuum. For an arbitrary refractive index $n(x, y, z)$, this equation can be solved numerically using the split-step method [222] to obtain an ESW out of a thick sample. The split-step method involves subdividing the sample into thin layers, as shown in Fig. 6.19; each layer modifies the phase and the amplitude of the propagating electric field, according to the refractive index in that layer $n(x, y, z_i)$, where i is the index of the layer. Propagation in between the layers is computed by applying a free-space spatial filter in Fourier space [222]. However, for a weakly scattering magnetic domain sample, the method can be simplified. Because the probability of a

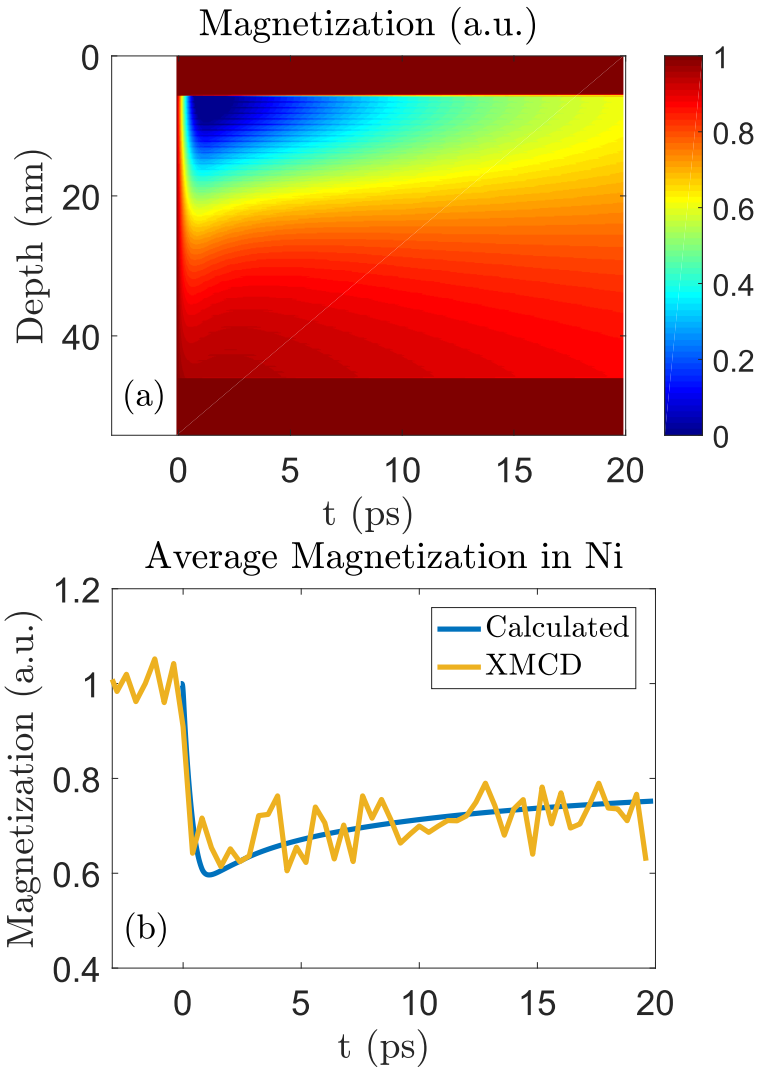

Figure 6.18: Calculated (a) depth-dependent and (b) depth-averaged time-dependent magnetization. The average calculated magnetization agrees well with the experimental XMCD trace.

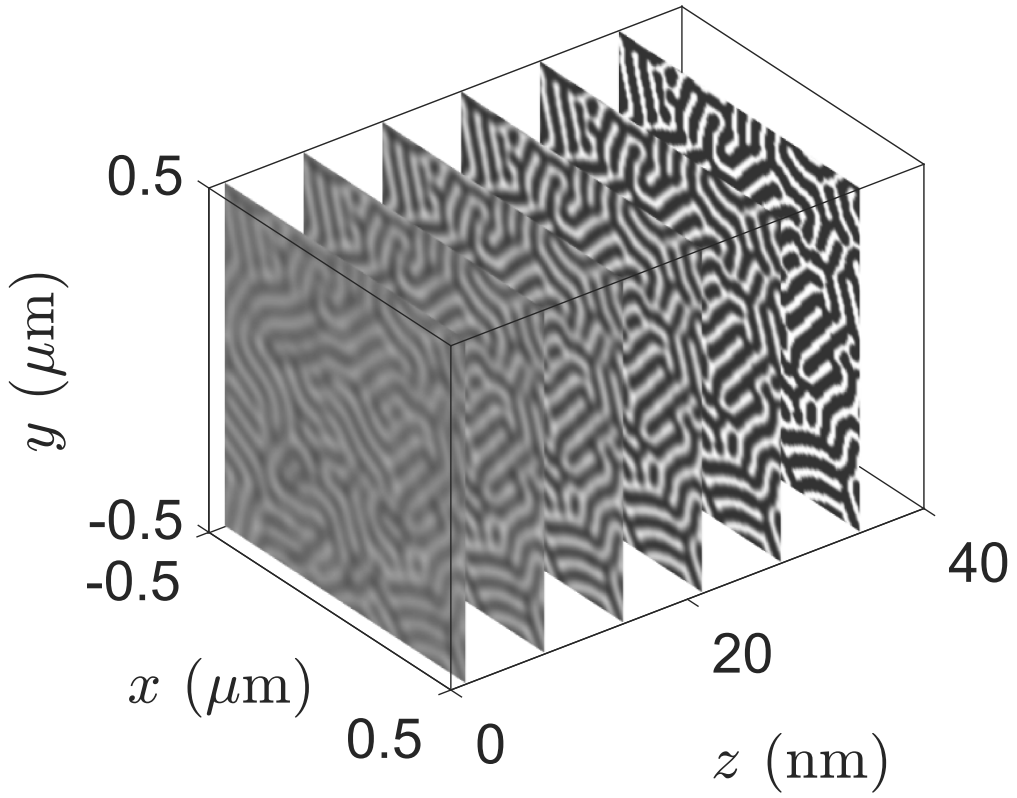

Figure 6.19: Subdivision of a thick domain sample into layers. The transverse magnetization profile varies with depth.

scattering event is small compared to non-magnetic scattering, the likelihood that a photon can scatter twice as it travels through the sample is negligible. As such, the ESW can be written as a sum of the waves coming from individual layers

$$ESW = \sum_{i}^{N} s(x, y, z_i), \tag{6.30}$$

where N is the total number of layers, and s is a spatially-dependent magnetic profile as defined in eq. (6.2). It should be noted that the phase and amplitude of each $s(x, y, z_i)$ is determined only by the transverse variations of the magnetization in layer i. The total accumulated phase and attenuation for each layer do not depend on the position of the layer z_i and are determined by the total thickness of the film and its composition. In the detector plane, the field S_q is a Fourier transform of the ESW

$$S_q(q_x, q_y) = \mathcal{F}\left\{\sum_{i}^{N} s(x, y, z_i)\right\} = \sum_{i}^{N} \mathcal{F}\left\{s(x, y, z_i)\right\} = \sum_{i}^{N} S_q^{(i)}, \tag{6.31}$$

and is equal to the sum of Fourier transforms of the scattered waves coming from individual layers. Assuming that the transverse magnetization profile is the same for all z_i at $t = 0$ ps, eq. (6.23) can be applied to each layer

$$S_q^{(i)}(t) = g_q^{(i)}(t)\Delta S_q(t = 0), \tag{6.32}$$

where $\Delta S_q(t = 0)$ corresponds to the field in the detector plane scattered from a single layer at $t = 0$ ps. From eqs. (6.32), (6.31), and (6.24), an expression for the net measured spatial filter can be derived

$$g_q^{\Sigma}(t) = \sqrt{\frac{\left|\sum_i^N g_q^{(i)}(t)\Delta S_q(t = 0)\right|^{2^2}}{\left|\sum_i^N \Delta S_q(t = 0)\right|}}. \tag{6.33}$$

The factors $|\Delta S_q(t = 0)|^2$ in the numerator and denominator cancel one another, and eq. (6.33) is simplified to

$$g_q^{\Sigma}(t) = \frac{1}{N}\sum_{i}^{N} g_q^{(i)}(t). \tag{6.34}$$

Therefore, for a thick sample, the measured spatial filter in reciprocal space $g_q^{\Sigma}(t)$, i.e., a root of the RMS intensity at time t normalized by the static RMS intensity, is equal to the depth-average of

the spatial filters for the layers at different depths z_i. Since the scattering amplitude is proportional to the magnitude of the magnetization component M_z at a particular depth, with a magnetization gradient, layers that are demagnetized stronger would contribute less to the detected RMS intensity.

6.9.1 Evolution of the magnetic anisotropy

I now consider the effect of the magnetic anisotropy K_u. Its temperature dependence measured with a VSM is shown in Fig. 6.20. Assuming that the anisotropy energy depends on the

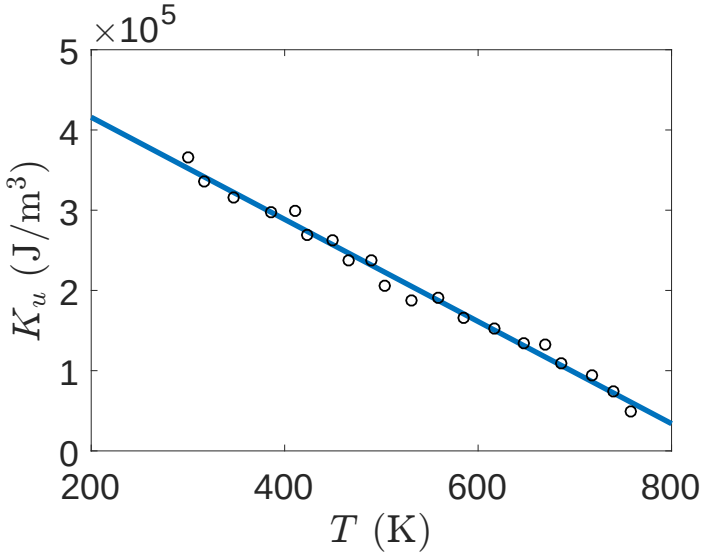

Figure 6.20: Experimental temperature dependence of the magnetic anisotropy K_u for the FeCo/Ni sample.

lattice temperature, the time-dependent depth profile of K_u can be found by use of the calculated lattice temperature in Fig. 6.17. The anisotropy energy determines the domain wall width [8]

$$d = \pi\sqrt{\frac{A}{K_u}}, \tag{6.35}$$

where A is the exchange stiffness. According to Ref. [147], $A(T) \propto M^2(T)$. Hence, the time-dependent domain wall width z-profile can be found from eq. (6.35) using the lattice temperature in Fig. 6.17(b), the temperature dependence of K_u in Fig. 6.20, and the transient magnetization profile in Fig. 6.18. A proper calculation of the depth-averaged domain wall width needs to take

into account account the magnetization gradient because, as mentioned above, film layers that are demagnetized stronger contribute less to the scattering signal. For that reason, the RMS data should be expected to be more sensitive to the colder bottom layers of the sample. I, therefore, define the average domain wall width as

$$\langle d \rangle (t) = \frac{\int_0^L M(z,t) d(z,t) dz}{\int_0^L M(z,t) dz} \tag{6.36}$$

and plot it from 8 to 20 ps in Fig. 6.21. The result in Fig. 6.21 is rather qualitative and has to be

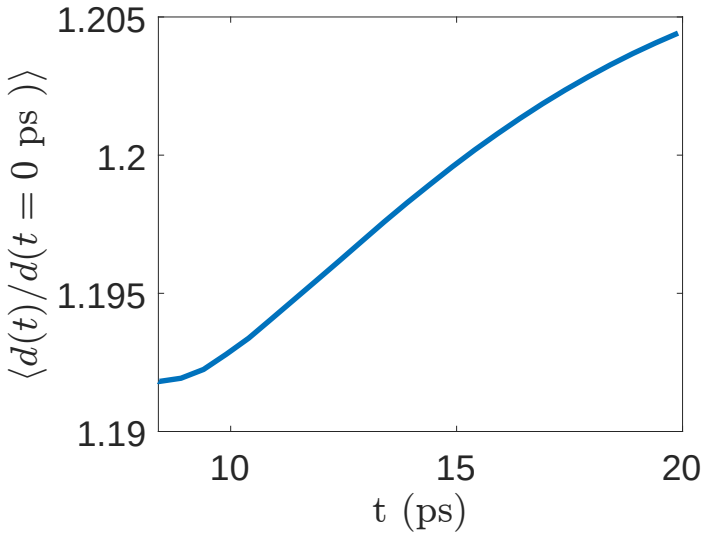

Figure 6.21: Calculated time-dependent domain wall width changes relative to the static case.

interpreted with caution because the true temperature dependence of the exchange stiffness for the sample considered here is unknown. In addition, it is not entirely clear whether the magnetization and temperature gradients can be converted directly into a domain wall width gradient using eq. (6.35) which is applicable in thermal equilibrium (I only used the data at times greater than 8 ps for that reason). Nonetheless, even with such a qualitative approach, there is evidence of a slow increase of the domain wall width with time. This suggests that the observed slow decrease of the magnitude of the third order in Fig. 6.7(c) could be caused by an increase in the domain wall width related to the thermal diffusion throughout the thickness of the sample.

Further investigation of this phenomenon is needed, and additional insight can be gained from both rigorous micromagnetic simulations as well as time-resolved experiments, which employ techniques, such as X-ray vector nanotomography, capable of imaging magnetic structures in three dimensions [223].

6.10 Conclusions

In this chapter, experimental results on time-resolved resonant magnetic scattering of soft X-rays from a magnetic domain sample were presented. The scattering data were collected at high q-vectors, which, in contrast with previous work, allowed an extraction of the magnetization dynamics of small spatial features, such as domain walls. Spatially-dependent demagnetization can be represented as a convolution of the static domain pattern with a time dependent spatial filter, and such filter can be extracted from the scattering data. By applying this filter to a simulated domain pattern, spatially-resolved transient changes in the transverse magnetization profile were reconstructed. The reconstructions showed that the demagnetization process was spatially non-uniform with stronger quenching of smaller domains and domain ends. In addition, the demagnetization of domain walls was found to be surprisingly weak, and their broadening occurred only on long timescales. The spatial non-uniformity of the demagnetization and the persistence of domain walls was explained with a phenomenological spin transport model that included a reduced transport at the walls, thus confirming that the laser induced demagnetization process in a domain network is primarily driven by spin-polarized currents which facilitate a direct exchange of angular momentum between domains of opposite magnetization. The slow broadening of domain walls on long timescales was confirmed by energy transport simulations in combination with simulations of the propagation of X-rays through a thick sample. This broadening was attributed to a slow reduction of the temperature and magnetization gradients—initially caused by a non-uniform absorption of the laser pump—through thermal diffusion. In the future, further insight can be gained from experiments that can capture magnetic structures in three dimensions as well as rigorous simulations.

Chapter 7

Outlook: Towards Time-Resolved Element-Specific Magnetic Microscopy

Magnetic materials exhibit a rich variety of spin textures ranging from macroscopic domains to nanoscale topologically protected magnetic vortices known as skyrmions. Those textures play a very important role because they correspond to the minimum-energy or meta-stable states of a particular material system and, as discussed in Chapter 6, can provide additional dissipation channels, e.g. via spin currents, after the system has been excited by a laser pulse. Thus magnetism and its dynamics are inherently spatially dependent. Most spectroscopic studies overlook this spatial dependence by either magnetically saturating the sample in a specific direction and thus erasing the features or by effectively averaging across them. Yet, an ability to observe magnetism not only with a high temporal but also with a high spatial resolution is critical for its fundamental understanding.

There are multiple techniques that can provide a spatial resolution for studying magnetic materials. With resonant magnetic scattering discussed in Chapters 5 and 6, the spatial information is accessible in reciprocal space. Real-space imaging techniques include Kerr and Faraday microscopy [224, 225], scanning Hall probe [226, 227] and SQUID [228, 229] microscopy, Lorentz microscopy [230], scanning transmission X-ray microscopy [231], photoemission electron microscopy [232, 233, 234], magnetic force microscopy [235, 236], holographic methods [188, 237, 238, 239, 203, 204], and coherent diffractive imaging (CDI) techniques also known as lensless imaging [187, 210, 212, 214, 213, 240, 241, 242, 243]. Detailed reviews of various imaging techniques can be found in Refs. [244] and [230].

An ideal technique for magnetic microscopy would have to have both a high spatial and temporal resolution. These requirements necessitate the use of a small wavelength probe with a short pulse duration. HHG driven EUV and soft X-ray coherent light sources are particularly suited for this purpose. With such sources, magnetic microscopy can be implemented on a tabletop in a laboratory setting. EUV microscopes that rely on re-imaging with Fresnel zone plates [245] are inefficient and suffer from aberrations. Their resolution is limited by the width of the outer ring. Similarly, the resolution of holographic approaches is limited by the size of reference holes, and, due to the small size of the latter, such approaches are also lossy. This is particularly important for weakly scattering objects such as magnetic textures. Lensless imaging techniques are very attractive since they require imaging geometries that are very similar to those used for resonant magnetic scattering and thus can be easily adapted to existing scattering experiments (see Chapters 5 and 6). In addition, their resolution is truly diffraction limited meaning that for a wavelength of $\lambda \sim 20$ nm near the M-edges of the $3d$ ferromagnets the theoretical resolution limit is ~ 10 nm.

CDI has been used for imaging magnetic textures with both synchrotron [246, 247] and HHG sources [187]. A remarkable example is a reconstruction of a three-dimensional magnetization map in a microscopic rod using X-ray vector nanotomography [223]. FELs can also be used for time-resolved magnetic CDI and can provide a high spatial resolution. However, HHG sources have a better temporal resolution and an added advantage of easy access, relative compactness, and comparatively low operation costs. Thus developing an approach for time-resolved CDI magnetic microscopy with an HHG source would be beneficial.

As mentioned above, static CDI has been demonstrated with an HHG source in Ref. [187]. However, this work utilized circularly polarized harmonics, for which the information about the magnetization magnitude and direction is mixed in the reconstructed phase and amplitude, and the method relied on a holographic reconstruction thus making the sample design quite complicated. Below, I demonstrate the feasibility of lensless magnetic imaging with linearly polarized HHG, for which the experimental setup is simpler, and show that the reconstructed amplitude represents the magnitude of the out-of-plane magnetization component, and the phase represents its direction.

The method does not rely on holography and, therefore, no special considerations are required in designing the sample. At the end of this chapter, I also provide an outlook for future work which includes studying antiferromagnets and phase transition materials.

7.1 Principles of lensless imaging

A basic lensless imaging problem is shown in Fig. 5.1. A coherent EUV probe interacts with the object and the scattered electric field forms a diffracted intensity distribution in the CCD plane. Because the detector only measures the intensity, the information about the phase is lost. If the phase were known, however, the electric field from the detector plane could be propagated back to the object, and, with a known probe, the phase and amplitude of the object could be found. Hence, the lensless imaging problem becomes a phase retrieval problem, which can be solved by a number of iterative algorithms. CDI has a lot in common with the phase retrieval problem in crystallography, although the two fields have developed largely independently [248]. Historically, the first optical phase retrieval algorithm was proposed in 1971 and is known as the error reduction algorithm [249]. In this algorithm, the phase is found by iteratively propagating the field between the two planes and setting the amplitude of the field to be equal to the measured amplitudes in both the detector and the object planes at each iteration. The constraint that the solution must satisfy the measured intensities in both planes allows the algorithm to converge. Generally speaking, the solution does not have to be constrained in terms of the measured intensities only; any other set of constraints suited for the problem will also work. The scalar propagation between the object and the detector planes is described by the Helmholtz equation [221]

$$\nabla^2 E(\vec{r}) + k^2 E(\vec{r}) = 0, \tag{7.1}$$

where $k = 2\pi/\lambda$. Assuming that z is the propagation direction, a Fourier transform of (7.1) in the transverse direction reads

$$\left(-|\vec{q}_\perp|^2 + \partial_z^2 + k^2\right) \tilde{E}(\vec{q}_\perp) = 0, \tag{7.2}$$

where $\vec{q}_\perp = k\Delta\vec{r}_\perp/z$ denotes the spatial frequencies in the transverse plane, and $\tilde{E}(\vec{q}_\perp)$ is the Fourier transform of $E(\vec{r})$. In the definition of $\vec{q}_\perp$, I introduced $\Delta\vec{r}_\perp = \vec{r}_\perp - \vec{R}_\perp$, where $\vec{R}_\perp$ is the transverse coordinate in the object plane (see Fig. 7.1 for notations). The solution to eq. (7.2) is

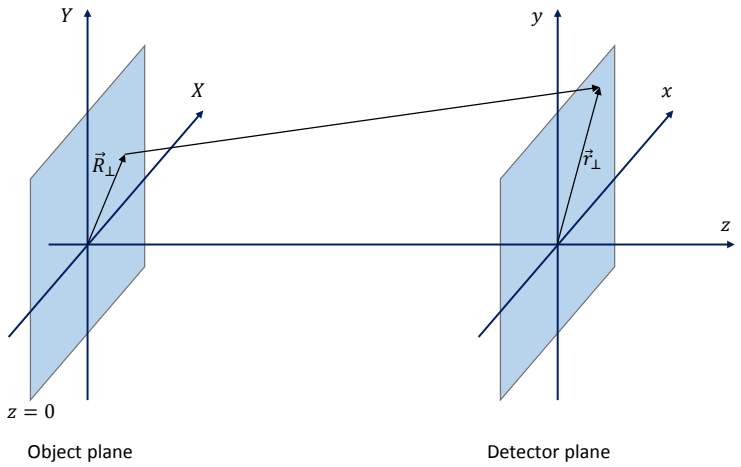

Figure 7.1: Geometry and notations for a diffraction problem.

$$\tilde{E}(\vec{q}_\perp, z) = \tilde{E}(\vec{q}_\perp, z=0)\exp\left(i\sqrt{k^2 - |\vec{q}_\perp|^2}z\right). \tag{7.3}$$

In real-space, the field at the detector is then found as an inverse Fourier transform

$$E(\vec{r}_\perp, z) = \mathcal{F}^{-1}\left\{\tilde{E}(\vec{q}_\perp, z)\right\} = \mathcal{F}^{-1}\left\{\tilde{E}(\vec{q}_\perp, z=0)\exp\left(i\sqrt{k^2 - |\vec{q}_\perp|^2}z\right)\right\}. \tag{7.4}$$

In the paraxial approximation, the diffraction angle is small, and the transverse components of the wavevector are much smaller than the longitudinal component, i.e., $|\vec{q}_\perp| \ll k$. The square root in the exponent can then be Taylor expanded up to a second order, which yields

$$E(\vec{r}_\perp, z) = \mathcal{F}^{-1}\left\{\tilde{E}(\vec{q}_\perp, z=0)\exp\left[ikz\left(1 - \frac{|\vec{q}_\perp|^2}{2k^2}\right)\right]\right\}. \tag{7.5}$$

Eq. (7.5) can be written in terms of a convolution of the field at $z = 0$ with a Fresnel propagation kernel [250, 222]

$$E(\vec{r}_\perp, z) = E(\vec{r}_\perp, z=0) \otimes h(\vec{r}), \tag{7.6}$$

where, using the definition of $\vec{q}_\perp$ above and eq. (7.5), $h(\vec{r})$ is defined as

$$h(\vec{r}) = e^{ikz} e^{\frac{ik}{2z} r_\perp^2}. \tag{7.7}$$

Note that for simplicity, a factor $1/i\lambda z$ present in the Fresnel-Huygens integral is not included in the definition of $h(\vec{r})$. For a more rigorous derivation see Refs. [250] and [222]. The convolution, up to a phase factor, can be written explicitly as

$$E(\vec{r}_\perp, z) = \iint E(\vec{R}_\perp, z=0) e^{i\frac{k(\vec{r}_\perp - \vec{R}_\perp)^2}{2z}} d^2\vec{R}_\perp, \tag{7.8}$$

where the integration is carried out over the entire spatial extent of the object, and the e^{ikz} phase factor, again, has been omitted. Expanding the square under the exponent in eq. (7.8) yields

$$E(\vec{r}_\perp, z) = e^{i\frac{kr_\perp^2}{2z}} \iint E(\vec{R}_\perp, z=0) e^{-i\frac{k\vec{r}_\perp \cdot \vec{R}_\perp}{z}} e^{i\frac{kR_\perp^2}{2z}} d^2\vec{R}_\perp. \tag{7.9}$$

If $z \gg a^2/\lambda$, which is known as the Fraunhofer approximation, where a is the characteristic size of an object, it holds that $e^{i\frac{kR_\perp^2}{2z}} \approx 1$, and eq. (7.9) simply becomes

$$E(\vec{r}_\perp, z) \propto \mathcal{F}\left\{E(\vec{R}_\perp, z=0)\right\}, \tag{7.10}$$

where the phase factor has been omitted. Eq. (7.10) has an important consequence, i.e., it tells us that the fields at the object and the detector are related via a Fourier transform. This is true if the condition $z \gg a^2/\lambda$ is satisfied. For typical parameters for EUV imaging of $\lambda \approx 20$ nm and $a \approx 10$ μm, $z \gg 5$ mm. In the scattering experiment discussed in Chapter 5, the distance between the sample and the detector was 3.6 cm, which satisfies the Fraunhofer approximation.

Now that the connection between the fields in the two planes has been established, a scheme for a CDI algorithm can be developed (see Fig. 7.2). In this scheme, the algorithm starts with a guess for the phase of the Fourier transform of the object and then interates between Fourier and object spaces. At each iteration, a set of constraints is applied. In Fourier space, the constraint is that the modulus of the Fourier transform of the object $G(\vec{q})$ must be equal to a square root of the measured diffracted intensity. In real space, various constraints are possible. They include [107]

the isolation constraint, the non-negativity constraint, and the overlap constraint for ptychography. Diffraction from magnetic samples leads to different constraints, which are discussed below.

The phase retrieval procedure in Fig. 7.2 guarantees an almost unique solution (up to a translation, reflection, and phase conjugation) in two dimensions as long as the diffraction pattern is oversampled in the Fourier domain [215]. It is a consequence of the Nyquist-Shannon theorem, which states that a continuous signal can be recovered from a discrete dataset if the data are sampled at a rate above a certain frequency, known as the Nyquist frequency [251]. The data is

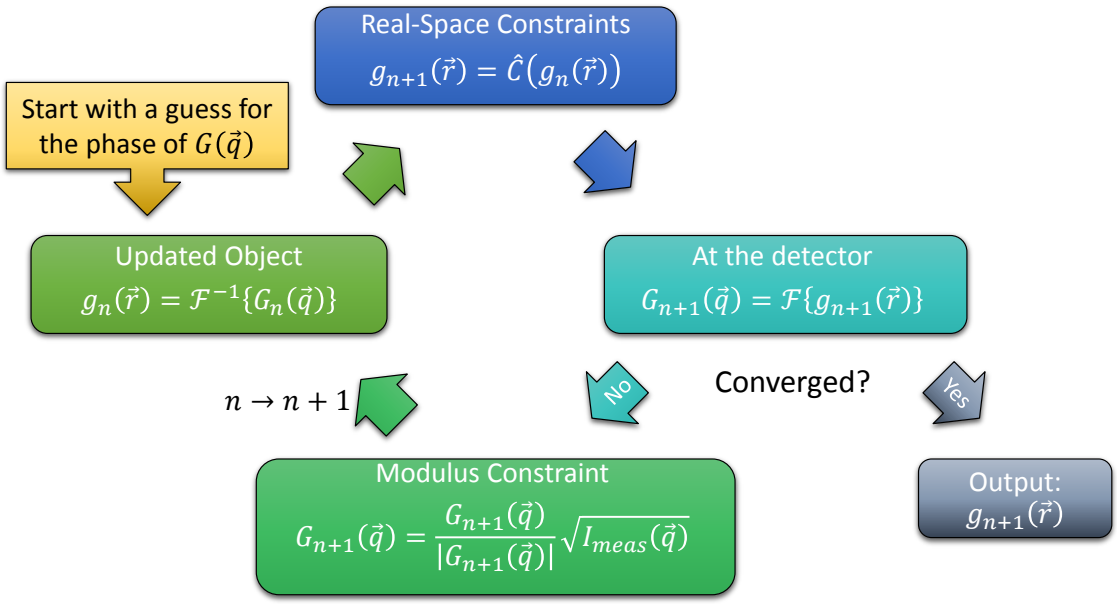

Figure 7.2: CDI algorithm. n is the current iteration number, $g(\vec{r})$ is the complex object, $G(\vec{q})$ is its Fourier transform, I_{meas} is the measured diffraction intensity, and $\hat{C}$ represents a set of real-space constraints.

said to be oversampled if the oversampling ratio $\rho \geq \sqrt{2}$ [215]. The ratio is given by

$$\rho = \frac{\lambda z}{pD}, \tag{7.11}$$

where λ is the wavelength of the probe, z is the distance between the object and the detector, D is the size of the illuminated area of the object, and p is the detector pixel size.

The convergence criterion for the algorithm in Fig. 7.2 is the difference between the modulus of the Fourier transform of the reconstructed object and the measured diffraction amplitude $\sqrt{I_{meas}}$,

for which the metric is the sum squared error $\chi_n^2 = \sum_{\vec{q}} \left(I_{meas}(\vec{q}) - |G_n(\vec{q})|^2 \right)^2$. The iterations are stopped when a specified error tolerance is reached.

Apart from the update condition in Fig. 7.2, there are multiple other ways to update the object at each iteration, which give rise to faster converging CDI algorithms such as the hybrid input-output (HIO) [210] and relaxed averaged alternating reflections (RAAR) [252]. These algorithms rely on a single exposure and are thus well suited for single-shot dynamic imaging of magnetic textures that are non-repeatable, such as magnetic domains, which can nucleate differently each time after being excited by a laser pulse. For static and stroboscopic imaging, where a magnetic texture can be repeated reliably at each time step, a ptychographic phase retrieval, which is a scanning technique that relies on multiple exposures, is preferable due to its superior performance and reliability [242, 253, 254]. In addition, ptychography can reconstruct not only the object, but also the profile of the probe [242]. Repeatable dynamic magnetic textures include magnon waveguides and spintronic logic elements. If magnetic domains are weakly excited, they can also relax to the original configuration and could thus be repeatable. In the following, I briefly outline an approach to ptychography and derive constraints for magnetic samples that are applicable for most CDI algorithms. Using these constraints, I simulate a ptychographic reconstruction of nanoscale magnetic domains.

7.2 Ptychography CDI of magnetic textures with linearly polarized light

Because ptychography is a scanning technique, it can be used for imaging extended objects, which relaxes the requirements on the sample fabrication because microscopic apertures no longer need to be made. An extend ptychographical algorithm (ePIE) [242] does not require an accurate model of the illumination, and would, therefore, be most useful in dealing with actual data, for which the exact illumination is, in general, unknown. In ptychography, a complex object $O(\vec{r})$ is illuminated by a complex probe $P(\vec{r} - \vec{R}_s)$, where the illumination position $\vec{R}_s$ is scanned across the object (the subscript s enumerates the illumination position), and the main constraint in real space ($\hat{C}$ in Fig. 7.2) is an overlap of the illuminated areas at various positions $\vec{R}_s$. An exit surface

wave $g(\vec{r})$ is simply a product of P and O

$$g(\vec{r}) = O(\vec{r})P(\vec{r} - \vec{R}_s). \tag{7.12}$$

One iteration of ePIE involves a loop over all illumination positions, which are addressed in a random order to avoid artifacts associated with the periodicity in the reconstructed object and probe. At each position, the object and the probe are updated separately. The object is updated by dividing out the probe from the ESW and vice versa. The update condition for the object is

$$O_{n+1}(\vec{r}) = O_n(\vec{r}) + \alpha \frac{P_n^*(\vec{r} - \vec{R}_s(n))}{\left|P_n(\vec{r} - \vec{R}_s(n))\right|^2_{max}} \left(g'_n(\vec{r}) - g_n(\vec{r})\right), \tag{7.13}$$

where n is the current iteration number, α is an algorithm feedback parameter (typically, $\alpha = 1$), $g_n(\vec{r})$ is the current guess for the ESW, and $g'_n(\vec{r})$ is an updated guess, calculated according to

$$g'_n(\vec{r}) = \mathcal{F}^{-1}\left\{\sqrt{I_{s(n)}(\vec{q})}\frac{\mathcal{F}\{g_n(\vec{r})\}}{|\mathcal{F}\{g_n(\vec{r})\}|}\right\}, \tag{7.14}$$

where $I_{s(n)}$ is the diffracted intensity measured at the illumination position $\vec{R}_s$. An update for the probe is written similarly to eq. (7.13)

$$P_{n+1}(\vec{r}) = P_n(\vec{r}) + \beta \frac{O_n^*(\vec{r} + \vec{R}_s(n))}{\left|O_n(\vec{r} + \vec{R}_s(n))\right|^2_{max}} \left(g'_n(\vec{r}) - g_n(\vec{r})\right). \tag{7.15}$$

Again, the feedback parameter β is typically set to 1. The overlap constraint is implicitly contained in eqs. (7.13), (7.14), and (7.15). With these update conditions, the flowchart in Fig. 7.2 is modified, and, for the ePIE algorithm, it is shown in Fig 7.3. Next, I discuss real-space constraints that are specific for magnetic imaging and are applicable for ePIE as well as for other CDI algorithms.

7.2.1 Algorithm constraints for magnetic samples

In order to derive the constraints, the interaction of linearly polarized light with a magnetic sample must be considered. A detailed analysis of such interaction was conducted in Chapter 5, and it was found that, at normal incidence, the polarization of the transmitted magnetically scattered light is orthogonal to the polarization of the incident probe beam, while the unscattered light

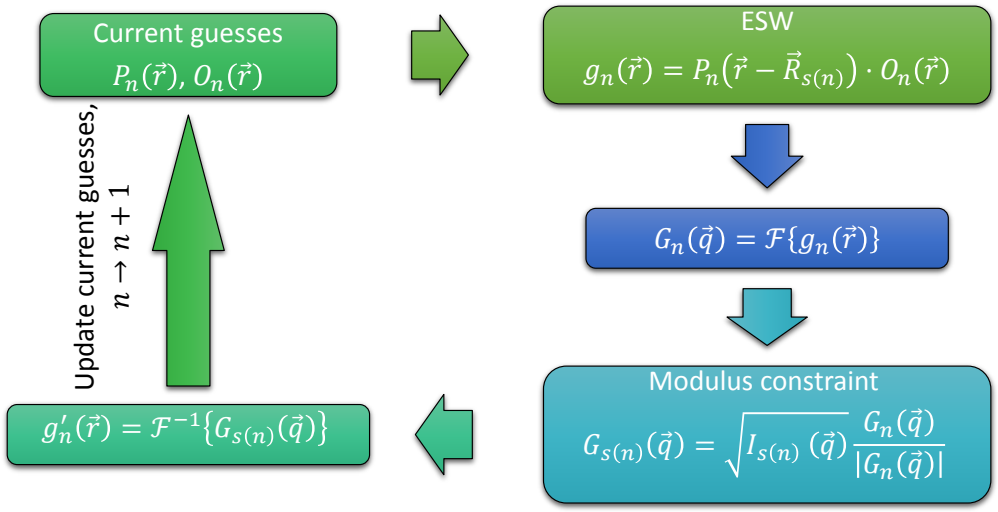

Figure 7.3: Flow of the ePIE algorithm. At $n = 1$, ePIE uses supplied guesses for the object $O(\vec{r})$ and the probe $P(\vec{r})$. All illumination positions $\vec{R}_{s(n)}$ must be iterated over before the algorithm proceeds to the $n + 1$ iteration. For magnetic imaging with linear polarization, an additional real-space constraint must be added.

maintains the original polarization but contains no magnetic information (see eq. (5.12)). The magnetic contrast thus arises due to the Faraday rotation (in combination with XMCD), and, in the first approximation, the amount of rotation is proportional locally to an out-of-plane magnetization component m_z. A larger rotation results in a larger orthogonal, i.e., magnetically scattered, polarization component, and the amplitude of the ESW thus maps the magnitude of $m_z(x, y)$. The direction of the rotation depends on the local sign of m_z. For the two opposite rotations, the magnetically scattered polarization components have opposite signs, which amounts to a π phase shift. This phase shift, therefore, maps the sign of $m_z(x, y)$. These two statements are mathematically expressed as

$$ESW(x, y) = A_0(x, y)\,|m_z(x, y)|\,e^{i\frac{\pi}{2}\left(1+\frac{m_z(x,y)}{|m_z(x,y)|}\right)}, \tag{7.16}$$

where $A_0(x, y)$ is the incident probe. Note that the expression above includes only the magnetically scattered polarization component, which is orthogonal to the incident polarization. In eq. (7.16), the phase only takes the values of 0 and π, which, makes the object purely real. Therefore, a constraint that is specific for magnetic samples probed with linearly polarized light is simply that the object is real

$$O(x, y) = O^*(x, y). \tag{7.17}$$

The fact that the object can be negative seemingly contradicts the non-negativity constraint commonly used in CDI. However, it does not mean that the absorption becomes negative. Rather, it indicates that, due to magnetism, locally, the absorption can be less than its mean value. In addition, according to eq. (7.16), the magnetically scattered ESW has no undiffracted (DC) component, which is a consequence of $m_z(x, y)$ changing sign across the sample. This means that the DC peak has no magnetic information in it and can be disregarded, which is convenient because in an actual experiment, the DC peak has to be blocked due to its much higher intensity compared to the RMS intensity (see the discussion in Chapter 5), in order to avoid saturating the detector.

A simulation of a ptychographic reconstruction of magnetic domains was performed using ePIE with the constraint given by eq. (7.17). The results shown in Fig. 7.4 demonstrate a

successful reconstruction of the original domain pattern. The parameters of the simulation where chosen to be close to the experimental parameters: the energy of the EUV probe was 53 eV, the domain size was ∼80 nm. With the probe spot size of approximately 1.5 μm, a field of view of ∼2.5 μm was achieved by scanning the probe spot across the sample. The resolution of the spatial grid in the simulations was ∼20 nm/pixel. Note that the sign of the reconstructed m_z is reversed compared to the original domain texture. This is a manifestation of the ambiguity of the sign of the phase in the solution of the phase retrieval problem. The simulation demonstrates the feasibility of magnetic imaging with a linearly polarized tabletop HHG source.

7.3 Element-specific spectro-microscopy

Using a technique known as ptychographic information multiplexing (PIM) [255, 256, 257], it is possible to reconstruct multiple objects corresponding to different modes of illumination that add incoherently at the detector. The modes can include illumination with different polarizations, spatial profiles, or wavelengths [258, 259, 260]. The latter is particularly important as it can be used for visualization of magnetic textures at the M-shell absorption edges of multiple $3d$ ferromagnets simultaneously, which paves a way for lensless magnetic microscopy with an elemental contrast. A repeatable magnetic texture, e.g. a patterned nanoscale magnetic device, can be imaged stroboscopically in a pump-probe experiment using PIM, and thus spatially-resolved dynamics of multiple elements can be measured with femtosecond time resolution. Finally, the dynamics of the deterministic all-optical magnetization reversal [62] can be studied stroboscopically using ptychographic imaging.

7.4 Further work

In addition to magnetic microscopy, there are multiple other promising areas of interest. Ferromagnets represent a rather narrow class of strongly correlated materials. Another class is antiferromagnets, which play an important role in high-T_C superconductivity [261]. An antiferromagnetic spin alignment typically occurs in transition metal compounds such as FeMn and NiO

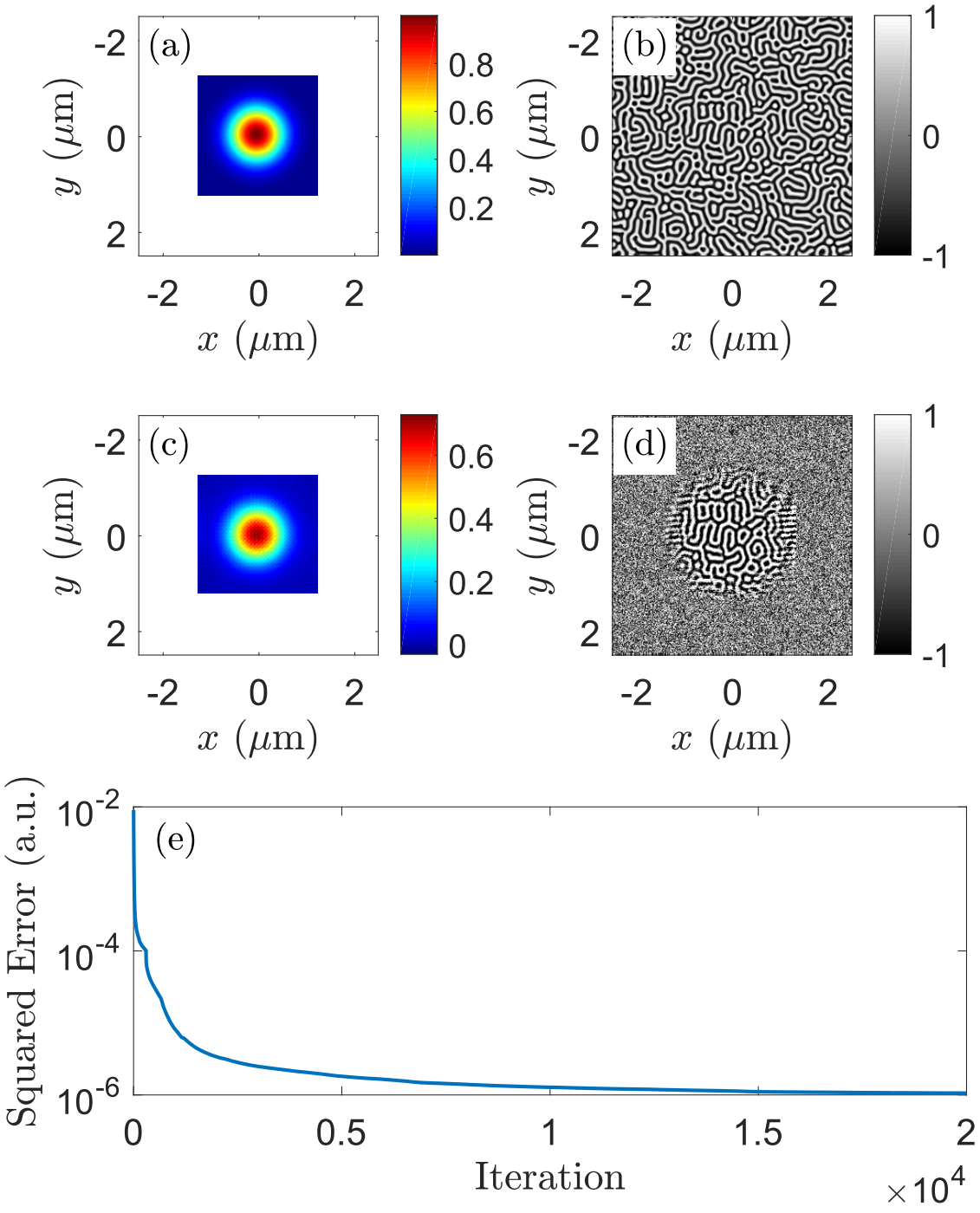

Figure 7.4: Simulation of a ptychographic reconstruction of magnetic domains. (a) and (b) are the original probe beam profile and domain texture, respectively; (c) and (d) are the corresponding reconstructions; (e) is the evolution of the squared error with the number of algorithm iterations.

and can be studied magneto-optically using X-ray magnetic linear dichroism (XMLD) [73, 128], which has been used in combination with photoelectron microscopy to image antiferromagnetic domains [262, 263, 264]. Due to its small magnitude, XMLD requires an improvement in the photon flux and stability of HHG sources, but, in principle, can be readily implemented in a pump-probe experiment to study laser-induced spin dynamics in antiferromagnets.

Studying magnetization dynamics in these and other complex magnetic systems, such as half-metals (Heusler alloys) [265, 266] and materials with phase transitions at cryogenic temperatures, e.g. magnetite [267, 268, 269], with EUV resonant magneto-optical spectroscopy can improve the understanding of magnetism in the context of strongly correlated quantum phenomena and bring us closer to the ultimate goal of its coherent control.

Bibliography

[1] S. A. Wolf, A. Y. Chtchelkanova, and D. M. Treger. Spintronics – A retrospective and perspective. IBM Journal of Research and Development, 50(1):101–110, January 2006.

[2] S. A. Wolf, D. D. Awschalom, R. A. Buhrman, J. M. Daughton, S. von Molnár, M. L. Roukes, A. Y. Chtchelkanova, and D. M. Treger. Spintronics: A Spin-Based Electronics Vision for the Future. Science, 294(5546):1488–1495, November 2001.

[3] David D. Awschalom and Michael E. Flatté. Challenges for semiconductor spintronics. Nature Physics, 3(3):153, March 2007.

[4] N. Locatelli, A. F. Vincent, A. Mizrahi, J. S. Friedman, D. Vodenicarevic, J. V. Kim, J. O. Klein, W. Zhao, J. Grollier, and D. Querlioz. Spintronic devices as key elements for energy-efficient neuroinspired architectures. In 2015 Design, Automation Test in Europe Conference Exhibition (DATE), pages 994–999, March 2015.

[5] Yue Zhang, Weisheng Zhao, Jacques-Olivier Klein, Wang Kang, Damien Querlioz, Youguang Zhang, Dafiné Ravelosona, and Claude Chappert. Spintronics for Low-power Computing. In Proceedings of the Conference on Design, Automation & Test in Europe, DATE '14, pages 303:1–303:6, 3001 Leuven, Belgium, Belgium, 2014. European Design and Automation Association.

[6] Shimeng Yu. Introduction to Neuro-Inspired Computing Using Resistive Synaptic Devices. In Neuro-inspired Computing Using Resistive Synaptic Devices, pages 1–15. Springer, Cham, 2017. DOI: 10.1007/978-3-319-54313-0_1.

[7] A. Enders, R. Skomski, and J. Honolka. Magnetic surface nanostructures. Journal of Physics: Condensed Matter, 22(43):433001, 2010.

[8] Joachim Stöhr and Hans Christoph Siegmann. Magnetism: From Fundamentals to Nanoscale Dynamics. Springer Science & Business Media, January 2007.

[9] A. K. Petford-Long and J. N. Chapman. Lorentz Microscopy. In Magnetic Microscopy of Nanostructures, NanoScience and Technology, pages 67–86. Springer, Berlin, Heidelberg, 2005. DOI: 10.1007/3-540-26641-0_4.

[10] Philippe Antoine, Anne L'Huillier, and Maciej Lewenstein. Attosecond pulse trains using high-order harmonics. Physical Review Letters, 77(7):1234–1237, August 1996.

[11] Ivan P. Christov, Margaret M. Murnane, and Henry C. Kapteyn. High-Harmonic Generation of Attosecond Pulses in the "Single-Cycle" Regime. Physical Review Letters, 78(7):1251–1254, February 1997.

[12] B. Dromey, M. Zepf, A. Gopal, K. Lancaster, M. S. Wei, K. Krushelnick, M. Tatarakis, N. Vakakis, S. Moustaizis, R. Kodama, M. Tampo, C. Stoeckl, R. Clarke, H. Habara, D. Neely, S. Karsch, and P. Norreys. High harmonic generation in the relativistic limit. Nature Physics, 2(7):456, July 2006.

[13] H. J. Wörner, J. B. Bertrand, D. V. Kartashov, P. B. Corkum, and D. M. Villeneuve. Following a chemical reaction using high-harmonic interferometry. Nature, 466(7306):604, July 2010.

[14] P. M. Paul, E. S. Toma, P. Breger, G. Mullot, F. Augé, Ph Balcou, H. G. Muller, and P. Agostini. Observation of a Train of Attosecond Pulses from High Harmonic Generation. Science, 292(5522):1689–1692, June 2001.

[15] P. Emma, R. Akre, J. Arthur, R. Bionta, C. Bostedt, J. Bozek, A. Brachmann, P. Bucksbaum, R. Coffee, F.-J. Decker, Y. Ding, D. Dowell, S. Edstrom, A. Fisher, J. Frisch, S. Gilevich, J. Hastings, G. Hays, Ph Hering, Z. Huang, R. Iverson, H. Loos, M. Messerschmidt, A. Miahnahri, S. Moeller, H.-D. Nuhn, G. Pile, D. Ratner, J. Rzepiela, D. Schultz, T. Smith, P. Stefan, H. Tompkins, J. Turner, J. Welch, W. White, J. Wu, G. Yocky, and J. Galayda. First lasing and operation of an ångstrom-wavelength free-electron laser. Nature Photonics, 4(9):641, September 2010.

[16] Jinfeng Yang, Yoichi Yoshida, and Hiromi Shibata. Femtosecond Time-Resolved Electron Microscopy. Electronics and Communications in Japan, 98(11):50–57, November 2015.

[17] Nara Rubiano da Silva, Marcel Möller, Armin Feist, Henning Ulrichs, Claus Ropers, and Sascha Schäfer. Nanoscale mapping of ultrafast magnetization dynamics with femtosecond Lorentz microscopy. arXiv:1710.03307 [cond-mat, physics:physics], October 2017. arXiv: 1710.03307.

[18] Stoner Edmund C. Collective electron specific heat and spin paramagnetism in metals. Proc. R. Soc. Lond. A, 154(883):656–678, May 1936.

[19] Edmund C. Stoner and F. R. S. Collective electron ferronmagnetism. Proc. R. Soc. Lond. A, 165(922):372–414, April 1938.

[20] N. F. Mott. A discussion of the transition metals on the basis of quantum mechanics. Proceedings of the Physical Society, 47(4):571, 1935.

[21] J. C. Slater. The Ferromagnetism of Nickel. Physical Review, 49(7):537–545, April 1936.

[22] J. C. Slater. The Ferromagnetism of Nickel. II. Temperature Effects. Physical Review, 49(12):931–937, June 1936.

[23] Jürgen Kübler. Theory of Itinerant Electron Magnetism. Oxford University Press, March 2017. Google-Books-ID: tat0DgAAQBAJ.

[24] K. Baberschke, M. Donath, and W. Nolting. Band-Ferromagnetism: Ground-State and Finite-Temperature Phenomena. Springer, January 2008.

[25] R. O. Jones and O. Gunnarsson. The density functional formalism, its applications and prospects. Reviews of Modern Physics, 61(3):689–746, July 1989.

[26] Dimitris A. Papaconstantopoulos. Handbook of the Band Structure of Elemental Solids. Springer US, December 1986.

[27] W. Kohn and L. J. Sham. Self-Consistent Equations Including Exchange and Correlation Effects. Physical Review, 140(4A):A1133–A1138, November 1965.

[28] P. Hohenberg and W. Kohn. Inhomogeneous Electron Gas. Physical Review, 136(3B):B864–B871, November 1964.

[29] Charles Kittel. Introduction to Solid State Physics. Wiley, 1996. Google-Books-ID: 1X8pAQAAMAAJ.

[30] The Elk FP-LAPW Code. `http://elk.sourceforge.net/`. Accessed: 2018-04-11.

[31] M. D. Kuz'min. Shape of Temperature Dependence of Spontaneous Magnetization of Ferromagnets: Quantitative Analysis. Physical Review Letters, 94(10):107204, March 2005.

[32] Pierre Weiss. L'hypothèse du champ moléculaire et la propriété ferromagnétique. Journal de Physique Théorique et Appliquée, 6(1):661–690, 1907.

[33] R. K. Pathria and Paul D. Beale. Statistical Mechanics. Butterworth-Heinemann, September 1996. Google-Books-ID: PIk9sF9j2oUC.

[34] W. Pauli. The Connection Between Spin and Statistics. Physical Review, 58(8):716–722, October 1940.

[35] J. J. Sakurai and Jim Napolitano. Modern Quantum Mechanics. Cambridge University Press, September 2017. Google-Books-ID: v89CDwAAQBAJ.

[36] Richard P. Feynman, Robert B. Leighton, and Matthew Sands. The Feynman Lectures on Physics, Vol. III: The New Millennium Edition: Quantum Mechanics. Basic Books, October 2011. Google-Books-ID: KsnbNL_rh04C.

[37] F. Bloch. Zur Theorie des Ferromagnetismus. Zeitschrift für Physik, 61(3-4):206–219, March 1930.

[38] S. V. Halilov, A. Y. Perlov, P. M. Oppeneer, and H. Eschrig. Magnon spectrum and related finite-temperature magnetic properties: A first-principle approach. EPL (Europhysics Letters), 39(1):91, July 1997.

[39] Toru Moriya. Spin Fluctuations in Itinerant Electron Magnetism. Springer Science & Business Media, December 2012.

[40] A. J. Freeman and R. E. Watson. Theoretical Investigation of Some Magnetic and Spectroscopic Properties of Rare-Earth Ions. Physical Review, 127(6):2058–2075, September 1962.

[41] J. H. van Vleck. On the Anisotropy of Cubic Ferromagnetic Crystals. Physical Review, 52(11):1178–1198, December 1937.

[42] Patrick Bruno. Tight-binding approach to the orbital magnetic moment and magnetocrystalline anisotropy of transition-metal monolayers. Physical Review B, 39(1):865–868, January 1989.

[43] S. V. Halilov, A. Ya. Perlov, P. M. Oppeneer, A. N. Yaresko, and V. N. Antonov. Magnetocrystalline anisotropy energy in cubic Fe, Co, and Ni: Applicability of local-spin-density theory reexamined. Physical Review B, 57(16):9557–9560, April 1998.

[44] U. Gradmann. Magnetism in Oligatomic Films. Journal of Applied Physics, 40(3):1182–1186, March 1969.

[45] C. Chappert, K. Le Dang, P. Beauvillain, H. Hurdequint, and D. Renard. Ferromagnetic resonance studies of very thin cobalt films on a gold substrate. Physical Review B, 34(5):3192–3197, September 1986.

[46] A. Hubert and R. Schäfer. Magnetic Domains: The Analysis of Magnetic Microstructures. Springer Science & Business Media, October 2008.

[47] A. N. Bogdanov and U. K. Rößler. Chiral Symmetry Breaking in Magnetic Thin Films and Multilayers. Physical Review Letters, 87(3):037203, June 2001.

[48] Albert Fert, Vincent Cros, and João Sampaio. Skyrmions on the track, March 2013.

[49] Pin-Jui Hsu, André Kubetzka, Aurore Finco, Niklas Romming, Kirsten von Bergmann, and Roland Wiesendanger. Electric-field-driven switching of individual magnetic skyrmions. Nature Nanotechnology, 12(2):123–126, February 2017.

[50] I. Dzyaloshinsky. A thermodynamic theory of "weak" ferromagnetism of antiferromagnetics. Journal of Physics and Chemistry of Solids, 4(4):241–255, January 1958.

[51] Tôru Moriya. Anisotropic Superexchange Interaction and Weak Ferromagnetism. Physical Review, 120(1):91–98, October 1960.

[52] M. Finazzi, M. Savoini, A. R. Khorsand, A. Tsukamoto, A. Itoh, L. Duò, A. Kirilyuk, Th. Rasing, and M. Ezawa. Laser-Induced Magnetic Nanostructures with Tunable Topological Properties. Physical Review Letters, 110(17):177205, April 2013.

[53] J. C. T Lee, J. J. Chess, S. A. Montoya, X. Shi, N. Tamura, S. K. Mishra, P. Fischer, B. J. McMorran, S. K. Sinha, E. E. Fullerton, S. D. Kevan, and S. Roy. Synthesizing skyrmion bound pairs in Fe-Gd thin films. Applied Physics Letters, 109(2):022402, July 2016.

[54] X. Z. Yu, K. Shibata, W. Koshibae, Y. Tokunaga, Y. Kaneko, T. Nagai, K. Kimoto, Y. Taguchi, N. Nagaosa, and Y. Tokura. Thermally activated helicity reversals of skyrmions. Physical Review B, 93(13):134417, April 2016.

[55] Niklas Romming, Christian Hanneken, Matthias Menzel, Jessica E. Bickel, Boris Wolter, Kirsten von Bergmann, André Kubetzka, and Roland Wiesendanger. Writing and Deleting Single Magnetic Skyrmions. Science, 341(6146):636–639, August 2013.

[56] Xichao Zhang, Motohiko Ezawa, and Yan Zhou. Magnetic skyrmion logic gates: conversion, duplication and merging of skyrmions. Scientific Reports, 5, March 2015.

[57] E. Beaurepaire, J.-C. Merle, A. Daunois, and J.-Y. Bigot. Ultrafast Spin Dynamics in Ferromagnetic Nickel. Physical Review Letters, 76(22):4250–4253, May 1996.

[58] B. Koopmans, G. Malinowski, F. Dalla Longa, D. Steiauf, M. Fähnle, T. Roth, M. Cinchetti, and M. Aeschlimann. Explaining the paradoxical diversity of ultrafast laser-induced demagnetization. Nature Materials, 9(3):259–265, March 2010.

[59] Alexey Melnikov, Helena Prima-García, M Lisowski, T Giessel, R Weber, R Schmidt, C Gahl, Nadezhda Bulgakova, Uwe Bovensiepen, and M Weinelt. Nonequilibrium Magnetization Dynamics of Gadolinium Studied by Magnetic Linear Dichroism in Time-Resolved 4 f Core-Level Photoemission. Physical review letters, 100:107202, April 2008.

[60] J Wang, C Sun, Junichiro Kono, Akira Oiwa, H Munekata, L Cywiński, and L J Sham. Ultrafast Quenching of Ferromagnetism in InMnAs Induced by Intense Laser Irradiation. Physical review letters, 95:167401, October 2005.

[61] Uwe Bovensiepen. Coherent and incoherent excitations of the Gd(0001) surface on ultrafast timescales. Journal of Physics: Condensed Matter, 19(8):083201, 2007.

[62] C. D. Stanciu, F. Hansteen, A. V. Kimel, A. Kirilyuk, A. Tsukamoto, A. Itoh, and Th. Rasing. All-Optical Magnetic Recording with Circularly Polarized Light. Physical Review Letters, 99(4):047601, July 2007.

[63] S. Mangin, M. Gottwald, C.-H. Lambert, D. Steil, V. Uhlíř, L. Pang, M. Hehn, S. Alebrand, M. Cinchetti, G. Malinowski, Y. Fainman, M. Aeschlimann, and E. E. Fullerton. Engineered materials for all-optical helicity-dependent magnetic switching. Nature Materials, 13(3):286–292, March 2014.

[64] C.-H. Lambert, S. Mangin, B. S. D. Ch S. Varaprasad, Y. K. Takahashi, M. Hehn, M. Cinchetti, G. Malinowski, K. Hono, Y. Fainman, M. Aeschlimann, and E. E. Fullerton. All-optical control of ferromagnetic thin films and nanostructures. Science, 345(6202):1337–1340, September 2014.

[65] T. Henighan, M. Trigo, S. Bonetti, P. Granitzka, D. Higley, Z. Chen, M. P. Jiang, R. Kukreja, A. Gray, A. H. Reid, E. Jal, M. C. Hoffmann, M. Kozina, S. Song, M. Chollet, D. Zhu, P. F. Xu, J. Jeong, K. Carva, P. Maldonado, P. M. Oppeneer, M. G. Samant, S. S. P. Parkin, D. A. Reis, and H. A. Dürr. Generation mechanism of terahertz coherent acoustic phonons in Fe. Physical Review B, 93(22):220301, June 2016.

[66] Kathleen M. Hoogeboom-Pot, Jorge N. Hernandez-Charpak, Xiaokun Gu, Travis D. Frazer, Erik H. Anderson, Weilun Chao, Roger W. Falcone, Ronggui Yang, Margaret M. Murnane, Henry C. Kapteyn, and Damiano Nardi. A new regime of nanoscale thermal transport: Collective diffusion increases dissipation efficiency. Proceedings of the National Academy of Sciences, 112(16):4846–4851, April 2015.

[67] B. Koopmans, M. van Kampen, J. T. Kohlhepp, and W. J. M. de Jonge. Ultrafast Magneto-Optics in Nickel: Magnetism or Optics? Physical Review Letters, 85(4):844–847, July 2000.

[68] T. Kampfrath, R. G. Ulbrich, F. Leuenberger, M. Münzenberg, B. Sass, and W. Felsch. Ultrafast magneto-optical response of iron thin films. Physical Review B, 65(10):104429, February 2002.

[69] Wenjing You, Phoebe Tengdin, Cong Chen, Xun Shi, Dmitriy Zusin, Yingchao Zhang, Christian Gentry, Adam Blonsky, Mark Keller, Peter M. Oppeneer, Henry Kapteyn, Zhensheng Tao, and Margaret Murnane. Revealing the Nature of the Ultrafast Magnetic Phase Transition in Ni by Correlating Extreme Ultraviolet Magneto-Optic and Photoemission Spectroscopies. Physical Review Letters, 121(7):077204, August 2018.

[70] J. L. Erskine and E. A. Stern. Calculation of the ${M}_{23}$ magneto-optical absorption spectrum of ferromagnetic nickel. Physical Review B, 12(11):5016–5024, December 1975.

[71] G. Schütz, W. Wagner, W. Wilhelm, P. Kienle, R. Zeller, R. Frahm, and G. Materlik. Absorption of circularly polarized x rays in iron. Physical Review Letters, 58(7):737–740, February 1987.

[72] J. Stöhr and Y. Wu. X-Ray Magnetic Circular Dichroism: Basic Concepts and Theory for 3d Transition Metal Atoms. In A. S. Schlachter and F. J. Wuilleumier, editors, New Directions in Research with Third-Generation Soft X-Ray Synchrotron Radiation Sources, NATO ASI Series, pages 221–250. Springer Netherlands, Dordrecht, 1994.

[73] Peter M. Oppeneer. Handbook of Magnetic Materials. 2001.

[74] R. Kubo. A general expression for the conductivity tensor. Canadian Journal of Physics, 34(12A):1274–1277, December 1956.

[75] Ryogo Kubo. Statistical-Mechanical Theory of Irreversible Processes. I. General Theory and Simple Applications to Magnetic and Conduction Problems. Journal of the Physical Society of Japan, 12(6):570–586, June 1957.

[76] F. R. Elder, A. M. Gurewitsch, R. V. Langmuir, and H. C. Pollock. Radiation from Electrons in a Synchrotron. Physical Review, 71(11):829–830, June 1947.

[77] A. McPherson, G. Gibson, H. Jara, U. Johann, T. S. Luk, I. A. McIntyre, K. Boyer, and C. K. Rhodes. Studies of multiphoton production of vacuum-ultraviolet radiation in the rare gases. Journal of the Optical Society of America B, 4(4):595–601, April 1987.

[78] M. Ferray, A. L'Huillier, X. F. Li, L. A. Lompre, G. Mainfray, and C. Manus. Multiple-harmonic conversion of 1064 nm radiation in rare gases. Journal of Physics B: Atomic, Molecular and Optical Physics, 21(3):L31, February 1988.

[79] J. J. Macklin, J. D. Kmetec, and C. L. Gordon. High-order harmonic generation using intense femtosecond pulses. Physical Review Letters, 70(6):766–769, February 1993.

[80] Anne L'Huillier and Ph. Balcou. High-order harmonic generation in rare gases with a 1-ps 1053-nm laser. Physical Review Letters, 70(6):774–777, February 1993.

[81] M. Yu. Kuchiev. Atomic antenna. Soviet Journal of Experimental and Theoretical Physics Letters, 45:404, April 1987.

[82] P. B. Corkum. Plasma perspective on strong field multiphoton ionization. Physical Review Letters, 71(13):1994–1997, September 1993.

[83] K. C. Kulander, K. J. Schafer, and J. L. Krause. Dynamics of Short-Pulse Excitation, Ionization and Harmonic Conversion. In Super-Intense Laser-Atom Physics, NATO ASI Series, pages 95–110. Springer, Boston, MA, 1993.

[84] P. Maine, D. Strickland, P. Bado, M. Pessot, and G. Mourou. Generation of ultrahigh peak power pulses by chirped pulse amplification. IEEE Journal of Quantum Electronics, 24(2):398–403, February 1988.

[85] Sterling Backus, Charles G. Durfee, Margaret M. Murnane, and Henry C. Kapteyn. High power ultrafast lasers. Review of Scientific Instruments, 69(3):1207–1223, March 1998.

[86] Maxim V. Ammosov, Nikolai B. Delone, and Vladimir P. Krainov. Tunnel Ionization Of Complex Atoms And Atomic Ions In Electromagnetic Field. In High Intensity Laser Processes, volume 0664, pages 138–142. International Society for Optics and Photonics, October 1986.

[87] Jeffrey L. Krause, Kenneth J. Schafer, and Kenneth C. Kulander. High-order harmonic generation from atoms and ions in the high intensity regime. Physical Review Letters, 68(24):3535–3538, June 1992.

[88] M. Lewenstein, Ph. Balcou, M. Yu. Ivanov, Anne L'Huillier, and P. B. Corkum. Theory of high-harmonic generation by low-frequency laser fields. Physical Review A, 49(3):2117–2132, March 1994.

[89] J. W. Cooley. An improved eigenvalue corrector formula for solving the Schrödinger equation for central fields. Mathematics of Computation, 15(76):363–374, 1961.

[90] H. F. Trotter. On the product of semi-groups of operators. Proceedings of the American Mathematical Society, 10(4):545–551, 1959.

[91] Brian C. Hall. Quantum Theory for Mathematicians. Graduate Texts in Mathematics, Springer Nature Textbooks – HE site. Springer-Verlag, New York, 2013.

[92] John David Jackson. Classical Electrodynamics. Wiley, 2012.

[93] Boris Vodungbo, Anna Barszczak Sardinha, Julien Gautier, Guillaume Lambert, Constance Valentin, Magali Lozano, Grégory Iaquaniello, Franck Delmotte, Stéphane Sebban, Jan Lüning, and Philippe Zeitoun. Polarization control of high order harmonics in the EUV photon energy range. Optics Express, 19(5):4346–4356, February 2011.

[94] H. Eichmann, A. Egbert, S. Nolte, C. Momma, B. Wellegehausen, W. Becker, S. Long, and J. K. McIver. Polarization-dependent high-order two-color mixing. Physical Review A, 51(5):R3414–R3417, May 1995.

[95] S. Long, W. Becker, and J. K. McIver. Model calculations of polarization-dependent two-color high-harmonic generation. Physical Review A, 52(3):2262–2278, September 1995.

[96] Avner Fleischer, Ofer Kfir, Tzvi Diskin, Pavel Sidorenko, and Oren Cohen. Spin angular momentum and tunable polarization in high-harmonic generation. Nature Photonics, 8(7):543–549, July 2014.

[97] Ofer Kfir, Patrik Grychtol, Emrah Turgut, Ronny Knut, Dmitriy Zusin, Dimitar Popmintchev, Tenio Popmintchev, Hans Nembach, Justin M. Shaw, Avner Fleischer, Henry Kapteyn, Margaret Murnane, and Oren Cohen. Generation of bright phase-matched circularly-polarized extreme ultraviolet high harmonics. Nature Photonics, 9(2):99–105, February 2015.

[98] Dejan B. Milošević, Wilhelm Becker, and Richard Kopold. Generation of circularly polarized high-order harmonics by two-color coplanar field mixing. Physical Review A, 61(6):063403, May 2000.

[99] Cong Chen, Zhensheng Tao, Carlos Hernández-García, Piotr Matyba, Adra Carr, Ronny Knut, Ofer Kfir, Dimitry Zusin, Christian Gentry, Patrik Grychtol, Oren Cohen, Luis Plaja, Andreas Becker, Agnieszka Jaron-Becker, Henry Kapteyn, and Margaret Murnane. Tomographic reconstruction of circularly polarized high-harmonic fields: 3d attosecond metrology. Science Advances, 2(2):e1501333, February 2016.

[100] Daniel D. Hickstein, Franklin J. Dollar, Patrik Grychtol, Jennifer L. Ellis, Ronny Knut, Carlos Hernández-García, Dmitriy Zusin, Christian Gentry, Justin M. Shaw, Tingting Fan, Kevin M. Dorney, Andreas Becker, Agnieszka Jaroń-Becker, Henry C. Kapteyn, Margaret M. Murnane, and Charles G. Durfee. Non-collinear generation of angularly isolated circularly polarized high harmonics. Nature Photonics, 9(11):743–750, November 2015.

[101] Tingting Fan, Patrik Grychtol, Ronny Knut, Carlos Hernández-García, Daniel D. Hickstein, Dmitriy Zusin, Christian Gentry, Franklin J. Dollar, Christopher A. Mancuso, Craig W. Hogle, Ofer Kfir, Dominik Legut, Karel Carva, Jennifer L. Ellis, Kevin M. Dorney, Cong Chen, Oleg G. Shpyrko, Eric E. Fullerton, Oren Cohen, Peter M. Oppeneer, Dejan B. Milošević, Andreas Becker, Agnieszka A. Jaroń-Becker, Tenio Popmintchev, Margaret M. Murnane, and Henry C. Kapteyn. Bright circularly polarized soft X-ray high harmonics for X-ray magnetic circular dichroism. Proceedings of the National Academy of Sciences, page 201519666, November 2015.

[102] Robert W. Boyd. Nonlinear Optics. Elsevier, May 2008.

[103] Eric Constant, David Garzella, P Breger, E Mével, Ch Dorrer, Charles Le Blanc, Francois Salin, and Patrick Agostini. Optimizing High Harmonic Generation in Absorbing Gases: Model and Experiment. Physical Review Letters - PHYS REV LETT, 82:1668–1671, February 1999.

[104] Andy Rundquist, Charles G. Durfee, Zenghu Chang, Catherine Herne, Sterling Backus, Margaret M. Murnane, and Henry C. Kapteyn. Phase-Matched Generation of Coherent Soft X-rays. Science, 280(5368):1412–1415, May 1998.

[105] Charles G. Durfee, Andy R. Rundquist, Sterling Backus, Catherine Herne, Margaret M. Murnane, and Henry C. Kapteyn. Phase Matching of High-Order Harmonics in Hollow Waveguides. Physical Review Letters, 83(11):2187–2190, September 1999.

[106] M.-C. Chen, P. Arpin, T. Popmintchev, M. Gerrity, B. Zhang, M. Seaberg, D. Popmintchev, M. M. Murnane, and H. C. Kapteyn. Bright, Coherent, Ultrafast Soft X-Ray Harmonics Spanning the Water Window from a Tabletop Light Source. Physical Review Letters, 105(17):173901, October 2010.

[107] Matthew D. Seaberg. Nanoscale EUV Microscopy on a Tabletop: A General Transmission and Reflection Mode Microscope Based on Coherent Diffractive Imaging with High Harmonic Illumination. PhD thesis, 2014.

[108] Amy Louise Lytle. Phase Matching and Coherence of High-Order Harmonic Generation in Hollow Waveguides. PhD thesis, University of Colorado Boulder, 2008.

[109] Ofer Kfir, Patrik Grychtol, Emrah Turgut, Ronny Knut, Dmitriy Zusin, Avner Fleischer, Eliyahu Bordo, Tingting Fan, Dimitar Popmintchev, Tenio Popmintchev, Henry Kapteyn, Margaret Murnane, and Oren Cohen. Helicity-selective phase-matching and quasi-phase matching of circularly polarized high-order harmonics: towards chiral attosecond pulses. Journal of Physics B: Atomic, Molecular and Optical Physics, 49(12):123501, 2016.

[110] John M. J. Madey. Stimulated Emission of Bremsstrahlung in a Periodic Magnetic Field. Journal of Applied Physics, 42(5):1906–1913, April 1971.

[111] J. Feldhaus, J. Arthur, and J. B. Hastings. X-ray free-electron lasers. Journal of Physics B Atomic Molecular Physics, 38:S799–S819, May 2005.

[112] P. Luchini and H. Motz. Undulators and Free-electron Lasers. Clarendon Press, Oxford England : New York, 1 edition edition, August 1990.

[113] R. Akre, D. Dowell, P. Emma, J. Frisch, S. Gilevich, G. Hays, Ph. Hering, R. Iverson, C. Limborg-Deprey, H. Loos, A. Miahnahri, J. Schmerge, J. Turner, J. Welch, W. White, and J. Wu. Commissioning the Linac Coherent Light Source injector. Physical Review Special Topics - Accelerators and Beams, 11(3):030703, March 2008.

[114] N. Hartmann, W. Helml, A. Galler, M. R. Bionta, J. Grünert, S. L. Molodtsov, K. R. Ferguson, S. Schorb, M. L. Swiggers, S. Carron, C. Bostedt, J.-C. Castagna, J. Bozek, J. M. Glownia, D. J. Kane, A. R. Fry, W. E. White, C. P. Hauri, T. Feurer, and R. N. Coffee. Sub-femtosecond precision measurement of relative X-ray arrival time for free-electron lasers. Nature Photonics, 8(9):706–709, September 2014.

[115] J. Amann, W. Berg, V. Blank, F.-J. Decker, Y. Ding, P. Emma, Y. Feng, J. Frisch, D. Fritz, J. Hastings, Z. Huang, J. Krzywinski, R. Lindberg, H. Loos, A. Lutman, H.-D. Nuhn, D. Ratner, J. Rzepiela, D. Shu, Yu Shvyd'ko, S. Spampinati, S. Stoupin, S. Terentyev, E. Trakhtenberg, D. Walz, J. Welch, J. Wu, A. Zholents, and D. Zhu. Demonstration of self-seeding in a hard-X-ray free-electron laser. Nature Photonics, 6(10):693–698, October 2012.

[116] T. Sato, A. Iwasaki, S. Owada, K. Yamanouchi, E. J. Takahashi, K. Midorikawa, M. Aoyama, K. Yamakawa, T. Togashi, K Fukami, T. Hatsui, T. Hara, T. Kameshima, H. Kitamura, N. Kumagai, S. Matsubara, M. Nagasono, H. Ohashi, T. Ohshima, Y Otake, T. Shintake, K. Tamasaku, H. Tanaka, T. Tanaka, K. Togawa, H. Tomizawa, T. Watanabe, M. Yabashi, and T. Ishikawa. Full-coherent free electron laser seeded by 13th- and 15th-order harmonics of near-infrared femtosecond laser pulses. Journal of Physics B: Atomic, Molecular and Optical Physics, 46(16):164006, 2013.

[117] Theophilos Maltezopoulos, Manuel Mittenzwey, Armin Azima, Jörn Bödewadt, Hatem Dachraoui, Marie Rehders, Christoph Lechner, Michael Schulz, Marek Wieland, Tim Laarmann, Jörg Roßbach, and Markus Drescher. A high-harmonic generation source for seeding a free-electron laser at 38 nm. Applied Physics B, 115(1):45–54, April 2014.

[118] S. Ackermann, A. Azima, S. Bajt, J. Bödewadt, F. Curbis, H. Dachraoui, H. Delsim-Hashemi, M. Drescher, S. Düsterer, B. Faatz, M. Felber, J. Feldhaus, E. Hass, U. Hipp, K. Honkavaara, R. Ischebeck, S. Khan, T. Laarmann, C. Lechner, Th. Maltezopoulos, V. Miltchev, M. Mittenzwey, M. Rehders, J. Rönsch-Schulenburg, J. Rossbach, H. Schlarb, S. Schreiber, L. Schroedter, M. Schulz, S. Schulz, R. Tarkeshian, M. Tischer, V. Wacker,

and M. Wieland. Generation of Coherent 19- and 38-nm Radiation at a Free-Electron Laser Directly Seeded at 38 nm. Physical Review Letters, 111(11):114801, September 2013.

[119] E. Allaria, A. Battistoni, F. Bencivenga, R. Borghes, C. Callegari, F. Capotondi, D. Castronovo, P. Cinquegrana, D Cocco, M. Coreno, P. Craievich, R. Cucini, F. D'Amico, M. B. Danailov, A. Demidovich, G. De Ninno, A. Di Cicco, S. Di Fonzo, M. Di Fraia, S. Di Mitri, B. Diviacco, W. M. Fawley, E. Ferrari, A. Filipponi, L. Froehlich, A. Gessini, E Giangrisostomi, L. Giannessi, D. Giuressi, C. Grazioli, R. Gunnella, R. Ivanov, B. Mahieu, N. Mahne, C Masciovecchio, I. P. Nikolov, G. Passos, E. Pedersoli, G. Penco, E. Principi, L. Raimondi, R. Sergo, P. Sigalotti, C Spezzani, C. Svetina, M. Trovò, and M. Zangrando. Tunability experiments at the FERMI@Elettra free-electron laser. New Journal of Physics, 14(11):113009, 2012.

[120] Toru Hara. Free-electron lasers: Fully coherent soft X-rays at FERMI. Nature Photonics, 7(11):852–854, November 2013.

[121] Z. J. Yang and M. R. Scheinfein. Combined three-axis surface magneto-optical Kerr effects in the study of surface and ultrathin-film magnetism. Journal of Applied Physics, 74(11):6810–6823, December 1993.

[122] Emrah Turgut, Dmitriy Zusin, Dominik Legut, Karel Carva, Ronny Knut, Justin M. Shaw, Cong Chen, Zhensheng Tao, Hans T. Nembach, Thomas J. Silva, Stefan Mathias, Martin Aeschlimann, Peter M. Oppeneer, Henry C. Kapteyn, Margaret M. Murnane, and Patrik Grychtol. Stoner versus Heisenberg: Ultrafast exchange reduction and magnon generation during laser-induced demagnetization. Physical Review B, 94(22):220408, December 2016.

[123] Chan La-O-Vorakiat, Emrah Turgut, Carson A. Teale, Henry C. Kapteyn, Margaret M. Murnane, Stefan Mathias, Martin Aeschlimann, Claus M. Schneider, Justin M. Shaw, Hans T. Nembach, and T. J. Silva. Ultrafast Demagnetization Measurements Using Extreme Ultraviolet Light: Comparison of Electronic and Magnetic Contributions. Physical Review X, 2(1):011005, January 2012.

[124] Emrah Turgut, Patrik Grychtol, Chan La-O-Vorakiat, Daniel E. Adams, Henry C. Kapteyn, Margaret M. Murnane, Stefan Mathias, Martin Aeschlimann, Claus M. Schneider, Justin M. Shaw, Hans T. Nembach, and Thomas J. Silva. Reply to "Comment on 'Ultrafast Demagnetization Measurements Using Extreme Ultraviolet Light: Comparison of Electronic and Magnetic Contributions' ". Physical Review X, 3(3):038002, September 2013.

[125] Dmitriy Zusin, Phoebe M. Tengdin, Maithreyi Gopalakrishnan, Christian Gentry, Adam Blonsky, Michael Gerrity, Dominik Legut, Justin M. Shaw, Hans T. Nembach, T. J. Silva, Peter M. Oppeneer, Henry C. Kapteyn, and Margaret M. Murnane. Direct measurement of the static and transient magneto-optical permittivity of cobalt across the entire M-edge in reflection geometry by use of polarization scanning. Physical Review B, 97(2):024433, January 2018.

[126] M. Hecker, S. Valencia, P. M. Oppeneer, H.-Ch. Mertins, and C. M. Schneider. Polarized soft-x-ray reflection spectroscopy of giant magnetoresistive Co/Cu multilayers. Physical Review B, 72(5):054437, August 2005.

[127] Chan La-O-Vorakiat, Mark Siemens, Margaret M. Murnane, Henry C. Kapteyn, Stefan Mathias, Martin Aeschlimann, Patrik Grychtol, Roman Adam, Claus M. Schneider, Justin M. Shaw, Hans Nembach, and T. J. Silva. Ultrafast Demagnetization Dynamics at the M Edges of Magnetic Elements Observed Using a Tabletop High-Harmonic Soft X-Ray Source. Physical Review Letters, 103(25):257402, December 2009.

[128] P. M. Oppeneer, H.-Ch Mertins, and O. Zaharko. Alternative geometries for the determination of x-ray magneto-optical coefficients. Journal of Physics: Condensed Matter, 15(45):7803, 2003.

[129] M. Pascolini, S. Bonora, A. Giglia, N. Mahne, S. Nannarone, and L. Poletto. Gratings in a conical diffraction mounting for an extreme-ultraviolet time-delay-compensated monochromator. Applied Optics, 45(14):3253–3262, May 2006.

[130] J. Zak, E. R. Moog, C. Liu, and S. D. Bader. Magneto-optics of multilayers with arbitrary magnetization directions. Physical Review B, 43(8):6423–6429, March 1991.

[131] William H. McMaster. Matrix Representation of Polarization. Reviews of Modern Physics, 33(1):8–28, January 1961.

[132] A. Scholl, L. Baumgarten, R. Jacquemin, and W. Eberhardt. Ultrafast Spin Dynamics of Ferromagnetic Thin Films Observed by fs Spin-Resolved Two-Photon Photoemission. Physical Review Letters, 79(25):5146–5149, December 1997.

[133] Jean-Yves Bigot, Mircea Vomir, and Eric Beaurepaire. Coherent ultrafast magnetism induced by femtosecond laser pulses. Nature Physics, 5(7):515, July 2009.

[134] Uwe Bovensiepen. Femtomagnetism: Magnetism in step with light. Nature Physics, 5(7):461–463, July 2009.

[135] G. P. Zhang, W. Hübner, Georgios Lefkidis, Yihua Bai, and Thomas F. George. Paradigm of the time-resolved magneto-optical Kerr effect for femtosecond magnetism. Nature Physics, 5(7):499–502, July 2009.

[136] Andrei Kirilyuk, Alexey V. Kimel, and Theo Rasing. Ultrafast optical manipulation of magnetic order. Reviews of Modern Physics, 82(3):2731–2784, September 2010.

[137] H.-S. Rhie, H. A. Dürr, and W. Eberhardt. Femtosecond Electron and Spin Dynamics in $\mathrm{N}\mathrm{i}/\mathrm{W}(110)$ Films. Physical Review Letters, 90(24):247201, June 2003.

[138] A. Fognini, T. U. Michlmayr, G. Salvatella, C. Wetli, U. Ramsperger, T. Bähler, F. Sorgenfrei, M. Beye, A. Eschenlohr, N. Pontius, C. Stamm, F. Hieke, M. Dell'Angela, S. de Jong, R. Kukreja, N. Gerasimova, V. Rybnikov, A. Al-Shemmary, H. Redlin, J. Raabe, A. Föhlisch, H. A. Dürr, W. Wurth, D. Pescia, A. Vaterlaus, and Y. Acremann. Ultrafast reduction of the total magnetization in iron. Applied Physics Letters, 104(3):032402, January 2014.

[139] Martin Teichmann, Björn Frietsch, Kristian Döbrich, Robert Carley, and Martin Weinelt. Transient band structures in the ultrafast demagnetization of ferromagnetic gadolinium and terbium. Physical Review B, 91(1):014425, January 2015.

[140] Beatrice Andres, Marc Christ, Cornelius Gahl, Marko Wietstruk, Martin Weinelt, and Jürgen Kirschner. Separating Exchange Splitting from Spin Mixing in Gadolinium by Femtosecond Laser Excitation. Physical Review Letters, 115(20):207404, November 2015.

[141] B. Frietsch, J. Bowlan, R. Carley, M. Teichmann, S. Wienholdt, D. Hinzke, U. Nowak, K. Carva, P. M. Oppeneer, and M. Weinelt. Disparate ultrafast dynamics of itinerant and localized magnetic moments in gadolinium metal. Nature Communications, 6:8262, September 2015.

[142] A. Weber, F. Pressacco, S. Günther, E. Mancini, P. M. Oppeneer, and C. H. Back. Ultrafast demagnetization dynamics of thin Fe/W(110) films: Comparison of time- and spin-resolved photoemission with time-resolved magneto-optic experiments. Physical Review B, 84(13):132412, October 2011.

[143] M. Cinchetti, M. Sánchez Albaneda, D. Hoffmann, T. Roth, J.-P. Wüstenberg, M. Krauß, O. Andreyev, H. C. Schneider, M. Bauer, and M. Aeschlimann. Spin-Flip Processes and Ultrafast Magnetization Dynamics in Co: Unifying the Microscopic and Macroscopic View of Femtosecond Magnetism. Physical Review Letters, 97(17):177201, October 2006.

[144] Phoebe Tengdin, Wenjing You, Cong Chen, Xun Shi, Dmitriy Zusin, Yingchao Zhang, Christian Gentry, Adam Blonsky, Mark Keller, Peter M. Oppeneer, Henry C. Kapteyn, Zhensheng Tao, and Margaret M. Murnane. Critical behavior within 20 fs drives the out-of-equilibrium laser-induced magnetic phase transition in nickel. Science Advances, 4(3):eaap9744, March 2018.

[145] Wenjing You, Phoebe Tengdin, Cong Chen, Xun Shi, Dmitriy Zusin, Yingchao Zhang, Christian Gentry, Adam Blonsky, Mark Keller, Peter M. Oppeneer, Henry Kapteyn, Zhensheng Tao, and Margaret Murnane. Correlating EUV TMOKE and ARPES measurements to understand the temporal and spatial length scales underlying ultrafast demagnetization in ferromagnets. arXiv:1712.07085 [cond-mat], December 2017. arXiv: 1712.07085.

[146] A. B. Schmidt, M. Pickel, M. Donath, P. Buczek, A. Ernst, V. P. Zhukov, P. M. Echenique, L. M. Sandratskii, E. V. Chulkov, and M. Weinelt. Ultrafast Magnon Generation in an Fe Film on Cu(100). Physical Review Letters, 105(19):197401, November 2010.

[147] U. Atxitia, O. Chubykalo-Fesenko, N. Kazantseva, D. Hinzke, U. Nowak, and R. W. Chantrell. Micromagnetic modeling of laser-induced magnetization dynamics using the Landau-Lifshitz-Bloch equation. Applied Physics Letters, 91(23):232507, December 2007.

[148] E. Carpene, E. Mancini, C. Dallera, M. Brenna, E. Puppin, and S. De Silvestri. Dynamics of electron-magnon interaction and ultrafast demagnetization in thin iron films. Physical Review B, 78(17):174422, November 2008.

[149] E. Carpene, H. Hedayat, F. Boschini, and C. Dallera. Ultrafast demagnetization of metals: Collapsed exchange versus collective excitations. Physical Review B, 91(17):174414, May 2015.

[150] N. Kazantseva, U. Nowak, R. W. Chantrell, J. Hohlfeld, and A. Rebei. Slow recovery of the magnetisation after a sub-picosecond heat pulse. EPL, 81(2):27004, January 2008.

[151] D. Hinzke, U. Atxitia, K. Carva, P. Nieves, O. Chubykalo-Fesenko, P. M. Oppeneer, and U. Nowak. Multiscale modeling of ultrafast element-specific magnetization dynamics of ferromagnetic alloys. Physical Review B, 92(5):054412, August 2015.

[152] Maria Stamenova, Jacopo Simoni, and Stefano Sanvito. Role of spin-orbit interaction in the ultrafast demagnetization of small iron clusters. Physical Review B, 94(1):014423, July 2016.

[153] B. Y. Mueller, A. Baral, S. Vollmar, M. Cinchetti, M. Aeschlimann, H. C. Schneider, and B. Rethfeld. Feedback Effect during Ultrafast Demagnetization Dynamics in Ferromagnets. Physical Review Letters, 111(16):167204, October 2013.

[154] M. Battiato, K. Carva, and P. M. Oppeneer. Superdiffusive Spin Transport as a Mechanism of Ultrafast Demagnetization. Physical Review Letters, 105(2):027203, July 2010.

[155] M. Battiato, K. Carva, and P. M. Oppeneer. Theory of laser-induced ultrafast superdiffusive spin transport in layered heterostructures. Physical Review B, 86(2):024404, July 2012.

[156] Emrah Turgut, Chan La-o vorakiat, Justin M. Shaw, Patrik Grychtol, Hans T. Nembach, Dennis Rudolf, Roman Adam, Martin Aeschlimann, Claus M. Schneider, Thomas J. Silva, Margaret M. Murnane, Henry C. Kapteyn, and Stefan Mathias. Controlling the Competition between Optically Induced Ultrafast Spin-Flip Scattering and Spin Transport in Magnetic Multilayers. Physical Review Letters, 110(19):197201, May 2013.

[157] H. A. Mook and D. McK. Paul. Neutron-Scattering Measurement of the Spin-Wave Spectra for Nickel. Physical Review Letters, 54(3):227–229, January 1985.

[158] R. Vollmer, M. Etzkorn, P. S. Anil Kumar, H. Ibach, and J. Kirschner. Spin-Polarized Electron Energy Loss Spectroscopy of High Energy, Large Wave Vector Spin Waves in Ultrathin fcc Co Films on Cu(001). Physical Review Letters, 91(14):147201, September 2003.

[159] G. K. H. Madsen D. Kvasnicka P. Blaha, K. Schwarz and J. Luitz. WIEN2k: An Augmented Plane Wave plus Local Orbitals Program for Calculating Crystal Properties. Technische Universität Wien, Wien, 2008.

[160] B. L. Henke, E. M. Gullikson, and J. C. Davis. X-Ray Interactions: Photoabsorption, Scattering, Transmission, and Reflection at E = 50-30,000 eV, Z = 1-92. Atomic Data and Nuclear Data Tables, 54(2):181–342, July 1993.

[161] V. Lucarini, J. Saarinen, K.-E. Peiponen, and E. Vartiainen. Kramers-Kronig Relations in Optical Materials Research. Springer, March 2006.

[162] John S. Toll. Causality and the Dispersion Relation: Logical Foundations. Physical Review, 104(6):1760–1770, December 1956.

[163] C. T. Chen, Y. U. Idzerda, H.-J. Lin, N. V. Smith, G. Meigs, E. Chaban, G. H. Ho, E. Pellegrin, and F. Sette. Experimental Confirmation of the X-Ray Magnetic Circular Dichroism Sum Rules for Iron and Cobalt. Physical Review Letters, 75(1):152–155, July 1995.

[164] Hartmut Höchst, Dai Zhao, and David L. Huber. M2,3 magnetic circular dichroism (MCD) measurements of Fe, Co and Ni using a newly developed quadruple reflection phase shifter. Surface Science, 352:998–1002, May 1996.

[165] Z. Q Qiu and S. D Bader. Surface magneto-optic Kerr effect (SMOKE). Journal of Magnetism and Magnetic Materials, 200(1):664–678, October 1999.

[166] M. F. Tesch, M. C. Gilbert, H.-Ch Mertins, D. E. Bürgler, U. Berges, and C. M. Schneider. X-ray magneto-optical polarization spectroscopy: an analysis from the visible region to the x-ray regime. Applied Optics, 52(18):4294–4310, June 2013.

[167] H.-C. Mertins, S. Valencia, A. Gaupp, W. Gudat, P. M. Oppeneer, and C. M. Schneider. Magneto-optical polarization spectroscopy with soft X-rays. Applied Physics A, 80(5):1011–1020, February 2005.

[168] S. Valencia, A. Gaupp, W. Gudat, H.-Ch Mertins, P. M. Oppeneer, D. Abramsohn, and C. M. Schneider. Faraday rotation spectra at shallow core levels: 3 p edges of Fe, Co, and Ni. New Journal of Physics, 8(10):254, 2006.

[169] S. Valencia, A. Kleibert, A. Gaupp, J. Rusz, D. Legut, J. Bansmann, W. Gudat, and P. M. Oppeneer. Quadratic X-Ray Magneto-Optical Effect upon Reflection in a Near-Normal-Incidence Configuration at the M Edges of $3d$-Transition Metals. Physical Review Letters, 104(18):187401, May 2010.

[170] J. B. Kortright and Sang-Koog Kim. Resonant magneto-optical properties of Fe near its $2p$ levels: Measurement and applications. Physical Review B, 62(18):12216–12228, November 2000.

[171] Luca Guidoni, Eric Beaurepaire, and Jean-Yves Bigot. Magneto-optics in the Ultrafast Regime: Thermalization of Spin Populations in Ferromagnetic Films. Physical Review Letters, 89(1):017401, June 2002.

[172] Steffen Eich, Moritz Plötzing, Markus Rollinger, Sebastian Emmerich, Roman Adam, Cong Chen, Henry Cornelius Kapteyn, Margaret M. Murnane, Lukasz Plucinski, Daniel Steil, Benjamin Stadtmüller, Mirko Cinchetti, Martin Aeschlimann, Claus M. Schneider, and Stefan Mathias. Band structure evolution during the ultrafast ferromagnetic-paramagnetic phase transition in cobalt. Science Advances, 3(3):e1602094, March 2017.

[173] I. Thomann, A. Bahabad, X. Liu, R. Trebino, M. M. Murnane, and H. C. Kapteyn. Characterizing isolated attosecond pulses from hollow-core waveguides using multi-cycle driving pulses. Optics Express, 17(6):4611–4633, March 2009.

[174] Ming-Chang Chen, Christopher Mancuso, Carlos Hernández-García, Franklin Dollar, Ben Galloway, Dimitar Popmintchev, Pei-Chi Huang, Barry Walker, Luis Plaja, Agnieszka A. Jaroń-Becker, Andreas Becker, Margaret M. Murnane, Henry C. Kapteyn, and Tenio Popmintchev. Generation of bright isolated attosecond soft X-ray pulses driven by multicycle midinfrared lasers. Proceedings of the National Academy of Sciences, page 201407421, May 2014.

[175] Tenio Popmintchev, Ming-Chang Chen, Paul Arpin, Margaret M. Murnane, and Henry C. Kapteyn. The attosecond nonlinear optics of bright coherent X-ray generation. Nature Photonics, 4(12):822–832, December 2010.

[176] O. Klein and Y. Nishina. Über die Streuung von Strahlung durch freie Elektronen nach der neuen relativistischen Quantendynamik von Dirac. Zeitschrift für Physik, 52(11-12):853–868, November 1929.

[177] P. M. Platzman and N. Tzoar. Magnetic Scattering of X Rays from Electrons in Molecules and Solids. Physical Review B, 2(9):3556–3559, November 1970.

[178] F. De Bergevin and M. Brunel. Observation of magnetic superlattice peaks by X-ray diffraction on an antiferromagnetic NiO crystal. Physics Letters A, 39(2):141–142, April 1972.

[179] F. de Bergevin and M. Brunel. Diffraction of X-rays by magnetic materials. I. General formulae and measurements on ferro- and ferrimagnetic compounds. Acta Crystallographica Section A: Crystal Physics, Diffraction, Theoretical and General Crystallography, 37(3):314–324, May 1981.

[180] Doon Gibbs, D. E. Moncton, K. L. D'Amico, J. Bohr, and B. H. Grier. Magnetic x-ray scattering studies of holmium using synchro- tron radiation. Physical Review Letters, 55(2):234–237, July 1985.

[181] Doon Gibbs, D. R. Harshman, E. D. Isaacs, D. B. McWhan, D. Mills, and C. Vettier. Polarization and Resonance Properties of Magnetic X-Ray Scattering in Holmium. Physical Review Letters, 61(10):1241–1244, September 1988.

[182] Boris Vodungbo, Julien Gautier, Guillaume Lambert, Anna Barszczak Sardinha, Magali Lozano, Stéphane Sebban, Mathieu Ducousso, Willem Boutu, Kaigong Li, Bharati Tudu, Marina Tortarolo, Ranjit Hawaldar, Renaud Delaunay, Victor López-Flores, Jacek Arabski, Christine Boeglin, Hamed Merdji, Philippe Zeitoun, and Jan Lüning. Laser-induced ultrafast demagnetization in the presence of a nanoscale magnetic domain network. Nature Communications, 3:999, August 2012.

[183] B. Vodungbo, A. Barszczak Sardinha, J. Gautier, G. Lambert, M. Lozano, S. Sebban, E. Meltchakov, F. Delmotte, V. Lopez-Flores, J. Arabski, C. Boeglin, E. Beaurepaire, R. Delaunay, J. Lüning, and P. Zeitoun. Table-top resonant magnetic scattering with extreme ultraviolet light from high-order harmonic generation. EPL (Europhysics Letters), 94(5):54003, June 2011.

[184] Dimitar Popmintchev. Quantum and Extreme Nonlinear Optics Design of Coherent Ultrafast X-Ray Light and Applications. PhD thesis, January 2016.

[185] I. M. Boswarva, R. E. Howard, and A. B. Lidiard. Faraday effect in semiconductors. Proc. R. Soc. Lond. A, 269(1336):125–141, August 1962.

[186] W. H. Kleiner. Space-Time Symmetry of Transport Coefficients. Physical Review, 142(2):318–326, February 1966.

[187] Ofer Kfir, Sergey Zayko, Christina Nolte, Murat Sivis, Marcel Möller, Birgit Hebler, Sri Sai Phani Kanth Arekapudi, Daniel Steil, Sascha Schäfer, Manfred Albrecht, Oren Cohen, Stefan Mathias, and Claus Ropers. Nanoscale magnetic imaging using circularly polarized high-harmonic radiation. Science Advances, 3(12):eaao4641, December 2017.

[188] S. Eisebitt, J. Lüning, W. F. Schlotter, M. Lörgen, O. Hellwig, W. Eberhardt, and J. Stöhr. Lensless imaging of magnetic nanostructures by X-ray spectro-holography. Nature, 432(7019):885–888, December 2004.

[189] Ian McNulty, Janos Kirz, Chris Jacobsen, Erik H. Anderson, Malcolm R. Howells, and Dieter P. Kern. High-Resolution Imaging by Fourier Transform X-ray Holography. Science, 256(5059):1009–1012, May 1992.

[190] M. D. Perry, T. Ditmire, and B. C. Stuart. Self-phase modulation in chirped-pulse amplification. Optics Letters, 19(24):2149–2151, December 1994.

[191] A. E. Siegman. Lasers. University Science Books, 1986.

[192] S. A. Montoya, S. Couture, J. J. Chess, J. C. T. Lee, N. Kent, D. Henze, S. K. Sinha, M.-Y. Im, S. D. Kevan, P. Fischer, B. J. McMorran, V. Lomakin, S. Roy, and E. E. Fullerton. Tailoring magnetic energies to form dipole skyrmions and skyrmion lattices. Physical Review B, 95(2):024415, January 2017.

[193] Xiuzhen Yu, Maxim Mostovoy, Yusuke Tokunaga, Weizhu Zhang, Koji Kimoto, Yoshio Matsui, Yoshio Kaneko, Naoto Nagaosa, and Yoshinori Tokura. Magnetic stripes and skyrmions with helicity reversals. Proceedings of the National Academy of Sciences, 109(23):8856–8860, June 2012.

[194] X. Z. Yu, Y. Onose, N. Kanazawa, J. H. Park, J. H. Han, Y. Matsui, N. Nagaosa, and Y. Tokura. Real-space observation of a two-dimensional skyrmion crystal. Nature, 465(7300):901–904, June 2010.

[195] A. Hrabec, N. A. Porter, A. Wells, M. J. Benitez, G. Burnell, S. McVitie, D. McGrouther, T. A. Moore, and C. H. Marrows. Measuring and tailoring the Dzyaloshinskii-Moriya interaction in perpendicularly magnetized thin films. Physical Review B, 90(2):020402, July 2014.

[196] Frank Freimuth, Robert Bamler, Yuriy Mokrousov, and Achim Rosch. Phase-space Berry phases in chiral magnets: Dzyaloshinskii-Moriya interaction and the charge of skyrmions. Physical Review B, 88(21):214409, December 2013.

[197] S. Eich, A. Stange, A. V. Carr, J. Urbancic, T. Popmintchev, M. Wiesenmayer, K. Jansen, A. Ruffing, S. Jakobs, T. Rohwer, S. Hellmann, C. Chen, P. Matyba, L. Kipp, K. Rossnagel, M. Bauer, M. M. Murnane, H. C. Kapteyn, S. Mathias, and M. Aeschlimann. Time- and angle-resolved photoemission spectroscopy with optimized high-harmonic pulses using frequency-doubled Ti:Sapphire lasers. Journal of Electron Spectroscopy and Related Phenomena, 195:231–236, August 2014.

[198] Jürgen Fassbender. Magnetization Dynamics Investigated by Time-Resolved Kerr Effect Magnetometry. In Spin Dynamics in Confined Magnetic Structures II, Topics in Applied Physics, pages 59–92. Springer, Berlin, Heidelberg, 2003.

[199] I. Radu, C. Stamm, N. Pontius, T. Kachel, P. Ramm, J.-U. Thiele, H. A. Dürr, and C. H. Back. Laser-induced generation and quenching of magnetization on FeRh studied with time-resolved x-ray magnetic circular dichroism. Physical Review B, 81(10):104415, March 2010.

[200] Stefan Mathias, Chan La-o vorakiat, Justin M. Shaw, Emrah Turgut, Patrik Grychtol, Roman Adam, Dennis Rudolf, Hans T. Nembach, Thomas J. Silva, Martin Aeschlimann, Claus M. Schneider, Henry C. Kapteyn, and Margaret M. Murnane. Ultrafast element-specific magnetization dynamics of complex magnetic materials on a table-top. Journal of Electron Spectroscopy and Related Phenomena, 189:164–170, August 2013.

[201] Dennis Rudolf, Chan La-O-Vorakiat, Marco Battiato, Roman Adam, Justin M. Shaw, Emrah Turgut, Pablo Maldonado, Stefan Mathias, Patrik Grychtol, Hans T. Nembach, Thomas J. Silva, Martin Aeschlimann, Henry C. Kapteyn, Margaret M. Murnane, Claus M. Schneider, and Peter M. Oppeneer. Ultrafast magnetization enhancement in metallic multilayers driven by superdiffusive spin current. Nature Communications, 3:1037, September 2012.

[202] Ilya Razdolski, Alexandr Alekhin, Nikita Ilin, Jan P. Meyburg, Vladimir Roddatis, Detlef Diesing, Uwe Bovensiepen, and Alexey Melnikov. Nanoscale interface confinement of ultrafast spin transfer torque driving non-uniform spin dynamics. Nature Communications, 8:15007, April 2017.

[203] Tian-Min Liu, Tianhan Wang, Alexander H. Reid, Matteo Savoini, Xiaofei Wu, Benny Koene, Patrick Granitzka, Catherine E. Graves, Daniel J. Higley, Zhao Chen, Gary Razinskas, Markus Hantschmann, Andreas Scherz, Joachim Stöhr, Arata Tsukamoto, Bert Hecht, Alexey V. Kimel, Andrei Kirilyuk, Theo Rasing, and Hermann A. Dürr. Nanoscale Confinement of All-Optical Magnetic Switching in TbFeCo - Competition with Nanoscale Heterogeneity. Nano Letters, 15(10):6862–6868, October 2015.

[204] C. von Korff Schmising, B. Pfau, M. Schneider, C. M. Günther, M. Giovannella, J. Perron, B. Vodungbo, L. Müller, F. Capotondi, E. Pedersoli, N. Mahne, J. Lüning, and S. Eisebitt. Imaging Ultrafast Demagnetization Dynamics after a Spatially Localized Optical Excitation. Physical Review Letters, 112(21):217203, May 2014.

[205] B. Pfau, S. Schaffert, L. Müller, C. Gutt, A. Al-Shemmary, F. Büttner, R. Delaunay, S. Düsterer, S. Flewett, R. Frömter, J. Geilhufe, E. Guehrs, C. M. Günther, R. Hawaldar, M. Hille, N. Jaouen, A. Kobs, K. Li, J. Mohanty, H. Redlin, W. F. Schlotter, D. Stickler, R. Treusch, B. Vodungbo, M. Kläui, H. P. Oepen, J. Lüning, G. Grübel, and S. Eisebitt. Ultrafast optical demagnetization manipulates nanoscale spin structure in domain walls. Nature Communications, 3:1100, October 2012.

[206] Patrick W. Granitzka, Emmanuelle Jal, Loïc Le Guyader, Matteo Savoini, Daniel J. Higley, Tianmin Liu, Zhao Chen, Tyler Chase, Hendrik Ohldag, Georgi L. Dakovski, William F. Schlotter, Sebastian Carron, Matthias C. Hoffman, Alexander X. Gray, Padraic Shafer, Elke Arenholz, Olav Hellwig, Virat Mehta, Yukiko K. Takahashi, Jian Wang, Eric E. Fullerton, Joachim Stöhr, Alexander H. Reid, and Hermann A. Dürr. Magnetic Switching in Granular FePt Layers Promoted by Near-Field Laser Enhancement. Nano Letters, 17(4):2426–2432, April 2017.

[207] A. H. Reid, X. Shen, P. Maldonado, T. Chase, E. Jal, P. W. Granitzka, K. Carva, R. K. Li, J. Li, L. Wu, T. Vecchione, T. Liu, Z. Chen, D. J. Higley, N. Hartmann, R. Coffee, J. Wu, G. L. Dakovski, W. F. Schlotter, H. Ohldag, Y. K. Takahashi, V. Mehta, O. Hellwig, A. Fry, Y. Zhu, J. Cao, E. E. Fullerton, J. Stöhr, P. M. Oppeneer, X. J. Wang, and H. A. Dürr. Beyond a phenomenological description of magnetostriction. Nature Communications, 9(1):388, January 2018.

[208] Heinz-Dieter Nuhn, Scott Anderson, Jens Buck, Ryan Coffee, Yuantao Ding, Gregor Hartmann, Zhirong Huang, Markus Ilchen, Yurii Levashov, Anton Lindahl, Alberto Lutman, James MacArthur, Agostino Marinelli, Stefan Moeller, Franz Peters, Alexander Temnykh, Jens Viefhaus, and Zachary Wolf. Commissioning of the Delta Polarizing Undulator at LCLS. page WED01, December 2015.

[209] CXRO X-Ray Database. http://henke.lbl.gov/optical_constants/. Accessed: 2018-06-12.

[210] J. R. Fienup. Phase retrieval algorithms: a comparison. Applied Optics, 21(15):2758, August 1982.

[211] S. Marchesini, H. He, H. N. Chapman, S. P. Hau-Riege, A. Noy, M. R. Howells, U. Weierstall, and J. C. H. Spence. X-ray image reconstruction from a diffraction pattern alone. Physical Review B, 68(14):140101, October 2003.

[212] Jianwei Miao, R.L. Sandberg, and Changyong Song. Coherent X-Ray Diffraction Imaging. IEEE Journal of Selected Topics in Quantum Electronics, 18(1):399–410, January 2012.

[213] Heinz H. Bauschke, Patrick L. Combettes, and D. Russell Luke. Phase retrieval, error reduction algorithm, and Fienup variants: a view from convex optimization. Journal of the Optical Society of America A, 19(7):1334, 2002.

[214] H. M. L. Faulkner and J. M. Rodenburg. Movable Aperture Lensless Transmission Microscopy: A Novel Phase Retrieval Algorithm. Physical Review Letters, 93(2):023903, July 2004.

[215] Jianwei Miao, Tetsuya Ishikawa, Erik H. Anderson, and Keith O. Hodgson. Phase retrieval of diffraction patterns from noncrystalline samples using the oversampling method. Physical Review B, 67(17):174104, May 2003.

[216] A. Vansteenkiste and B. Van de Wiele. MuMax: A new high-performance micromagnetic simulation tool. Journal of Magnetism and Magnetic Materials, 323(21):2585–2591, November 2011.

[217] V. P. Zhukov, E. V. Chulkov, and P. M. Echenique. Lifetimes and inelastic mean free path of low-energy excited electrons in Fe, Ni, Pt, and Au: Ab initio $\mathrm{GW}+\mathrm{T}$ calculations. Physical Review B, 73(12):125105, March 2006.

[218] Shlomo Havlin and Daniel Ben-Avraham. Diffusion in disordered media. Advances in Physics, 51(1):187–292, January 2002.

[219] S. Iihama, Y. Xu, M. Deb, G. Malinowski, M. Hehn, J. Gorchon, E. E. Fullerton, and S. Mangin. Single-shot multi-level all-optical magnetization switching mediated by spin-polarized hot electron transport. arXiv:1805.02432 [cond-mat], May 2018. arXiv: 1805.02432.

[220] Yong Xu, Marwan Deb, Grégory Malinowski, Michel Hehn, Weisheng Zhao, and Stéphane Mangin. Ultrafast Magnetization Manipulation Using Single Femtosecond Light and Hot-Electron Pulses. Advanced Materials, 29(42):1703474.

[221] Max Born and Emil Wolf. Principles of Optics: Electromagnetic Theory of Propagation, Interference and Diffraction of Light. Elsevier, June 2013.

[222] Okan K. Ersoy. Diffraction, Fourier Optics and Imaging. John Wiley & Sons, December 2006.

[223] Claire Donnelly, Manuel Guizar-Sicairos, Valerio Scagnoli, Sebastian Gliga, Mirko Holler, Jörg Raabe, and Laura J. Heyderman. Three-dimensional magnetization structures revealed with X-ray vector nanotomography. Nature, 547(7663):328–331, July 2017.

[224] Jeffrey McCord. Progress in magnetic domain observation by advanced magneto-optical microscopy. Journal of Physics D: Applied Physics, 48(33):333001, 2015.

[225] I. V. Soldatov and R. Schäfer. Advances in quantitative Kerr microscopy. Physical Review B, 95(1):014426, January 2017.

[226] A. M. Chang, H. D. Hallen, L. Harriott, H. F. Hess, H. L. Kao, J. Kwo, R. E. Miller, R. Wolfe, J. van der Ziel, and T. Y. Chang. Scanning Hall probe microscopy. Applied Physics Letters, 61(16):1974–1976, October 1992.

[227] A. Oral, S. J. Bending, and M. Henini. Scanning Hall probe microscopy of superconductors and magnetic materials. Journal of Vacuum Science & Technology B: Microelectronics and Nanometer Structures Processing, Measurement, and Phenomena, 14(2):1202–1205, March 1996.

[228] J. R. Kirtley, M. B. Ketchen, K. G. Stawiasz, J. Z. Sun, W. J. Gallagher, S. H. Blanton, and S. J. Wind. High-resolution scanning SQUID microscope. Applied Physics Letters, 66(9):1138–1140, February 1995.

[229] J. R. Kirtley, M. B. Ketchen, C. C. Tsuei, J. Z. Sun, W. J. Gallagher, L. S. Yu-Jahnes, A. Gupta, K. G. Stawiasz, and S. J. Wind. Design and applications of a scanning SQUID microscope. IBM Journal of Research and Development, 39(6):655–668, November 1995.

[230] Herbert Hopster and Hans Peter Oepen. Magnetic Microscopy of Nanostructures. Springer Science & Business Media, March 2006.

[231] Siddharth Rao, Jan Rhensius, Andre Bisig, Mohamad-Assaad Mawass, Markus Weigand, Mathias Kläui, Charanjit S. Bhatia, and Hyunsoo Yang. Time-resolved imaging of pulse-induced magnetization reversal with a microwave assist field. Scientific Reports, 5:10695, May 2015.

[232] Simone Anders, Howard A. Padmore, Robert M. Duarte, Timothy Renner, Thomas Stammler, Andreas Scholl, Michael R. Scheinfein, Joachim Stöhr, Laurent Séve, and Boris Sinkovic. Photoemission electron microscope for the study of magnetic materials. Review of Scientific Instruments, 70(10):3973–3981, September 1999.

[233] E. Bauer. LEEM studies of the early stages of epitaxial growth. Applied Surface Science, 92:20–29, February 1996.

[234] F. Kronast, J. Schlichting, F. Radu, S. K. Mishra, T. Noll, and H. A. Dürr. Spin-resolved photoemission microscopy and magnetic imaging in applied magnetic fields. Surface and Interface Analysis, 42(10-11):1532–1536.

[235] Y. Martin and H. K. Wickramasinghe. Magnetic imaging by ‘‘force microscopy’’ with 1000 å resolution. Applied Physics Letters, 50(20):1455–1457, May 1987.

[236] J. J. Sáenz, N. García, P. Grütter, E. Meyer, H. Heinzelmann, R. Wiesendanger, L. Rosenthaler, H. R. Hidber, and H.-J. Güntherodt. Observation of magnetic forces by the atomic force microscope. Journal of Applied Physics, 62(10):4293–4295, November 1987.

[237] Maurizio Sacchi, Horia Popescu, Nicolas Jaouen, Marina Tortarolo, Franck Fortuna, Renaud Delaunay, and Carlo Spezzani. Magnetic imaging by Fourier transform holography using linearly polarized x-rays. Optics Express, 20(9):9769–9776, April 2012.

[238] Carlo Spezzani, Franck Fortuna, Renaud Delaunay, Horia Popescu, and Maurizio Sacchi. X-ray holographic imaging of magnetic order in patterned Co/Pd multilayers. Physical Review B, 88(22):224420, December 2013.

[239] Stefan Schaffert, Bastian Pfau, Jan Geilhufe, Christian M. Günther, Michael Schneider, Clemens von Korff Schmising, and Stefan Eisebitt. High-resolution magnetic-domain imaging by Fourier transform holography at 21 nm wavelength. New Journal of Physics, 15(9):093042, 2013.

[240] J. M. Rodenburg, A. C. Hurst, A. G. Cullis, B. R. Dobson, F. Pfeiffer, O. Bunk, C. David, K. Jefimovs, and I. Johnson. Hard-X-Ray Lensless Imaging of Extended Objects. Physical Review Letters, 98(3):034801, January 2007.

[241] H. M. L. Faulkner and J. M. Rodenburg. Error tolerance of an iterative phase retrieval algorithm for moveable illumination microscopy. Ultramicroscopy, 103(2):153–164, May 2005.

[242] Andrew M. Maiden and John M. Rodenburg. An improved ptychographical phase retrieval algorithm for diffractive imaging. Ultramicroscopy, 109(10):1256–1262, September 2009.

[243] S. Marchesini. Invited Article: A unified evaluation of iterative projection algorithms for phase retrieval. Review of Scientific Instruments, 78(1):011301, January 2007.

[244] Peter Fischer. Magnetic imaging with polarized soft x-rays. Journal of Physics D: Applied Physics, 50(31):313002, 2017.

[245] Albert V. Baez. Fresnel Zone Plate for Optical Image Formation Using Extreme Ultraviolet and Soft X Radiation. JOSA, 51(4):405–412, April 1961.

[246] Ashish Tripathi, Jyoti Mohanty, Sebastian H. Dietze, Oleg G. Shpyrko, Erik Shipton, Eric E. Fullerton, Sang Soo Kim, and Ian McNulty. Dichroic coherent diffractive imaging. Proceedings of the National Academy of Sciences, 108(33):13393–13398, August 2011.

[247] Joshua J. Turner, Xiaojing Huang, Oleg Krupin, Keoki A. Seu, Daniel Parks, Stephen Kevan, Enju Lima, Kim Kisslinger, Ian McNulty, Richard Gambino, Stephane Mangin, Sujoy Roy, and Peter Fischer. X-Ray Diffraction Microscopy of Magnetic Structures. Physical Review Letters, 107(3):033904, July 2011.

[248] R. P. Millane. Phase retrieval in crystallography and optics. JOSA A, 7(3):394–411, March 1990.

[249] R.W. Gerchberg and A Saxton W. O. A practical algorithm for the determination of phase from image and diffraction plane pictures. Optik, 35:237–250, November 1971.

[250] Joseph W. Goodman. Introduction to Fourier Optics. Roberts and Company Publishers, 2005.

[251] D. Sayre. Some implications of a theorem due to Shannon. Acta Crystallographica, 5(6):843–843, November 1952.

[252] D. Russell Luke. Relaxed averaged alternating reflections for diffraction imaging. Inverse Problems, 21(1):37, 2005.

[253] J. M. Rodenburg and H. M. L. Faulkner. A phase retrieval algorithm for shifting illumination. Applied Physics Letters, 85(20):4795–4797, November 2004.

[254] R. M. Karl, G. F. Mancini, D. Gardner, E. Shanblatt, J. Knobloch, T. Frazer, J. Hernandez-Charpak, B. Abad Mayor, M. Tanksalvala, C. Porter, C. Bevis, D. Adams, H. Kapteyn, and M. Murnane. Full-Field Functional Imaging of Nanoscale Dynamics Using Tabletop High Harmonics. In Conference on Lasers and Electro-Optics (2017), paper JTh5C.8, page JTh5C.8. Optical Society of America, May 2017.

[255] Darren J. Batey, Daniel Claus, and John M. Rodenburg. Information multiplexing in ptychography. Ultramicroscopy, 138:13–21, March 2014.

[256] Pierre Thibault and Andreas Menzel. Reconstructing state mixtures from diffraction measurements. Nature, 494(7435):68–71, February 2013.

[257] D. J. Batey, T. B. Edo, C. Rau, U. Wagner, Z. D. Pešić, T. A. Waigh, and J. M. Rodenburg. Reciprocal-space up-sampling from real-space oversampling in x-ray ptychography. Physical Review A, 89(4):043812, April 2014.

[258] Daniel Claus and John M. Rodenburg. Multiwavelength Ptychography. In Fringe 2013, pages 689–694. Springer, Berlin, Heidelberg, 2014.

[259] Charles Bevis, Robert Karl, Jonathan Reichanadter, Dennis F. Gardner, Christina Porter, Elisabeth Shanblatt, Michael Tanksalvala, Giulia F. Mancini, Henry Kapteyn, Margaret Murnane, and Daniel Adams. Multiple beam ptychography for large field-of-view, high throughput, quantitative phase contrast imaging. Ultramicroscopy, 184:164–171, January 2018.

[260] Robert Karl, Charles Bevis, Raymond Lopez-Rios, Jonathan Reichanadter, Dennis Gardner, Christina Porter, Elisabeth Shanblatt, Michael Tanksalvala, Giulia F. Mancini, Margaret Murnane, Henry Kapteyn, and Daniel Adams. Spatial, spectral, and polarization multiplexed ptychography. Optics Express, 23(23):30250–30258, November 2015.

[261] S. Sachdev. Entangling Superconductivity and Antiferromagnetism. Science, 336(6088):1510–1511, June 2012.

[262] J. Stöhr, A. Scholl, T. J. Regan, S. Anders, J. Lüning, M. R. Scheinfein, H. A. Padmore, and R. L. White. Images of the Antiferromagnetic Structure of a NiO(100) Surface by Means of X-Ray Magnetic Linear Dichroism Spectromicroscopy. Physical Review Letters, 83(9):1862–1865, August 1999.

[263] A. Scholl, J. Stöhr, J. Lüning, J. W. Seo, J. Fompeyrine, H. Siegwart, J.-P. Locquet, F. Nolting, S. Anders, E. E. Fullerton, M. R. Scheinfein, and H. A. Padmore. Observation of Antiferromagnetic Domains in Epitaxial Thin Films. Science, 287(5455):1014–1016, February 2000.

[264] F. Nolting, A. Scholl, J. Stöhr, J. W. Seo, J. Fompeyrine, H. Siegwart, J.-P. Locquet, S. Anders, J. Lüning, E. E. Fullerton, M. F. Toney, M. R. Scheinfein, and H. A. Padmore. Direct observation of the alignment of ferromagnetic spins by antiferromagnetic spins. Nature, 405(6788):767–769, June 2000.

[265] P. Elliott, T. Müller, J. K. Dewhurst, S. Sharma, and E. K. U. Gross. Ultrafast laser induced local magnetization dynamics in Heusler compounds. Scientific Reports, 6:38911, December 2016.

[266] R. Chimata, E. K. Delczeg-Czirjak, J. Chico, M. Pereiro, B. Sanyal, O. Eriksson, and D. Thonig. Ultrafast magnetization dynamics in pure and doped Heusler and inverse Heusler alloys. arXiv:1802.07195 [cond-mat], February 2018. arXiv: 1802.07195.

[267] Jiro Yoshida and Shuichi Iida. X-Ray Study of the Phase Transition in Magnetite. Journal of the Physical Society of Japan, 47(5):1627–1633, November 1979.

[268] J. E. Lorenzo, C. Mazzoli, N. Jaouen, C. Detlefs, D. Mannix, S. Grenier, Y. Joly, and C. Marin. Charge and Orbital Correlations at and above the Verwey Phase Transition in Magnetite. Physical Review Letters, 101(22):226401, November 2008.

[269] Sungbae Lee, Alexandra Fursina, John T. Mayo, Cafer T. Yavuz, Vicki L. Colvin, R. G. Sumesh Sofin, Igor V. Shvets, and Douglas Natelson. Electrically driven phase transition in magnetite nanostructures. Nature Materials, 7(2):130–133, February 2008.

[270] Ki-Suk Lee, Dae-Eun Jeong, Sang-Koog Kim, and J. B. Kortright. Soft x-ray resonant magneto-optical Kerr effect as a depth-sensitive probe of magnetic heterogeneity: A simulation approach. Journal of Applied Physics, 97(8):083519, April 2005.

[271] Sang-Koog Kim, Ki-Suk Lee, J. B. Kortright, and Sung-Chul Shin. Soft x-ray resonant Kerr rotation measurement and simulation of element-resolved and interface-sensitive magnetization reversals in a NiFe/FeMn/Co trilayer structure. Applied Physics Letters, 86(10):102502, March 2005.

[272] H. L. Meyerheim, J.-M. Tonnerre, L. Sandratskii, H. C. N. Tolentino, M. Przybylski, Y. Gabi, F. Yildiz, X. L. Fu, E. Bontempi, S. Grenier, and J. Kirschner. New Model for Magnetism in Ultrathin fcc Fe on Cu(001). Physical Review Letters, 103(26):267202, December 2009.

[273] K. Postava, J. Hamrle, J. Hamrlová, D. Hrabovskš, O. Životskš, J. Pištora, and D. Lukáš. Depth and material sensitivity in magneto–optic nanostructures. International Journal of Nanotechnology, 9(8-9):784–808, January 2012.

[274] J. Hamrle, J. Ferré, M. Nývlt, and Š. Višňovský. In-depth resolution of the magneto-optical Kerr effect in ferromagnetic multilayers. Physical Review B, 66(22):224423, December 2002.

[275] A. J. Schellekens, N. de Vries, J. Lucassen, and B. Koopmans. Exploring laser-induced interlayer spin transfer by an all-optical method. Physical Review B, 90(10):104429, September 2014.

[276] J. Wieczorek, A. Eschenlohr, B. Weidtmann, M. Rösner, N. Bergeard, A. Tarasevitch, T. O. Wehling, and U. Bovensiepen. Separation of ultrafast spin currents and spin-flip scattering in Co/Cu(001) driven by femtosecond laser excitation employing the complex magneto-optical Kerr effect. Physical Review B, 92(17):174410, November 2015.

[277] Andrea Eschenlohr, Jens Wieczorek, Jinghao Chen, Boris Weidtmann, Malte Rösner, Nicolas Bergeard, Alexander Tarasevitch, Tim O. Wehling, and Uwe Bovensiepen. Analyzing ultrafast laser-induced demagnetization in Co/Cu(001) via the depth sensitivity of the time-resolved transversal magneto-optical Kerr effect. page 97461E, March 2016.

[278] G. Traeger, L. Wenzel, and A. Hubert. Computer experiments on the information depth and the figure of merit in magnetooptics. ResearchGate, 131(1):201–227, May 1992.

[279] S Macke and E Goering. Magnetic reflectometry of heterostructures. Journal of Physics: Condensed Matter, 26(36):363201, September 2014.

[280] M. G. Moharam and T. K. Gaylord. Rigorous coupled-wave analysis of planar-grating diffraction. JOSA, 71(7):811–818, July 1981.

[281] M. G. Moharam, T. K. Gaylord, Eric B. Grann, and Drew A. Pommet. Formulation for stable and efficient implementation of the rigorous coupled-wave analysis of binary gratings. JOSA A, 12(5):1068–1076, May 1995.

[282] M. G. Moharam, T. K. Gaylord, Drew A. Pommet, and Eric B. Grann. Stable implementation of the rigorous coupled-wave analysis for surface-relief gratings: enhanced transmittance matrix approach. JOSA A, 12(5):1077–1086, May 1995.

[283] Raymond Rumpf. DESIGN AND OPTIMIZATION OF NANO-OPTICAL ELEMENTS BY COUPLING FABRICATION TO OPTICAL BEHAVIOR. PhD thesis, University of Central Florida, 2006.

[284] Robert M. Gray. Toeplitz and Circulant Matrices: A Review. Now Publishers Inc, 2006. Google-Books-ID: PrOi92L5dAUC.

[285] Richard Bellman. Introduction to Matrix Analysis: Second Edition. SIAM, December 1997.

[286] D. L. Connelly, J. S. Loomis, and D. E. Mapother. Specific Heat of Nickel near the Curie Temperature. Physical Review B, 3(3):924–934, February 1971.

[287] G. K. White. Electrons in transition metals at high temperatures. Australian Journal of Physics, 46:707, 1993.

[288] ROBERT B. GRIFFITHS. Ferromagnetic Heat Capacity in an External Magnetic Field near the Critical Point. Physical Review, 188(2):942–947, December 1969.

[289] Richard Bozorth. Ferromagnetism. IEEE Press, 1993.

[290] Jr. Chase, M.W. NIST-JANAF Themochemical Tables, Fourth Edition, Monograph 9. Journal of Physical and Chemical Reference Data, 1998.

[291] Johannes Kimling, Judith Kimling, R. B. Wilson, Birgit Hebler, Manfred Albrecht, and David G. Cahill. Ultrafast demagnetization of FePt:Cu thin films and the role of magnetic heat capacity. Physical Review B, 90(22):224408, December 2014.

[292] Johannes Kimling and David G. Cahill. Spin diffusion induced by pulsed-laser heating and the role of spin heat accumulation. Physical Review B, 95(1):014402, January 2017.

[293] Johannes Kimling, R. B. Wilson, Karsten Rott, Judith Kimling, Günter Reiss, and David G. Cahill. Spin-dependent thermal transport perpendicular to the planes of Co/Cu multilayers. Physical Review B, 91(14):144405, April 2015.

[294] Sergei I. Anisimov and Baerbel Rethfeld. Theory of ultrashort laser pulse interaction with a metal. volume 3093, pages 192–204. International Society for Optics and Photonics, April 1997.

[295] Dmitriy S. Ivanov and Leonid V. Zhigilei. Combined atomistic-continuum modeling of short-pulse laser melting and disintegration of metal films. Physical Review B, 68(6):064114, August 2003.

[296] Yeram Sarkis Touloukian, R. W. Powell, and C. Y. Ho. Thermal Conductivity. Springer, 1990. Google-Books-ID: jDfDmwEACAAJ.

[297] Hossein Ftouni, Christophe Blanc, Dimitri Tainoff, Andrew D. Fefferman, Martial Defoort, Kunal J. Lulla, Jacques Richard, Eddy Collin, and Olivier Bourgeois. Thermal conductivity of silicon nitride membranes is not sensitive to stress. Physical Review B, 92(12):125439, September 2015.

[298] Colin D. Landon, Rudeger H. T. Wilke, Michael T. Brumbach, Geoff L. Brennecka, Mia Blea-Kirby, Jon F. Ihlefeld, Matthew J. Marinella, and Thomas E. Beechem. Thermal transport in tantalum oxide films for memristive applications. Applied Physics Letters, 107(2):023108, July 2015.

[299] Zhibin Lin, Leonid V. Zhigilei, and Vittorio Celli. Electron-phonon coupling and electron heat capacity of metals under conditions of strong electron-phonon nonequilibrium. Physical Review B, 77(7):075133, February 2008.

[300] G. Grimvall. The Electron-Phonon Interaction in Normal Metals. Physica Scripta, 14(1-2):63, 1976.

[301] W. L. McMillan. Transition Temperature of Strong-Coupled Superconductors. Physical Review, 167(2):331–344, March 1968.

[302] T. Jarlborg and M. Peter. Electronic structure, magnetism and curie temperatures in Fe, Co and Ni. Journal of Magnetism and Magnetic Materials, 42(1):89–99, March 1984.

[303] T Jarlborg. Spin fluctuations, electron–phonon coupling and superconductivity in near-magnetic elementary metals—Fe, Co, Ni and Pd. Physica C: Superconductivity, 385(4):513–524, April 2003.

[304] P. B. Allen. Electron-Phonon Effects in the Infrared Properties of Metals. Physical Review B, 3(2):305–320, January 1971.

[305] Abdrabuh Al-Lehaibi, James C. Swihart, William H. Butler, and Frank J. Pinski. Electron-phonon interaction effects in tantalum. Physical Review B, 36(8):4103–4111, September 1987.

[306] Pui-Wai Ma, S. L. Dudarev, and C. H. Woo. Spin-lattice-electron dynamics simulations of magnetic materials. Physical Review B, 85(18):184301, May 2012.

Appendix A

Depth Sensitivity of T-MOKE

To date, depth resolution has been achieved by simultaneously measuring Kerr ellipticity and Kerr rotation, which is known as the complex Kerr effect and has been used to capture the depth profiles of the magnetization in thin films, multilayers, and nano-strucures [270, 271, 272, 273, 274] as well as to measure transient changes to the depth profile in the course of ultrafast demagnetization and thus uncover the role of ultrafast spin transport [275, 202, 276]. The depth sensitivity of T-MOKE, which is a pure intensity measurement, was also used in simulations in order to determine the role of laser-induced spin currents in Co [277] as well as to understand the depth-resolved critical behavior in Ni [144]. Below, I present a calculation of the depth sensitivity of T-MOKE.

Assuming that an infinitesimally thin layer of thickness dz at a depth z contributes an amount $\xi(z)dz$ to the total asymmetry A, the latter can be expressed as

$$A = \int_0^d \xi(z)dz, \tag{A.1}$$

where d is the film thickness and $\xi(z)$ is called the depth sensitivity function.

In deriving the depth sensitivity function I follow the approach of Ref. [278]. The approach is based on subdividing a magnetic film into thin layers of thickness dz and setting the magnetization of all but one layer at depth z to zero, as shown in Fig. A.1. At each position z of the layer, the T-MOKE asymmetry dA is calculated using the multilayer formalism described in Chapter 4, and the depth sensitivity is then determined as $\xi(z) = \frac{\partial A}{\partial z}\big|_z$. Such an approach is based on the assumption that the responses of individual layers are independent of one another. Generally

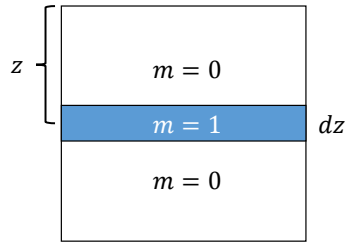

Figure A.1: An approach for a depth-sensitive T-MOKE calculation. The depth sensitivity function is found by calculating the T-MOKE asymmetry at each position of the magnetized sublayer.

speaking, this is not necessarily true, and small corrections need to be made to $\xi(z)$ calculated in the manner described above. I implement the corrections by repeating the calculation for the structure in Fig. A.1, with the only difference that a non-magnetized thin layer is now translated along the depth of a magnetized material. The resulting calculated quantity at each layer position is $A_0 - \xi(z)dz$, where A_0 is the net T-MOKE asymmetry of the film. The corrected depth sensitivity is found as an average of the depth sensitivities calculated using the two methods described above. An example of $\xi(z)$ calculated at a 52° incidence for a 10 nm Co film with a multilayer composition of SiO_2 (150 nm)/Co (10 nm)/GeO_2 (3 nm) and grown on a Si substrate is shown in Fig. A.2. Interestingly, the depth sensitivity switches sign a ∼5 nm due to a phase accumulation in the probe wave propagating through the film, which could mean that the T-MOKE asymmetry can be optimized by adjusting the thicknesses of the sample's layers, and, particularly, making the magnetic film somewhat thinner.

It is sometimes assumed that T-MOKE is only sensitive to interfaces, where there is a discontinuity in the optical properties of two media, which gives rise to a reflected wave, and thus any changes of the magnetization in the bulk of the film cannot be detected. This assumption is incorrect because any variations of the magnetization within the magnetic film are mapped onto spatial inhomogeneities of its optical properties, which reflect light and, therefore, affect the T-MOKE signal. Mathematically, this is expressed as

$$A\left[m(z)\right] = \int_0^d m(z)\xi(z)dz. \tag{A.2}$$

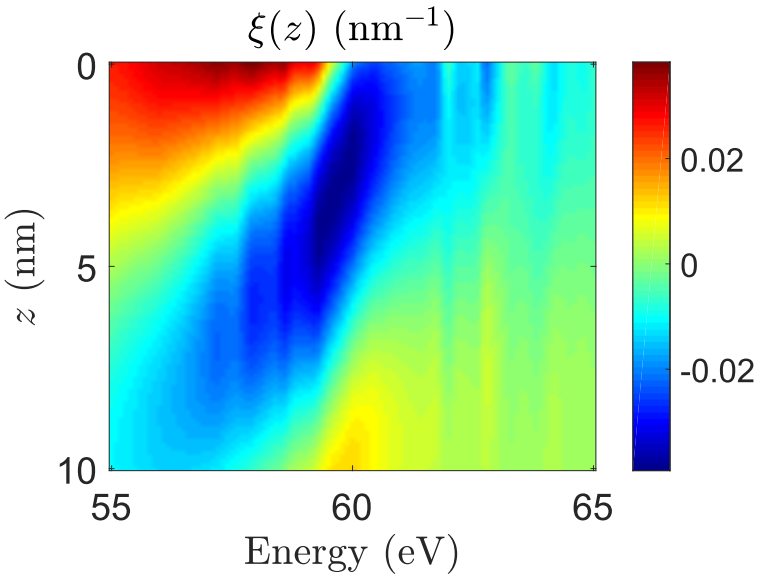

Figure A.2: T-MOKE EUV depth sensitivity function of a 10 nm Co film with a multilayer composition of SiO_2 (150 nm)/Co (10 nm)/GeO_2 (3 nm) at a 52° incidence. The magneto-optical Voigt parameter Q was taken from Ref. [168].

Hence, T-MOKE should, in principle, be able to capture a non-uniform depth profile of the magnetization $m(z)$. The idea is similar to that of X-ray reflectometry, where element composition profiles are deduced from angle-dependent reflectivity curves [279]. In order to perform such a measurement, a series of configurations has to be found, for example, by taking T-MOKE measurements at different angles of incidence, for which the corresponding functions $\xi(z)$ are sufficiently different from one another and sample different depths of the film. In that case, a system of equations can be obtained based on eq. (A.2), and problem (A.2) can thus be inverted. For EUV T-MOKE, however, sweeping the energy, polarization, magnetization direction, and angle of incidence parameter spaces did not result in a well-conditioned system of equations that could yield a unique solution for $m(z)$. The knowledge of the depth sensitivity function is, nonetheless, useful because it allows an optimization of the sample design in order to maximize the T-MOKE asymmetry, and can also be used in simulations, e.g. for understanding the response of a sample to an ultrafast laser excitation.

Appendix B

Rigorous Coupled-Wave Analysis

In this appendix, I provide a brief overview of the Rigorous Coupled-Wave Analysis (RCWA) method. RCWA was proposed by M.G. Moharam and T.K. Gaylord in the early 1980's [280] as an efficient semi-analytical method to treat the problem of diffraction of light by a general planar grating. Subsequent developments of the method, such as the Enhanced Transmittance Matrix approach (ETM), improved the stability and convergence of RCWA [281, 282]. A comprehensive and thorough review of RCWA as well as additional references can be found in Ref. [283]. I follow [283] in deriving the RCWA below.

RCWA solves Maxwell's equations without any approximations (hence the name "rigorous") in the Fourier space. The propagation in the longitudinal z-direction is treated analytically, while the solution for the transverse components of the electric and magnetic fields in the (x, y) plane is obtained numerically. The method treats any scattering object, such as, for example, a diffraction grating, as a three-dimensional distribution of the dielectric constant $\epsilon_r(x, y, z)$ and requires a periodicity of ϵ_r in the transverse directions, such as shown in Fig. B.1. RCWA finds the eigenmodes of the fields in a unit cell of ϵ_r and stitches them with the fields outside of the scattering object in a way that satisfies Maxwell's boundary conditions. If ϵ_r is non-uniform in z, it can be subdivided into layers that are approximately uniform in z, and the stitching of the eigenmodes will have to be done between the subdividing layers as well. This procedure is known as the staircase approximation. With it, a structure of any complexity in z can be treated, but because each layer requires its own eigenmode calculation, very complex structures quickly become computationally intensive. Because

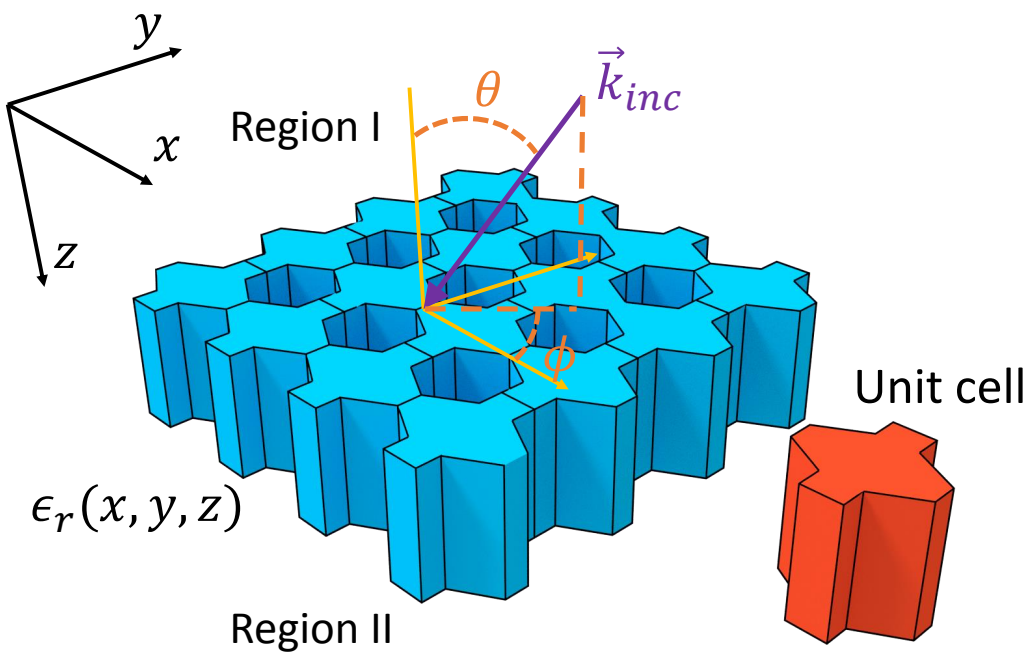

Figure B.1: RCWA geometry. The dielectric constant of the scattering structure $\epsilon_r(x, y, z)$ must be periodic. A unit cell is shown in red. The wave vector of an incident wave is $\vec{k}_{inc}$. Region I above the scattering structure contains the incident and reflected waves. Region II below the structure contains the transmitted waves.

RCWA solves Maxwell's equations separately for each Fourier component, or spatial harmonic, of the field. Problems that can be represented well by a small number of spatial harmonics are best suited for this method. As a consequence, this puts a constraint on the transverse contrast in ϵ_r: it needs to be relatively smooth without sharp edges. The sharper the features in ϵ_r, the more spatial harmonics are required to adequately describe the problem and the higher the computational cost.

I start with Maxwell's curl equations, which in a source-free material are written as

$$\begin{aligned} \nabla \times \vec{E} &= k_0 \mu_r \vec{\tilde{H}}, \\ \nabla \times \vec{\tilde{H}} &= k_0 \epsilon_r \vec{E}, \end{aligned} \tag{B.1}$$

where the normalized magnetic field $\vec{\tilde{H}}$ is defined as $\vec{\tilde{H}} = -i\sqrt{\mu_0/\epsilon_0}\vec{H}$, and k_0 is the wavenumber of the incident wave. Using the Levi-Civita symbol e_{ijk} and Einstein's summation convention (summation over repeated indices), these equations can be re-written in a compact form

$$\begin{aligned} e_{ijk}\frac{\partial}{\partial x_j}E_k &= k_0 \mu_r \tilde{H}_i, \\ e_{ijk}\frac{\partial}{\partial x_j}\tilde{H}_k &= k_0 \epsilon_r E_i, \end{aligned} \tag{B.2}$$

where the indices i, j, k run through x, y, z each. A Fourier series expansion in the (x, y) plane of the fields in each z-layer labeled with an index j yields

$$\begin{aligned} \vec{E}_j(x,y,z) &= \sum_{m=-\infty}^{m=+\infty}\sum_{n=-\infty}^{n=+\infty} \vec{S}_{j,m,n}(z)\exp\left[-i\left(k^x_{m,n}x + k^y_{m,n}y\right)\right], \\ \vec{\tilde{H}}_j(x,y,z) &= \sum_{m=-\infty}^{m=+\infty}\sum_{n=-\infty}^{n=+\infty} \vec{U}_{j,m,n}(z)\exp\left[-i\left(k^x_{m,n}x + k^y_{m,n}y\right)\right]. \end{aligned} \tag{B.3}$$

In (B.3), the wavevector components of the $(m,n)^{\text{th}}$ spatial harmonic (Fourier component) are

$$\begin{aligned} k^{(x)}_{m,n} &= k^{(x)}_{inc} - \left(m\vec{G}_1 + n\vec{G}_2\right)\cdot\hat{x}, \\ k^{(y)}_{m,n} &= k^{(y)}_{inc} - \left(m\vec{G}_1 + n\vec{G}_2\right)\cdot\hat{y}, \\ k^{(z)}_{j,m,n} &= \sqrt{k_0^2\epsilon_r^{(j)} - \left(k^{(x)}_{m,n}\right)^2 - \left(k^{(y)}_{m,n}\right)^2}. \end{aligned} \tag{B.4}$$

Note that in these equations, depending on the sign of the expression under the square root, the z-component of the wavevector is either purely real or purely imaginary. The latter represents

evanescent waves. In order to complete the Fourier series expansion of Maxwell's equations, the dielectric constant and the magnetic permeability need to be expanded. Their inverses are expanded as well, for better convergence. Defining $\vec{G}_{m,n}$ as $\vec{G}_{m,n} = m\vec{G}_1 + n\vec{G}_2$ and $\vec{r}$ as $\vec{r} = x \cdot \hat{x} + y \cdot \hat{y}$, $\epsilon_r^{(i)}$ and $\mu_r^{(i)}$ and their inverses can be expressed as

$$\begin{aligned}
\epsilon_r^{(j)} &= \sum_{m=-\infty}^{m=+\infty} \sum_{n=-\infty}^{n=+\infty} a_{j,m,n} \exp\left(i\vec{G}_{m,n} \cdot \vec{r}\right), \\
\mu_r^{(j)} &= \sum_{m=-\infty}^{m=+\infty} \sum_{n=-\infty}^{n=+\infty} c_{j,m,n} \exp\left(i\vec{G}_{m,n} \cdot \vec{r}\right), \\
\left(\epsilon_r^{(j)}\right)^{-1} &= \sum_{m=-\infty}^{m=+\infty} \sum_{n=-\infty}^{n=+\infty} b_{j,m,n} \exp\left(i\vec{G}_{m,n} \cdot \vec{r}\right), \\
\left(\mu_r^{(j)}\right)^{-1} &= \sum_{m=-\infty}^{m=+\infty} \sum_{n=-\infty}^{n=+\infty} d_{j,m,n} \exp\left(i\vec{G}_{m,n} \cdot \vec{r}\right).
\end{aligned} \tag{B.5}$$

The Fourier coefficients $a_{j,m,n}$, $b_{j,m,n}$, $c_{j,m,n}$, and $d_{j,m,n}$ are given by

$$\phi_{j,m,n} = \frac{1}{A} \iint_A f_j(x,y) \exp\left(-i\vec{G}_{m,n} \cdot \vec{r}\right) d^2\vec{r}, \tag{B.6}$$

where $\phi_{j,m,n}$ stands for $a_{j,m,n}$, $b_{j,m,n}$, $c_{j,m,n}$, or $d_{j,m,n}$, and $f_j(x,y)$ stands for $\epsilon_r^{(j)}$,$\left(\epsilon_r^{(j)}\right)^{-1}$, $\mu_r^{(j)}$, or $\left(\mu_r^{(j)}\right)^{-1}$, respectively. A is the area of the unit cell in the (x,y) plane.

Substituting eqs. (B.3) and (B.6) into eq. (B.2), one obtains a system of Maxwell's equations in reciprocal space for the $(m,n)^{\text{th}}$ spatial harmonic (see Ref. [283] for details)

$$\begin{aligned}
-ik_{m,n}^{(y)} S_{j,m,n}^{(z)}(z) - \frac{dS_{j,m,n}^{(y)}(z)}{dz} &= k_0 \mu_j^x \otimes U_j^{(x)}(z), \\
ik_{m,n}^{(x)} S_{j,m,n}^{(z)}(z) + \frac{dS_{j,m,n}^{(x)}(z)}{dz} &= k_0 \mu_j^y \otimes U_j^{(y)}(z), \\
-ik_{m,n}^{(x)} S_{j,m,n}^{(y)}(z) + ik_{m,n}^{(y)} S_{j,m,n}^{(x)}(z) &= k_0 \mu_j^z \otimes U_j^{(z)}(z), \\
-ik_{m,n}^{(y)} U_{j,m,n}^{(z)}(z) - \frac{dU_{j,m,n}^{(y)}(z)}{dz} &= k_0 \epsilon_j^x \otimes S_j^{(x)}(z), \\
ik_{m,n}^{(x)} U_{j,m,n}^{(z)}(z) + \frac{dU_{j,m,n}^{(x)}(z)}{dz} &= k_0 \epsilon_j^y \otimes S_j^{(y)}(z), \\
-ik_{m,n}^{(x)} U_{j,m,n}^{(y)}(z) + ik_{m,n}^{(y)} U_{j,m,n}^{(x)}(z) &= k_0 \epsilon_j^z \otimes S_j^{(z)}(z),
\end{aligned} \tag{B.7}$$

where the symbol $\otimes$ denotes the convolution operation. Since for an arbitrary system, in general, one needs an infinite number of spatial harmonics (terms in the Fourier expansion), the system

(B.7) is also infinite. However, in an actual implementation of RCWA on a computer, the number of harmonics is finite, and, as mentioned above, the fewer harmonics are needed for an accurate description of the scattering object the better. With a finite number of spatial harmonics, the system of equations can be re-written in a matrix form (with the introduction of a non-dimensionalized wavevector $\vec{\tilde{k}} = \vec{k}/k_0$ and longitudinal coordinate $\tilde{z} = k_0 z$)

$$\begin{aligned}
-i\tilde{\mathbf{K}}_y \mathbf{s}_z - \frac{d\mathbf{s}_y}{d\tilde{z}} &= [\![\mu_r]\!]\mathbf{u}_x, \\
i\tilde{\mathbf{K}}_x \mathbf{s}_z + \frac{d\mathbf{s}_x}{d\tilde{z}} &= [\![\mu_r]\!]\mathbf{u}_y, \\
-i\tilde{\mathbf{K}}_x \mathbf{s}_y + i\tilde{\mathbf{K}}_y \mathbf{s}_x &= [\![\mu_r]\!]\mathbf{u}_z, \\
-i\tilde{\mathbf{K}}_y \mathbf{u}_z - \frac{d\mathbf{u}_y}{d\tilde{z}} &= [\![\epsilon_r]\!]\mathbf{s}_x, \\
i\tilde{\mathbf{K}}_x \mathbf{u}_z + \frac{d\mathbf{u}_x}{d\tilde{z}} &= [\![\epsilon_r]\!]\mathbf{s}_y, \\
-i\tilde{\mathbf{K}}_x \mathbf{u}_y + i\tilde{\mathbf{K}}_y \mathbf{u}_x &= [\![\epsilon_r]\!]\mathbf{s}_z,
\end{aligned} \tag{B.8}$$

where the matrix $\tilde{\mathbf{K}}$ and vectors $\mathbf{u}$ and $\mathbf{s}$ are defined as follows

$$\tilde{\mathbf{K}}_q = \begin{bmatrix} \tilde{k}_q(1,1) & 0 & \dots & 0 \\ 0 & \tilde{k}_q(1,2) & \dots & 0 \\ \vdots & \vdots & \ddots & \vdots \\ 0 & \dots & 0 & \tilde{k}_q(M,N) \end{bmatrix}, \tag{B.9}$$

$$\mathbf{u}_q = \begin{bmatrix} U_q(1,1) \\ U_q(1,2) \\ \vdots \\ U_q(M,N) \end{bmatrix}, \quad \mathbf{s}_q = \begin{bmatrix} S_q(1,1) \\ S_q(1,2) \\ \vdots \\ S_q(M,N) \end{bmatrix}, \tag{B.10}$$

where index q represents the subscripts x, y, or z. Note that $[\![\epsilon_r]\!]$ and $[\![\mu_r]\!]$ are square matrix operators that perform the convolution operation mentioned above. They are not dielectric constant and magnetic permeability matrices defined on a real-space grid. $[\![\epsilon_r]\!]$ and $[\![\mu_r]\!]$ can be found by computing Fourier coefficients of $\epsilon_r(x,y)$ and $\mu_r(x,y)$ and re-arranging them along the matrix diagonals. The number of coefficients is equal to the total number of spatial harmonics used to

describe a given problem. More details on the re-arrangement of the Fourier coefficients can be found in Ref. [283]. For a one-dimensional problem, the convolution matrices $[\![\epsilon_r]\!]$ and $[\![\mu_r]\!]$ become matrices with constant left-to-right diagonals known as Toeplitz matrices [284]. This is relevant for the case of a one-dimensional sawtooth-shaped diffraction grating which I consider in this thesis.

In the next step, the longitudinal field components are eliminated from the system of equations (B.8). This can be done by using the third and sixth equation of the system, which yields

$$\begin{aligned} \mathbf{u}_z &= [\![\mu_r]\!]^{-1}\left(-i\tilde{\mathbf{K}}_x\mathbf{s}_y + i\tilde{\mathbf{K}}_y\mathbf{s}_x\right), \\ \mathbf{s}_z &= [\![\epsilon_r]\!]^{-1}\left(-i\tilde{\mathbf{K}}_x\mathbf{u}_y + i\tilde{\mathbf{K}}_y\mathbf{u}_x\right). \end{aligned} \tag{B.11}$$

Substituting these expressions into (B.8) leaves only four differential equations for the transverse components of the fields

$$\begin{aligned} \frac{d\mathbf{u}_x}{d\tilde{z}} &= \tilde{\mathbf{K}}_x[\![\mu_r]\!]^{-1}\tilde{\mathbf{K}}_y\mathbf{s}_x + \left([\![\epsilon_r]\!] - \tilde{\mathbf{K}}_x[\![\mu_r]\!]^{-1}\tilde{\mathbf{K}}_x\right)\mathbf{s}_y, \\ \frac{d\mathbf{u}_y}{d\tilde{z}} &= \left(\tilde{\mathbf{K}}_y[\![\mu_r]\!]^{-1}\tilde{\mathbf{K}}_y - [\![\epsilon_r]\!]\right)\mathbf{s}_x - \tilde{\mathbf{K}}_y[\![\mu_r]\!]^{-1}\tilde{\mathbf{K}}_x\mathbf{s}_y, \\ \frac{d\mathbf{s}_x}{d\tilde{z}} &= \tilde{\mathbf{K}}_x[\![\epsilon_r]\!]^{-1}\tilde{\mathbf{K}}_y\mathbf{u}_x + \left([\![\mu_r]\!] - \tilde{\mathbf{K}}_x[\![\epsilon_r]\!]^{-1}\tilde{\mathbf{K}}_x\right)\mathbf{u}_y, \\ \frac{d\mathbf{s}_y}{d\tilde{z}} &= \left(\tilde{\mathbf{K}}_y[\![\epsilon_r]\!]^{-1}\tilde{\mathbf{K}}_y - [\![\epsilon_r]\!]\right)\mathbf{u}_x - \tilde{\mathbf{K}}_y[\![\epsilon_r]\!]^{-1}\tilde{\mathbf{K}}_x\mathbf{u}_y. \end{aligned} \tag{B.12}$$

These equations can be re-written in a block-matrix form

$$\begin{aligned} \frac{d}{d\tilde{z}}\begin{bmatrix}\mathbf{u}_x \\ \mathbf{u}_y\end{bmatrix} &= \mathbf{Q}\begin{bmatrix}\mathbf{s}_x \\ \mathbf{s}_y\end{bmatrix}, \\ \frac{d}{d\tilde{z}}\begin{bmatrix}\mathbf{s}_x \\ \mathbf{s}_y\end{bmatrix} &= \mathbf{P}\begin{bmatrix}\mathbf{u}_x \\ \mathbf{u}_y\end{bmatrix}, \end{aligned} \tag{B.13}$$

where the matrices $\mathbf{Q}$ and $\mathbf{P}$ are defined as

$$\begin{aligned} \mathbf{Q} &= \begin{bmatrix} \tilde{\mathbf{K}}_x[\![\mu_r]\!]^{-1}\tilde{\mathbf{K}}_y & [\![\epsilon_r]\!] - \tilde{\mathbf{K}}_x[\![\mu_r]\!]^{-1}\tilde{\mathbf{K}}_x \\ \tilde{\mathbf{K}}_y[\![\mu_r]\!]^{-1}\tilde{\mathbf{K}}_y - [\![\epsilon_r]\!] & -\tilde{\mathbf{K}}_y[\![\mu_r]\!]^{-1}\tilde{\mathbf{K}}_x \end{bmatrix}, \\ \mathbf{P} &= \begin{bmatrix} \tilde{\mathbf{K}}_x[\![\epsilon_r]\!]^{-1}\tilde{\mathbf{K}}_y & [\![\mu_r]\!] - \tilde{\mathbf{K}}_x[\![\epsilon_r]\!]^{-1}\tilde{\mathbf{K}}_x \\ \tilde{\mathbf{K}}_y[\![\epsilon_r]\!]^{-1}\tilde{\mathbf{K}}_y - [\![\mu_r]\!] & -\tilde{\mathbf{K}}_y[\![\epsilon_r]\!]^{-1}\tilde{\mathbf{K}}_x \end{bmatrix}. \end{aligned} \tag{B.14}$$

From eqs. (B.13), matrix wave equations can be derived. They have an identical form for both the electric and magnetic fields. For this reason, I only write down the wave equation for the transverse Fourier components of the electric field

$$\frac{d^2}{d^2\tilde{z}}\begin{bmatrix}\mathbf{s}_x\\ \\ \mathbf{s}_y\end{bmatrix} - \mathbf{\Omega}^2\begin{bmatrix}\mathbf{s}_x\\ \\ \mathbf{s}_y\end{bmatrix} = 0, \tag{B.15}$$

where $\mathbf{\Omega}^2 = \mathbf{PQ}$. The general solution of eq. (B.15) is expressed in terms of forward (+) and backward (−) propagating waves

$$\begin{bmatrix}\mathbf{s}_x\\ \\ \mathbf{s}_y\end{bmatrix} = e^{-\mathbf{\Omega}\tilde{z}}\mathbf{s}^{(+)}(0) + e^{\mathbf{\Omega}\tilde{z}}\mathbf{s}^{(-)}(0). \tag{B.16}$$

In this equation, the terms $s^{(\pm)}(0)$ are the initial transverse Fourier amplitudes of the forward and backward propagating waves. An exponent of a square diagonalizable matrix $\exp(\mathbf{A}) = \mathbf{W}\exp(\boldsymbol{\lambda})\mathbf{W}^{-1}$ [285], where $\boldsymbol{\lambda}$ is a diagonal matrix of the eigenvalues of $\mathbf{A}$, and $\mathbf{W}$ is a matrix of the eigenvectors of $\mathbf{A}$ in which each column is an eigenvector corresponding to its respective eigenvalue on the diagonal of $\boldsymbol{\lambda}$. The solution (B.16) can thus be expressed in terms of the eigenvectors $\mathbf{W}$ and eigenvalues $\boldsymbol{\lambda}^2$ matrices of $\mathbf{\Omega}^2$ as

$$\begin{bmatrix}\mathbf{s}_x\\ \\ \mathbf{s}_y\end{bmatrix} = \mathbf{W}e^{-\boldsymbol{\lambda}\tilde{z}}\mathbf{W}^{-1}\mathbf{s}^{(+)}(0) + \mathbf{W}e^{\boldsymbol{\lambda}\tilde{z}}\mathbf{W}^{-1}\mathbf{s}^{(-)}(0) = \mathbf{W}e^{-\boldsymbol{\lambda}\tilde{z}}\mathbf{c}^{(+)} + \mathbf{W}e^{\boldsymbol{\lambda}\tilde{z}}\mathbf{c}^{(-)}, \tag{B.17}$$

where I defined the coefficients $\mathbf{c}^{(\pm)} = \mathbf{W}^{-1}\mathbf{s}^{(\pm)}(0)$.

A similar procedure can be performed for the transverse Fourier components (spatial harmonics) of the magnetic field. It can be shown by substituting expression (B.17) into the first equation in (B.13) that the relation between the eigenvector matrix $\mathbf{V}$ for the magnetic field and the eigenvector matrix $\mathbf{W}$ for the electric field is $\mathbf{V} = \mathbf{QW}\boldsymbol{\lambda}^{-1}$ [283], and by combining the electric and magnetic fields into a single vector, an entire solution can be expressed as

$$\boldsymbol{\psi} = \begin{bmatrix}\mathbf{s}_x\\ \\ \mathbf{s}_y\\ \\ \mathbf{u}_x\\ \\ \mathbf{u}_y\end{bmatrix} = \begin{bmatrix}\mathbf{W} & \mathbf{W}\\ \\ -\mathbf{V} & \mathbf{V}\end{bmatrix}\begin{bmatrix}\exp(-\boldsymbol{\lambda}\tilde{z}) & \mathbf{0}\\ \\ \mathbf{0} & \exp(\boldsymbol{\lambda}\tilde{z})\end{bmatrix}\begin{bmatrix}\mathbf{c}^{(+)}\\ \\ \mathbf{c}^{(-)}\end{bmatrix}. \tag{B.18}$$

In order to calculate the fields reflected from and transmitted through a periodic structure, one needs to evaluate the mode coefficients $\mathbf{c}^{(\pm)}$ outside of the structure. This can be done by applying Maxwell's boundary conditions for the **s** and **u** transverse field components. At an interface, the tangential components of the $\vec{E}$ and $\vec{H}$ fields are continuous in the absence of surface charges and currents. Therefore, at the boundary between the layers i and $i+1$, it follows that $\boldsymbol{\psi}_i = \boldsymbol{\psi}_{i+1}$. This condition can be written as

$$\begin{bmatrix} \mathbf{W}_i & \mathbf{W}_i \\ -\mathbf{V}_i & \mathbf{V}_i \end{bmatrix} \begin{bmatrix} e^{-\boldsymbol{\lambda}_i \tilde{d}_i} & \mathbf{0} \\ \mathbf{0} & \mathbf{1} \end{bmatrix} \begin{bmatrix} \mathbf{c}_i^{(+)} \\ \mathbf{c}_i^{(-)} \end{bmatrix} = \begin{bmatrix} \mathbf{W}_{i+1} & \mathbf{W}_{i+1} \\ -\mathbf{V}_{i+1} & \mathbf{V}_{i+1} \end{bmatrix} \begin{bmatrix} \mathbf{1} & \mathbf{0} \\ \mathbf{0} & e^{-\boldsymbol{\lambda}_{i+1} \tilde{d}_{i+1}} \end{bmatrix} \begin{bmatrix} \mathbf{c}_{i+1}^{(+)} \\ \mathbf{c}_{i+1}^{(-)} \end{bmatrix}, \tag{B.19}$$

where $\tilde{d}_i$ is the thickness of the i^{th} layer normalized by k_0. Note that in deriving (B.19) from (B.18) I have introduced a substitution $\tilde{z}_i \to \tilde{z}_i - \sum_{j=1}^{i-1} \tilde{d}_j$, which leaves only the negative exponential $\exp(-\boldsymbol{\lambda}_i \tilde{d}_i)$ when $\tilde{z}_i = \sum_{j=1}^{i-1} \tilde{d}_j$, which is the coordinate of the boundary of the i^{th} and $(i-1)^{\text{st}}$ layers, or when $\tilde{z}_i = \tilde{d}_i + \sum_{j=1}^{i-1} \tilde{d}_j$, which is the coordinate of the boundary of the i^{th} and $(i+1)^{\text{st}}$ layers. The expression above can be re-written in a more compact form by introducing

$$\mathbf{F}_i = \begin{bmatrix} \mathbf{W}_i & \mathbf{W}_i \\ -\mathbf{V}_i & \mathbf{V}_i \end{bmatrix}, \quad \mathbf{X}_i = \exp(-\boldsymbol{\lambda}_i \tilde{d}_i), \quad \mathbf{C}_i = \begin{bmatrix} \mathbf{c}_i^{(+)} \\ \mathbf{c}_i^{(-)} \end{bmatrix}. \tag{B.20}$$

With these substitutions, the boundary condition (B.19) simplifies to

$$\mathbf{F}_i \begin{bmatrix} \mathbf{X}_i & \mathbf{0} \\ \mathbf{0} & \mathbf{1} \end{bmatrix} \mathbf{C}_i = \mathbf{F}_{i+1} \begin{bmatrix} \mathbf{X}_{i+1} & \mathbf{0} \\ \mathbf{0} & \mathbf{1} \end{bmatrix} \mathbf{C}_{i+1}. \tag{B.21}$$

Special care must be taken when considering boundary conditions at the first and last interfaces of the scattering structure as these are responsible for coupling the incident light into the structure correctly as well as giving the correct reflections and transmissions of the structure as a whole. I label the region that contains the incident and reflected waves as Region I and the region that contains the transmitted waves as Region II. In Fig. B.1, Region I is above the blue structure, and Region II is below it. The boundary condition (B.21) at the first and last interfaces, which are the interfaces between Region I and the first layer of the structure and Region II and the last layer

of the structure, respectively, can be written as

$$\boldsymbol{\psi}_{\mathrm{I\ (II)}} = \mathbf{F}_{first(last)} \begin{bmatrix} \mathbf{X}_{first(last)} & \mathbf{0} \\ \mathbf{0} & \mathbf{1} \end{bmatrix} \mathbf{C}_{first(last)}. \tag{B.22}$$

In Region I, $\boldsymbol{\psi}_{\mathrm{I}}$ is a sum of the forward propagating incident wave and a backward propagating reflected wave. In Region II, $\boldsymbol{\psi}_{\mathrm{II}}$ is a forward propagating transmitted wave. If the incident electric field

$$\vec{E}_{inc} = \vec{P} \exp\left(-i\vec{k}_{inc} \cdot \vec{r}\right), \tag{B.23}$$

where $\vec{P}$ is the polarization vector, it can be shown by substitution into eq. (B.2) that the corresponding transverse components of the incident magnetic field are

$$\begin{bmatrix} \tilde{H}_x \\ \tilde{H}_y \end{bmatrix}_{inc} = \frac{i \exp\left(-i\vec{k}_{inc} \cdot \vec{r}\right)}{\mu_{\mathrm{I}} k_0} \begin{bmatrix} k_{inc}^{(z)} p_y - k_{inc}^{(y)} p_z \\ k_{inc}^{(x)} p_z - k_{inc}^{(z)} p_x \end{bmatrix}. \tag{B.24}$$

The same relationship holds for the Fourier components of the fields. The transverse Fourier components of the incident electric field are

$$\begin{bmatrix} \mathbf{s}_x \\ \mathbf{s}_y \end{bmatrix}_{inc} = \begin{bmatrix} p_x \boldsymbol{\delta}_{m,n=0} \\ p_y \boldsymbol{\delta}_{m,n=0} \end{bmatrix}, \tag{B.25}$$

where I introduced a vector $\boldsymbol{\delta}_{m,n=0}$ that has the same number of elements as the number of spatial harmonics in a given problem, but all elements of the vector are zero except for the element at $m = n = 0$. This is a representation of an incident plane wave as a 0^{th} order spatial harmonic. From eqs. (B.25) and (B.24), the Fourier components of the incident magnetic field are

$$\begin{bmatrix} \mathbf{u}_x \\ \mathbf{u}_y \end{bmatrix}_{inc} = \frac{i}{\mu_{\mathrm{I}}} \begin{bmatrix} \left(\tilde{k}_{inc}^{(z)} p_y - \tilde{k}_{inc}^{(y)} p_z\right) \boldsymbol{\delta}_{m,n=0} \\ \left(\tilde{k}_{inc}^{(x)} p_z - \tilde{k}_{inc}^{(z)} p_x\right) \boldsymbol{\delta}_{m,n=0} \end{bmatrix}. \tag{B.26}$$

Denoting the reflected Fourier components of the electric field in Region I as $\mathbf{r}_x$ and $\mathbf{r}_y$, the total electric field in that region as a sum of the incident and reflected waves is

$$\begin{bmatrix} \mathbf{s}_x \\ \mathbf{s}_y \end{bmatrix}_{\mathrm{I}} = \begin{bmatrix} p_x \boldsymbol{\delta}_{m,n=0} \\ p_y \boldsymbol{\delta}_{m,n=0} \end{bmatrix} + \begin{bmatrix} \mathbf{r}_x \\ \mathbf{r}_y \end{bmatrix}. \tag{B.27}$$

The associated reflected magnetic field in Region I can be found with the help of the first equation in (B.13). The reader is referred to [283] for more details. Just like the electric field, the magnetic field in Region I is a sum of the incident and reflected waves

$$\begin{bmatrix}\mathbf{u}_x\\ \mathbf{u}_y\end{bmatrix}_{\mathrm{I}} = \frac{i}{\mu_{\mathrm{I}}}\begin{bmatrix}\left(\tilde{k}_{inc}^{(z)}p_y - \tilde{k}_{inc}^{(y)}p_z\right)\boldsymbol{\delta}_{m,n=0}\\ \left(\tilde{k}_{inc}^{(x)}p_z - \tilde{k}_{inc}^{(z)}p_x\right)\boldsymbol{\delta}_{m,n=0}\end{bmatrix} + \frac{i}{\mu_{\mathrm{I}}}\begin{bmatrix}-\frac{\tilde{\mathbf{K}}_x\tilde{\mathbf{K}}_y}{\tilde{\mathbf{K}}_{\mathrm{I},z}} & -\frac{\tilde{\mathbf{K}}_{\mathrm{I},z}^2+\tilde{\mathbf{K}}_y^2}{\tilde{\mathbf{K}}_{\mathrm{I},z}}\\ \frac{\tilde{\mathbf{K}}_{\mathrm{I},z}^2+\tilde{\mathbf{K}}_x^2}{\tilde{\mathbf{K}}_{\mathrm{I},z}} & \frac{\tilde{\mathbf{K}}_x\tilde{\mathbf{K}}_y}{\tilde{\mathbf{K}}_{\mathrm{I},z}}\end{bmatrix}\begin{bmatrix}\mathbf{r}_x\\ \mathbf{r}_y\end{bmatrix}. \tag{B.28}$$

A similar derivation can be performed for the fields transmitted through the scattering structure. With the transmitted transverse Fourier components of the electric field $\mathbf{t}_x$ and $\mathbf{t}_y$, the magnetic field in Region II is

$$\begin{bmatrix}\mathbf{u}_x\\ \mathbf{u}_y\end{bmatrix}_{\mathrm{II}} = \frac{i}{\mu_{\mathrm{II}}}\begin{bmatrix}\frac{\tilde{\mathbf{K}}_x\tilde{\mathbf{K}}_y}{\tilde{\mathbf{K}}_{\mathrm{II},z}} & \frac{\tilde{\mathbf{K}}_{\mathrm{II},z}^2+\tilde{\mathbf{K}}_y^2}{\tilde{\mathbf{K}}_{\mathrm{II},z}}\\ -\frac{\tilde{\mathbf{K}}_{\mathrm{II},z}^2+\tilde{\mathbf{K}}_x^2}{\tilde{\mathbf{K}}_{\mathrm{I},z}} & -\frac{\tilde{\mathbf{K}}_x\tilde{\mathbf{K}}_y}{\tilde{\mathbf{K}}_{\mathrm{II},z}}\end{bmatrix}\begin{bmatrix}\mathbf{t}_x\\ \mathbf{t}_y\end{bmatrix}. \tag{B.29}$$

Having determined the fields, and hence vector $\boldsymbol{\psi}$ in Regions I and II, it is now possible to write explicitly the boundary conditions (eq. (B.22)) at the interfaces between the scattering structure and the surrounding media. In order to write them in a more compact form, I first introduce some auxiliary matrices and vectors

$$\mathbf{A} = \frac{i}{\mu_{\mathrm{I}}}\begin{bmatrix}-i\mu_{\mathrm{I}}\mathbf{1} & \mathbf{0}\\ \mathbf{0} & -i\mu_{\mathrm{I}}\mathbf{1}\\ -\frac{\tilde{\mathbf{K}}_x\tilde{\mathbf{K}}_y}{\tilde{\mathbf{K}}_{\mathrm{I},z}} & -\frac{\tilde{\mathbf{K}}_{\mathrm{I},z}^2+\tilde{\mathbf{K}}_y^2}{\tilde{\mathbf{K}}_{\mathrm{I},z}}\\ \frac{\tilde{\mathbf{K}}_{\mathrm{I},z}^2+\tilde{\mathbf{K}}_x^2}{\tilde{\mathbf{K}}_{\mathrm{I},z}} & \frac{\tilde{\mathbf{K}}_x\tilde{\mathbf{K}}_y}{\tilde{\mathbf{K}}_{\mathrm{I},z}}\end{bmatrix}. \tag{B.30}$$

$$\mathbf{B} = \frac{i}{\mu_{\mathrm{II}}}\begin{bmatrix}-i\mu_{\mathrm{II}}\mathbf{1} & \mathbf{0}\\ \mathbf{0} & -i\mu_{\mathrm{II}}\mathbf{1}\\ \frac{\tilde{\mathbf{K}}_x\tilde{\mathbf{K}}_y}{\tilde{\mathbf{K}}_{\mathrm{II},z}} & \frac{\tilde{\mathbf{K}}_{\mathrm{II},z}^2+\tilde{\mathbf{K}}_y^2}{\tilde{\mathbf{K}}_{\mathrm{II},z}}\\ -\frac{\tilde{\mathbf{K}}_{\mathrm{II},z}^2+\tilde{\mathbf{K}}_x^2}{\tilde{\mathbf{K}}_{\mathrm{I},z}} & -\frac{\tilde{\mathbf{K}}_x\tilde{\mathbf{K}}_y}{\tilde{\mathbf{K}}_{\mathrm{II},z}}\end{bmatrix}. \tag{B.31}$$

$$\boldsymbol{\psi}_{inc} = \begin{bmatrix}p_x\boldsymbol{\delta}_{m,n=0}\\ p_y\boldsymbol{\delta}_{m,n=0}\\ \frac{i}{\mu_{\mathrm{I}}}\left(\tilde{k}_{inc}^{(z)}p_y - \tilde{k}_{inc}^{(y)}p_z\right)\boldsymbol{\delta}_{m,n=0}\\ \frac{i}{\mu_{\mathrm{I}}}\left(\tilde{k}_{inc}^{(x)}p_z - \tilde{k}_{inc}^{(z)}p_x\right)\boldsymbol{\delta}_{m,n=0}\end{bmatrix},\quad \mathbf{R} = \begin{bmatrix}\mathbf{r}_x\\ \mathbf{r}_y\\ \mathbf{r}_x\\ \mathbf{r}_y\end{bmatrix},\quad \mathbf{T} = \begin{bmatrix}\mathbf{t}_x\\ \mathbf{t}_y\\ \mathbf{t}_x\\ \mathbf{t}_y\end{bmatrix}. \tag{B.32}$$

With these definitions, the first boundary condition between Region I and the scattering structure is

$$\boldsymbol{\psi}_{inc} + \mathbf{AR} = \mathbf{F}_1 \begin{bmatrix} \mathbf{1} & \mathbf{0} \\ \mathbf{0} & \mathbf{X}_1 \end{bmatrix} \mathbf{C}_1, \tag{B.33}$$

and the condition between the structure and Region II for a structure with N interfaces is

$$\mathbf{BT} = \mathbf{F}_N \begin{bmatrix} \mathbf{X}_N & \mathbf{0} \\ \mathbf{0} & \mathbf{1} \end{bmatrix} \mathbf{C}_N. \tag{B.34}$$

These boundary conditions (eqs. (B.33), (B.21), and (B.34)) can be solved for an entire structure in order to find the total reflection and transmission as well as diffraction efficiencies for various spatial harmonic orders and, if required, electric and magnetic fields inside the structure. There are several ways of solving this problem.

The solution method that I describe below is called the Enhanced Transmittance Matrix (ETM) approach. It was first proposed in Ref. [282] in 1995 and is a stable implementation of RCWA. The stability is ensured by analytically avoiding growing exponential terms of the form $\mathbf{X}_i^{-1} = \exp(\boldsymbol{\lambda}_i \tilde{d}_i)$ which could lead to ill-conditioned matrices when eqs. (B.21) are solved.

The unknowns that need to be solved for are the reflection and transmission vectors $\mathbf{R}$ and $\mathbf{T}$ in eqs. (B.33) and (B.34). ETM starts with the last interface. The mode coefficients $\mathbf{C}_N$ are found from (B.34)

$$\mathbf{C}_N = \begin{bmatrix} \mathbf{X}_N^{-1} & \mathbf{0} \\ \mathbf{0} & \mathbf{1} \end{bmatrix} \mathbf{F}_N^{-1} \mathbf{BT} = \begin{bmatrix} \mathbf{X}_N^{-1} & \mathbf{0} \\ \mathbf{0} & \mathbf{1} \end{bmatrix} \begin{bmatrix} \mathbf{a}_N \\ \mathbf{b}_N \end{bmatrix} \mathbf{T}. \tag{B.35}$$

In the equation above, the following definition has been introduced

$$\begin{bmatrix} \mathbf{a}_N \\ \mathbf{b}_N \end{bmatrix} = \mathbf{F}_N^{-1} \mathbf{B}. \tag{B.36}$$

In order to eliminate the growing exponential term $\mathbf{X}_N^{-1}$ in eq. (B.35), an auxiliary transmittance vector $\mathbf{T}_N$ is introduced, and the unknown vector $\mathbf{T}$ is expressed in terms of $\mathbf{T}_N$ as

$$\mathbf{T} = \mathbf{a}_N^{-1} \mathbf{X}_N \mathbf{T}_N. \tag{B.37}$$

With the auxiliary vector $\mathbf{T}_N$ eq. (B.35) becomes

$$\mathbf{C}_N = \begin{bmatrix} \mathbf{1} \\ \mathbf{b}_N \mathbf{a}_N^{-1} \mathbf{X}_N \end{bmatrix} \mathbf{T}_N. \tag{B.38}$$

By going backwards through the layers using eq. (B.21) and introducing auxiliary variables $\mathbf{a}_i$, $\mathbf{b}_i$, and $\mathbf{T}_i$ for each layer, one can arrive at expressions similar to eqs. (B.36), (B.37), and (B.38)

$$\begin{gathered} \mathbf{C}_i = \begin{bmatrix} \mathbf{1} \\ \mathbf{b}_i \mathbf{a}_i^{-1} \mathbf{X}_i \end{bmatrix} \mathbf{T}_i, \quad \mathbf{T}_{i+1} = \mathbf{a}_i^{-1} \mathbf{X}_i \mathbf{T}_i, \\ \begin{bmatrix} \mathbf{a}_i \\ \mathbf{b}_i \end{bmatrix} = \mathbf{F}_i^{-1} \mathbf{F}_{i+1} \begin{bmatrix} \mathbf{1} & \mathbf{0} \\ \mathbf{0} & \mathbf{X}_{i+1} \end{bmatrix} \begin{bmatrix} \mathbf{1} \\ \mathbf{b}_{i+1} \mathbf{a}_{i+1}^{-1} \mathbf{X}_{i+1} \end{bmatrix}. \end{gathered} \tag{B.39}$$

With $\mathbf{C}_1$ determined by (B.39), the boundary condition (B.33) at the first interface (between the structure and Region I) is modified to

$$\boldsymbol{\psi}_{inc} + \mathbf{A}\mathbf{R} = \mathbf{F}_1 \begin{bmatrix} \mathbf{1} & \mathbf{0} \\ \mathbf{0} & \mathbf{X}_1 \end{bmatrix} \begin{bmatrix} \mathbf{1} \\ \mathbf{b}_1 \mathbf{a}_1^{-1} \mathbf{X}_1 \end{bmatrix} \mathbf{T}_1. \tag{B.40}$$

From here, $\mathbf{R}$ and $\mathbf{T}_1$ can be found

$$\begin{bmatrix} \mathbf{R} \\ \mathbf{T}_1 \end{bmatrix} = \left[-\mathbf{A}\tilde{\mathbf{B}} \right]^{-1} \boldsymbol{\psi}_{inc}, \quad \text{where} \quad \tilde{\mathbf{B}} = \mathbf{F}_1 \begin{bmatrix} \mathbf{1} \\ \mathbf{X}_1 \mathbf{b}_1 \mathbf{a}_1^{-1} \mathbf{X}_1 \end{bmatrix}. \tag{B.41}$$

If only reflected spatial harmonics need to be solved for, the method can stop here. To find the total transmission through the scattering structure, work forward through the layers using

$$\mathbf{T} = \mathbf{a}_N^{-1} \mathbf{X}_N \mathbf{a}_{N-1}^{-1} \mathbf{X}_{N-1} \ldots \mathbf{a}_2^{-1} \mathbf{X}_2 \mathbf{a}_1^{-1} \mathbf{X}_1 \mathbf{T}_1. \tag{B.42}$$

Now that the electric and magnetic fields are known everywhere in space, the reflection and transmission diffraction efficiencies, defined as fractions of the incident power, or the magnitude of the Poynting vector, scattered into a particular reflected or transmitted spatial harmonic $D_{m,n} = P_{m,n}^{(z)} / P_{inc}^{(z)}$, can be found according to [283]

$$\begin{aligned} \mathbf{D}_\mathbf{R} &= \left(|\mathbf{R}_x|^2 + |\mathbf{R}_y|^2 + \left| \tilde{\mathbf{K}}_{\mathrm{I},z}^{-1} \left(\tilde{\mathbf{K}}_x \mathbf{R}_x + \tilde{\mathbf{K}}_y \mathbf{R}_y \right) \right|^2 \right) \mathrm{Re} \left[\frac{\tilde{\mathbf{K}}_{\mathrm{I},z}}{\tilde{k}_{inc}^{(z)}} \right], \\ \mathbf{D}_\mathbf{T} &= \left(|\mathbf{T}_x|^2 + |\mathbf{T}_y|^2 + \left| \tilde{\mathbf{K}}_{\mathrm{II},z}^{-1} \left(\tilde{\mathbf{K}}_x \mathbf{T}_x + \tilde{\mathbf{K}}_y \mathbf{T}_y \right) \right|^2 \right) \mathrm{Re} \left[\frac{\mu_\mathrm{I}}{\mu_\mathrm{II}} \frac{\tilde{\mathbf{K}}_{\mathrm{II},z}}{\tilde{k}_{inc}^{(z)}} \right]. \end{aligned} \tag{B.43}$$

Below, I provide a step-by-step procedure to implement RCWA using the ETM approach:

(1) Define the parameters of the incident wave: direction, wavelength and polarization.

(2) Define the parameters of the scattering structure: ϵ_r and μ_r for each layer of the structure as well as in the transmission and reflection regions, period in the x and y directions, layer thicknesses of the structure, the number of spatial harmonics in the x and y directions.

(3) Given the parameters defined in the previous step, construct the scattering structure on a high-resolution spatial grid.

(4) For each layer of the structure, compute the convolution matrices $[\![\epsilon_r]\!]$ and $[\![\mu_r]\!]$.

(5) Compute matrices $\tilde{\mathbf{K}}_x$, $\tilde{\mathbf{K}}_x$ and $\tilde{\mathbf{K}}_y$, as defined by (B.9), and, in the reflection and transmission regions, matrix $\tilde{\mathbf{K}}_z$.

(6) Compute matrices $\mathbf{A}$ and $\mathbf{B}$ as defined by eqs. (B.30) and (B.31), respectively.

(7) Work backwards through the layers starting from the last one and, for each layer, solve an eigenvalue problem for matrix $\boldsymbol{\Omega}^2 = \mathbf{PQ}$, where matrices $\mathbf{P}$ and $\mathbf{Q}$ are defined by eq. (B.14). With the computed eigenvector and eigenvalue matrices, obtain matrices $\mathbf{F}$ and $\mathbf{X}$ defined by eq. (B.20), and with those, solve for the matrices $\mathbf{a}_i$ according to the second equation in (B.39). In order to calculate $\mathbf{a}_N$ for the last layer (first iteration), use eq. (B.36).

(8) When the first boundary is reached, solve for the reflected spatial harmonics $\mathbf{R}$ and the auxiliary transmission $\mathbf{T}_1$ using eq. (B.41).

(9) Propagate forward through the layers to determine the transmitted spatial harmonics $\mathbf{T}$ from eq. (B.42).

(10) Compute the reflected and transmitted diffraction efficiencies $\mathbf{D_R}$ and $\mathbf{D_T}$ according to (B.43). The total reflection and transmission of the structure can be found by summing

the diffraction efficiencies over all spatial harmonics. This can be used to ensure the conservation of energy, which is a very powerful criterion that determines whether the output of the algorithm is meaningful. The sum of the total reflection and transmission is equal to 1 when there is no loss or gain in the structure, and is less or greater than 1 when there is loss or gain, respectively.

In addition to the reflected and transmitted waves, fields within the scattering structure can also be calculated. This is useful for gaining insight into the coupling of incident light to a device, but it requires keeping track of additional parameters as the algorithm proceeds, which, in turn, requires more memory. For the case considered in this thesis of an EUV beam reflected from a sawtooth diffraction grating, such a calculation was not necessary, and for that reason I do not discuss it here. More details on the calculation of the fields within the structure can be found in Ref. [283].

Because the ETM approach requires that multiple matrix variables be stored in memory for each layer, it can very quickly become computationally intensive. Since the size of the matrices is determined by the number of spatial harmonics needed to describe the problem, and the number of matrices depends on the number of layers, the memory requirements of the algorithm grow rapidly as the complexity of the scattering structure increases, i.e., if more layers and/or spatial harmonics are needed for its adequate description. Nonetheless, to date, ETM is one of the fastest and most stable implementations of RCWA.

Appendix C

Material Parameters for the 3-Temperature Model

In this appendix, I provide the material parameters used in the simulation of the electron, lattice, and spin temperatures in the CoFe/Ni multilayer film in Chapter 6. The model requires the following inputs for each material that are, in general, temperature dependent

(1) Electron specific $C_e(T_e)$

(2) Lattice specific heat $C_l(T_l)$

(3) Magnetic specific heat $C_s(T_s)$

(4) Electron thermal conductivity $\kappa_e(T_e, T_l)$

(5) Lattice thermal conductivity $\kappa_l(T_e, T_l)$

(6) Electron-lattice coupling $G_{el}(T_e)$

(7) Electron-spin coupling $G_{es}(T_e)$

(8) Lattice-spin coupling G_{ls}

(9) Material refractive indices to calculate the source term [1]

The layer structure of the sample of interest is Si_3N_4(50)/ Ta(3)/ Cu(5)/ ($Co_{0.9}Fe_{0.1}$(0.2)/ Ni(0.6))x50/ CoFe(0.2)/ Cu(3)/ Ta_2O_5(3), where the layer thicknesses in parentheses are in nm. Because the fraction of Fe in the CoFe layer is only 0.1, I assume that the material properties of that layer are

[1] Available at `https://refractiveindex.info/`

adequately described by those of pure Co. The sample thus includes six different materials, and for each one of those materials, nine properties need to be specified, according to the list above. This amounts to a total of 36 material properties, many of them being temperature dependent.

C.1 Electron specific heat

Specific heat is defined as a derivative of the total internal energy E with respect to temperature $C(T) = \frac{dE}{dT}$. The total internal energy of a statistical system is

$$E(T) = \int_0^\infty \epsilon g(\epsilon) f(\epsilon, T) d\epsilon, \tag{C.1}$$

where $g(\epsilon)$ is the density of states of the system, and $f(\epsilon, T)$ is its distribution function. Electrons are described by the Fermi-Dirac distribution for which

$$f(\epsilon, T) = \frac{1}{e^{\frac{\epsilon - \mu(T)}{kT}} + 1}, \tag{C.2}$$

where $\mu(T)$ is a chemical potential. With eqs. (C.1) and (C.2), the specific heat of the electron thermal bath can be found

$$C_e(T) = \int_0^\infty g(\epsilon)(\epsilon - \mu(T)) \frac{e^{\frac{\epsilon-\mu}{kT}}}{\left(e^{\frac{\epsilon-\mu}{kT}} + 1\right)^2} \left(\frac{\epsilon - \mu}{kT^2} + \frac{1}{kT}\frac{\partial \mu}{\partial T}\right) \mathrm{d}\epsilon. \tag{C.3}$$

The temperature dependence of the chemical potential on T, which is required for the calculation of the specific heat according to the equation above, is found from the conservation of the total electron number density

$$N = \int_0^\infty g(\epsilon) f(\epsilon, T) d\epsilon. \tag{C.4}$$

The formalism described above is applicable in metals where electrons are not strongly bound to their respective nuclei and are free to move in the periodic potential of the lattice. The electron heat capacities for Ni, Co, Cu, and Ta (all with the fcc crystal structure) are shown in Fig. C.1. Note that eq. (C.3) requires the knowledge of the electron density of states $g(\epsilon)$. For the metals shown in the figure, $g(\epsilon)$ was calculated with the ELK package [30]. All the other materials in the multilayer structure are insulators, and, because electrons in those materials are strongly bound,

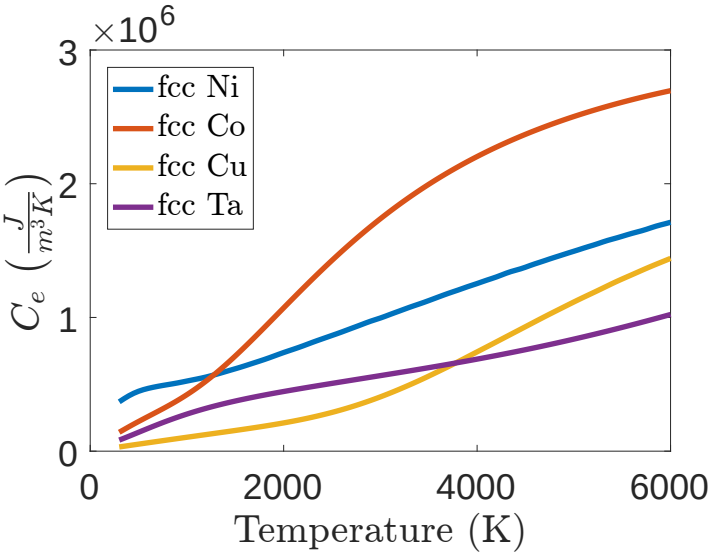

Figure C.1: Electron specific heat of Ni, Co, Cu, and Ta.

their heat capacity is negligible. As can be seen from Fig. C.1, the dependence of the specific on the temperature is non-linear, and thus the Sommerfeld model in which $C_e = \gamma_e T$ [29] does not provide an accurate estimate of the electron specific heat, particularly at high temperatures.

C.2 Lattice specific heat

The lattice (or phonon) specific heat is given by the Debye model [29].

$$C_l = 9Nk_B \left(\frac{T}{T_D}\right)^3 \int_0^{T_D/T} \frac{x^4 e^x}{(e^x - 1)^2} \mathrm{d}x \tag{C.5}$$

where N is the number of atoms per unit volume, T_D is the Debye temperature, and k_B is the Boltzmann constant. Because the functional form of $C_l(T)$ for different materials is the same, according to eq. (C.5), I only show the lattice specific heat for Ni in Fig. C.2 as an example. Notice

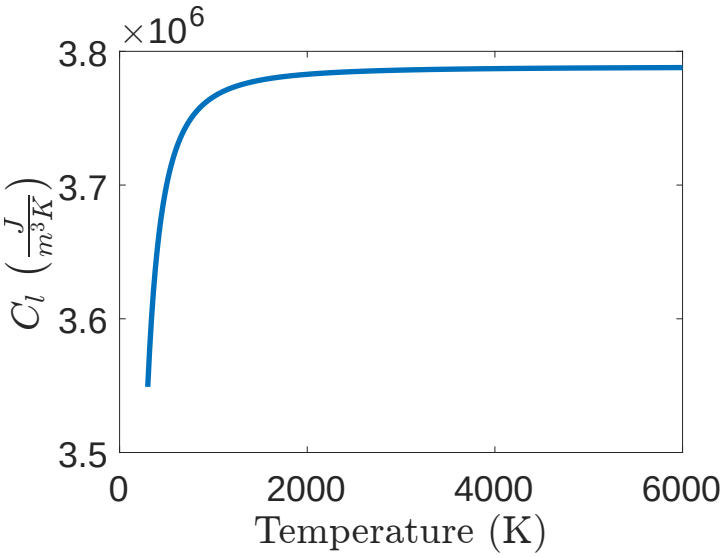

Figure C.2: Lattice specific heat of Ni.

that at high temperature the electron specific heat in Fig. C.1 is of the same order of magnitude as that of the lattice. The Debye temperatures can be found online. [2]

[2] http://www.knowledgedoor.com/2/elements_handbook/debye_temperature.html

C.3 Magnetic specific heat

The only magnetic materials in the sample being considered here are Ni and the $Co_{0.9}Fe_{0.1}$ alloy. At low temperatures, low energy magnons are responsible for magnetic excitations and thus act as a thermal reservoir. Thus, the total internal energy of the magnetic degree of freedom should be described by expression (C.1). With $f(\epsilon, T)$ equal to the Bose-Einstein distribution for magnons and a known magnon density of states, which can be calculated using DFT packages, the magnetic part of the specific heat of a material can in principle be calculated. However, because at higher temperatures Stoner excitations start to play an important role, this approach is only valid at low temperatures. Particularly, near the Curie temperature, special considerations must be taken into account [286, 287, 288]. The situation is complicated by a lack of a first principles theory of magnetism. A good approximation to the specific heat of the spin degree of freedom can be obtained from the Weiss mean-field theory [289]

$$C_s = \frac{\mu_A N_a k_B \rho}{A} \frac{x^2 \tanh x}{\tanh x \cosh^2 x - x}, \tag{C.6}$$

where μ_A is the magnetic moment per atom measured in Bohr magnetons, A is the atomic weight, N_a is the Avogadro number, ρ is the mass density, and

$$x = \frac{M_s/M(0K)}{T/T_c},$$

where the ratio $M_s/M(0K)$ is defined implicitly through the Weiss law [289]

$$\frac{M_s}{M(0K)} = \tanh\left(\frac{M_s/M(0K)}{T_s/T_c}\right).$$

In practice, however, a more accurate estimate of the magnetic specific heat can be obtained by subtracting the electron and lattice contributions from the total specific heat or by simply using experimentally measured values if those are available. Since the three-temperature model is phenomenological, such an approach can be considered reasonable, and should produce more accurate results than with purely theoretical values of the magnetic specific heat. For Ni, experimental values for the total specific heat are available in Ref. [286], and for Co in Ref. [290]. The magnetic

specific heat of Ni and Co used in this thesis is shown in Fig. C.3. In simulations, the magnetic heat capacity is often neglected [58]; however, Fig. C.3 clearly shows that near the Curie temperature, the magnetic specific heat is actually on the same order of magnitude as the lattice, and thus cannot be neglected. In fact, it can play an important role in the transport of energy in a magnetic sample [291, 292, 293].

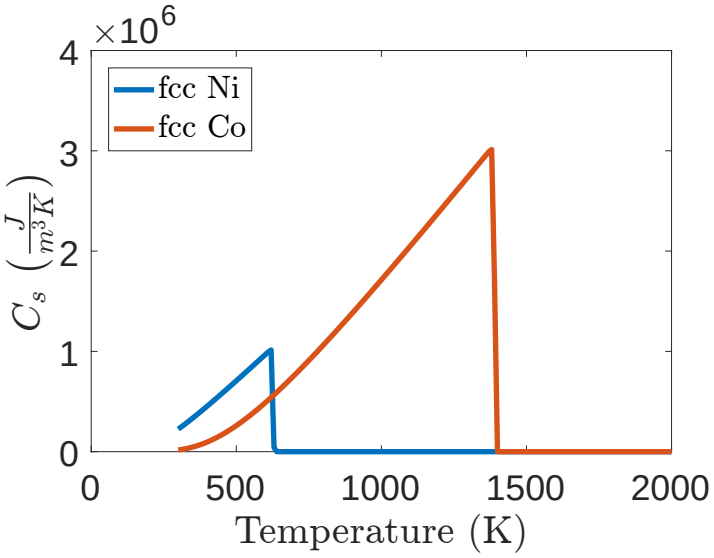

Figure C.3: Magnetic specific heat of Ni and Co.

It is important to understand that the values in Figs. C.1-C.3 are for bulk materials. In multilayer samples they might be altered due to confinement effects and interfaces. This can be especially significant in magnetic multilayers where sub-nanometer layers can interact and thus modify the magnon spectrum responsible for the specific heat of the spin energy bath.

Finally, as a practical note, in the calculations presented in this thesis, values of C_s above the Curie temperature were set to a small positive number rather than zero in order to avoid numerical instabilities in cases where the laser pump fluence is sufficiently large to drive the material above its Curie temperature.

C.4 Thermal conductivity

Thermal transport may play a very important role in laser-induced material dynamics, especially in an optically thick sample, i.e., when there is a strong gradient in the absorbed laser pump fluence throughout the sample. Specifically, for the FeCo/Ni multilayer considered in Chapter 6, there is a strong gradient in the absorption of the pump light, which affects the magnetization dynamics. In order to accurately describe such dynamics, the dependence of the thermal conductivity of materials on the electron and phonon temperatures needs to be taken into account.

First, I consider the case for metals. There, thermal transport is mediated by electrons in the conduction band. Qualitatively, the temperature dependence of thermal conductivity κ_e can be understood by considering energy excitations of such electrons. In simple terms, the more excited an electron is the farther it is from its parent nucleus and the less it feels the atomic potential. Hot electrons should thus move more freely than cold electrons, and κ_e should increase with electron temperature. On the other hand, electron-phonon scattering limits the mean free path of electrons. The hotter the lattice, the more phonon states are occupied and, for a given electron-phonon scattering rate, the net probability of a scattering event increases. Therefore, κ_e should decrease with the lattice temperature. This behavior is not universal and depends on the electron band structure and the phonon spectrum for a given material. More details can be found in Refs. [294, 295]. According to Ref. [294], a good approximation for the temperature-dependent electron thermal conductivity is

$$\kappa_e(\theta_e, \theta_l) = C\frac{(\theta_e^2 + 0.16)^{5/4}(\theta_e^2 + 0.44)\theta}{(\theta_e^2 + 0.092)^{1/2}(\theta_e^2 + b\theta_l)}, \tag{C.7}$$

where $\theta_e = k_B T_e/\epsilon_F$, $\theta_l = k_B T_l/\epsilon_F$, and C and b are fitting parameters. The latter two can be found by fitting expression (C.7) to the experimental data in Ref. [296]. The fitting parameters are provided in Table C.1, and the result for Ni is shown in Fig. C.4 as an example. The lattice thermal conductivity for metals is, in general, negligible and I thus set $\kappa_l = 0$ for the metals in the table. The spin thermal conductivity for magnetic materials is also assumed to be zero because I am not considering spin-dependent thermal transport (not to be confused with the transport of

Table C.1: Fitting parameters for the electron thermal conductivities of Ni, Co, Cu, and Ta and their Fermi energies.

Material	C (W/m·K)	b	ϵ_F (eV)
Ni	0.94	0.0017	13.97
Co	2.49	0.005	7.97
Cu	79.06	0.06	7.00
Ta	3070	18	10.79

the spin), and, as such, κ_s should be absorbed in κ_e.

For the insulators in the multilayer stack, namely, Si_3N_4 and Ta_2O_5, $\kappa_e = 0$ because electrons are bound and do not contribute to the heat conduction which is mediated by phonons. Since the thermal conductivity of Si_3N_4 and Ta_2O_5 is much smaller than that of the metallic layers in the sample, the coupling of the thermal energy into the Si_3N_4 membrane and the Ta_2O_5 cap is very slow, and the temperature dependence of κ_l can be neglected. For Si_3N_4, $\kappa_l = 3$ W/m·K, according to [297], and for Ta_2O_5, $\kappa_l = 1$ W/m·K, according to [298].

C.5 Electron-lattice-spin coupling

The strength of the electron-lattice coupling G_{el} depends on the electron phonon-scattering rate. In most simulations, it is assumed to be constant and is used as a model fitting parameter. However, the electron-phonon interaction depends on the electrons' energy and momentum and should thus depend on the electron temperature. Ref. [299] provides an expression for the temperature-dependent electron-phonon coupling factor

$$G_{el}(T) = \frac{\pi \hbar k_B \lambda \left\langle \omega^2 \right\rangle}{g(\epsilon_F)} \int_{-\infty}^{\infty} g^2(\epsilon) \left(-\frac{\partial f}{\partial \epsilon} \right) d\epsilon, \tag{C.8}$$

where λ is an electron-phonon mass enhancement parameter [300] and $\left\langle \omega^2 \right\rangle$ is the second moment of the phonon spectrum by McMillan [301]. The factor $\lambda \left\langle \omega^2 \right\rangle$ can be approximated by $\lambda (k_B T_D)^2$ [299]. In the simulations presented in this thesis, I used $\lambda = 0.26$ for Ni [302], $\lambda = 0.41$ for Co [303], $\lambda = 0.13$ for Cu [304], and $\lambda = 0.88$ for Ta [305]. The resulting electron-phonon temperature-dependent coupling parameters for the four metals are shown in Fig. C.5. In the figure, the

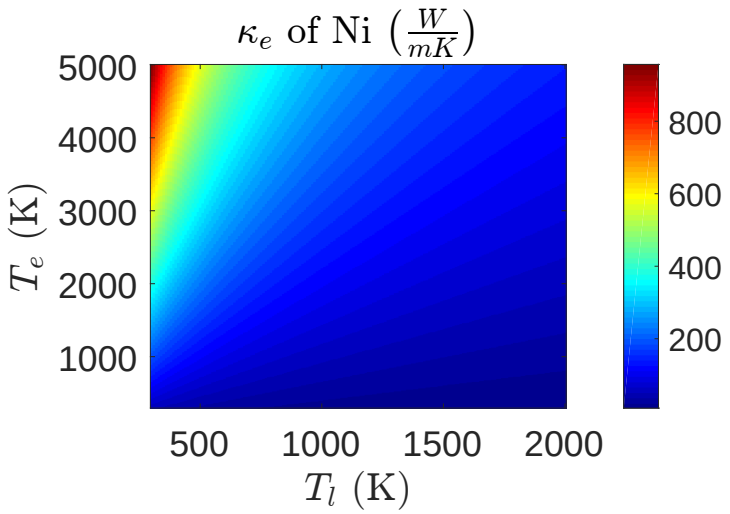

Figure C.4: Electron thermal conductivity of Ni.

temperature of the lattice is assumed to be 300 K. There is no universal trend for the curves. For Ni, the coupling becomes weaker with temperature, while for Cu and Ta it increases. For Co, the behavior is non-monotonic. An optical excitation can increase the electron temperature by almost 2 orders magnitude from the room temperature. The coupling parameter may change significantly over such a broad range of temperatures and thus should not be approximated by a constant value.

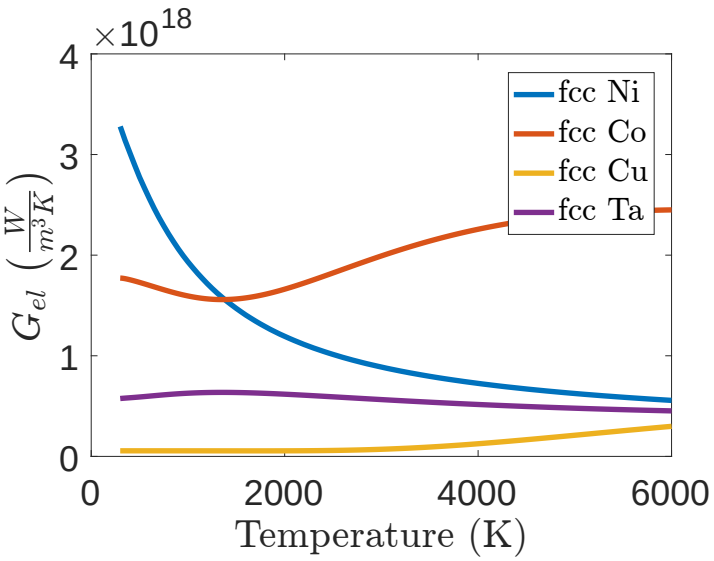

Figure C.5: Electron-phonon coupling of Ni, Co, Cu, and Ta.

For the insulating layers Si_3N_4 and Ta_2O_5, the concept of electron-phonon coupling is not applicable, but because the three-temperature model requires those inputs, I set this parameter to a small number $\sim 3 \times 10^8$ W/m^{3}K.

The electron-spin G_{es} and the lattice-spin G_{ls} coupling parameters are not known and are varied in order to fit the experimental data. Because G_{es} and G_{ls} are not independent with respect to the fitting procedure, one of them needs to be specified explicitly. I set G_{ls} to 6×10^{16} W/m^{3}K for both Ni and Co. This is in agreement with an approximate value of 1.6×10^{16} W/m^{3}K for Fe given in Ref. [306]. With $G_{es} = 3 \times 10^{17}$ W/m^{3}K for both Ni and Co, a good fit of the magnetization predicted by the three-temperature model to the experimental data is found.

As a final note for this Appendix, there is a useful online resource for the electron-lattice coupling parameter, electron specific heat, chemical potential, and density of states of multiple materials. [3]

[3] http://www.faculty.virginia.edu/CompMat/electron-phonon-coupling/

Appendix D

Bad Pixel Map for the Tabletop RMS Experiment

A map of bad pixels is shown in Fig. D.1. These pixels do not carry any information because they have either been obscured by the beam block or exposed to unblocked scattered IR light. The analysis of the RMS data in Chapter 5 takes the map in Fig. D.1 into account.

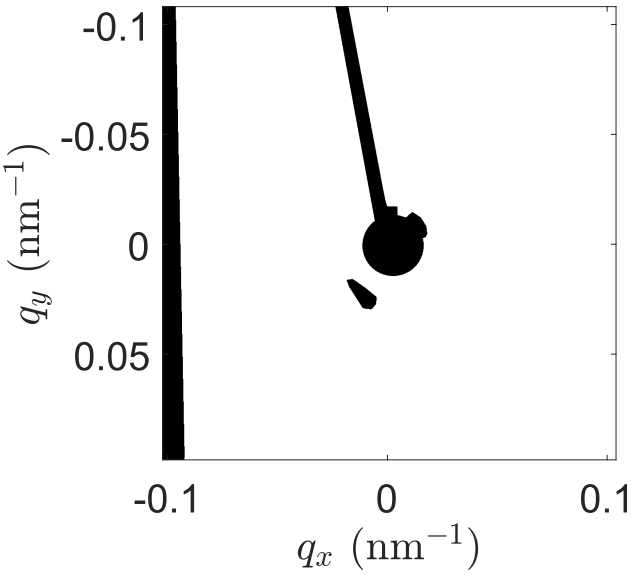

Figure D.1: Bad pixel map for the tabletop RMS expereiment. The areas with bad pixels are shown in black